Self-Assembly of Polyelectrolytes and Oppositely Charged Multivalent Cations

Dissertation

zur Erlangung des Grades eines
Doktors der Naturwissenschaften

Dr. rer. nat.

von

Nico Carl

geboren am
24.10.1992
in Coburg

Paderborn
November 2019

Die vorliegende Arbeit wurde im Zeitraum von November 2016 bis November 2019 im Fachbereich für Physikalische Chemie der Fakultät für Naturwissenschaften der Universität Paderborn unter der Betreuung von Prof. Dr. Klaus Huber angefertigt.

Prüfungsausschuss:

Prof. Dr. Klaus Huber	Erstgutachter
Prof. Dr. Stephan Förster	Zweitgutachter
Prof. Dr. Thomas Kühne	
Prof. Dr. Dirk Kuckling	Vorsitz

Tag der Einreichung:	25.11.2019
Tag der mündlichen Prüfung:	09.01.2020

Hiermit erkläre ich, die vorliegende Dissertation selbstständig verfasst zu haben. Die dazu genutzte Literatur, zu Hilfeleistungen herangezogene Institutionen sowie Beiträge anderer Personen zu dieser Arbeit werden im Rahmen der Dissertation vollständig angegeben bzw. kenntlich gemacht.

Grenoble, November 2019

Nico Carl

Acknowledgments

Mein Dank gilt meinem Doktorvater Herrn Prof. Dr. Klaus Huber für die Betreuung dieser Doktorarbeit und das in mich gesetzte Vertrauen. Die Freiheiten, die ich in den letzten drei Jahren genießen konnte und die intensiven fachlichen Diskussionen haben erheblich zum Erfolg dieser Arbeit und meiner persönlichen Entwicklung beigetragen.

Bei Herrn Prof. Dr. Stephan Förster möchte ich mich für die Übernahme der Rolle des Zweitgutachters bedanken. Weiterhin danke ich für die exzellenten Vorlesungen in physikalischer Chemie. Letztendlich, konnten mich diese für Streumethoden begeistern.

Ein großer Dank geht an Dr. Ralf Schwein für die Hilfe in den letzten drei Jahren. Du hattest stets ein offenes Ohr für mich und mich immer auf die richtige Spur geleitet. Dein Einsatz hat wesentlich dazu beigetragen, dass ich eine grandiose Zeit am ILL hatte.

Un grand merci à Dr. Sylvain Prévost pour ton soutien et ta disponibilité constante pour discuter au cours des quatre dernières années. Tu m'as beaucoup appris sur la diffusion et tu m'as toujours donné de précieux conseils.

Vielen Dank an Benni, Fabian, Kate, Marina, Markus, Nico, Rita und Susi vom Arbeitskreis Huber für die Unterstützung und die gute Arbeitsatmosphäre. Herrn Dr. Hans Egold und Frau Karin Stolte danke ich für das stets zügige und zuverlässige Messen von NMR Spektren.

Frau Dr. Xiaoqian Yu und Herrn Prof. Dr. Dirk Kuckling danke ich für die Einführung in die RAFT Polymerisation und die Möglichkeit erste Synthesen in den Labors der OC durchzuführen.

Danke an Prof. Dr. Matthias Karg für die Förderung in Bayreuth und den steten Einsatz noch offene gemeinsame Publikationen abzuschließen.

Meinen Praktikaten Miguel, Marco, Fabian und Wenke danke ich für das Interesse an den gestellten Themen und den engagierten Einsatz während der Praktika.

Thanks Aljosa for being an excellent colleague and friend during the last 2.5 years. You often reminded me, that there is more than polymers and neutrons. I am very curious what the future will bring!

A big thanks to my colleagues and friends Andrea, Sebastian, Tetiana and Marco for the support, and the pleasant atmosphere at ILL and after work.

Ein großes Dankeschön an das Institut Laue-Langevin für die Finanzierung des Projekts, die Bereitstellung von Messzeiten und die vielen Freiheiten die ich als Doktorand am ILL genießen konnte. Der Partnership for Soft Condensed Matter und dem ESRF danke ich herzlich für die Bereitstellung von Infrastruktur, Instrumenten und Messzeit.

Außerdem danke ich der Claussen-Simon Stiftung für die Förderung im Rahmen eines Masterstipendiums und dem Bundesministerium für Bildung und Forschung sowie INEOS Strylution für die Förderung im Rahmen eines Deutschlandstipendiums.

Ein großes Dankschön geht an meine Familie: Mama, Papa und Laura. Danke für euer Verständnis und die Unterstützung während des Studiums und der Promotion. Ohne euch wäre das nicht möglich gewesen.

Emilie, je te remercie pour le soutien que tu m'apportes toujours. Merci!

Zusammenfassung

Das Ziel der vorliegenden Arbeit ist die Untersuchung neuer Strategien für die Selbstorganisation von Polyelektrolyten in Gegenwart von mehrwertigen Kationen. Dafür werden zwei verschiedene Strategien verfolgt.

Der erste Ansatz nutzt die Tatsache, dass die beiden anionischen Polyelektrolyte Natriumpolyacrylat (PA) und Natriumpolystyrolsulfonat (PSS) sehr unterschiedliche Wechselwirkungen mit bivalenten Erdalkalimetallkationen aufweisen. Blockcopolymere aus PA und PSS mit unterschiedlichen PA:PSS-Verhältnissen werden synthetisiert, um diese unterschiedlichen Interaktionsmuster zur Selbstassemblierung zu nutzen. Im ersten Schritt wird das Phasenverhalten der Blockcopolymere in Gegenwart von Ca^{2+} untersucht. Stabile Blockcopolymer-Mizellen werden mit Blockcopolymeren mit relativ langen PA- und kurzen PSS-Blöcken sowie für Polymere mit gleich langen PA- und PSS-Blöcken gebildet. Im Gegensatz dazu wird keine Mizellierung beobachtet, wenn der PA-Block wesentlich kürzer ist als der PSS-Block. Es wird gezeigt, dass die spezifische Interaktion von PA mit Ca^{2+} zur Bildung eines mizellaren Kerns führt, der aus PA/Ca^{2+} besteht. PSS bildet die Korona der Mizellen, da PSS nicht spezifisch mit Ca^{2+} interagiert. Darüber hinaus wird die Wirkung der zwei Erdalkalikationen Sr^{2+} und Ba^{2+} untersucht. Beide Kationen führen zur Bildung von Blockcopolymer-Mizellen mit ähnlicher Struktur wie in Gegenwart von Ca^{2+}, wobei PA/M^{2+} den mizellaren Kern bildet.

Der Temperatureinfluss auf die Bindung von Erdalkalikationen an die jeweiligen Polyelektrolytblöcke wird als externer Trigger für die Mizellbildung genutzt. In Gegenwart von Ca^{2+} begünstigt ein Temperaturanstieg die Mizellbildung mit PA/Ca^{2+} im Mizellkern, da die Bindung von Ca^{2+} ein entropisch getriebener Prozess ist. In Anwesenheit von Sr^{2+} und Ba^{2+} ist die Situation komplexer. Eine Temperaturerhöhung führt ähnlich wie bei Ca^{2+} zur Bildung von Mizellen mit einem PA/M^{2+} Kern und einer PSS Korona. Eine Temperaturabsenkung begünstigt jedoch die Bindung von Sr^{2+} und Ba^{2+} an den PSS-Block, da es sich um einen Prozess handelt, der mit einer negativen Bindungsenthalpie verbunden ist. Kleinwinkelneutronenstreuung mit Kontrastvariation zeigt, dass Mizellen mit einem PSS/Sr^{2+} oder PSS/Ba^{2+} Kern bei niedrigen Temperaturen gebildet werden, während sich PA in der Korona der Mizellen befindet. Dieser Übergang von Mizellen mit PA/M^{2+} Kernen bei hohen Temperaturen zu PSS/M^{2+} Ker-

nen bei niedrigen Temperaturen durchläuft den Zustand von einzelnen Blockcopolymerketten bei mittleren Temperaturen. Damit sind PA-*b*-PSS-Blockcopolymere ein invertierbares mizellares System, bei dem der Kernbildungsblock durch Temperaturvariation verändert werden kann.

Für den zweiter Ansatz zur Selbstassemblierung von Polyelektrolyten wird die Komplexität des multivalenten Kations erhöht. Anstatt atomarer mehrwertige Kationen wie Ca^{2+} zu verwenden, wird ein zweiwertiger Azobenzolfarbstoff diAzoEt synthetisiert. Das Mischen des anionischen Polyelektrolyten PA mit diAzoEt führt zur Bildung einer trüben und langzeitstabilen Lösung. Kleinwinkelneutronenstreuung zeigt, dass kugelförmige und gut definierte Aggregate gebildet werden, die aus PA-Ketten bestehen, die durch den zweiwertigen Farbstoff verbunden sind. Bestrahlung mit Licht führt zur *trans* $\longrightarrow$ *cis* Isomerisierung des Azobenzolfarbstoffs und resultiert in einer Auflösung der Komplexe in einzelne PA-Ketten und *cis*-diAzoEt, welches die Ladungen des Polyelektrolyten abschirmt. Nach der Rückkehr zum thermodynamisch stabilen *trans*-Isomer werden die Komplexe neu gebildet und es kann gezeigt werden, dass die Temperatur während dieses Schritts die Größe der Aggregate steuert. Je höher die Temperatur, desto kleiner sind die resultierenden Aggregate. Dies ergibt sich aus einem Keimbildungs- und Wachstumsmechanismus, der mittels zeitaufgelöster Kleinwinkelneutronenstreuung verfolgt wird.

Abstract

The scope of the present work is to investigate new strategies for the self-assembly of polyelectrolytes in the presence of multivalent cations. This is pursued by following two different approaches.

The first approach makes use of the fact, that the two anionic polyelectrolytes sodium polyacrylate (PA) and sodium polystyrenesulfonate (PSS) show vastly different interactions with bivalent alkaline earth metal cations. Blockcopolymers of PA and PSS with varying PA:PSS ratios are synthesized, in order to use these different interaction patterns for self-assembly. In the first step, the phase behavior of the block copolymers in the presence of Ca^{2+} is investigated. Stable block copolymer micelles are found for block copolymers with relatively long PA and short PSS blocks, as well as for polymers where the PA and PSS blocks are equally long. In contrast, micellization is not observed when the PA block is considerably shorter than the PSS block. It turns out, that the specific interaction of PA with Ca^{2+} results in the formation of a micellar core composed of PA/Ca^{2+}, while PSS forms the corona of the micelles as PSS does not interact specifically with Ca^{2+}. Furthermore, the effect of two other earth alkaline cations Sr^{2+} and Ba^{2+} is investigated. Both cations result in the formation of block copolymer micelles with similar structure as in the presence of Ca^{2+}, where PA/M^{2+} forms the micellar core.

The effect of temperature on the binding of earth alkaline cations to the respective polyelectrolyte blocks is used as an external trigger for micelle formation. For Ca^{2+}, a temperature increase favors the micelle formation with PA/Ca^{2+} micellar cores, as the binding of Ca^{2+} is an entropically driven process. In the presence of Sr^{2+} and Ba^{2+}, the situation becomes more complex. An increase of temperature triggers formation of micelles with a PA/M^{2+} core and a PSS corona, similar as found for Ca^{2+}. However, a temperature decrease favors the binding of Sr^{2+} and Ba^{2+} to the PSS block, as it is a process associated with a negative binding enthalpy. Contrast variation small-angle neutron scattering (SANS) experiments provide clear-cut evidence that micelles with a PSS/Sr^{2+} or PSS/Ba^{2+} core are formed at low temperatures, while PA is located in the corona of the micelles. This transition from micelles with PA/M^{2+} cores at high temperatures to PSS/M^{2+} cores at low tmperatures passes the state of single block

copolymer chains at intermediate temperatures. This makes PA-*b*-PSS block copolymers an invertible micellar system, where the core forming block can be varied by means of temperature variation.

As a second approach for self-assembly of polyelectrolytes, the complexity of the multivalent cation is increased. Instead of using atomic multivalent cations such as Ca^{2+}, a divalent azobenzene dye diAzoEt is synthesized. Mixing the anionic polyelectrolyte PA with diAzoEt results in the formation of a turbid and long-term stable solution. SANS reveals that spherical and well-defined aggregates are formed, which are composed of PA chains connected through the divalent dye. Light irradiation triggers the *trans* $\longrightarrow$ *cis* isomerization of the azobenzene dye and results in a disassembly of the complexes into individual PA chains and *cis*-diAzoEt acting as a screening salt. Upon return to the thermodynamically stable *trans*-isomer, the complexes are reformed and it is observed, that the temperature during this reassembly step controls the size of the aggregates. The higher the temperature during reassembly, the smaller the resulting aggregates. This arises from a nucleation and growth mechanism, which was followed by time-resolved SANS.

List of Abbreviations

AFM	Atomic force microscopy
DLS	Dynamic light scattering
EDTA	Ethylenediaminetetraacetic acid
ESRF	European Synchrotron Radiation Facility
ILL	Institut Max von Laue — Paul Langevin
ITC	Isothermal titration calorimetry
LCST	Lower critical solution temperature
NMR	Nuclear magnetic resonance
PA	Sodium polyacrylate
PHEA	Poly (2-hydroxyethyl acrylate)
PSS	Sodium polystyrene sulfonate
SANS	Small-angle neutron scattering
SAS	Small-angle scattering
SAXS	Small-angle X-ray scattering
SEC	Size exclusion chromatography
SIC	Specifically interacting cation
SLS	Static light scattering
TEM	Transmission electron microscopy
UCST	Upper critical solution temperature

Table of Contents

Zusammenfassung **vii**

Abstract **ix**

List of Abbreviations **xi**

1 Introduction **1**
- 1.1 State of the art 1
- 1.2 Objective of the thesis 14
- 1.3 References 16

2 Synopsis **25**
- 2.1 Block copolymers of two negatively charged polyelectrolytes 25
- 2.2 Self-assembly of polyelectrolytes and diazobenzene dyes 29
- 2.3 Outlook 31
- 2.4 References 33

3 Presentation of own contribution **37**

4 Ion-selective binding as a new trigger for micellization of block copolyelectrolytes with two anionic blocks **41**
- 4.1 Introduction 42
- 4.2 Results and discussion 43
- 4.3 Conclusion 51
- 4.4 Supporting Information 53
- 4.5 References 74

5 Contrast variation of micelles composed of Ca^{2+} and block copolymers of two negatively charged polyelectrolytes **79**
- 5.1 Introduction 80
- 5.2 Experimental details 82
- 5.3 Results and discussion 87

5.4 Conclusion 105
5.5 Supporting Information 107
5.6 References 114

6 Invertible micelles based on ion specific interactions of Sr^{2+} and Ba^{2+} with double anionic block copolyelectrolytes 119
6.1 Introduction 120
6.2 Experiments and Data Analysis 122
6.3 Results and Discussion 128
6.4 Conclusions 144
6.5 Supporting Information 146
6.6 References 164

7 Controlling self-assembly with light and temperature 169
7.1 Introduction 170
7.2 Experimental Details 172
7.3 Results 173
7.4 Conclusions 187
7.5 Supporting Information 189
7.6 Reversibility of structure formation 196
7.7 References 201

8 List of publications 205

9 List of conference contributions 207

Chapter 1

Introduction

1.1 State of the art

1.1.1 Polyelectrolytes and specific interaction with multivalent cations

Polyelectrolytes are macromolecules with a repeating unit carrying an electrolyte group. In aqueous solution these groups can dissociate into its ions resulting in a charged polymer chain. Depending on the charge of the electrolyte group, polyelectrolytes can be separated into polyanions and polycations. Polyampholytes carry cationic as well as anionic moieties.[1] The present work deals with two common polyanions, namely sodium polyacrylate (PA) and sodium polystyrene sulfonate (PSS), shown in Figure 1.1. The sulfonate group of PSS is a strong acid resulting in deprotonation over nearly the whole pH range, which classifies PSS as a strong polyelectrolyte. In contrast, the protonation state of PA strongly depends on the pH of the solution, as PA has a pK_a of around 6.8.[2] This classifies PA as a weak polyelectrolyte.

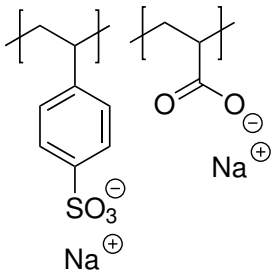


Figure 1.1: Chemical structure of sodium polystyrene sulfonate (PSS, left) and sodium polyacrylate (PA, right).

Polyelectrolytes are widely applied in a range of industrial processes, cosmetic products and food, mostly based on their ability to change flow properties or stabilize aqueous dispersions. For example, so-called superplasticizer are able to modify the flow behavior of concrete by interacting with oppositely charged colloidal particles such as calcium silicate hydrate.[3,4] As a result, the workability of curing cement is improved dramatically.[3,4] Another application of anionic polyelectrolytes is based on their ability to efficiently complex multivalent cations. This feature is employed to remove heavy metal ions in the treatment of waste water[5] or to avoid formation of limestone from hard water with a high content of Ca^{2+} and Mg^{2+} cations.

Neutral polymers can be sufficiently described by a Kuhn length l_K and an excluded volume parameter.[6] In contrast, for the correct description and understanding of polyelectrolyte solutions electrostatic forces have to be considered additionally.[7] Intensive experimental and theoretical studies were performed to understand the behavior of charged polymers in dilute and semi-dilute conditions.[8–14] In aqueous solution and in the absence of added electrolyte, the long range electrostatic repulsion of the charged monomer units leads to an extension of the polymer chain. This results in considerably larger dimensions compared to a neutral polymer of comparable molecular weight. However, the polymer conformation is still far away from a completely stretched rigid rod.[11]

Once electrolyte is added to a polyelectrolyte solution, electrostatic interaction acting between the charged monomer units is screened.[10–14] This results in shrinkage of the highly extended polymer chains, allowing it to adopt a more compact coil conformation. Increasing the electrolyte concentration further, results in stronger screening and a stronger shrinkage of the polymer chain.[10,11] Eventually, the polylelectrolyte adopts a chain conformation similar to neutral polymers. This permits adjusting good and θ-solvent conditions by varying the salt concentration at a given temperature.[10,12–14] For example, for PSS θ-conditions are reached at $4.17\,\mathrm{mol\,L^{-1}}$ of NaCl at 16.4 °C or $3.1\,\mathrm{mol\,L^{-1}}$ of KCl at 25 °C,[14,15]. For PA θ conditions are reached at $1.5\,\mathrm{mol\,L^{-1}}$ of KCl at 15 °C or $1.5\,\mathrm{mol\,L^{-1}}$ of NaCl at 25 °C.[10,12] At even higher electrolyte concentration, the polymer chains precipitate from solution, giving rise to the "salting out" effect.[16]

In principle, multivalent ions have the same screening effect on the polyelectrolyte as "inert salts" like NaCl or KCl. However, Wall *et al.*[17] showed that precipitation of the anionic polyelectrolyte PA occurs at considerably smaller electrolyte concentrations when multivalent cations such as Ca^{2+} are employed. This was considered as a type of interaction, which goes beyond pure electrostatic effects. It was assumed that the acrylate group has a certain affinity towards Ca^{2+}.[17] Indeed, it was demonstrated later that multivalent cations actually bind to the functional groups of polyelectrolytes,[18–21] giving rise to the name "specific interaction". Specifically interacting cations (SIC) lead to a more pronounced shrinking compared to "inert salts". They bind to the polyelectrolyte groups, which leads to a neutralization of monomer units and increases the hydrophobicity of the polymer chain. Eventually this leads to precipitation. Typically, SIC are multivalent cations, but also monovalent cations such as Ag^{+} are specifically interacting with polyelectrolytes.[22,23] A common approach to investigate the effect of SIC on polyelectrolytes is to add a certain amount of "inert salt" to the polyelectrolyte solution

and subsequently replace part of it by increasing the concentration of SIC. Addition of "inert salt" screens the charges of the polyelectrolyte, which prevents aggregation of the polymers due to like-charged attractions. Moreover, the structure factor between the chains is suppressed. This facilitates the interpretation of scattering experiments as only the conformation of individual chains is probed. A typical experimental approach is to prepare a solution of polyelectrolyte, for example in $100\,\mathrm{mmol\,L^{-1}}$ NaCl and dilute with a solution of $50\,\mathrm{mmol\,L^{-1}}$ $CaCl_2$ solution. Using such a procedure, keeps the concentration of positive charges $[+]$ $\left([+] = 2[Ca^{2+}] + [Na^{+}]\right)$ constant, e.g. in this case at $100\,\mathrm{mmol\,L^{-1}}$. This procedure was found to be very robust, even though the ionic strength is not kept constant. Often this effect can be neglected as the amount of added SIC is relatively small. Furthermore, binding of SIC to the polyelectrolyte effectively removes the SIC from equilibrium and makes calculation of the ionic strength prone to errors anyway.

Because a large fraction of applications of polyelectrolytes are based on the interaction with oppositely charged ions, the behavior of synthetic and natural polyelectrolytes in the presence of multivalent ions was intensively studied.[20,21,24–41] As the number of multivalent anions is limited, most of the works focus on negatively charged polyelectrolytes. The phase behavior of different polyelectrolyte/ion combinations was investigated as a function of cation,[42] polymer concentration, temperature[26,38,43] or ionic strength.[44] A variety of different phase behaviors was found ranging from precipitation of the polyelectrolyte salt above a certain cation concentration[18], to solubility over the whole range of cation concentrations[26,40] and so-called re-entrance phases.[33] Here the polymer goes again into solution at very high SIC concentrations after previously precipitating.

Polyacrylate in the presence of earth alkaline cations

Various works investigated the solution behavior of PA in the presence of the earth alkaline cations Ca^{2+}, Sr^{2+}, and Ba^{2+}.[17,18,20,21,36,42] Typically, these experiments are performed at a pH of around 9 to ensure that the carboxylate groups are fully dissociated. In general, addition of earth alkaline cations results in a decrease of the intrinsic viscosity and of the polymer dimensions, measured by the radius of gyration in static light scattering.[18] This decrease in dimension arises from the binding of SIC to the polyelectrolyte. This leads to a collapse of the polymer chain, changing from a coiled state to

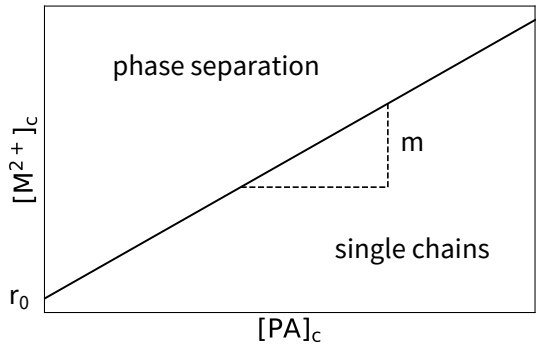


Figure 1.2: General phase diagram of PA in the presence of earth alkaline cations.

a dense sphere-like structure.[18,20,21] Upon further increase of the SIC concentration, PA starts to aggregate and eventually precipitate from the solution.

The precipitation threshold for PA/earth alkaline cations can be expressed by[20,42]

$$[M^{2+}]_c = r_0 + m[PA]_c, \tag{1.1}$$

with $[M^{2+}]_c$ being the critical cation concentration and $[PA]_c$ the critical concentration of PA monomer units where precipitation takes place. r_0 is the minimum concentration of multivalent cation required to induce precipitation at infinite polymer concentration and m reflects the stochiometry of binding. Figure 1.2 illustrates the phase diagram of PA in the presence of earth alkaline cations.

It was observed that the value for r_0 increases with increasing concentration of "inert salt" such as NaCl.[20] Increasing the concentration of Na^+ results in a higher exchange pressure necessary to replace one earth alkaline metal cation by two sodium cations. A phase behavior according to equation 1.1 implies that with increasing polymer concentration, more SIC is required to precipitate the polymer. This shows, that the binding is associated with a certain stochiometry. Therefore, complementary work on the binding of Ca^{2+} and PA as well as some industrial scale inhibitors was performed.[19] It was demonstrated, that the specific binding of Ca^{2+} to PA is an entropically driven process associated with a positive binding enthalpy ΔH. This arises from a two-step mechanism. First, two sodium cations are replaced by one Ca^{2+} and second several water molecules are released upon binding of Ca^{2+} to two carboxylate groups. Both processes are associated with a positive binding enthalpy, but the second process is dominating the recorded heat traces. In the titration experiments the small entropic contribution

from the cation exchanges is therefore hidden and a single-step process, dominated by the actual binding, is recorded. Inspired by these findings, temperature dependent light scattering experiments of PA in the presence of Ca^{2+} and Sr^{2+} were performed.[43] Samples close to the phase boundary, but still in the single chain regions were investigated. A decrease of the polymer dimensions was observed with increasing temperatures. This is expected for a process with positive binding enthalpy[43] as the free energy ΔG is given by[45]

$$\Delta G = \Delta H - T\Delta S, \tag{1.2}$$

with ΔH being the enthalpy of binding, T the temperature and ΔS the entropy of binding.

An increase of temperature results in a more dominant entropy term $T\Delta S$ and therefore enhances binding of SIC to the polyelectrolyte chain. Atomic force microscopy (AFM) and small-angle neutron scattering (SANS) showed, that pearl-necklace structures can be found when approaching the phase boundary by means of temperature variation.[36] Similar structures have been found when the phase boundary was approached by means of increasing the SIC concentration at a given temperature.[21,41]

Polystyrene sulfonate in the presence of earth alkaline cations

The specific interaction of PSS in the presence of various multivalent cations was also studied during the last years.[24,26,37,40,46–49] An extensive study investigated several cations, among them Ca^{2+}, Sr^{2+} and Ba^{2+}. It has been shown, that the precipitation of the PSS only takes place in the presence of Ba^{2+}.[40] The precipitation threshold for PSS/Ba^{2+} is independent of the PSS concentration and follows[26,47,48]:

$$[Ba^{2+}]_c = r_0. \tag{1.3}$$

$[Ba^{2+}]_c$ is the critical Ba^{2+} concentration where precipitation takes place and r_0 the minimum concentration of Ba^{2+} required to precipitate PSS. As the precipitation threshold is independent of the PSS concentration, eq. 1.3 does not contain the polymer concentration. Figure 1.3 illustrates the phasediagram of PSS/Ba^{2+}.

Upon approach of the phase boundary of Ba^{2+}/PSS the chains shrink in the presence. This takes place in semidilute[47] as well as dilute conditions[26]. The shrinkage is accompanied by the formation of compact domains, resulting in the formation of rugged cylindrical structures.[26]

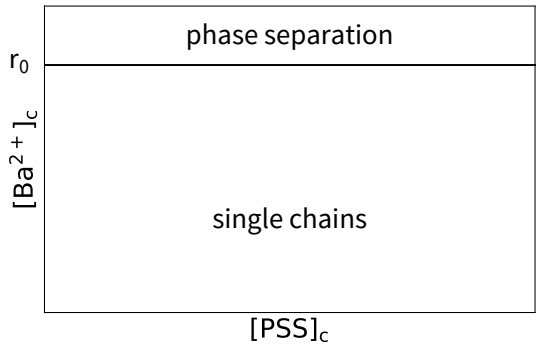


Figure 1.3: General phase diagram of PSS in the presence of Ba^{2+}.

The impact of temperature on the phase behavior for the system PSS/Ba^{2+} was also studied in detail. In contrast to PA in the presence of earth alkaline cations, PSS shrinks at low temperatures in the presence of Ba^{2+}. This occurs in semidilute[47] and dilute solution[26] and can be used to induce aggregation and precipitation of PSS chains.

Isothermal titration calorimetry (ITC) revealed, that the binding of Ba^{2+} to PSS is actually composed of two distinct contributions: First, two Na^+ cations in the polyelectrolyte domain are replaced by one Ba^{2+} cation, resulting in a relatively small gain in entropy. This is associated with a positive enthalpic contribution $\Delta H > 0$. The second step, which is the actual binding of Ba^{2+} to PSS, is a process with negative binding enthalpy $\Delta H < 0$.[24] This is in agreement with the observed solution behavior, where a decrease in temperature results in shrinkage of the polyelectrolyte and aggregation and precipitation.[26]

It was also shown by ITC, that the titration of PSS with Ca^{2+} is only associated with a relatively small entropic contribution ($\Delta H > 0$). It arises from the exchange of two sodium cations by one Ca^{2+} cation in the polyelectrolyte domains.[24] This supports the observations made for the solution behavior of PSS/Ca^{2+}, where even at Ca^{2+} concentrations as high as $1.6\,\mathrm{mol\,L^{-1}}$, no signs for shrinkage or aggregation were found.[24] It is worth mentioning, that the replacement of two sodium cations by one SIC also occurs for the titration of earth alkaline cations with PA as the first step. However, in this case the signal from the second step corresponding to the actual binding is much stronger and also associated with a positive binding enthalpy. Therefore, the small entropic contribution from the exchange of cations in the polyelectrolyte domains is hidden.

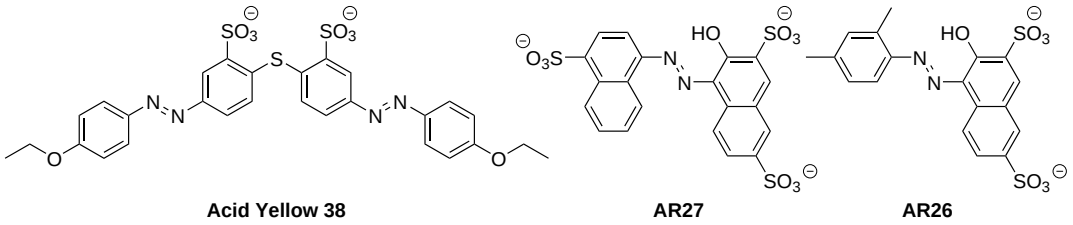


Figure 1.4: Chemical structures of some commonly used multivalent dyes.

Multivalent dyes

Instead of using multivalent atomic ions such as Ca^{2+} or Ba^{2+}, multivalent organic ions can be used for complexation with oppositely charged polyelectrolytes. To give an example, water-soluble organic dye molecules can be utilized. These have an extended aromatic system, which allows to use the optical properties of dye molecules to monitor the aggregation state of the dye.[50–52] Using dyes as counterions has the advantage that these ions allow introducing complexity and functionality into the system. As dye molecules are structurally more complex compared to their atomic equivalents, new types of interactions play a role in their association behavior with polyelectrolytes. These include electrostatic, hydrophobic and π-π interactions.[53,54] The balance between all these interactions can already lead to aggregation of the ions themselves in the absence of polyelectrolyte. This was for example shown for a mixture of two anionic azo dyes, which form worm-like aggregates in the presence of earth alkaline cations.[55–57]

Intensive work was carried out for a large variety of dye/polyelectrolyte combinations. The rich variety of dye molecules and polyelectrolytes investigated, revealed a wide range of well-defined supramolecular structures ranging from spheres, ellipsoids, cylinders and vesicles. The shape depends on the polymer type, architecture, valency of the dye, pH, ionic strength and the ratio between building blocks.[52–54,58–61] Figure 1.4 shows a few representative chemical structures of dyes used in previous works. It was shown, that for complexes formed by cationic dendrimers and anionic dyes, the anisotropy of the resulting aggregates is related to the dendrimer generation and the dye counterion structure. The higher the dendrimer generation was, the higher the anisotropy of the forming particles. Moreover, it was demonstrated that the interaction between the building blocks directs the shape of the resulting complex. Anisotropic shapes are favored when strong π-π interactions are present between the dye molecules. Also, a threshold for the dye-polyelectrolyte interaction was detected,

separating anisotropic and isotropic shapes.[53] The role of the polymer morphology was investigated by using different generations of dendrimers and linear polymers.[52] Stable aggregates were found for all polymers, except dendrimers of generation 0. However, the assemblies formed with linear polymers were more prone to be kinetically trapped.[52]

In order to introduce functionality, the effect of pH on aggregates between weak polyelectrolytes and oppositely charged dyes was investigated. This not only allows switching between the aggregated and non aggregated state by means of pH variation,[62] but also changing the morphology of the nanoparticles.[63] Another step towards more functional assemblies, is to use the *trans* $\longrightarrow$ *cis* isomerization of the divalent azo dye Acid Yellow 38 (Figure 1.4) to create light-tunable structures.[64,65] For complexes with linear polyelectrolytes, light irradiation resulted in a decrease of the aggregate size,[65] accompanied by a change of the shape from cylinders to ellipsoids.[66] Isomerization effectively varies the dye-dye interaction and leads to a different packing of the dye molecules within the aggregate.[65,66]

1.1.2 Block copolyelectrolytes

Block copolyelectrolytes combine structural elements of block copolymers and polyelectrolytes. This leads to a new class of polymers with unusual and unique properties. The majority of previous works deals with block copolymers possessing one water-soluble polyelectrolyte block and one hydrophobic block such as polystyrene.[67] In dilute aqueous solution, such polymers self-assemble into micelles composed of a core formed by the hydrophobic block and a polyelectrolyte shell.[68–73] Usage of a hydrophobic block with high glass transition temperature leads to a very low solubility of the block copolymers, as thermal energy is insufficient for molecular dissolution. The use of organic co-solvents makes it possible to dissolve the block copolymers. A subsequent dialysis against water removes the co-solvent and results in formation of block copolymer micelles. These micelles are frozen at room temperature as they are non-equilibrium structures. The use of hydrophobic blocks with a low glass transition temperature allows establishing equilibrium structures.[67]

The volume fraction of the hydrophobic polymer in the core of the micelle in aqueous solution is close to 1.[67] The corona of the micelles consists of poylelectrolyte and is swollen by water or aqueous salt solution. It has a radial density profile decaying with increasing distance from the center.[74] When polymers are densely grafted onto

the surface, in this case onto the hydrophobic core, they form a polymer brush.[75,76] Depending on the added salt concentration, two different regimes are found. In the "osmotic brush" regime, the added salt concentration is smaller than the counterion concentration of the brush. This results in a stretching of the polyelectrolyte chains and a brush thickness which is independent of the added salt concentration.[67] In contrast, in the "salted brush" regime, the added salt concentration exceeds the counterion concentration of the brush and the brush thickness decreases according to $D \propto c_s^{-\alpha}$.[75,76] For planar brushes a value of $\alpha = \frac{1}{3}$ was predicted theoretically[75] and also found experimentally.[77] However, for coronas where the brush is grafted onto a curved surface, as is the case for block copolymer micelles, considerably smaller values ranging between $0.11 < \alpha < 0.17$ were found.[74,78,79]

In order to study the structure of the polyelectrolyte block copolymers, various scattering and imaging techniques were used and combined.[67,74] These include small-angle neutron scattering (SANS), small-angle X-ray scattering (SAXS), static light scattering (SLS), dynamic light scattering (DLS), cryogenic transmission electron microscopy (cryo-TEM) and atomic force microscopy (AFM). Using such techniques showed that the corona formed by the polyelectrolyte consists of a dense inner part and an outer part with a lower density.[74]

The recent progress in controlled radical polymerization techniques, in particular reversible-addition fragmentation transfer polymerization (RAFT),[80] allows synthesizing novel types of polymers and opens routes to new types of block copolymers. This includes the direct synthesis of polyelectrolytes from the corresponding monomers in aqueous solution.[81,82] Typically, the synthesis of polyelectrolytes or polyelectrolyte block copolymers with controlled polymerization techniques, such as anionic polymerization, requires the use of protection groups. In order to obtain a polyelectrolyte as a final product, the protection groups are removed after the polymerization. An alternative synthetic route to polyelectrolytes is to use polymer-analogous reactions, such as sulfonation.[69,83,84] Both types of reactions rarely reach quantitative conversion, resulting in a partly functionalized and therefore locally hydrophobic polymer chain. Such polymers may exhibit a solution behavior and rheological properties significantly different from fully functionalized polyelectrolytes.[85] Using RAFT allows for example to synthesize double hydrophilic block copolymers composed of PA and poly(*N*-isopropylacrylamide)[86] or block copolymers of PA and PSS without the need of any protection groups.[87]

1.1.3 Small-angle scattering

Polyelectrolytes are typically studied in aqueous solution and have low contrast for imaging techniques such as electron microscopy. This makes it difficult to obtain structural information in real space. Small-angle scattering (SAS) techniques on the other hand yield ensemble averaged data of polymers in solution. This allows to easily change the sample temperature or observe *in situ* the formation of structures as a function of time.[88]

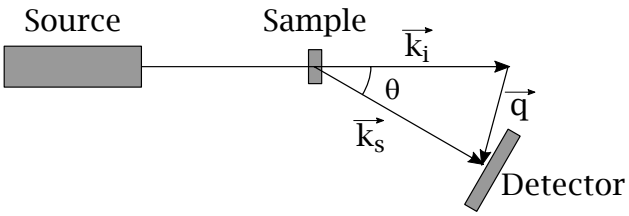


Figure 1.5: Sketch of a typical scattering experiment.

Figure 1.5 shows the layout of a typical SAS experiment. The incoming beam of highly collimated neutrons or X-rays impinges on the sample and gets scattered under a scattering angle θ. The scattered beam is detected by a detector, allowing to measure the scattering intensity as a function of scattering angle θ. In practice, instead of using the scattering angle θ the scattering vector $\vec{q}$ is defined as[88]

$$\vec{q} = \vec{k_s} - \vec{k_i}, \tag{1.4}$$

with $\vec{k_s}$ and $\vec{k_i}$ being the propagation vector of the scattered beam and incident beam, respectively. For elastic and quasielastic scattering, the only type of scattering considered in this work, the magnitude of $\vec{k_i}$ and $\vec{k_s}$ are identical. The magnitude of the scattering vector or so-called momentum transfer q corresponds to the length of $\vec{q}$ as illustrated in Figure 1.5 and is given by[88]

$$q = |\vec{q}| = \frac{4\pi}{\lambda} \sin\left(\frac{\theta}{2}\right), \tag{1.5}$$

with λ being the wavelength of neutrons in small-angle neutron scattering (SANS) or X-rays in small-angle X-ray scattering (SAXS).

In general, the scattered intensity is expressed as differential scattering cross-section per unit sample volume $\frac{d\Sigma}{d\Omega}(q)$, also called macroscopic scattering cross-section. It describes the scattering probability from the unit sample volume into the solid angle dΩ and is a quantitative description of the interaction of the radiation with the sample.

Therefore, it only depends on the structure of the sample and the type of radiation used in the experiment. It is given in absolute units and allows comparison of scattering experiments performed at different instruments.[88]

The macroscopic scattering cross-section for a system composed of particles is given by

$$\frac{d\Sigma}{d\Omega}(q) = NV^2 (\Delta\rho)^2 P(q) S(q), \tag{1.6}$$

with N being the number concentration of particles, V the volume of the particle and $\Delta\rho$ the excess scattering length density, which depends on the type of radiation used in the experiment. $P(q)$ is the form factor of the particles, characteristic for the shape and dimension of the objects and $S(q)$ is the structure factor of the particles describing the interactions between the particles.[88]

$\Delta\rho$ is given by the difference in scattering length density of the object and the solvent

$$\Delta\rho = \rho - \rho_{solvent} \tag{1.7}$$

The scattering length density is defined as:

$$\rho = \frac{b}{V_m} \tag{1.8}$$

with V_m being the molecular volume and b the scattering length for neutrons or X-rays. As the scattering length b for neutrons depends on the isotope and is considerably different for hydrogen and deuterium, it is common to use deuterated compounds or solvents for SANS. Varying the solvent composition, for example by using mixtures of light (H_2O) and heavy water (D_2O), $\rho_{solvent}$ is modified without changing the chemical nature of the solvent. This gives rise to the so-called contrast variation technique.[89,90] It allows changing $\Delta\rho$ by varying $\rho_{solvent}$ and can be used to highlight or match certain parts of multi-component systems in a SANS experiment.

For dilute systems $S(q) \approx 1$ and equation 1.6 simplifies to:

$$\frac{d\Sigma}{d\Omega} = NV^2 (\Delta\rho)^2 P(q). \tag{1.9}$$

In order to describe the experimental data properly, an appropriate model for the form factor $P(q)$ is necessary. In the limit of $q \cdot R_g < 1$, the form factor can be described by the Guinier approximation:

$$P(q) \approx \exp\left(\frac{-q^2 R_g^2}{3}\right), \tag{1.10}$$

with R_g being the radius of gyration of the particle. Equation 1.10 can be used in model-free analysis to determine information such as R_g and the forward scattering $\frac{d\Sigma}{d\Omega}(q = 0)$ without *a priori* knowledge of characteristics of the system.[88]

In order to accurately describe the experimentally measured macroscopic scattering cross-section, preliminary informations about the system are required. These can be derived from the sample concentration, molar volumes and scattering length as well as complementary techniques such as electron microscopy, AFM or nuclear magnetic resonance (NMR) spectroscopy.

Combining these information helps to develop and choose appropriate expressions for $P(q)$. Form factors for a wide variety of structures such as homogeneous spheres,[91] polymer chains,[92,93] cylinders[94,95] and block copolymer micelles[96,97] were derived and are summarized in reference [98].

1.1.4 Static and dynamic light scattering

Instead of using X-rays or neutrons one can also use visible light for a scattering experiment. For elastic scattering this technique is commonly referred to as static light scattering (SLS). Modern laser light sources provide coherent laser beams with high intensities, which are linearly polarized in SLS. Due to the use of visible light as radiation the refractive index n has to be taken into account for the calculation of the momentum transfer q[99]

$$q = \frac{4\pi n}{\lambda_0} \sin\left(\frac{\theta}{2}\right), \tag{1.11}$$

with λ_0 being the wavelength of the light *in vacuo*.

In a SLS experiment, the macroscopic scattering cross-section $\frac{d\Sigma}{d\Omega}(q)$ is measured and commonly denoted as Rayleigh ratio $\Delta R_\theta(q)$. Equation 1.9 can be reformulated as[88,100]

$$\frac{d\Sigma}{d\Omega}(q) = \Delta R_\theta(q) = KcM_w P(q), \tag{1.12}$$

with K being the optical constant, c the mass concentration, M_w the weight-averaged molecular weight and $P(q)$ the form factor. K is given by

$$K = \frac{4\pi^2}{\lambda_0^4 N_A} \left(n_{\text{Standard}} \frac{dn}{dc}\right)^2, \tag{1.13}$$

with N_A being the Avogadro constant, n_{Standard} the refractive index of the standard used for calibration of absolute intensity and $\frac{dn}{dc}$ the refractive index increment. $\frac{dn}{dc}$ is the equivalent of the scattering length density $\Delta\rho$ used in SANS and SAXS. The

advantage of expressing the Rayleigh ratio by equation 1.12 is that with knowledge of the optical constant K and the concentration c, the weight-average molecular weight is easily accessible.[88]

The form factor at low q can be described by the Guinier approximation (equation 1.10) or by the Zimm approximation:

$$\frac{1}{P(q)} \approx 1 + \frac{1}{3} q^2 R_g^2. \tag{1.14}$$

Taking into account sample-solvent interactions by means of the second virial coefficient A_2 and rearranging equation 1.12 and 1.14 one obtains the Zimm equation[101]:

$$\frac{Kc}{\Delta R_\theta} = \frac{1}{M_w} + 2A_2 c + \frac{R_g^2}{3M_w} q^2. \tag{1.15}$$

Equation 1.15 can be used together with the refractive index increment $\frac{dn}{dc}$ and a series of measurements at various concentrations c to determine A_2 and extrapolate M_w and R_g to $c = 0$ and $q = 0$.

Another scattering technique, which is highly suitable for the characterization of polyelectrolytes in solution is dynamic light scattering (DLS) or photon correlation spectroscopy. This technique exploits quasi-elastic scattering, probing temporal fluctuations of the scattering intensity and thereby making use of the large coherence of the laser light.[99]

DLS measures the intensity-time correlation function $g_2(q, \tau)$

$$g_2(q, \tau) = \frac{\left\langle I(q,t)\, I(q, t+\tau) \right\rangle}{\left\langle I(q,t) \right\rangle^2} \tag{1.16}$$

The function describes the correlation of the scattering intensity $I(q,t)$ at a given time t with the scattering intensity $I(q, t+\tau)$ at a time $t+\tau$. Consequently, g_2 does not depend on the time t but on the lag or correlation time τ. The brackets $\langle ... \rangle$ indicate that the correlation is averaged over the time t of the measurement, and the denominator $\langle I(q,t) \rangle^2$ corresponds to normalization by the averaged squared scattering intensity.[99]

The Siegert relation connects the intensity-time autocorrelation function to the field-time autocorrelation function $g_1(q, \tau)$ and is crucial for data analysis of DLS:

$$g_2(q, \tau) = 1 + \left[g_1(q, \tau) \right]^2. \tag{1.17}$$

The field-time autocorrelation $g_1(q, \tau)$

$$g_1(q, \tau) = \frac{\left\langle E(t) E(t+\tau) \right\rangle}{\left\langle E(q,t) \right\rangle^2} \tag{1.18}$$

correlates the scattered field $E(t)$ at a time t with the field $E(q, t+\tau)$ at a time $t+\tau$.

$g_1(q,\tau)$ for monodisperse dilute particles can be described by an exponential function with a relaxation rate Γ:

$$g_1(q,t) = \exp(-\Gamma\tau). \tag{1.19}$$

For polydisperse samples $g_1(q,t)$ can be described by a sum of different relaxation rates Γ_i weighted by μ_i:[102,103]

$$g_1(q,t) = \sum_{i=1}^{N} \mu_i \exp(-\Gamma_i\tau). \tag{1.20}$$

A series expansion of equation 1.20 results in an expression which is used for the so-called cumulant analysis of g_1

$$\ln(g_1(q,\tau)) = -\bar{\Gamma}\tau + \frac{\mu_2}{2!}\tau^2 - \frac{\mu_3}{3!}\tau^3 + ..., \tag{1.21}$$

with $\bar{\Gamma}$ being the average relaxation rate, μ_2 the second and μ_3 the third cumulant.[102] $\bar{\Gamma}$ allows to determine the appararent diffusion coefficient D_{app}:

$$D_{app} = \frac{\bar{\Gamma}}{q^2}. \tag{1.22}$$

In case of sample interaction, the diffusion coefficient is extrapolated to $q = 0$ and $c = 0$ yielding the z-averaged diffusion coefficient D_0 according to:[104,105]

$$D = D_0\left(1 + k_D c + C R_g^2 q^2\right), \tag{1.23}$$

where k_D and C are constants accounting for the concentration and q dependence of the apparent diffusion coefficient D_{app}.

The Stokes-Einstein equation allows to calculate the hydrodynamic radius R_h with knowledge of the diffusion coefficient D_0[99]

$$R_h = \frac{k_B T}{6\pi\eta D_0}, \tag{1.24}$$

where k_B is the Boltzmann constant, T the temperature and η the dynamic viscosity of the sample.

1.2 Objective of the thesis

The objective of this dissertation is to investigate new strategies for the self-assembly of polyelectrolytes and oppositely charged cations. Two different strategies are pursued to achieve this goal:

The first strategy makes use of a new class of like charged block copolyelectrolytes, consisting of the two anionic polyelectrolytes polyacrylate (PA) and polystyrene sulfonate (PSS).[87] The combination of two anionic polyelectrolytes with vastly different interaction schemes towards multivalent cations offers a large playground for self-assembled structures, which was largely overlooked so far. In the dissertation, preferential binding of earth alkaline cations to individual blocks of PA-*b*-PSS will be used to control self-assembly of the copolymers. The structure and morphology of the self-assembled structures will be studied by scattering methods. As described in section 1.1.1, the effect of temperature on the binding of alkaline earth cations to PA and PSS can be entirely different. For PA an increase of the temperature promotes binding of earth alkaline cations,[19,26,42,43] while for PSS a decrease of temperature promotes the binding of Ba^{2+}.[24,26,49] In both cases, coil shrinkage and eventually aggregation of the homopolyelectrolytes was achieved by means of temperature variation. Motivated by this behavior, PA-*b*-PSS block copolymers were selected as a promising candidate for a controlled response of SIC binding. This allows to tune the hydrophobicity of the polyelectrolyte blocks by temperature variation. Therefore, the effect of temperature on the self-assembly of PA-*b*-PSS will be studied and it will be elucidated if an invertible micellar system can be realized in the presence of earth alkaline cations.

The second strategy for self-assembly of polyelectrolytes and oppositely charged cations is to increase the complexity of the multivalent cation. For this purpose a divalent cationic diazobenzene dye is synthesized.[106] The diazobenzene dye undergoes a *trans* $\longrightarrow$ *cis* isomerization upon irradiation with UV light which results in an increased polarity of the dye.[107] In contrast to previous studies,[53,66,108] the π-π interaction between the dye molecules are rather weak making electrostatic interactions the main driving force for complex formation with oppositely charged polyelectrolytes. It will be investigated if the isomerization influences the binding of the cation to polyelectrolytes and therefore the structure of the polyelectrolyte-dye complexes. In addition, the reverse process will be studied as the *cis*-isomer is a metastable state and conversion back to the *trans*-isomer takes place. It will be elucidated if the initial structures are reformed upon return to the *trans* state, which is of utter importance for the design of functional light-responsive materials.[64,65,108] In conclusion, a potential system will be developed, where the specific interaction can be controlled by an external stimulus such as light.

The present work is a cumulative thesis and therefore presents the results in terms of four separate chapters based on four individual peer-reviewed articles.

Chapter 4 presents the synthesis of PA-*b*-PSS block copolymers and their self-assembly in the presence of Ca^{2+}. Equally important, it demonstrates that this micelle formation is reversible either through a change in temperature or by addition of a complexing agent such as EDTA. Moreover, a preliminary characterization of the micelle structure is presented using contrast variation SANS.

Chapter 5 extends chapter 4 by providing an in-depth model-independent and model-dependent analysis of contrast variation SANS experiments on PA-*b*-PSS micelles and combines this with SAXS and light scattering experiments. This robust approach is also employed on samples which show an isotope effect during the contrast variation experiment and on samples with a fully hydrogenated block copolymer.

Chapter 6 demonstrates that invertible micelles can be realized by combining PA-*b*-PSS block copolymers with Sr^{2+} and Ba^{2+}. Temperature is used as a main stimulus to form block copolymer micelles at low and high temperatures, with an intermediate regime of single chains. The structure of the micelles at low and high temperatures is entirely different, as will be probed by SANS, SAXS and light scattering. This can be well understood by the thermodynamics of binding of the multivalent cations to the corresponding polyelectrolyte blocks.

Chapter 7 deals with the self-assembly of a PA homopolymer and a divalent azobenzene cation. Dye and polyelectrolyte form well-defined spherical aggregates, which can be disassembled by shining UV-light on the sample. This triggers the *trans* $\longrightarrow$ *cis* isomerization of the dye. During relaxation of the *cis* back to the *trans*-state, structures are reformed. The size of those structures can be precisely tailored by controlling the temperature during isomerization. Monitoring the self-assembly process with time-resolved SANS gives valuable insight into the mechanism of structure formation.

1.3 References

1. Tieke, B., *Makromolekulare Chemie*, 3. Edition; Wiley-VCH Verlag GmbH & Co. KGaA: Weinheim, Germany, 2014.
2. Charman, W. N.; Christy, D. P.; Geunin, E. P.; Monkhouse, D. C. *Drug Dev. Ind. Pharm.* **1991**, *17*, 271–280, DOI: 10.3109/03639049109043824.
3. Marchon, D.; Sulser, U.; Eberhardt, A.; Flatt, R. J. *Soft Matter* **2013**, *9*, 10719–10728, DOI: 10.1039/c3sm51030a.

4. Flatt, R. J.; Schober, I.; Raphael, E.; Plassard, C.; Lesniewska, E. *Langmuir* **2009**, *25*, 845–855, DOI: 10.1021/la801410e.
5. Mundkur, S. D.; Watters, J. C. *Sep. Sci. Technol.* **1993**, *28*, 1157–1168, DOI: 10.1080/01496399308018026.
6. Rubinstein, M.; Colby, R. H., et al., *Polymer physics*; Oxford university press New York: 2003; Vol. 23.
7. Muthukumar, M. *Macromolecules* **2017**, *50*, 9528–9560, DOI: 10.1021/acs.macromol.7b01929.
8. Dobrynin, A. V.; Colby, R. H.; Rubinstein, M. *Macromolecules* **1995**, *28*, 1859–1871, DOI: 10.1021/ma00110a021.
9. Dobrynin, A. V.; Rubinstein, M. *Prog. Polym. Sci.* **2005**, *30*, 1049–1118, DOI: 10.1016/j.progpolymsci.2005.07.006.
10. Schweins, R.; Hollmann, J.; Huber, K. *Polymer* **2003**, *44*, 7131–7141, DOI: 10.1016/j.polymer.2003.07.005.
11. Flory, P. J.; Osterheld, J. E. *J. Phys. Chem.* **1954**, *58*, 653–661, DOI: 10.1021/j150518a014.
12. Hara, M.; Nakajima, A. *Polym. J.* **1980**, *12*, 701–709, DOI: 10.1295/polymj.12.701.
13. Takahashi, A.; Kato, T.; Nagasawa, M. *J. Phys. Chem.* **1967**, *71*, 2001–2010, DOI: 10.1021/j100866a600.
14. Hirose, E.; Iwamoto, Y.; Norisuye, T. *Macromolecules* **1999**, *32*, 8629–8634, DOI: 10.1021/ma990813b.
15. Takahashi, A.; Kato, T.; Nagasawa, M. *Phys. Chem.* **1967**, *71*, 2001–2010, DOI: 10.1021/j100866a600.
16. Ikegami, A.; Imai, N. *J. Polym. Sci.* **1962**, *56*, 133–152, DOI: 10.1002/pol.1962.1205616312.
17. Wall, F. T.; Drenan, J. W. *J. Polym. Sci.* **1951**, *7*, 83–88, DOI: 10.1002/pol.1951.120070107.
18. Huber, K. *J. Phys. Chem.* **1993**, *97*, 9825–9830, DOI: 10.1021/j100140a046.
19. Sinn, C. G.; Dimova, R.; Antonietti, M. *Macromolecules* **2004**, *37*, 3444–3450, DOI: 10.1021/ma030550s.

20. Schweins, R.; Huber, K. *Eur. Phys. J. E* **2001**, *5*, 117–126, DOI: 10 . 1007 / s101890170093.
21. Schweins, R.; Lindner, P.; Huber, K. *Macromolecules* **2003**, *36*, 9564–9573, DOI: 10.1021/ma0347722.
22. Huber, K.; Witte, T.; Hollmann, J.; Keuker-Baumann, S. *J. Am. Chem. Soc.* **2007**, *129*, 1089–1094, DOI: 10.1021/ja063368q.
23. Ezhova, A.; Huber, K. *Macromolecules* **2014**, *47*, 8002–8011, DOI: 10 . 1021 / ma501146m.
24. Hansch, M.; Kaub, H. P.; Deck, S.; Carl, N.; Huber, K. *J. Chem. Phys.* **2018**, *148*, 114906, DOI: 10.1063/1.5019877.
25. Dubois, E.; Boué, F. *Macromolecules* **2001**, *34*, 3684–3697, DOI: 10.1021/ma000956u.
26. Hansch, M.; Hämisch, B.; Schweins, R.; Prévost, S.; Huber, K. *J. Chem. Phys.* **2018**, *148*, 014901, DOI: 10.1063/1.5006618.
27. Sabbagh, I.; Delsanti, M. *Eur. Phys. J. E* **2000**, *1*, 75–86, DOI: 10 . 1007 / s101890050009.
28. Matulis, D.; Rouzina, I.; Bloomfield, V. A. *J. Mol. Biol.* **2000**, *296*, 1053–1063, DOI: 10.1006/jmbi.1999.3470.
29. Sabbagh, I.; Delsanti, M.; Lesieur, P. *Eur. Phys. J. B* **1999**, *12*, 253–260, DOI: DOI10.1007/s100510051002.
30. Xu, X.; Mastropietro, D.; Ruths, M.; Tirrell, M.; Yu, J. *Langmuir* **2019**, DOI: 10.1021/acs.langmuir.9b01984.
31. Braun, M. K.; Wolf, M.; Matsarskaia, O.; Da Vela, S.; Roosen-Runge, F.; Sztucki, M.; Roth, R.; Zhang, F.; Schreiber, F. *J. Phys. Chem. B* **2017**, *121*, 1731–1739, DOI: 10.1021/acs.jpcb.6b12814.
32. Combet, J.; Rawiso, M.; Rochas, C.; Hoffmann, S.; Boué, F. *Macromolecules* **2011**, *44*, 3039–3052, DOI: 10.1021/ma102226v.
33. De la Cruz, M. O.; Belloni, L.; Delsanti, M.; Dalbiez, J. P.; Spalla, O.; Drifford, M. *J. Chem. Phys.* **1995**, *103*, 5781–5791, DOI: 10.1063/1.470459.
34. Satoh, M.; Hayashi, M.; Komiyama, J.; Iijima, T. *Polymer* **1990**, *31*, 501–505, DOI: 10.1016/0032-3861(90)90393-D.

35. Drifford, M.; Delsanti, M. In *Phys. Chem. polyelectrolytes*; CRC Press: 2001, pp 157–184.

36. Lages, S.; Lindner, P.; Sinha, P.; Kiriy, A.; Stamm, M.; Huber, K. *Macromolecules* **2009**, *42*, 4288–4299, DOI: 10.1021/ma8027547.

37. De la Cruz, M. O.; Belloni, L.; Delsanti, M.; Dalbiez, J. P.; Spalla, O.; Drifford, M. *J. Chem. Phys.* **1995**, *103*, 5781–5791, DOI: 10.1063/1.470459.

38. Lee, C. L.; Muthukumar, M. *J. Chem. Phys.* **2009**, *130*, 1–9, DOI: 10.1063/1.3054140.

39. Ikeda, Y.; Beer, M.; Schmidt, M.; Huber, K. *Macromolecules* **1998**, *31*, 728–733, DOI: 10.1021/ma970540p.

40. Narh, K. A.; Keller, A. *J. Polym. Sci. Part B Polym. Phys.* **1993**, *31*, 231–234, DOI: 10.1002/polb.1993.090310213.

41. Lages, S.; Goerigk, G.; Huber, K. *Macromolecules* **2013**, *46*, 3570–3580, DOI: 10.1021/ma400427d.

42. Schweins, R.; Goerigk, G.; Huber, K. *Eur. Phys. J. E* **2006**, *21*, 99–110, DOI: 10.1140/epje/i2006-10047-7.

43. Lages, S.; Schweins, R.; Huber, K. *J. Phys. Chem. B* **2007**, *111*, 10431–10437, DOI: 10.1021/jp068258k.

44. Schweins, R. Gestaltsänderung gelöster anionischer Polyacrylatketten in Gegenwart von Erdalkaliionen, PhD Thesis, University of Paderborn, 2002.

45. Atkins, P.; de Paula, J., *Atkins' Physical Chemistry*; OUP Oxford: 2010.

46. Drifford, M.; Dalbiez, J.-P.; Delsanti, M.; Belloni, L. *Berichte der Bunsengesellschaft für Phys. Chemie* **1996**, *100*, 829–835, DOI: 10.1002/bbpc.19961000624.

47. Prabhu, V.; Muthukumar, M.; Wignall, G.; Melnichenko, Y. *Polymer* **2001**, *42*, 8935–8946, DOI: 10.1016/S0032-3861(01)00382-2.

48. Prabhu, V. M.; Muthukumar, M.; Wignall, G. D.; Melnichenko, Y. B. *J. Chem. Phys.* **2003**, *119*, 4085–4098, DOI: 10.1063/1.1592496.

49. Kanai, S.; Muthukumar, M. *J. Chem. Phys.* **2007**, *127*, 244908, DOI: 10.1063/1.2806299.

50. Gröhn, F.; Klein, K.; Brand, S. *Chem. - A Eur. J.* **2008**, *14*, 6866–6869, DOI: 10.1002/chem.200800650.

51. Willerich, I.; Ritter, H.; Gröhn, F. *J. Phys. Chem. B* **2009**, *113*, 3339–3354, DOI: 10.1021/jp8096605.
52. Willerich, I.; Schindler, T.; Gröhn, F. *J. Phys. Chem. B* **2011**, *115*, 9710–9719, DOI: 10.1021/jp204368t.
53. Mariani, G.; Moldenhauer, D.; Schweins, R.; Gröhn, F. *J. Am. Chem. Soc.* **2016**, *138*, 1280–1293, DOI: 10.1021/jacs.5b11497.
54. Mariani, G.; Schweins, R.; Gröhn, F. *Macromolecules* **2016**, *49*, 8661–8671, DOI: 10.1021/acs.macromol.6b00565.
55. Michels, R.; Hertle, Y.; Hellweg, T.; Huber, K. *J. Phys. Chem. B* **2013**, *117*, 15165–15175, DOI: 10.1021/jp405206p.
56. Michels, R.; Goerigk, G.; Vainio, U.; Gummel, J.; Huber, K. *J. Phys. Chem. B* **2014**, *118*, 7618–7629, DOI: 10.1021/jp502347b.
57. Michels, R.; Sinemus, T.; Hoffmann, J.; Brutschy, B.; Huber, K. *J. Phys. Chem. B* **2013**, *117*, 8611–8619, DOI: 10.1021/jp403985m.
58. Gröhn, F.; Klein, K.; Koynov, K. *Macromol. Rapid Commun.* **2010**, *31*, 75–80, DOI: 10.1002/marc.200900386.
59. Mariani, G.; Schweins, R.; Gröhn, F. *Macromol. Chem. Phys.* **2017**, *218*, 1–9, DOI: 10.1002/macp.201700191.
60. Willerich, I.; Li, Y.; Gröhn, F. *J. Phys. Chem. B* **2010**, *114*, 15466–15476, DOI: 10.1021/jp107358q.
61. Gröhn, F. *Soft Matter* **2010**, *6*, 4296, DOI: 10.1039/cosm00411a.
62. Willerich, I.; Gröhn, F. *Chem. - A Eur. J.* **2008**, *14*, 9112–9116, DOI: 10.1002/chem.200801167.
63. Mariani, G.; Schweins, R.; Gröhn, F. *J. Phys. Chem. B* **2016**, *120*, 1380–1389, DOI: 10.1021/acs.jpcb.5b10966.
64. Willerich, I.; Gröhn, F. *Angew. Chemie - Int. Ed.* **2010**, *49*, 8104–8108, DOI: 10.1002/anie.201003271.
65. Moldenhauer, D.; Gröhn, F. *J. Polym. Sci. Part B Polym. Phys.* **2013**, *51*, 802–816, DOI: 10.1002/polb.23276.
66. Mariani, G.; Krieger, A.; Moldenhauer, D.; Schweins, R.; Gröhn, F. *Macromol. Rapid Commun.* **2018**, *1700860*, 1700860, DOI: 10.1002/marc.201700860.

67. Förster, S.; Abetz, V.; Müller, A. H. E. In *Polyelectrolytes with Defin. Mol. Archit. II*, 2004; Vol. 166, pp 173–210, DOI: 10.1007/b11351.

68. Selb, J.; Ganot, Y. *Makromol Chem* **1980**, *181*, 809–822, DOI: 10.1002/macp.1980.021810405.

69. Valint, P. L.; Bock, J. *Macromolecules* **1988**, *21*, 175–179, DOI: 10.1021/ma00179a035.

70. Astafieva, I.; Zhong, X. F.; Eisenberg, A. *Macromolecules* **1993**, *26*, 7339–7352, DOI: 10.1021/ma00078a034.

71. Astafieva, I.; Khougaz, K.; Eisenberg, A. *Macromolecules* **1995**, *28*, 7127–7134, DOI: 10.1021/ma00125a015.

72. Zhang, L.; Eisenberg, A. *Science (80-.).* **1995**, *268*, 1728–1731, DOI: 10.1126/science.268.5218.1728.

73. Zhang, L.; Barlow, R. J.; Eisenberg, A. *Macromolecules* **1995**, *28*, 6055–6066, DOI: 10.1021/ma00122a010.

74. Förster, S.; Hermsdorf, N.; Böttcher, C.; Lindner, P. *Macromolecules* **2002**, *35*, 4096–4105, DOI: 10.1021/ma011565y.

75. Pincus, P. *Macromolecules* **1991**, *24*, 2912–2919, DOI: 10.1021/ma00010a043.

76. Argillier, J. F.; Tirrell, M. *Theor. Chim. Acta* **1992**, *82*, 343–350, DOI: 10.1007/BF01113936.

77. Guenoun, P.; Schalchli, A.; Sentenac, D.; Mays, J. W.; Benattar, J. J. *Phys. Rev. Lett.* **1995**, *74*, 3628–3631, DOI: 10.1103/PhysRevLett.74.3628.

78. Guenoun, P.; Davis, H. T.; Tirrell, M.; Mays, J. W. *Macromolecules* **1996**, *29*, 3965–3969, DOI: 10.1021/ma946438z.

79. Hariharan, R.; Biver, C.; Russel, W. B. *Macromolecules* **1998**, *31*, 7514–7518, DOI: 10.1021/ma9718199.

80. Barner-Kowollik, C., *Handbook of RAFT Polymerization*; Barner-Kowollik, C., Ed.; Wiley-VCH Verlag GmbH & Co. KGaA: Weinheim, Germany, 2008, DOI: 10.1002/9783527622757.

81. Chaduc, I.; Lansalot, M.; D'Agosto, F.; Charleux, B. *Macromolecules* **2012**, *45*, 1241–1247, DOI: 10.1021/ma2023815.

82. Chaduc, I.; Crepet, A.; Boyron, O.; Charleux, B.; D'Agosto, F.; Lansalot, M. *Macromolecules* **2013**, *46*, 6013–6023, DOI: 10.1021/ma401070k.

83. Li, H.-M.; Liu, J.-C.; Zhu, F.-M.; Lin, S.-A. *Polym. Int.* **2001**, *50*, 421–428, DOI: 10.1002/pi.646.

84. Zhang, M.; Breiner, T.; Mori, H.; Müller, A. H. *Polymer* **2003**, *44*, 1449–1458, DOI: 10.1016/S0032-3861(02)00774-7.

85. Filippov, A. D.; van Hees, I. A.; Fokkink, R.; Voets, I. K.; Kamperman, M. *Macromolecules* **2018**, *51*, 8316–8323, DOI: 10.1021/acs.macromol.8b01440.

86. Schilli, C. M.; Zhang, M.; Rizzardo, E.; Thang, S. H.; Chong,) Y. K.; Edwards, K.; Karlsson, G.; Müller, A. H. E. *Macromolecules* **2004**, *37*, 7861–7866, DOI: 10.1021/ma035838w.

87. Yap, H. P.; Hao, X.; Tjipto, E.; Gudipati, C.; Quinn, J. F.; Davis, T. P.; Barner-Kowollik, C.; Stenzel, M. H.; Caruso, F. *Langmuir* **2008**, *24*, 8981–8990, DOI: 10.1021/la8011074.

88. Zemb, T.; Lindner, P., *Neutrons, X-rays and light: scattering methods applied to soft condensed matter*; North-Holland: 2002.

89. Stuhrmann, H. B. *J. Appl. Crystallogr.* **1974**, *7*, 173–178, DOI: 10.1107/S0021889874009071.

90. Ibel, K.; Stuhrmann, H. *J. Mol. Biol.* **1975**, *93*, 255–265, DOI: 10.1016/0022-2836(75)90131-X.

91. Rayleigh, L. *Proc. Roy. Soc. London* **1911**, *A84*, 25–38.

92. Hammouda, B. *Polym. Charact.* **1993**, *106*, 87–133, DOI: 10.1007/BFb0025862.

93. Debye, P. *J. Phys. Colloid Chem.* **1947**, *51*, 18–32, DOI: 10.1021/j150451a002.

94. Fournet, G. *Bull. Minéralogie* **1951**, *74*, 37–172.

95. Fournet, G.; Guinier, A. *J. Phys. le Radium* **1950**, *11*, 516–520, DOI: 10.1051/jphysrad:01950001108-9051600.

96. Pedersen, J. S.; Gerstenberg, M. C. *Macromolecules* **1996**, *29*, 1363–1365, DOI: 10.1021/ma9512115.

97. Svaneborg, C.; Pedersen, J. S. *Macromolecules* **2002**, *35*, 1028–1037, DOI: 10.1021/ma011046v.

98. Pedersen, J. S. *Adv. Colloid Interface Sci.* **1997**, *70*, 171–210, DOI: 10.1016/S0001-8686(97)00312-6.

99. Berne, B. J.; Pecora, R., *Dynamic Light Scattering: With Applications to Chemistry, Biology, and Physics*; Dover Publications: Mineola, New York, USA, 2000.

100. Johnson, C. S.; Gabriel, D. A., *Laser Light Scattering*; Dover Publications: Mineola, New York, USA, 1995.

101. Zimm, B. H. *J. Chem. Phys.* **1948**, *16*, 1093–1099, DOI: 10.1063/1.1746738.

102. Koppel, D. E. *J. Chem. Phys.* **1972**, *57*, 4814–4820, DOI: 10.1063/1.1678153.

103. Frisken, B. J. *Appl. Opt.* **2001**, *40*, 4087, DOI: 10.1364/AO.40.004087.

104. Schmidt, M.; Stockmayer, W. H. *Macromolecules* **1984**, *17*, 509–514, DOI: 10.1021/ma00134a001.

105. Stockmayer, W. H.; Schmidt, M. *Pure Appl. Chem.* **1982**, *54*, 407–414, DOI: 10.1351/pac198254020407.

106. Zinchenko, A. A.; Tanahashi, M.; Murata, S. *ChemBioChem* **2012**, *13*, 105–111, DOI: 10.1002/cbic.201100492.

107. Hartley, G. S.; Le Fèvre, R. J. W. *J. Chem. Soc.* **1939**, 531–535, DOI: 10.1039/JR9390000531.

108. Mariani, G.; Kutz, A.; Di, Z.; Schweins, R.; Gröhn, F. *Chem. - A Eur. J.* **2017**, *23*, 6249–6254, DOI: 10.1002/chem.201605194.

Chapter 2

Synopsis

The dissertation includes four publications and manuscripts outlined in Chapter 4, 5, 6 and 7. The results of these chapters are summarized in Sections 2.1 and 2.2 of the present chapter, followed by an outlook.

2.1 Block copolymers of two negatively charged polyelectrolytes

One of the main themes in the present work is to employ block copolymers of two anionic polyelectrolytes for self-assembly. This is realized by using polyelectrolyte blocks, which have different interaction patterns with earth alkaline cations.[1–10] In Chapter 4, the synthesis and characterization of such block copolymers composed of sodium polyacrylate (PA) and sodium polystyrene sulfonate (PSS) is described. Figure 2.1 shows the chemical structure of this type of block copolymers. The left structure shows a polymer with both blocks being hydrogenated and the right structure shows a polymer with the PSS block being hydrogenated and the PA block deuterated. In order to investigate the influence of the block ratio of PA and PSS on the self-assembly in the presence of multivalent cations, several block copolymers with varying PA/PSS ratios are synthesized.

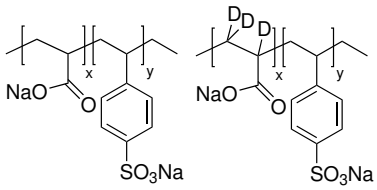


Figure 2.1: Chemical structure of PA-*b*-PSS block copolymers with fully hydrogenated blocks (left) and the PA block being fully deuterated (right).

Table 2.1 lists the synthesized polymers together with the realized ratios between PA and PSS blocks. The subscript number denotes the degree of polymerization of the corresponding block. As SANS is used as one of the main techniques to characterize the structure of the polyelectrolytes a part of the polymers carries a deuterated PA block, denoted as d_3-PA, while h_3-PA indicates a hydrogenated PA block.

Ca^{2+} is chosen as a cation to start the investigation of the phase behavior of the block copolymers, as it is expected to only interact with PA but not with PSS.[2,8] This makes

Table 2.1: Overview of PA-*b*-PSS polymers used in the present work. The subscript number denotes the degree of polymerization and d_3-PA and h_3-PA deuteration and hydrogenation of the PA block.

Sample	PA:PSS /mol%
h_3-$PA_{1190}PSS_{70}$	94:6
d_3-$PA_{1190}PSS_{70}$	94:6
d_3-$PA_{360}PSS_{400}$	47:53
h_3-$PA_{100}PSS_{750}$	12:88

it an ideal reference state for more complex interaction patterns. For block copolymers with a long PA and a short PSS block (d_3-$PA_{1190}PSS_{70}$ and h_3-$PA_{1190}PSS_{70}$), as well as with equal ratios of PA and PSS blocks (d_3-$PA_{360}PSS_{400}$) stable micelles are found in the presence of Ca^{2+}. Micelles formation arises from the specific binding of Ca^{2+} to the PA block. In contrast, the polymer with a long PSS and a short PA block (h_3-$PA_{100}PSS_{750}$) does not show micellization in the presence of Ca^{2+}, as the PA block required to form micelles is not sufficiently long.

In order to demonstrate the role of Ca^{2+} binding to the PA block, self-assembly is reversed by addition of ethylenediaminetetraacetic acid (EDTA). EDTA complexes the Ca^{2+} cations, which were previously bound to PA, resulting in a return to the single chain state. Alternating Ca^{2+} and EDTA additions results in formation and dissolution of the micelles, proving that the process is fully reversible. More insight into the role of Ca^{2+} binding to the PA block is obtained by preparing a sample in the single chain regime close to the micelle transition. Increase of the temperature promotes the binding of Ca^{2+} to PA as it is an entropically driven process[11,12] and initiates the formation of micelles. Performing temperature cycles between 25 °C and 65 °C with this specimen allows to switch between single chains and micelles. This nicely illustrates that triggering self-assembly by means of temperature variation is also a fully reversible process.

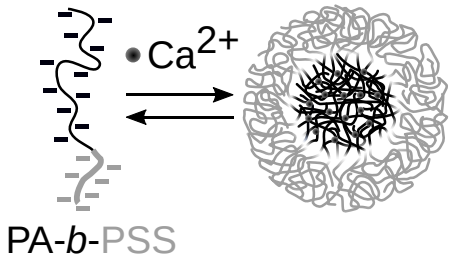


Figure 2.2: Scheme of the block copolymers of PA-*b*-PSS formed in the presence of Ca^{2+}.

In order to get an insight into the structure of the micelles, the two polymers with deuterated PA blocks d_3-$PA_{1190}PSS_{70}$ and d_3-$PA_{360}PSS_{400}$ are employed for a contrast variation SANS experiment.[13,14] This is realized by utilizing different ratios of H_2O/D_2O as solvent. The theoretical match point is calculated from the chemical composition and the scattering length density[15] and compared to the experimentally found one. Both values are in excellent agreement, confirming the success of the block copolymer synthesis and the validity of the polymer characterization. A preliminary analysis of the scattering data reveals, that indeed d_3-PA forms the core of the micelles. This is in agreement with the previous results and highlights that the binding of Ca^{2+} to PA is the main origin for the self-assembly. PSS forms the corona of the well-defined spherical block copolymer micelles and stabilizes them. Figure 2.2 schematically shows the micellization of PA-*b*-PSS in the presence of Ca^{2+}.

Chapter 5 provides an in-depth analysis of the contrast-variation experiment with a suitable form factor model.[16] In addition to the two deuterated samples, the fully hydrogenated polymer h_3-$PA_{1190}PSS_{70}$ is investigated. The SANS data are complemented by SAXS and DLS data, with SAXS and DLS being performed on the same samples as used for contrast variation SANS. Comparison of the SAXS profiles of d_3-$PA_{360}PSS_{400}$ at varying H_2O/D_2O ratios shows, that change of solvent from light to heavy water has no influence on the micellar structure. However, for d_3-$PA_{1190}PSS_{70}$ and h_3-$PA_{1190}PSS_{70}$, the SAXS data show a continuous shift of the form factor minima to higher momentum transfers q when the D_2O content is increased. This corresponds to a slight decrease of the micelle size with increasing D_2O content and highlights the importance of combining SAXS and SANS. A form factor model composed of a homogeneous PA core and a PSS corona[16] is applied simultaneously to all SANS data at variable H_2O/D_2O ratios and the corresponding SAXS profiles. This approach yields reliable information about the structure and dimensions of the micelles. d_3-$PA_{360}PSS_{400}$ micelles have a considerably smaller aggregation number of 19 compared to d_3-$PA_{1190}PSS_{70}$ and h_3-$PA_{1190}PSS_{70}$ with aggregation numbers of $168 \geqslant N_{agg} \geqslant 126$ and $145 \geqslant 117$, respectively. It turned out that the micelle core is highly swollen by solvent, with water contents between 83 % and 85 %. The resulting micellar core radius from d_3-$PA_{360}PSS_{400}$ is 8.8 nm and is considerably smaller than the core radius of micelles from d_3-$PA_{1190}PSS_{70}$ (23.7 nm) and from h_3-$PA_{1190}PSS_{70}$ (22.3 nm).

The analysis of the scattering data also shows that the structure of the corona varies with changing block ratio.[17] For the polymer with the short PSS block, the corona is rather thin with a radius of gyration of the PSS chains of 2.1 nm. In contrast, the radius

of gyration of the PSS chains for d_3-$PA_{360}PSS_{400}$ is 8.6 nm, which results in a considerably thicker corona. The reduced surface coverage $\frac{\Sigma}{\Sigma^*}$, which is the two-dimensional equivalent of $\frac{c}{c^*}$ with c being the concentration and c^* the overlap concentration, is used to obtain more information about the polymer chains in the corona.[16, 17] For d_3-$PA_{360}PSS_{400}$ micelles $\frac{\Sigma}{\Sigma^*}$ is larger than the critical value of unity showing that the PSS chains overlap. This leads to excluded volume effects of the chains in the corona. In contrast, values of $\frac{\Sigma}{\Sigma*}$ around 0.2 are found for d_3-$PA_{1190}PSS_{70}$ and h_3-$PA_{1190}PSS_{70}$ micelles, indicating that the PSS chains of those micelles are not overlapping.

The isotope effect observed for d_3-$PA_{1190}PSS_{70}$ and h_3-$PA_{1190}PSS_{70}$ when changing the solvent from H_2O to D_2O is also investigated in greater detail. As the effect only occurs for the polymers with the long PA block, it is obvious that the binding of Ca^{2+} to PA plays an important role. The binding of Ca^{2+} to PA in H_2O and D_2O is measured using ITC, which reveals that the binding constant and stochiometry of binding are essentially identical in both solvents. Nevertheless, the binding enthalpy ΔH is slightly larger in D_2O compared to H_2O. It is concluded that this slight difference controls the binding of Ca^{2+} and obviously the aggregation number of the micelles.

Moreover, a model free analysis of the scattering data only requiring the chemical composition of the block copolymers and the scattering length densities is carried out.[13] The analysis confirms once more that d_3-PA forms the core of the micelles and PSS the corona. In addition, it allows the determination of the micelle dimensions.[13,14,18] The found values are in excellent agreement with the results from the form factor fits. Finally, the model free analysis is successfully employed to the fully hydrogenated polymer h_3-$PA_{1190}PSS_{70}$, using the fact that the scattering length densities of h_3-PA and PSS are not identical. In conclusion, the used method is a powerful approach for systems where no mathematical expressions for the form factor are available and even works on systems where deuteration is not practical or feasible.

After understanding the phase behavior of PA-*b*-PSS in the presence of Ca^{2+}, Chapter 6 extends this knowledge to the earth alkaline cations Sr^{2+} and Ba^{2+}. It is demonstrated, that a similar phase behavior as found for Ca^{2+} is also observed for Sr^{2+} and Ba^{2+}. The resulting micelles also have a core formed by PA/M^{2+} and a corona of PSS. Micelle formation for Sr^{2+} is based on the fact, that PSS does not show a specific interaction with Sr^{2+} at room temperature.[7] For Ba^{2+} the binding situation is more complex. It interacts with PA as well as PSS specifically.[7,8,19] However, the precipitation threshold of Ba^{2+}/PA is considerably lower as the one for Ba^{2+}/PSS. As a result the interaction of Ba^{2+} with PA dominates the phase behavior of PA-*b*-PSS.

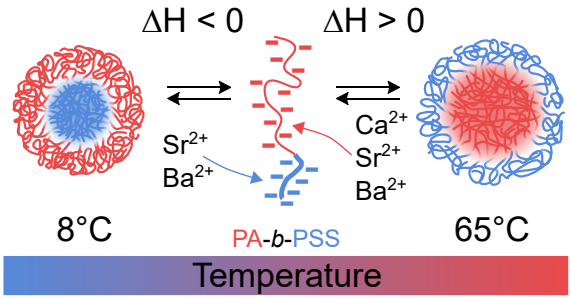


Figure 2.3: Scheme of the invertible micelles realized with PA-*b*-PSS.

Based on previous works, it was anticipated that temperature has a strong influence on the binding of earth alkaline cations to the polyelectrolytes. Therefore, samples of a selected PA-*b*-PSS (d_3-$PA_{1190}PSS_{70}$) are prepared close to the micellization threshold in the presence of Ca^{2+}, Sr^{2+} and Ba^{2+}. For all three samples, the polymer is present as a single chain at room temperature and upon increase of temperature micelle formation is observed. This arises from the entropic binding of M^{2+} to the PA block.[11,12] In contrast, micelle formation is observed at low temperatures only in the presence of Sr^{2+} and Ba^{2+}. This can be attributed to the different thermodynamics of binding of those cations to PSS. As in the case of PA, M^{2+} binding is composed of a two-step process. First, M^{2+} penetrates into the domains of PSS and releases sodium cation, which is entropically favorable. Next, the actual binding of M^{2+} to PSS takes place, which is associated with a negative binding enthalpy.[19] This second process is responsible for the promoted binding of Sr^{2+} and Ba^{2+} to PSS at low temperatures. A SANS experiment with a partly deuterated block copolymer indeed shows that PA forms the core at high temperatures, while PSS forms the micelle core at low temperatures. As a conclusion, an invertible micellar system can be realized with PA-*b*-PSS in the presence of Sr^{2+} and Ba^{2+}. Figure 2.3 summarizes the temperature dependent phase behavior of PA-*b*-PSS in the presence of earth alkaline cations.

2.2 Self-assembly of polyelectrolytes and diazobenzene dyes

After increasing the complexity of the polymer by introducing a new type of block-copolyelectrolytes, Chapter 7 deals with increasing the complexity of the multivalent cation. For this purpose, a divalent diazobenzene cation diAzoEt is synthesized, which

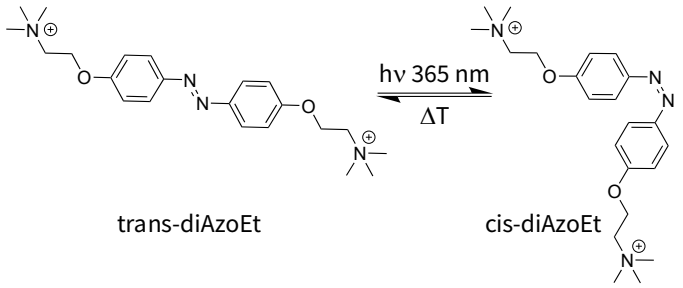


Figure 2.4: Chemical structure of the *trans* and *cis*-isomer of diAzoEt.

can undergo a *trans* $\longrightarrow$ *cis* isomerization under light irradiation as shown in Figure 2.4.

Mixing the anionic polyelectrolyte PA with diAzoEt results in the formation of highly turbid solutions, indicating the formation of large assemblies. The aggregates are only stable, when 80 %-100 % of the PA monomer units are complexed by the cation. Beyond charge neutrality the structures precipitate from solution. Complexes between PSS and diAzoEt are only stable in a very narrow regime around charge neutrality and are therefore not further investigated. The structure of the PA/diAzoEt assemblies is characterized by SANS and it is shown that spherical complexes composed of PA/diAzoEt are formed.[20] Similarly, as previously observed for PA-*b*-PSS micelles, the spherical aggregates are highly swollen by water. Illumination of the complexes with UV light at 365 nm triggers the *trans* $\longrightarrow$ *cis* isomerization of diAzoEt and turns the highly turbid solutions into clear ones. SANS shows that the assemblies are effectively dissolved into individual PA chains. The *cis*-dye is more polar compared to the *trans*-isomer and has a higher water solubility.[21] This results in a higher hydrophilicity and lower tendency of binding to the oppositely charged PA. Effectively, *cis*-diAzoEt acts as an inert salt and screens the charges of the individual PA chains.

Relaxation of the *cis*-isomer back into the thermodynamically stable *trans*-isomer promotes the binding to PA and results in reformation of well-defined PA-diAzoEt aggregates. It turns out that the temperature during this step strongly influences the size of the aggregates, with smaller sizes occurring at higher temperatures. Monitoring the reformation step with time-resolved SANS allows to follow the structure formation *in-situ*. This experiment reveals that the self-assembly process takes place in three distinct steps: first *cis*-dye is converted back to the *trans*-isomer and immediately binds to the PA chain. Once a sufficient amount of dye is converted to the *trans*-isomer, the second step entitled as nucleation phase, takes place. This very rapid process is followed by the

third step which is the growth step to the final aggregate size. Control of the nucleation phase through temperature allows to influence the number of nuclei and therefore the final size of the structures.

2.3 Outlook

New strategies for the self-assembly of polyelectrolytes with multivalent cations are explored in the present thesis. One strategy utilizes block copolymers of PA and PSS and makes use of the specific interaction of earth alkaline cations with the corresponding blocks. At room temperature Ca^{2+} and Sr^{2+} only interact with PA but not with PSS. In contrast, Ba^{2+} interacts with the PA as well as with the PSS block of the copolymer. As the precipitation threshold of PA/Ba^{2+} is found to be considerably lower than the one for PSS/Ba^{2+}, the binding of Ba^{2+} to the PA block still dominates the association behavior at moderate concentrations of Ba^{2+}. This results in block copolymer micelles with a PA/Ba^{2+} core and PSS corona.

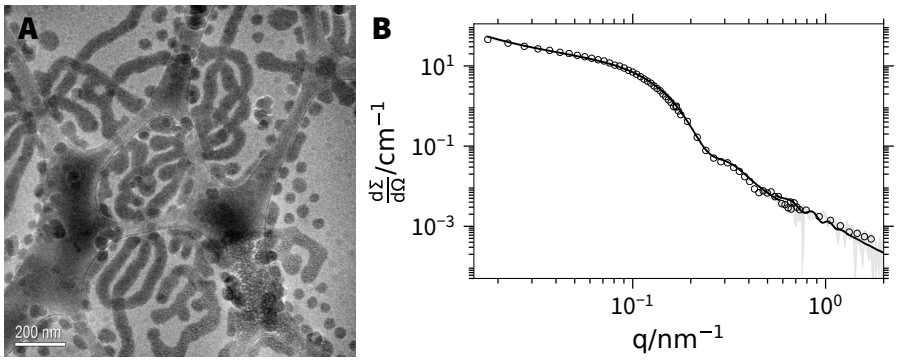


Figure 2.5: **A** Cryo-TEM micrography and **B** SANS profile of PA-*b*-PSS in the presence of Ba^{2+}. The solid line represents a fit to the form factor model of a mixture of spherical[22] and worm-like block copolymer micelles.[23]

When the concentration of Ba^{2+} for such a micellar sample is increased beyond 20 mmol L^{-1} Ba^{2+} the polymer precipitates from solution. This is attributed to the precipitation threshold of the PSS block with Ba^{2+}[8] and leads to a vanishing stabilization of the micelles by the PSS corona and finally precipitation of the micelles. Investigation of samples close to this precipitation threshold shows a transition from spherical micelles to worm-like micelles. Figure 2.5 shows a micrograph obtained from cryogenic transmission-electron microscopy and a SANS profile of such a sample. Both techniques

provide evidence for the presence of elongated structures. It is expected that the precipitation of PSS/Ba^{2+} plays an important role in this morphological transition. However, the region where these structures can be studied is rather small as they precipitate from solution once the Ba^{2+}/PSS threshold is crossed.

In order to prevent precipitation of the block copolymer another block, acting as stabilizing block, can be introduced. Therefore, a block copolymer is synthesized, containing PA, PSS and poly (2-hydroxyethyl acrylate) (PHEA). PHEA is a water soluble but non-ionic polymer and Figure 2.6 shows the chemical structure of the PA-*b*-PSS-*b*-PHEA triblock copolymer. First experiments with such a polymer show that block copolymer micelles are formed in the presence of Ba^{2+} and that those are stable up to very high Ba^{2+} concentrations of 250 $mmol\,L^{-1}$. So far, worm-like micelles for PA-*b*-PSS-*b*-PHEA blockcopolymer are only found at very high Ba^{2+} concentrations of 250 $mmol\,L^{-1}$ Ba^{2+}. This probably arises from the unfavorable ratios between hydrophilic (PHEA) and hydrohpobic (PA/Ba^{2+} and PSS/Ba^{2+}) blocks, which favors the formation of spherical rather than worm-like micelles. However, this nicely demonstrates that introducing PHEA as a stabilizing block is an effective approach and a promising route for the study of the transition from spherical to worm-like micelles. A detailed study of the phase behavior and the influence of the block ratios of PA, PSS and PHEA is highly promising but unfortunately beyond the scope of this work.

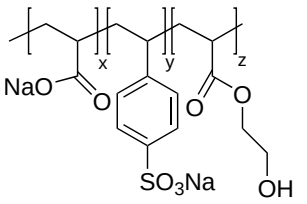


Figure 2.6: Chemical structure of PA-*b*-PSS-*b*-PHEA a triblock copolymer.

The second strategy for the self-assembly of polyelectrolytes employs the divalent dye cation diAzoEt. Complexes between PA and diAzoEt result in well-defined spherical aggregates, which can be manipulated by triggering the *trans* $\longrightarrow$ *cis* isomerization of the dye with UV light. However, the PA-diAzoEt aggregates are only stable up to charge neutrality between polyelectrolyte and dye. Beyond they precipitate from solution. Introducing PHEA as a water-soluble but non-ionic stabilizing block may also be interesting for this system. Employing a PA-*b*-PHEA block copolymer could extend the stability of the complexes beyond charge neutrality. This would dramatically increase the versatility of the light controlled self-assembly process.

A constant challenge during this work is the characterization of block copolymers. In the present work a combination of SLS, DLS and NMR is used to characterize the synthesized polymers. However, the standard technique for the determination of the

molecular weight and polydispersity of block copolymers is size-exclusion chromatography (SEC).[24] Characterizing polyelectrolytes with SEC requires suitable column materials and the use of aqueous solvents.[25,26] Reliable protocols for aqueous SEC only exist for homopolymers of polyelectrolytes. Identifying suitable solvents and column materials for the characterization of block copolyelectrolytes with SEC would provide an important tool for the characterization of such materials. This is highly relevant in respect of the rapid progress in controlled radical polymerization techniques as the use of polyelectrolytes and water-soluble polymers is expected to increase.[27,28]

2.4 References

1. Wall, F. T.; Drenan, J. W. *J. Polym. Sci.* **1951**, *7*, 83–88, DOI: 10.1002/pol.1951.120070107.
2. Huber, K. *J. Phys. Chem.* **1993**, *97*, 9825–9830, DOI: 10.1021/j100140a046.
3. Schweins, R.; Lindner, P.; Huber, K. *Macromolecules* **2003**, *36*, 9564–9573, DOI: 10.1021/ma0347722.
4. Schweins, R.; Huber, K. *Eur. Phys. J. E* **2001**, *5*, 117–126, DOI: 10.1007/s101890170093.
5. Schweins, R.; Goerigk, G.; Huber, K. *Eur. Phys. J. E* **2006**, *21*, 99–110, DOI: 10.1140/epje/i2006-10047-7.
6. Lages, S.; Lindner, P.; Sinha, P.; Kiriy, A.; Stamm, M.; Huber, K. *Macromolecules* **2009**, *42*, 4288–4299, DOI: 10.1021/ma8027547.
7. Narh, K. A.; Keller, A. *J. Polym. Sci. Part B Polym. Phys.* **1993**, *31*, 231–234, DOI: 10.1002/polb.1993.090310213.
8. Hansch, M.; Hämisch, B.; Schweins, R.; Prévost, S.; Huber, K. *J. Chem. Phys.* **2018**, *148*, 014901, DOI: 10.1063/1.5006618.
9. Prabhu, V.; Muthukumar, M.; Wignall, G.; Melnichenko, Y. *Polymer* **2001**, *42*, 8935–8946, DOI: 10.1016/S0032-3861(01)00382-2.
10. Prabhu, V. M.; Muthukumar, M.; Wignall, G. D.; Melnichenko, Y. B. *J. Chem. Phys.* **2003**, *119*, 4085–4098, DOI: 10.1063/1.1592496.
11. Sinn, C. G.; Dimova, R.; Antonietti, M. *Macromolecules* **2004**, *37*, 3444–3450, DOI: 10.1021/ma030550s.

12. Lages, S.; Schweins, R.; Huber, K. *J. Phys. Chem. B* **2007**, *111*, 10431–10437, DOI: 10.1021/jp068258k.

13. Stuhrmann, H. B. *J. Appl. Crystallogr.* **1974**, *7*, 173–178, DOI: 10.1107/S0021889874009071.

14. Ibel, K.; Stuhrmann, H. *J. Mol. Biol.* **1975**, *93*, 255–265, DOI: 10.1016/0022-2836(75)90131-X.

15. Zemb, T.; Lindner, P., *Neutrons, X-rays and light: scattering methods applied to soft condensed matter*; North-Holland: 2002.

16. Svaneborg, C.; Pedersen, J. S. *Macromolecules* **2002**, *35*, 1028–1037, DOI: 10.1021/ma011046v.

17. Svaneborg, C.; Pedersen, J. S. *Phys. Rev. E* **2001**, *64*, 010802, DOI: 10.1103/PhysRevE.64.010802.

18. Moore, P. B. In *Methods Exp. Phys.* Elsevier: 1982; Vol. 20, pp 337–390.

19. Hansch, M.; Kaub, H. P.; Deck, S.; Carl, N.; Huber, K. *J. Chem. Phys.* **2018**, *148*, 114906, DOI: 10.1063/1.5019877.

20. Pedersen, J. S.; Hamley, I. W.; Ryu, C. Y.; Lodge, T. P. *Macromolecules* **2000**, *33*, 542–550, DOI: 10.1021/ma990740w.

21. Hartley, G. S.; Le Fèvre, R. J. W. *J. Chem. Soc.* **1939**, 531–535, DOI: 10.1039/JR9390000531.

22. Pedersen, J. S.; Gerstenberg, M. C. *Macromolecules* **1996**, *29*, 1363–1365, DOI: 10.1021/ma9512115.

23. Pedersen, J. S. *J. Appl. Crystallogr.* **2000**, *33*, 637–640, DOI: 10.1107/S0021889899012248.

24. Tieke, B., *Makromolekulare Chemie*, 3. Edition; Wiley-VCH Verlag GmbH & Co. KGaA: Weinheim, Germany, 2014.

25. Lacík, I. et al. *Macromol. Chem. Phys.* **2015**, *216*, 23–37, DOI: 10.1002/macp.201400339.

26. Bruessau, R. J. *Makromol. Chemie. Macromol. Symp.* **1992**, *61*, 190–218, DOI: 10.1002/masy.19920610116.

27. Moad, G.; Rizzardo, E.; Thang, S. H. *Aust. J. Chem.* **2012**, *65*, 985–1076, DOI: 10.1071/CH12295.

28. Barner-Kowollik, C., *Handbook of RAFT Polymerization*; Barner-Kowollik, C., Ed.; Wiley-VCH Verlag GmbH & Co. KGaA: Weinheim, Germany, 2008, DOI: 10.1002/9783527622757.

Chapter 3

Presentation of own contribution

Chapter 4

The chapter was published under the title *Ion-selective binding as a new trigger for micellization of block copolyelectrolytes with two anionic blocks* in Soft Matter.
Own contribution

- Synthesis and characterization of the polymers and their phase behavior
- Preparation of all samples for the SANS, SAXS and light scattering experiments
- Performance of all experiments
- Data analysis
- Discussion of the presented results
- Co-authorship of the publication

Coauthors' contribution

- Dr. Sylvain Prévost and Dr. Ralf Schweins provided help for the SANS measurements, contributed to the interpretation and discussion of the results as well as writing the publication.
- Prof. Dr. Klaus Huber contributed to the discussion and interpretation of the results and wrote the majority of the publication.

Chapter 5

The chapter was accepted for publication under the title *Contrast variation of micelles composed of Ca^{2+} and block copolymers of two negatively charged polyelectrolytes* in Colloid and Polymer Science.
Own contribution

- Synthesis and characterization of the polymers and their phase behavior

- Preparation of all samples for the SANS, SAXS and light scattering experiments
- Performance of all experiments
- Data analysis
- Discussion of the presented results
- Authorship of the publication

Coauthors' contribution

- Dr. Sylvain Prévost and Dr. Ralf Schweins provided help for the SANS measurements, contributed to the interpretation and discussion the results as well as writing the publication.
- Prof. Dr. Klaus Huber contributed to the discussion and interpretation of the results and contributed to writing the publication.

Chapter 6

The chapter was published under the title *Invertible Micelles Based on Ion Specific Interactions of Sr^{2+} and Ba^{2+} with Double Anionic Block Copolyelectrolytes* in Macromolecules.
Own contribution

- Synthesis and characterization of the polymers and their phase behavior
- Preparation of all samples for the SANS, SAXS, ITC and light scattering experiments
- Performance of all experiments
- Data analysis
- Discussion of the presented results
- Authorship of the publication

Coauthors' contribution

- Dr. Sylvain Prévost provided help for the SAXS measurements at ID02 (ESRF, Grenoble) and SANS measurements, contributed to the interpretation and discussion of the results.
- Dr. Ralf Schweins provided help for the SAXS measurements at D2AM (ESRF, Grenoble) and SANS measurements, contributed to the interpretation and discussion of the results and to writing the publication.
- Dr. Judith Houston assisted with the SANS measurements at KWS II (FRM Munich) and data reduction.
- Dr. Isabelle Morfin assisted with the SAXS measurements at D2AM (ESRF, Grenoble) and data reduction.
- Prof. Dr. Klaus Huber contributed to the discussion and interpretation of the results and contributed to writing the publication.

Chapter 7

The chapter was published under the title *Controlling self-assembly with light and temperature* to Langmuir.
Own contribution

- Synthesis and characterization of the polymer and the azobenzene dye
- Preparation of all samples for SANS experiments
- Performance of the SANS experiments.
- Analysis of the SANS data.
- Discussion of the presented results.
- Authorship of the publication.

Coauthors' contribution

- Wenke Müller performed the UV-Vis absorbance experiments and analyzed the obtained data under my supervision.
- Dr. Ralf Schweins provided help for the SANS measurements and contributed to the interpretation and discussion of the results.
- Prof. Dr. Klaus Huber contributed to the discussion and interpretation of the results and to writing the publication.

Chapter 4

Ion-selective binding as a new trigger for micellization of block copolyelectrolytes with two anionic blocks

Abstract

This work presents well-defined and switchable micelles of block copolymers consisting of the two anionic polyelectrolytes sodium polyacrylate (NaPA) and sodium polystyrene sulfonate (NaPSS). Micellization occurs due to the specific binding of Ca^{2+} to acrylate groups, which results in neutralization of the corresponding block and thereby formation of the hydrophobic core of the micelles. In contrast, the PSS block remains charged and forms the stabilizing shell. Micellization is triggered by variations of the Ca^{2+} concentration or the temperature and is a fully reversible and repeatable process. Small-Angle Neutron Scattering (SANS) could unambiguously reveal the structure of the micelles, using a partially deuterated polymer and the contrast variation technique. Considering the variety of metal cations and their broad spectrum of interactions with polyelectrolytes, this new class of like-charged block copolymers opens the door to a broad range of switchable and responsive polyelectrolyte-based systems.

This chapter is based on Carl, N.; Prévost, S.; Schweins, R.; Huber, K.; Ion-selective binding as a new trigger for micellization of block copolyelectrolytes with two anionic blocks; *Soft Matter*, **2019**, 15, 8266-8271, DOI: 10.1039/C9SM01138B published by The Royal Society of Chemistry.

4.1 Introduction

Block copolymers establish a family of versatile macromolecules, capable of combining diverse properties and response patterns in one polymer chain.[1,2] They can mediate among different phases, acting as surfactants in aqueous media or compatibilizing two different non-miscible polymers.[2–4] Most of the works published so far on block copolymers deal with the combination of either two neutral polymers[5–8] or one neutral and one charged block.[9–13] The present work establishes an entirely new strategy, where characteristic features of two different anionic polyelectrolytes shall be introduced into block copolymeric systems. The motivation for pursuing such a strategy is based on a rich variety of interactions between polyelectrolytes and metal cations in aqueous solutions. Such interactions may be purely electrostatic in nature, leading to counterion condensation and charge screening or they may be chemically specific. Such specific interactions corresponding to complex binding of the cations to the anionic residues neutralize the polyelectrolyte chains partly or entirely and drastically change their solution behavior.[14] We employ this specific interaction to form micelles.

Previous work addressed the specific interaction of Ca^{2+} with sodium polyacrylate (NaPA),[15–21] where the cations form complex bonds with the negatively charged COO^- residues of the PA chain. Upon increase of the Ca^{2+} concentration the polyelectrolytes get increasingly neutralized by Ca^{2+} until a critical concentration $[Ca^{2+}]_c$ is reached, beyond which a precipitation threshold according to

$$[Ca^{2+}]_c = m + r_0[PE] \tag{4.1}$$

is crossed for this particular system, where [PE] is the concentration of polyelectrolyte monomer units, m the minimum concentration of Ca^{2+} required to precipitate the polymer at infinite dilution and r_0 reflects the stoichiometry of binding. Isothermal titration calorimetry with NaPA and Ca^{2+} revealed a strong endothermic reaction thus supporting the strong binding of Ca^{2+} to COO^-[22] due to the release of two sodium cations and several water molecules upon binding. Consequently, temperature variations can be used as a second mode to control the phase behavior in addition to a variation of the Ca^{2+} concentration.[23] An increase in temperature is expected to promote further binding of Ca^{2+} to anionic PA chains and thus to induce precipitation of a CaPA phase.

In contrast, sodium polystyrenesulfonate (NaPSS) and Ca^{2+} do not show specific interactions. No matter how large the concentration of Ca^{2+} gets PSS remains soluble

in water. Light scattering and isothermal titration calorimetry demonstrated that PSS chains do not aggregate in the presence of Ca^{2+} and no binding takes place.[24,25]

Blockcopolymers of PSS and PA combine this diverging response pattern toward Ca^{2+} cations in one polymer. Whereas the PA block is expected to become decorated with Ca^{2+} cations, thus changing its solution behavior in water drastically, the PSS block only interacts non-specifically with Ca^{2+}, thus staying soluble. Only one publication is known to the authors, which reports on the synthesis of a PA-*b*-PSS block copolymer and applies it to form multi-layers by a layer-by-layer assembly.[26]

In the present work, PA-*b*-PSS block copolymers are synthesized in order to investigate how the combination of the two different response patterns towards Ca^{2+} affect the solution behavior of such block copolyelectrolytes. The investigation is motivated by the chance to unravel a new toolbox for the design of switchable materials to be controlled via the selection of block lengths, type of cation or temperature.

4.2 Results and discussion

4.2.1 Polymer characterization

Four different block copolyelectrolytes of PSS and PA are investigated in this work. Two polymers have a deuterated PA block, one with a long PA and a short PSS block (d_3-$PA_{1190}PSS_{70}$) and one with a symmetric block ratio (d_3-$PA_{360}PSS_{400}$). Deuteration facilitates a meaningful small angle neutron scattering experiment (SANS) based on contrast variation, which shall provide clear insight in the block copolyelectrolyte morphology induced by Ca^{2+} cations. One further polymer serves as the fully hydrogenated reference for the asymmetrical case (h_3-$PA_{1190}PSS_{70}$) and the fourth polymer has a long PSS and a short PA block (h_3-$PA_{100}PSS_{750}$). The subscript denotes the degree of polymerization. Synthesis of the block copolymers proceeded via RAFT polymerization (Sec

Table 4.1: Overview of polymers, compositions, weight-averaged molecular weights M_w and hydrodynamic radii R_h determined from NMR and static/dynamic light scattering in $0.1\,mol\,L^{-1}$ NaCl in the absence of $CaCl_2$

Sample	PA:PSS /mol%	M_w /kg mol^{-1}	R_h /nm
h_3-$PA_{1190}PSS_{70}$	94:6	160 ± 3	13.8 ± 0.6
d_3-$PA_{1190}PSS_{70}$	94:6	181 ± 3	13.6 ± 0.5
d_3-$PA_{360}PSS_{400}$	47:53	127 ± 1	10.4 ± 0.2
h_3-$PA_{100}PSS_{750}$	12:88	220 ± 2	14.0 ± 0.2

4.4.1 of the ESI†). In all cases, the shorter block served as macro RAFT agent, which was successively exposed to the RAFT polymerization of the second monomer. Characterization of the resulting block copolyelectrolytes was carried out with NMR and static and dynamic light scattering (SLS and DLS). NMR revealed the ratio between PA and PSS blocks, fully in agreement with the anticipated values. Although compatible with the formation of block copolymers, NMR cannot entirely exclude coexistence of the blocks as separate coils. SLS and DLS further support the formation of the proper block copolyelectrolytes as the values for the respective weight averaged molar mass values M_w are in agreement with the values calculated from NMR and DLS in no case showed a second mode. Characterisation of polyelectrolytes with size exclusion chromatography (SEC), particularly in cases of more complex morphologies such as block copolyelectrolytes, is extremely challenging.[27] We tried to develop a SEC-protocol in aqueous $0.1\,\mathrm{mol\,L^{-1}}$ Na_2HPO_4 and failed to obtain meaningful results. As shall be outlined later on, SANS at variable scattering contrast, which is the major tool of the present work in unravelling the morphology of the resulting aggregates, provides an independent proof of the successful connection of the two blocks. The characterization of all four block copolyelectrolytes are summarized in Table 4.1. Detailed data are given in Sec 4.4.2 of the ESI†.

4.2.2 Phase behavior in the presence of Ca^{2+}

The set of block copolyelectrolytes reveals a remarkable response pattern in aqueous solutions of $CaCl_2$. At low Ca^{2+} concentrations, all samples show single chain behaviour. With increasing $CaCl_2$ concentration, the polymer with the longest PA block ($PA_{1190}PSS_{70}$) reaches a threshold beyond which stable aggregates are formed (Figure 4.1A). This is in contrast to pure PA, which exhibits a precipitation threshold instead. The line of aggregation shows the same trend as the respective precipitation threshold in case of pure PA.[15] Upon further increase of the Ca^{2+} concentration, a second threshold line appears depicting precipitation of the aggregates.

Noteworthy, the exchange of deuterated by hydrogenated PA (d_3-$PA_{1190}PSS_{70}$ versus h_3-$PA_{1190}PSS_{70}$) does not affect this solution behavior. By decreasing the PSS/PA block ratio to the symmetric case (d_3-$PA_{360}PSS_{400}$), the regime of stable single coils is even extended and the aggregation threshold gets almost horizontal. No second phase boundary indicating precipitation is detected in this case. Strikingly, the polymer with the long PSS and short PA block (h_3-$PA_{100}PSS_{750}$) remains stable in the state of single

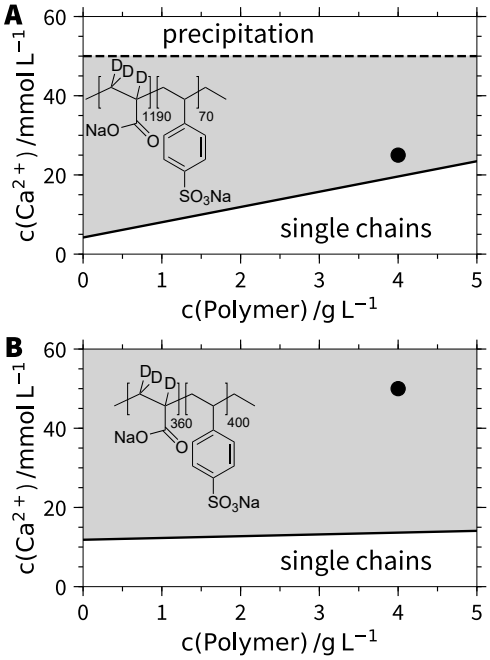


Figure 4.1: Phase diagrams of (A) d_3-$PA_{1190}PSS_{70}$/ h_3-$PA_{1190}PSS_{70}$ and (B) d_3-$PA_{360}PSS_{400}$ in the presence of Ca^{2+}. The black points indicate the points where SANS experiments with contrast variation were performed.

coils throughout the entire probed phase diagram. This complex pattern can be nicely reconciled with the response pattern of the two pure polyelectrolytes in solution. As PSS does not show any specific interactions within aqueous solution remaining soluble at any Ca^{2+} concentration, this feature also dominates as long as the PSS block is long enough. With increasing length of the PA block, specific interactions among PA and Ca^{2+} come into play, which induce a precipitation in case of pure PA and which lead to aggregates in case of block copolyelectrolytes, obviously stabilized by the PSS blocks. At short enough PSS blocks, the aggregation threshold starts to resemble the precipitation line of pure PA. Thus, the PSS blocks confine the typical precipitation threshold of pure PA (eq 4.1) now to domains of stable aggregates keeping them in solution. However, the short PSS blocks cannot prevent precipitation of the polymers at very high Ca^{2+} content establishing a second phase boundary.

These findings suggest that the aggregates adopt a micellar shape where the Ca^{2+}/PA complexes caused by specific interactions form the less soluble core with this core being stabilized by the dangling and still soluble anionic PSS blocks. This morphology justifies the use of the term micelles from now and the structure of those micelles

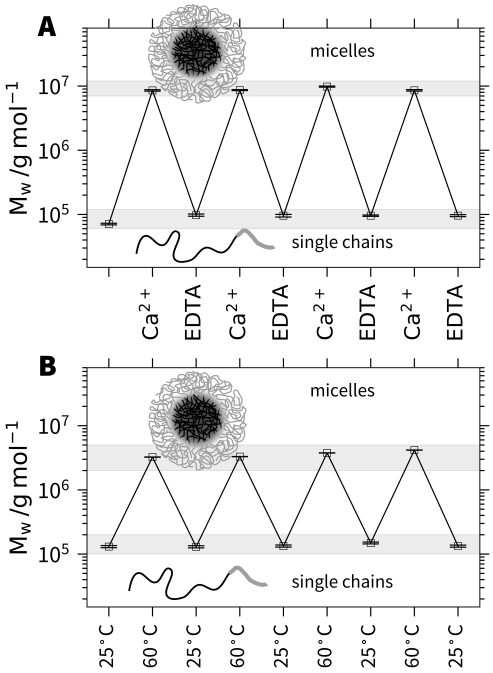


Figure 4.2: (A) Molecular weight M_w as a function of subsequent injections of $CaCl_2$ and Na_2EDTA. The first point refers to a solution of 1 g L^{-1} h_3-$PA_{1190}PSS_{70}$ in 0.1 mol L^{-1} NaCl. (B) Molecular weight M_w as a function of temperature cycles between 25 °C and 60 °C for h_3-$PA_{1190}PSS_{70}$ at a polymer concentration of 1 g L^{-1} and a Ca^{2+} concentration of 6.1 mmol L^{-1}.

will be intensively characterized by means of SANS at variable contrasts. However, before addressing this important question, an exciting feature, which can be inferred from our hypothesis shall be outlined. If the specific binding of Ca^{2+} to the PA block is responsible for the formation of stable aggregates, formation of micelles and subsequent re-dissolution may occur in reversible cycles upon repeated addition of Ca^{2+} and subsequent removal by addition of the disodium salt of ethylenediaminetetraacetic acid (Na_2EDTA).

In order to demonstrate this anticipated reversibility of micelle formation induced by Ca^{2+}, we added EDTA to a solution of h_3-$PA_{1190}PSS_{70}$ micelles. Figure 4.2A shows the molecular weight M_w from SLS for multiple subsequent additions of Ca^{2+} and EDTA. The first point of M_w corresponds to the polymer solution in 0.1 mol L^{-1} NaCl in the absence of Ca^{2+}. Each Ca^{2+} aliquot addition induces an increase of the molecular weight by more than two orders of magnitude. Upon subsequent addition of EDTA, M_w drops to close the initial value where Ca^{2+} was absent. Hence, the micelle formation

can be quantitatively reversed by the addition of a complexing agent such as EDTA, which removes Ca^{2+} from the equilibrium and subsequent addition of Ca^{2+} re-triggers micellization. The hydrodynamic radius R_h shows a similar trend and is shown in the ESI (Figure 4.18†).

The responsivity of the PA block towards Ca^{2+} cations offers another way to trigger the process of micellization. As the specific binding of Ca^{2+} to COO^- is driven by entropy due to the release of several water molecules and two sodium cations[22], temperature can be used to influence the binding and therefore the solubility of the PA block. An increase of temperature at a given level of decoration by Ca^{2+} is expected to increase the amount of bound Ca^{2+} and thus promote micellization.[23] In order to demonstrate this, we prepared a sample of h_3-$PA_{1190}PSS_{70}$ close to the threshold line separating single chains from micelles. As demonstrated in Figure 4.2B, we can repeatedly trigger the micelle formation and reverse it by increasing and lowering the temperature in cycles. The temperature effect arises from the entropy driven binding of Ca^{2+} to PA.[22,23] Both experiments revealed the reversible but specific binding of a metal cation selectively to only one of the two anionic blocks as a new system to trigger micellization at ambient conditions. This high versatility of the presented block copolyelectrolyte system should open the route to functional materials for sensing or schizophrenic micelles or for cargo transportation and release.

4.2.3 Micelle structure probed by SANS

Extended SANS and small-angle X-ray scattering (SAXS) experiments have been carried out on all four polymer samples in order to reveal the morphology of the micelles hold together by Ca^{2+} cations. The present work shall focus on the detailed contrast variation experiments carried out with the samples d_3-$PA_{360}PSS_{400}$ and d_3-$PA_{1190}PSS_{70}$. Two striking features can already be extracted from these contrast variation experiments without making any assumptions on a particular model of the aggregates. The first feature refers to the integrity of the block copolyelectrolytes and the second addresses the question whether the PA blocks establish the core or the corona of the micelles.

All parameters necessary to describe the scattering contrasts of the PSS blocks and of the PA blocks in terms of scattering length densities at variable H_2O/D_2O ratios are available in the Sec 4.4.4 of the ESI†. By using the chemical composition and the scattering length densities, the match point of the forward scattering can be predicted for both block copolyelectrolytes (Figure 4.3A). Since the chemical composition and

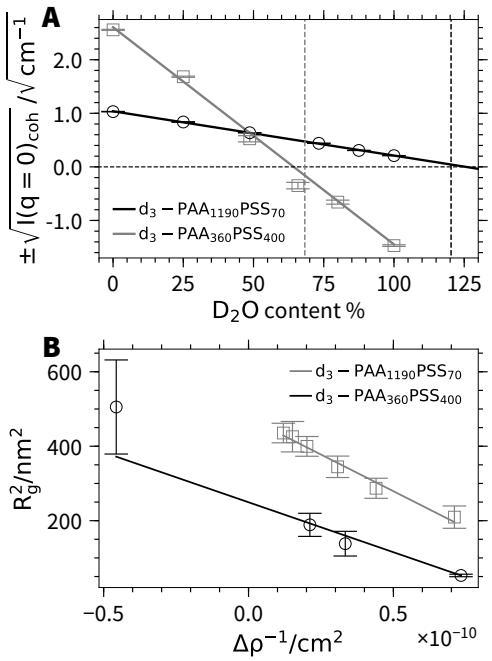


Figure 4.3: (A) Coherent forward scattering from SANS as a function of D_2O content for d_3-$PA_{360}PSS_{400}$ and d_3-$PA_{1190}PSS_{70}$. The vertical dashed lines indicate the theoretical match points calculated from the chemical composition. (B) Squared radius of gyration as a function of inverse scattering contrast for d_3-$PA_{360}PSS_{400}$ and d_3-$PA_{1190}PSS_{70}$.[28]

therefore the match point is independent on whether block copolymers are present as single chains or as micelles, we can use this information and the experimental forward scattering to verify the success of the block copolymer synthesis. As is outlined in Figure 4.3A, the experimentally found match point is identical within experimental uncertainty with the predicted one. This gets noticeable in the most straightforward manner with sample d_3-$PA_{360}PSS_{400}$ because the match point in this case lies in the middle of the probed contrast range spanned (corresponding to the entire range of H_2O/D_2O ratios). This rules out the existence of individual PA and PSS polymers as they would not show well-defined scattering patterns together with the predicted match point. Although the match point lies out of the range available by variation of the H_2O/D_2O ratio for d_3-$PA_{1190}PSS_{70}$, extrapolation of the data again reveals a point in full agreement with the value predicted by the corresponding block copolyelectrolyte chain. Thus, all samples under consideration are block copolyelectrolytes as characterized by NMR, SLS and DLS.

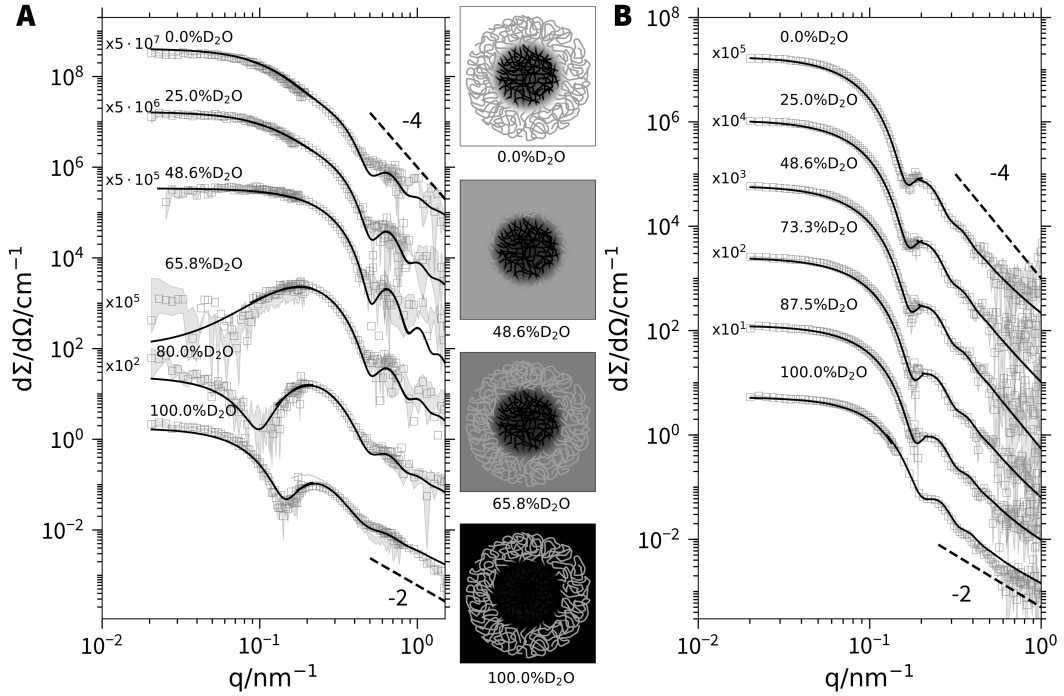


Figure 4.4: SANS profiles of (A) d_3-$PA_{360}PSS_{400}$ ($c_{polymer}$ = 4 g L^{-1}, $c_{Ca^{2+}}$ = 50 mmol L^{-1}) and (B) d_3-$PA_{1190}PSS_{70}$ micelles ($c_{polymer}$ = 4 g L^{-1}, $c_{Ca^{2+}}$ = 25 mmol L^{-1}) at various H_2O/D_2O ratios. The solid lines represent fits to the form factor of a polydisperse block copolymer micelle.[29] An overview of the fit results can be found in Table 4.4 of the ESI†. The sketches in the middle illustrate the scattering contrast of the d_3-$PA_{360}PSS_{400}$ micelles for selected H_2O/D_2O ratios.

As a next step, the chemical nature of the core and corona shall unambiguously be resolved by model independent data from SANS at variable contrast. All SANS (Figure 4.4) and SAXS (Figure 4.19†and 4.20†) scattering curves exhibit characteristic oscillations indicating particles with a regular shape like a spherical symmetry.[30] In the limit of high q, power laws may indicate fractal-like features. An exponent of -4, which is observed close to 48.6% D_2O, the match point for PSS chains, signals a sharp boundary of a core surface,[31] in line with a PA core. On the other hand, an exponent close to -2, which indicates scattering dominated by polymer coils,[32] is found in pure D_2O. As the scattering of deuterated PA is very weak in pure D_2O this exponent can be assigned to the PSS chains closing the corona with their dangling ends. Even stronger hints for the distribution of the two blocks among core and corona is received from the low q-limit. The radius of gyration extracted from the initial slopes of the scattering curves from particles with components or compartments differing in their

scattering contrast is an apparent value. The variation of this radius of gyration R_g with varying scattering contrast can be represented as a plot of R_g^2 *versus* the inverse averaged excess scattering length density of the total particle with respect to the solvent. Stuhrmann[28] demonstrated that this correlation depends on the morphology of the scattering particles. Trends for core-shell structures give a negative slope if the core has a higher local scattering length density than the shell or corona and a positive slope if the shell (or corona) has a higher density. As is shown in Figure 4.3B, the trends observed with the two present polymers is negative. This is a clear-cut evidence for the fact that PA forms the core.

Having provided compelling evidence for the Ca^{2+}-induced formation of micellar like aggregates of PA-*b*-PSS-block copolyelectrolytes with PA blocks in the core, the detailed SANS and SAXS data at variable scattering contrast shall finally be interpreted with a suitable micellar model being composed of block copolymers. Such a model has been provided by Pedersen et al.,[29] where one block species is forming the core and the other one the corona of a micellar like aggregate. The model parameters include an aggregation number N_{agg} based on a log-normal distribution, the radius of the core R_{core}, the molar volume of the Ca^{2+} cations and a variable content of water molecules in the core. Using the proper scattering contrast from Table 4.3†, a global fit with common fitting parameters of the SANS and SAXS curves has been performed. The procedure has been carried out for both polymer samples with deuterated PA blocks. A detailed outline of the fit procedure together with a complete list of fit parameters is given in Sec 4.4.5 of the ESI†.

In short, polymer d_3-$PA_{360}PSS_{400}$ reveals an aggregation number of $N_{agg} = 19.6$, independent of the composition of the solvent, resulting in a core radius $R_{core} = 8.8\,nm$. Strikingly, aggregation numbers for the polymer with the longer PA block d_3-$PA_{1190}PSS_{70}$ shows a much larger aggregation number of $N_{agg} = 168$ and along with it, a larger core of the micelles $R_{core} = 26\,nm$ compared to the micelles of the polymer with symmetric block lengths. Noteworthy, N_{agg} and R_{core} of the polymer with the much longer (and thus dominating) PA block show a weak dependence on the H_2O/D_2O ratio of the solvent, decreasing from 168 (H_2O) to 126 (D_2O) and from 26 nm (H_2O) to 24 nm (D_2O) respectively as the D_2O content increases from 0 to 100 %. This weak dependence is most likely an isotope effect on the solvent quality. Such effects are common in polymer science and are for instance observed for the theta temperature of polymers in ideal solvents, which also slightly changes if either the solvent or the polymer is deuterated.[33,34] Fits to all SANS curves are included in Figure 4.4A and B.

Fits where the core is formed by the PSS blocks instead of the PA blocks have also been carried out. However, this model is not able to describe the data (see Sec 4.4.5 of the ESI† for details) thus further supporting core formation by Ca^{2+}/PA complexes and not by PSS.

Finally, one observation revealed by the fits deserves special attention. The scattering curves could only be successfully reproduced with the present core-corona model[29] once a considerable amount of water molecules is incorporated into the core. The values received for both polymers are 12 water molecules per acrylate monomer, amounting to some 85 % by volume of the core. This nicely shows that the mechanism of the PA/Ca^{2+} core formation is a liquid-liquid phase separation as already found for the PA homopolymer and Ca^{2+}.[35,36]

4.3 Conclusion

To summarize, we succeeded in presenting block copolymers based on two anionic polyelectrolyte blocks as a new class of double hydrophilic block copolymers with an unusual solution behavior in aqueous solution containing Ca^{2+} cations. Whereas pure PA precipitates at large enough concentrations of Ca^{2+} due to specific interactions of the COO^- residues with Ca^{2+},[15–21] pure PSS only shows counter ion condensation and electrostatic screening.[24,25] A combination of these two features in one block copolyelectrolyte leads to micelle formation instead of PA precipitation, with the PA blocks forming the core. Micelle formation is triggered by alternately adding Ca^{2+} cations and Na_2EDTA to a polymer solution. Even more striking is the feature that the entropic nature of the Ca^{2+} binding to the NaPA-blocks can be used to switch micellization. Application of small temperature changes reversibly form ($\Delta T > 0$) and dissolve ($\Delta T < 0$) micelles. The micelles are stable and soluble due to the PSS blocks. Micelle formation is entirely reversible, indicating a new route for up-taking and releasing cargo. Increasing the ratio of the block length of PA/PSS increases the aggregation number and weakens the solubilizing power of the PSS corona. Micellization can be tuned by varying the amount of Ca^{2+} cations and by varying the temperature.[22,23] Given the large variety of metal cations, capable of interacting specifically with one or both blocks in the same or different way[14,15,24,37,38] and taking further into account the impact of environmental conditions like pH, ionic strength and temperature, an extremely rich pattern of responses can be expected from PA-*b*-PSS block copolymers. This prospective makes PA-*b*-PSS block copolymers a highly promising new material. Schizophrenic micelles,[39]

new contrast agents by utilizing Gd^{3+} or Eu^{3+} or new strategies for ion separation are just a few of the possible applications of like-charged block copolyelectrolytes.

Experimental details

polymer synthesis, characterization, details on the SANS and SAXS experiments, the used form factor model and scattering length densities can be found in the ESI†.

Conflicts of interest

There are no conflicts to declare.

Acknowledgements

In memoriam Isabelle Grillo. The authors thank the Institut Laue-Langevin (https://doi.ill.fr/10.5291/ILL-DATA.9-11-1888) and the European Synchrotron Radiation Facility for the provision of beam time, the Partnership for Soft Condensed Matter (PSCM) for supply of the light scattering, Dr Hans Egold and Karin Stolte of the University of Paderborn for NMR measurements, Isabelle Morfin on D2AM for local contacting and Narayanan Theyencheri and the ID02 team for the supply of in-house time at ID02. Nico Carl acknowledges funding for a PhD scholarship from Institut Laue-Langevin. The open access fee was covered by FILL2030, a European Union project within the European Commission's Horizon 2020 Research and Innovation programme under grant agreement No. 731096.

4.4 Supporting Information

4.4.1 Experimental details

Materials

Light water (H_2O) was purified using a Milli-Q-system (Millipore), resistivity 18.2 $M\Omega\,cm$). Heavy water (D_2O, Euriso-top, France, 99.90 atom% deuterium) was filtered with 100 nm PVDF filter (Merck Millex MPSLVV033RS) prior to use. Sodium styrene sulfonate (Sigma Aldrich, France), 4,4'-azobis(4-cyanovaleric acid) (Sigma Aldrich, France, $>$ 98 %), 2-(2-carboxyethylsulfanylthiocarbonylsulfanyl)propionic acid (Sigma Aldrich, France), $CaCl_2 \cdot 2\,H_2O$ (Sigma Aldrich, France, $>$ 99.9 %), NaCl (Sigma Aldrich, France, $>$ 99.9 %), NaOH (Sigma Aldrich, France), HCl (Sigma Aldrich, France, 37%), acrylic acid (Sigma Aldrich, France, $>$ 99 %), 3-(trimethylsilyl)propionic-2,2,3,3-d_4 acid sodium salt (abcr GmbH, Germany, 98 atom% deuterium), disodium ethylenediaminetetraacetic acid (Sigma Aldrich, France, $>$ 98.5 %) and d_4-acrylic acid (Polymersource, Canada, $>$ 98 % atom% deuterium) were used as received.

Polymer synthesis

The synthesis of h_3-$PA_{1190}PSS_{70}$ (sodium salt, the subscript numbers denote the degree of polymerization for PAA and PSS and the number of hydrogendated/deuterated protons in the PA block) will be described exemplarily.[26,40,41] For the blocks denoted as d_3-PA, acrylic acid was replaced by d_4 acrylic acid.

First a PSS macro RAFT agent was synthesized by dissolving 15 g of sodium styrene sulfonate (72.9 mmol), 264.5 mg of 4,4'-azobis(4-cyanovaleric acid) (1.04 mmol) and 29.2 mg of 2-(2-carboxyethylsulfanylthiocarbonylsulfanyl)propionic acid (0.10 mmol) in 150 mL of deionized water at room temperature. Subsequently, the mixture was degassed by flushing with argon for 30 min. The polymerization was carried out for 15 h at 70 °C under argon atmosphere. After the reaction the product was allowed to cool down and transferred into dialysis tubing (regenerated cellulose, Spectra/Por 6 MWCO = 1 kDa). The polymer was dialyzed against a large excess of water for 3 days with exchange of water every 12 h and finally freeze dried. Yield: 13.1 g (86 %)

In order to obtain a PA-*b*-PSS block copolymer, 1.714 g of the previously synthesized PSS macro RAFT agent (0.19 mmol), 5 mg of 4,4'-azobis(4-cyanovaleric acid) (0.018 mmol) and 11.43 mL of acrylic acid (166.6 mmol) were dissolved in 69 mL of deionized water at room temperature. The mixture was flushed with argon for 30 min.

The mixture was polymerized at 70 °C for 8 h. The product was allowed to cool down, brought to pH 10 by addition of 1 M NaOH and transferred into dialysis tubing (regenerated cellulose, Spectra/Por 6 MWCO = 1 kDa). The product was dialyzed against a large excess of water for 3 days with exchange of water every 12 h and finally freeze dried. Yield: 15.5 g (82 %).

Monomer conversion and block copolymer composition were determined by NMR spectroscopy. ^{1}H (^{2}H) NMR measurements were performed in D_2O (H_2O) using a Bruker Ascent 700 or Bruker AV 500. For block copolymers containing deuterated poly acrylic acid, 3-(trimethylsilyl)-1-propanesulfonic acid-d_6 sodium salt was added as a quantitative reference to be able to integrate between ^{1}H and ^{2}H spectra for the determination of the block copolymer composition. NMR spectra are shown in Figures 4.5–4.13.

Sample preparation

For the sample preparation, we followed an approached used in previous works.[15–17,23,42] The total number of positive charges for all samples was adjusted to 100 mmol L^{-1}. The total concentration of positive charges [+] is

$$[+] = [\mathrm{NaCl}] + 2 \cdot [\mathrm{CaCl_2}] = 100\,\mathrm{mmol\,L^{-1}} \tag{4.2}$$

with [NaCl] being the concentration of sodium chloride and [$CaCl_2$] the concentration of calcium chloride. This means a sample containing 25 mmol L^{-1} $CaCl_2$ also contained 50 mmol L^{-1} NaCl, whereas a sample containing 50 mmol L^{-1} $CaCl_2$ contains no additional NaCl. Since the final $CaCl_2$ concentration differs for the investigated samples we describe the sample preparation for d_3-PA_{1190} PSS_{70} / h_3-PA_{1190} PSS_{70} and d_3-PA_{360} PSS_{400} separately.

The sample preparation for d_3-PA_{1190} PSS_{70} and h_3-PA_{1190} PSS_{70} was identical. First, two stock solutions of the freeze-dried polymer d_3-PA_{1190} PSS_{70} (or h_3-PA_{1190} PSS_{70}) in 100 mmol L^{-1} NaCl solution in pure H_2O or 100 mmol L^{-1} NaCl in pure D_2O were prepared at twice (8 g L^{-1}) the final concentration and adjusted to pH/pD of 9 with a 100 mmol L^{-1} NaOH solution. Mixing these two solutions in appropriate ratios resulted in a new stock solution of polymer with the selected D_2O/H_2O content. Accordingly, stock solutions of 50 mmol L^{-1} $CaCl_2$ in pure H_2O or pure D_2O were prepared by dissolving $CaCl_2 \cdot 2\,H_2O$ in H_2O and D_2O. As done with the polymer solutions, mixing those $CaCl_2$ solutions in adequate ratio resulted in the $CaCl_2$ solution with the selected D_2O/H_2O ratio.

Mixing of the polymer solution with the $CaCl_2$ solution of a desired contrast in a 1 : 1 ratio was performed under vigorous stirring and dropwise addition of $CaCl_2$ solution to the polymer solution. This resulted in a polymer concentration of $4\,g\,L^{-1}$, a $CaCl_2$ concentration of $25\,mmol\,L^{-1}$ and a NaCl concentration of $50\,mmol\,L^{-1}$.

For d_3-$PA_{360}\,PSS_{400}$, two stock solutions ($8\,g\,L^{-1}$) of the freeze-dried polymer were prepared in pure H_2O and pure D_2O and adjusted to a pH/pD of 9 with a $100\,mmol\,L^{-1}$ NaOH solution. Mixing these two solutions in appropriate ratios resulted in a new stock solution of polymer with the selected D_2O/H_2O content. Analogously, stock solutions of $100\,mmol\,L^{-1}$ $CaCl_2$ in pure H_2O or pure D_2O were prepared by dissolving $CaCl_2 \cdot 2\,H_2O$ in H_2O and D_2O. As done with the polymer solutions, mixing those $CaCl_2$ solutions in adequate ratio resulted in the $CaCl_2$ solution with the selected D_2O/H_2O ratio.

Mixing of the polymer solution with the $CaCl_2$ solution of a desired contrast in a 1 : 1 ratio was performed under vigorous stirring and dropwise addition of $CaCl_2$ solution to the polymer solution. This resulted in a polymer concentration of $4\,g\,L^{-1}$ and a $CaCl_2$ concentration of $50\,mmol\,L^{-1}$.

The resulting solutions were allowed to equilibrate for at least 2 days prior to measurement. The polymer-free solutions which served as solvent background for SANS and SAXS were prepared in a similar way by mixing a $CaCl_2$ solution with the corresponding solvent without polymer (pure water for d_3-$PA_{360}\,PSS_{400}$ and $100\,mmol\,L^{-1}$ NaCl for d_3-$PA_{1190}\,PSS_{70}$/ h_3-$PA_{1190}\,PSS_{70}$). The usage of $CaCl_2 \cdot 2\,H_2O$ results in less than $0.2\,vol\,\%$ additional H_2O content and therefore does not influence the D_2O content.

SAXS

Small-angle X-Ray scattering was performed at the ID02 beamline of the European Synchrotron Radiation Facility (ESRF). Two sample to detector distances ($10\,m$ and $1\,m$) were measured at a X-Ray energy of $12.46\,keV$ ($0.0995\,nm$) using a Rayonix MX-170HS CCD detector to cover a q-range of $8 \times 10^{-3} - 6\,nm^{-1}$. Samples were filled in $2\,mm$ quartz glass capillaries (WJM Glas Müller, Berlin, Germany). The detector images were corrected for dark and flat-field, azimuthally averaged, corrected to transmission of the direct beam and scaled to absolute intensity using water as a secondary standard.[43,44] The scattering from the solvent was subtracted from the scattering curves. Details can

be found in Ref. [44]. Error bars were estimated as standard deviations from measurements of at least five different positions within the capillary.

SANS

SANS measurements were performed at the D11 small angle neutron scattering instrument of the Institut Laue-Langevin (Grenoble, France). Three sample to detector distances (39.0 m collimation 40.5 m, 8.0 m collimation 8.0 m, 1.4 m collimation 5.5 m) and a neutron wavelength of 0.5 nm (FWHM 9 %) were used to cover a q-range of $2 \times 10^{-2} - 5\,\mathrm{nm}^{-1}$. We used a circular neutron beam with a diameter of 15 mm. Scattered neutrons were detected with a ^{3}He MWPC detector (CERCA) with 256×256 pixels of $3.75\,\mathrm{mm} \times 3.75\,\mathrm{mm}$ pixel size. Samples were filled in 2 mm Hellma 404 Quartz Suprasil cells. The sample temperature was adjusted to 25 °C using a circulating water bath. The detector images were azimuthally averaged, corrected to transmission of the direct beam and scaled to absolute intensity using a 1 mm H_2O cell as secondary calibration standard ($\frac{d\Sigma}{d\Omega} = 0.929\,\mathrm{cm}^{-1}$) using the LAMP software. The scattering from the solvent and the incoherent background were subtracted from the scattering curves. Details for the data reduction can be found in Chapter 2 of Ref. [45].

4.4.2 Polymer characterization

NMR

We used NMR to characterize the (block) polymers as well as the macro RAFT agents and to estimate the block length and ratios. Directly at the end of the polymerization we withdrew an aliquot to determine the turnover of the reaction. In general, barely any monomer signal was visible, from which we concluded, that the monomer conversion is at least $> 95\,\%$.

In order to estimate the degree of polymerisation of the PSS macro RAFT agent we compared the signal of the RAFT polymer to the signal arising from the RAFT end group. This was possible for PSS_{70} (c.f. Figure 4.5), whereas for PSS_{400} we calculated M_n from the ratio RAFT agent to monomer and assuming 100 % conversion. Consequently, we determined the block ratios from the NMR spectra of the block copolymers. Based on this and the previsouly calculated length of the PSS block we determined the length of the PA block. For the polymers where we used deuterated acrylic acid, we added 3-(Trimethylsilyl)propionic-2,2,3,3-d_4 acid sodium salt (TSP$-d_4$) to be able to integrate between ^{1}H and ^{2}H spectra. The corresponding samples were measured in D_2O for the

^{1}H experiment, freeze-dried and redissolved in H_2O for the ^{2}H experiment in order to keep the amount of TSP$-d_4$ constant.

For the h_3-$PA_{100}PSS_{750}$ block copolymer we first synthesized a PA macro RAFT agent and consequently polymerized the PSS block. The estimation of the block ratios was done similar as for $PA_{1190}PSS_{70}$.

PSS_{70}: ^{1}H NMR (D_2O, 500 MHz): $\delta(ppm)$ = 0.84 to 1.06 (br, 3H, **d**), 1.09 to 2.54 (br, 3H, **c**), 2.54 to 2.91 (br, 2H, **f**), 3.26 to 3.80 (br, 2H, **e**), 6.12 to 7.29 (br, 2H, **b**), 7.32 to 8.03 (br, 2H, **a**).

h_3-$PA_{1190}PSS_{70}$: ^{1}H NMR (D_2O, 500 MHz): $\delta(ppm)$ = 0.71 to 2.54 (br, 6H, **c**), 6.15 to 7.19 (br, 2H, **b**), 7.27 to 7.95 (br, 2H, **a**).

d_3-$PA_{1190}PSS_{70}$: ^{1}H NMR (D_2O, 700 MHz): $\delta(ppm)$ = −0.11 to 0.09 (s, 9H, **d**), 1.09 to 1.97 (br, 3H, c), 6.31 to 7.09 (br, 2H, b), 7.22 to 7.86 (br, 2H, a). ^{2}H NMR (H_2O, 107 MHz): $\delta(ppm)$ = 0.41 to 0.67 (br, 2D, **c**), 0.73 to 3.57 (br, 5D, a & **b**, 1.85 to 2.06 (br, 2D, **b**).

PSS_{400}: ^{1}H NMR (D_2O, 700 MHz): $\delta(ppm)$ = 0.71 to 2.39 (br, 3H, **c**), 6.05 to 7.08 (br, 2H, **a**), 7.24 to 7.97 (br, 2H, **a**).

d_3-$PA_{360}PSS_{400}$: ^{1}H NMR (D_2O, 700 MHz): $\delta(ppm)$ = −0.12 to 0.10 (s, 9H, **d**), 0.99 to 2.44 (br, 3H, **c**), 5.82 to 7.24 (br, 2H, **b**), 7.24 to 7.92 (br, 2H, **a**). ^{2}H NMR (H_2O, 107 MHz): $\delta(ppm)$ = 0.43 to 0.80 (br, 2D, **c**), 0.95 to 3.47 (br, 5D, **a** & **b**), 1.80 to 2.15 (br, 2D, **b**).

h_3-PA_{100}: ^{1}H NMR (D_2O, 500 MHz): $\delta(ppm)$ = 0.94 to 1.08 (s, 3H, **d**), 1.27 to 2.54 (br, 3H, **c**), 2.54 to 2.68 (br, **?** not assigned), 2.68 to 2.83 (br, 2H, **b**), 3.44 to 3.58 (br, 2H, **a**), 4.10 to 4.30 (br, **?** not assigned).

h_3-$PA_{100}PSS_{750}$: ^{1}H NMR (D_2O, 500 MHz): $\delta(ppm)$ = 0.98 to 2.34 (br, 6H, **c**), 5.83 to 6.89 (br, 2H, **b**), 7.13 to 7.74 (br, 2H, **a**).

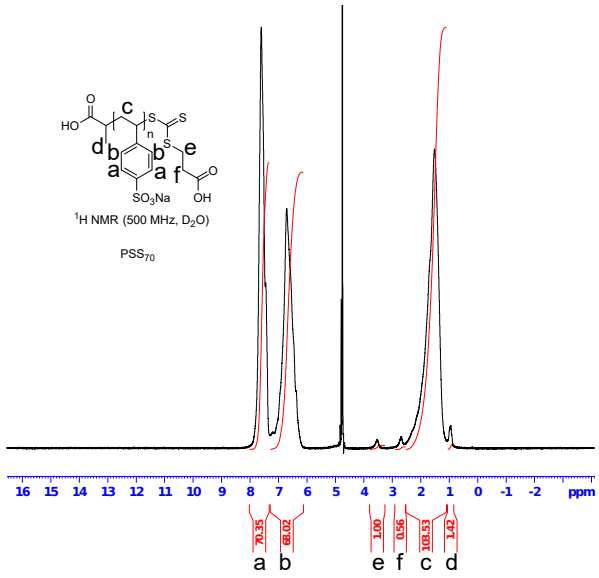


Figure 4.5: ^{1}H NMR spectrum of PSS_{70} in D_2O.

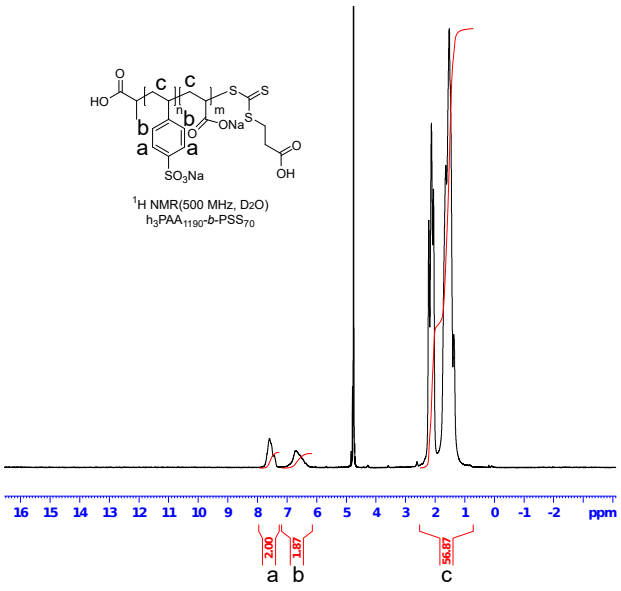


Figure 4.6: ^{1}H NMR spectrum of h_3-PA_{1190} PSS_{70} in D_2O.

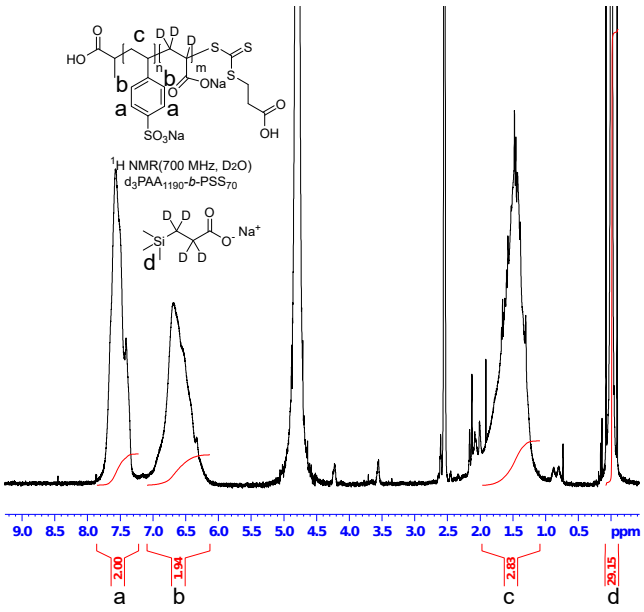


Figure 4.7: ^{1}H NMR spectrum of d_3-PA_{1190} PSS_{70} in D_2O.

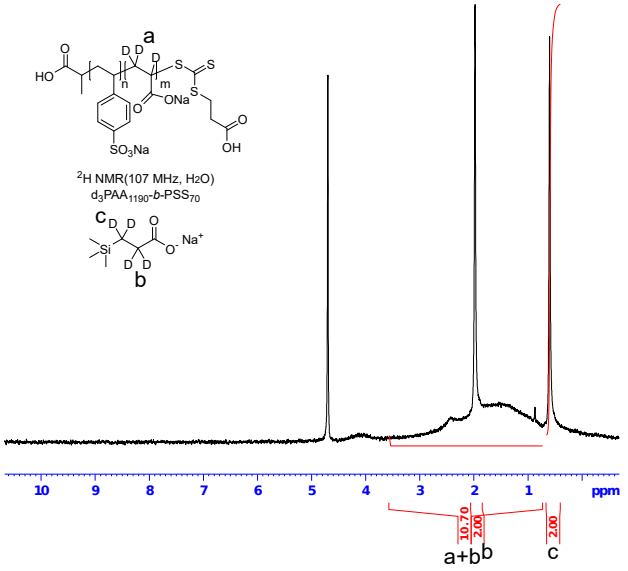


Figure 4.8: ^{2}H NMR spectrum of d_3-PA_{1190} PSS_{70} in H_2O.

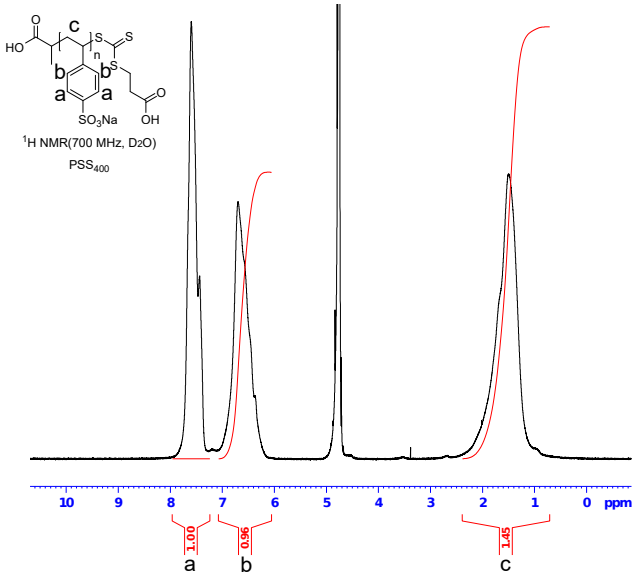


Figure 4.9: ^{1}H NMR spectrum of PSS_{400} in D_2O.

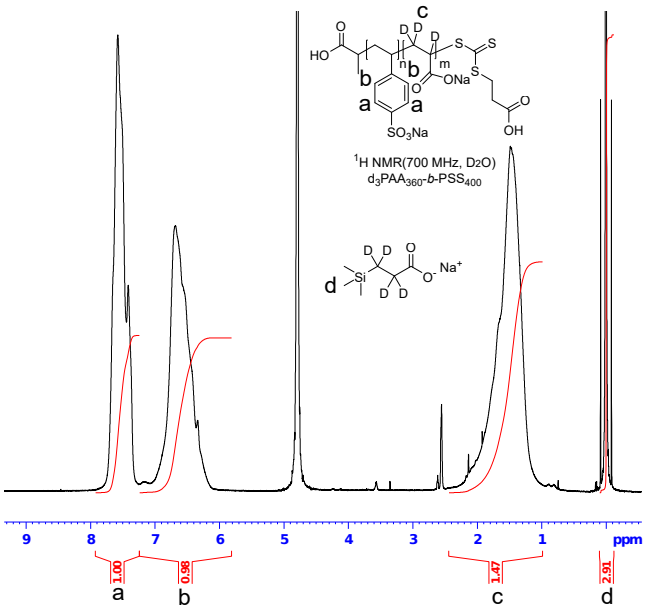


Figure 4.10: ^{1}H NMR spectrum of d_3-PA_{360} PSS_{400} in D_2O.

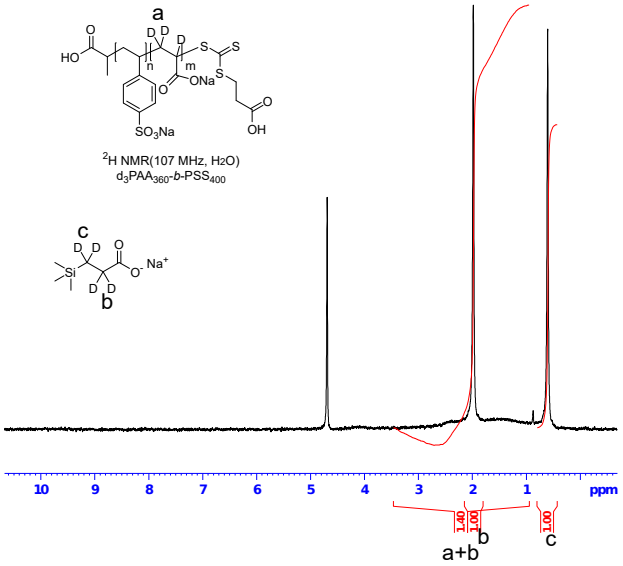


Figure 4.11: ^{2}H NMR spectrum of d_3-PA_{360} PSS_{400} in H_2O.

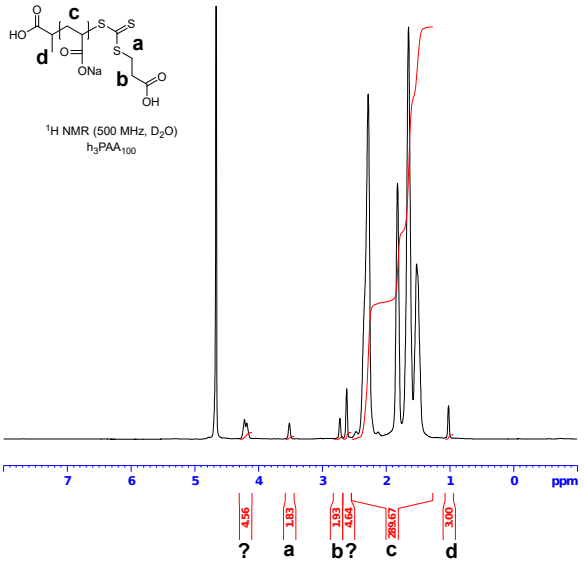


Figure 4.12: ^{1}H NMR spectrum of h_3-PA_{100} in D_2O.

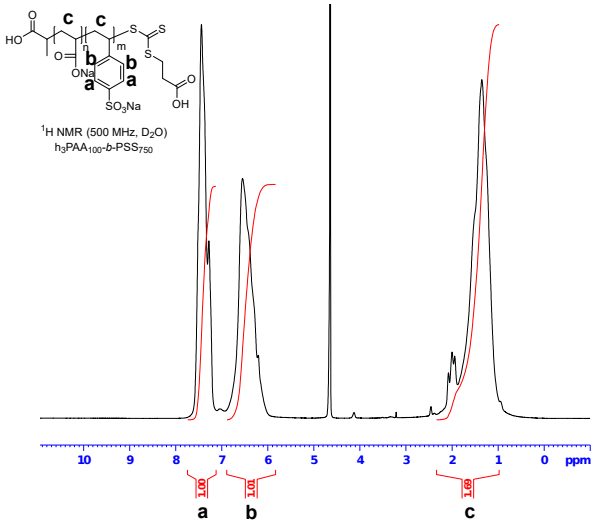


Figure 4.13: ^{1}H NMR spectrum of h_3-PA_{100} PSS_{750} in D_2O.

Static and dynamic light scattering

The intensity-time correlation function $g_2(\tau) - 1$ measured with dynamic light scattering was analyzed using the method of cumulants[46]

$$g_2(\tau) - 1 = B + \beta \exp(-2\Gamma\tau) \left(1 + \frac{\mu_2}{2!}\tau^2\right)^2 \tag{4.3}$$

B is a factor correcting the baseline, β a factor, which depends on the experimental setup, Γ the relaxation rate and μ_2 the the second cumulant. The apparent diffusion coefficient $D_{app}(c, q)$ for a given q is calculated according to

$$D_{app} = \frac{\Gamma}{q^2} \tag{4.4}$$

The diffusion coefficient is consequently extrapolated towards $q = 0$ and $c = 0$ according to[47,48]

$$D_{app}(c, q) = D_0 \left(1 + CR_g^2 q^2 + k_D c\right) \tag{4.5}$$

where C and k_D are constants describing q and the concentration dependence of D_0, respectively. The diffusion coefficient D_0 is used to calculate the hydrodynamic radius R_h using the Stokes-Einstein equation

$$R_h = \frac{k_B T}{6\pi\eta D_0} \tag{4.6}$$

where T is the temperature, k_B the Boltzmann constant and η the viscosity of the solvent. Static light scattering was evaluated with the Zimm equation[49]

$$\frac{Kc}{\Delta R_\theta} = \frac{1}{M_w} + 2A_2c + \frac{R_g^2}{3M_w}q^2 \tag{4.7}$$

where c is the mass concentration of the polymer, M_w the weight average molecular weight of the polymer, A_2 the second osmotic virial coefficient and R_g the radius of gyration. ΔR_θ is the Rayleigh ratio and identical with the macroscopic scattering cross-section $\frac{d\Sigma}{d\Omega}$ used to express the scattering intensity in SANS and SAXS. K is the contrast factor given by

$$K = \frac{4\pi^2}{N_A\lambda_0^4}\left(n_{\text{standard}}\frac{dn}{dc}\right)^2 \tag{4.8}$$

It contains the Avogadro constant N_A, the wavelength of the laser in vacuo λ_0, the refractive index of the standard (in this case toluene) n_{standard} and the refractive index increment of the polymer in the solvent $\frac{dn}{dc}$.

Figure 4.14–4.16 show the characterization of the used polymers with static and dynamic light scattering. As solvent we choose an aqueous solution of $100\,\text{mmol}\,L^{-1}$ NaCl at pH 9. In sub-figure A of each graph one can find the extrapolation of the diffusion coefficient to $c = 0$ and $q = 0$. The blue points indicate the extrapolation towards $q = 0$ for a given concentration. The blue line indicates the extrapolation of these points towards $c = 0$. The intercept defines D_0, which we used to calculate the hydrodynamic radius R_h. Similarly, figure B shows the extrapolation of the static light scattering data towards $c = 0$ and $q = 0$.

Figure C shows the measurement of the refractive index increment for this given polymer in the same solvent conditions. The refractive index increment $\frac{dn}{dc}$ was determined using a differential refractometer (DR3 by SLS Systemtechnik, Denzlingen, Germany). The instrument operates at a wavelength of $\lambda_0 = 635\,nm$. A stock solution of $10\,g\,L^{-1}$ polymer was prepared in $100\,\text{mmol}\,L^{-1}$ NaCl (H_2O), adjusted to pH 9 and dialyzed against the solvent solution prior to dilution.[50] The measured values of $\frac{dn}{dc}$ can be found in Table 4.2.

Table 4.2 summarizes the results from the light scattering characterization.

Table 4.2: Results from the light scattering analysis of the used polymers in aqueous 100 mmol L^{-1} NaCl solution in the absence of $CaCl_2$.

Polymer	c /g L^{-1}	D_0/nm^2 s^{-1}	R_h/nm	R_g/nm	M_w/kg mol^{-1}	$A_2/10^4$ cm^3 mol g^{-2}	k_D /cm^3 g^{-1}	R_g/R_h	dn/dc /cm^3 g^{-1}
h_3-PA_{1190} PSS_{70}	1.50	25370 ± 363	9.8 ± 0.1	13.4 ± 0.6	62835 ± 139				
	1.25	23802 ± 311	10.4 ± 0.1	15.2 ± 0.6	68633 ± 153				
	1.00	23013 ± 349	10.8 ± 0.2	14.7 ± 0.7	78395 ± 241				
	0.75	21495 ± 377	11.5 ± 0.2	17.5 ± 0.7	90381 ± 346				
	0.00	17871 ± 765	13.9 ± 0.6	23.5 ± 1.9	160093 ± 2117	32.6 ± 0.3	275 ± 48	1.7 ± 0.2	0.172 ± 0.001
d_3-PA_{1190} PSS_{70}	1.50	25723 ± 316	9.6 ± 0.1	14.3 ± 0.8	69549 ± 254				
	1.25	25359 ± 409	9.8 ± 0.2	14.8 ± 0.6	77736 ± 187				
	1.00	23515 ± 215	10.5 ± 0.1	14.6 ± 0.6	87389 ± 232				
	0.75	21883 ± 328	11.3 ± 0.2	18.9 ± 0.9	100969 ± 510				
	0.00	18249 ± 637	13.6 ± 0.5	24.0 ± 2.4	181393 ± 3170	29.5 ± 0.4	284 ± 41	1.8 ± 0.2	0.157 ± 0.001
d_3-PA_{360} PSS_{400}	1.50	27812 ± 185	8.9 ± 0.1	21.0 ± 0.6	87076 ± 326				
	1.25	27186 ± 187	9.1 ± 0.1	18.3 ± 0.6	89987 ± 264				
	1.00	26698 ± 290	9.3 ± 0.1	18.7 ± 0.7	96787 ± 363				
	0.75	25814 ± 248	9.6 ± 0.1	18.2 ± 0.7	102784 ± 353				
	0.00	23951 ± 486	10.4 ± 0.2	13.8 ± 2.4	126661 ± 1208	12.4 ± 0.3	108 ± 19	1.3 ± 0.2	0.177 ± 0.001
h_3-PA_{100} PSS_{750}	1.50	23733 ± 114	10.5 ± 0.1	16.3 ± 0.4	127905 ± 274				
	1.25	23155 ± 229	10.7 ± 0.1	17.5 ± 0.5	138356 ± 383				
	1.00	22334 ± 179	11.1 ± 0.1	17.7 ± 0.4	149516 ± 314				
	0.75	20641 ± 84	11.7 ± 0.1	18.5 ± 0.4	161840 ± 434				
	0.00	17669 ± 198	14.0 ± 0.2	21.6 ± 2.3	220195 ± 1628	10.7 ± 0.1	231 ± 13	1.5 ± 0.2	0.174 ± 0.001

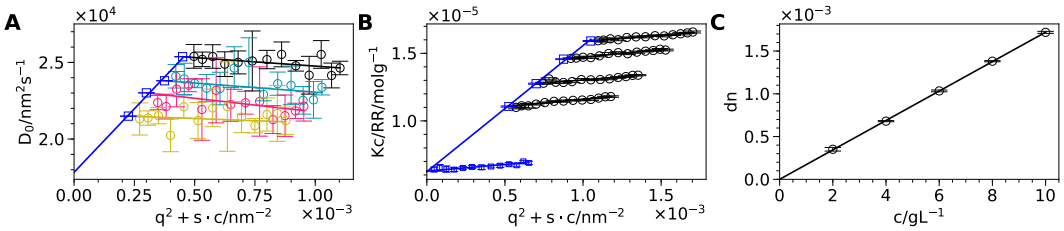


Figure 4.14: (**A**) Dynamic Zimm plot of h_3-PA_{1190} PSS_{70} in 100 mmol L^{-1} NaCl. (**B**) Zimm plot of h_3-PA_{1190} PSS_{70} in 100 mmol L^{-1} NaCl. (**C**) Refractive index increment as a function of concentration of h_3-PA_{1190} PSS_{70} in 100 mmol L^{-1} NaCl.

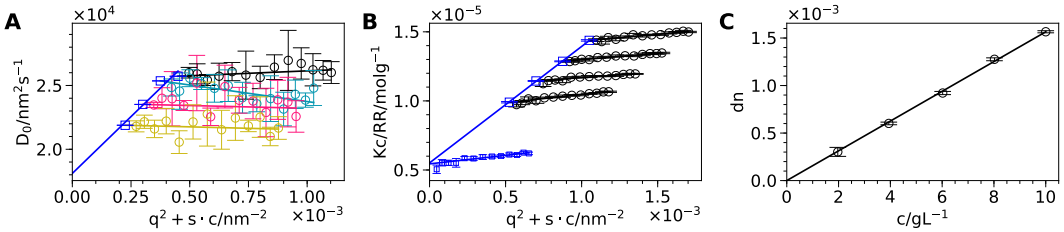


Figure 4.15: (**A**) Dynamic Zimm plot of d_3-PA_{1190} PSS_{70} in 100 mmol L^{-1} NaCl. (**B**) Zimm plot of d_3-PA_{1190} PSS_{70} in 100 mmol L^{-1} NaCl. (**C**) Refractive index increment as a function of concentration of d_3-PA_{1190} PSS_{70} in 100 mmol L^{-1} NaCl.

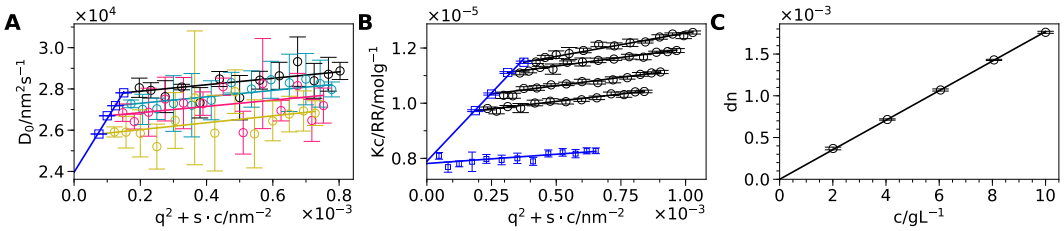


Figure 4.16: (**A**) Dynamic Zimm plot of d_3-PA_{360} PSS_{400} in 100 mmol L^{-1} NaCl. (**B**) Zimm plot of d_3-PA_{360} PSS_{400} in 100 mmol L^{-1} NaCl. (**C**) Refractive index increment as a function of concentration of d_3-PA_{360} PSS_{400} in 100 mmol L^{-1} NaCl.

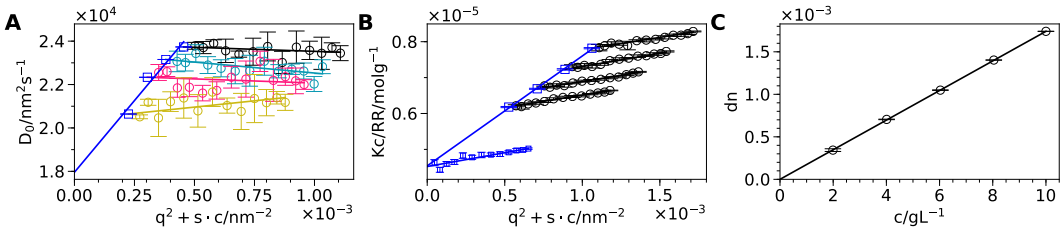


Figure 4.17: (**A**) Dynamic Zimm plot of h_3-PA_{100} PSS_{750} in 100 mmol L^{-1} NaCl. (**B**) Zimm plot of h_3-PA_{100} PSS_{750} in 100 mmol L^{-1} NaCl. (**C**) Refractive index increment as a function of concentration of h_{100}-PA_{360} PSS_{750} in 100 mmol L^{-1} NaCl.

4.4.3 Reversibility of micelle formation

The reversibility of micelle formation was shown by addition of Na_2EDTA to a micelle solution. For this an aqueous 200 mmol L^{-1} solution of Na_2EDTA was prepared and adjusted to pH 9 using 1 mol L^{-1} NaOH. In addition, an aqueous 200 mmol L^{-1} $CaCl_2$ solution was prepared and adjusted to pH 9 using 100 mmol L^{-1} NaOH solution. Both solutions were filtered using hydrophilic 100 nm PVDF filters (Merck Millipore).

First, a solution of h_3-$PA_{1190}PSS_{70}$ (1 g L^{-1}, pH 9, 1 mL) in 100 mmol L^{-1} NaCl was investigated using angular dependent DLS and SLS. To this solution an aliquot of 50 µL $CaCl_2$ solution was added to trigger micelle formation. Subsequently, aliquots of 25 µL of Na_2EDTA or $CaCl_2$ solution were added to switch between single chains and micelles. After each injection angular dependent DLS and SLS was performed. Four complete cycles were carried out. This increased the total volume of 1000 µL to 1225 µL.

Figure 4.18 shows the hydrodynamic radius R_h from DLS upon subsequent additions of Ca^{2+} and EDTA.

We also showed the reversibility of micelle formation by a change in temperature. For this we prepared a sample of h_3-$PA_{1190}PSS_{70}$ at 1 g L^{-1} and a concentration of Ca^{2+} of 6.1 mmol L^{-1}. This sample is close to the micelle transition but still in the single chain regime. Upon an increase of temperature the binding of Ca^{2+} to the PA block is promoted and micellization occurs. Various temperature cycles combined with angular dependent SLS and DLS were performed. Figure 4.18B shows the hydrodynamic radius for those experiments.

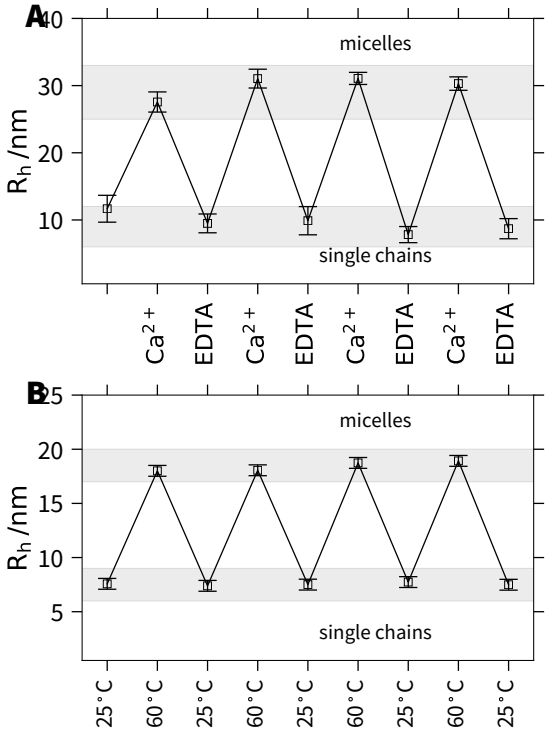


Figure 4.18: (**A**) Hydrodynamic radius R_h as a function of subsequent injections of $CaCl_2$ and Na_2EDTA. The first point refers to a solution of $1\,g\,L^{-1}$ h_3-$PA_{1190}PSS_{70}$ in $100\,mmol\,L^{-1}$ NaCl. (**B**) Hydrodynamic radius R_h as a function of temperature cycles between 25 °C and 65 °C for h_3-$PA_{1190}PSS_{70}$ at a polymer concentration of $1\,g\,L^{-1}$ and a Ca^{2+} concentration of $6.1\,mmol\,L^{-1}$.

4.4.4 Scattering length densities

Table 4.3 shows the molar volumes V_m, scattering length b and scattering length densities ρ for neutrons and X-rays (at $12.46\,keV$) used for the analysis of the data. The scattering length density of a given compound is given by

$$\rho = \frac{b}{V_m} N_a \tag{4.9}$$

with N_A being the Avogadro constant.

4.4.5 Analysis of scattering data

Form factor model

The form factor of self-assembled block copolymers with excluded volume interaction of the polymer chains was first treated by Pedersen under the assumption that the

Table 4.3: Molar volumes, neutron and X-ray scattering length and scattering length density of the used compounds. $\rho_{\text{X-rays}}$ was calculated for a X-ray energy of 12.46 keV.

Compound	V_m / $cm^3\ mol^{-1}$	$b_{neutrons}$ / fm	$b_{X\text{-}Rays}$ / fm	$\rho_{neutrons}$ / $10^{10}\ cm^{-2}$	$\rho_{X\text{-}rays}$ / $10^{14}\ cm^{-2}$
$h_3\,PA^-$	29.1[a]	20.327	107.269	4.208	22.21
$d_3\,PA^-$	29.1[a]	51.557	107.269	10.674	22.21
NaPSS	108.7	50.881	299.823	2.818	16.61
D_2O	18.141	19.145	28.242	6.355	9.375
H_2O	18.069	−1.675	28.242	−0.558	9.398
Ca^{2+}	17.0 ± 2.8[b]	4.7	51.652	1.665	1.830×10^{-3}
d_3-$PA_{1190}PSS_{70}$[c]			7.762		
d_3-$PA_{360}PSS_{400}$[c]			4.165		

[a] Taken from reference [51]. [b] The molar volume of Ca^{2+} was fitted. The shown value is the average value we obtained from analysis of the three different polymers. [c] We assumed that every PA monomer is complexed by 0.5 equivalents of Ca^{2+}.

polymers form spherical micellar-like structures.[29,30,52,53] The macroscopic scattering cross-section $\frac{d\Sigma}{d\Omega}(q)$ of a solution of micelles can be written as[29]

$$\begin{aligned}\frac{d\Sigma}{d\Omega}(q) = N\Big[&N_{agg}^2\beta_{core}^2 A_{core}^2(q) + \\ &N_{agg}\beta_{corona}^2 P'_{corona}(q) + \\ &2N_{agg}^2\beta_{core}\beta_{corona}A_{core}(q)\,A_{corona}(q) + \\ &N_{agg}\left(N_{agg} - P'_{corona}(0)\right)\beta_{corona}^2 A_{corona}^2(q)\Big]\end{aligned} \tag{4.10}$$

where N is the number density of micelles, N_{agg} the aggregation number of micelles, β_{core} and β_{corona} are the total excess scattering length of the block forming the spherical core and the corona, respectively. They are defined as

$$\beta_{corona} = V_{m,\,corona} DP_{corona} \Delta\rho_{corona} \tag{4.11}$$

and

$$\beta_{core} = V_{m,\,core} DP_{core} \Delta\rho_{core} \tag{4.12}$$

with V_m being the molecular volume of the respective monomer unit, DP_{corona} and DP_{core} the degree of polymerization of the corona and core block and $\Delta\rho$ the corresponding excess scattering length density.

Equation 4.10 consists of four different contributions: scattering from the spherical homogeneous core $A_{core}^2(q)$, scattering from the polymer chains in the corona $P'_{corona}(q)$, the cross-term between core and corona $A_{core}(q) \cdot A_{corona}(q)$ and the cross-term between different chains $A_{corona}^2(q)$. $A_{core}(q)$ is the scattering amplitude of a homogeneous

sphere[31] with radius R_{core}

$$A_{core}(q) = 3\frac{\sin(qR_{core}) - qR_{core}\cos(qR_{core})}{(qR_{core})^3} \tag{4.13}$$

$P'_{corona}(q)$ is the form factor of a chain in the corona. It contains the self-correlation of the chain $P_{exv}(q)$ as well as the interaction between the chains, which is expressed by the interaction parameter ν[29,54]

$$P'_{corona}(q) = \frac{P_{exv}(q)}{1 + \nu P_{exv}(q)} \tag{4.14}$$

where $P_{exv}(q)$ is the form factor of a semi flexible self-avoiding chain. This form factor was first derived by Pedersen and Schurtenberger[55] and later corrected.[56] In experiments ν typically adopts values between 0 and 8 and is related to the osmotic compressibility κ by[29,54,57]

$$\kappa = 1 + \nu \tag{4.15}$$

$A_{corona}(q)$ is given by

$$A_{corona}(q) = \frac{\int \rho_{corona}(r) r^2 \frac{\sin(qr)}{qr} dr}{\int \rho_{corona}(r) r^2 dr} \tag{4.16}$$

with $\rho_{corona}(r)$ as the scattering length density profile in the corona. In this work we use a Gaussian profile, which is defined as

$$\rho_{corona}(r) = \begin{cases} 0 & \text{for } r < R_{core} \\ 1 & \text{for } r = R_{core} \\ \exp\left(\frac{-(r-R_{core})^2}{2s^2}\right) & \text{for } r > R_{core} \end{cases} \tag{4.17}$$

with s controlling the thickness of the corona.

In order to take into account the size distribution of micelles we assumed a log-normal distribution of the aggregation number N_{agg}

$$p(N_{agg}) = \frac{1}{H\sqrt{2\pi}N_{agg}} \exp\left(\frac{-\log(N_{agg} - M)^2}{2H^2}\right) \tag{4.18}$$

where H and M define the distribution and are connected to the mean aggregation number $\overline{N_{agg}}$ and standard deviation $\sigma_{\overline{N_{agg}}}$ by

$$\overline{N_{agg}} = \exp\left(M + \frac{H^2}{2}\right) \tag{4.19}$$

$$\sigma_{\overline{N_{agg}}} = \sqrt{\exp(H^2 + 2M)(\exp(H^2) - 1)} \tag{4.20}$$

The macroscopic scattering cross-section is therefore

$$\frac{d\Sigma}{d\Omega}_{\text{polydisperse}}(q) = \int \frac{d\Sigma}{d\Omega}(q) p(N_{agg}) dN_{agg} \tag{4.21}$$

Instrumental resolution for SANS has been taken into account according to Ref. [58]. The macroscopic scattering function is convoluted with a resolution function $R(q, \sigma_q)$, which depends on wavelength spread, finite collimation of the beam and detector resolution

$$\frac{d\Sigma}{d\Omega}_{\text{smeared}}(q) = \int R(q, \sigma_q) \frac{d\Sigma}{d\Omega}_{\text{polydisperse}}(q) dq \tag{4.22}$$

Fitting procedure

For the form factor fits we used the SASET program,[59] which allows global fitting of several contrasts at the same time. During the data analysis of the SANS curves we took into account the instrumental resolution for each detector configuration and merged the data only for final representation. This approach allows us to increase the number of available data points since we do not truncate the data in the region of overlapping q. We performed a global fit to the SANS and SAXS data with a single set of shared fitting parameters. For the samples, where the aggregation number changes with D_2O content we attributed a common aggregation number to the corresponding SANS and SAXS curves but left the rest of the fitting parameters as global fitting parameters.

In order to constrain the fit we used the molar volumes of the individual blocks, known from the degree of polymerization and the molar volumes listed in Table 4.3. Moreover, we restricted the fit by giving the used polymer concentration. Together with the aggregation number N_{agg} (which is a fitting parameter) the number density N of micelles in L^{-1} is directly obtained by

$$N = \frac{c}{M_{\text{polymer}} N_{agg}} N_A \tag{4.23}$$

with c the polymer concentration in $g\,L^{-1}$, the molecular weight of the polymer M_{polymer} and the aggregation number N_{agg}.

SAXS

Figure 4.19 and 4.20 show the SAXS profiles of d_3-$PA_{1190}PSS_{70}$ and d_3-$PA_{360}PSS_{400}$ micelles in the presence of Ca^{2+} at various D_2O/H_2O ratios. The solid lines represents

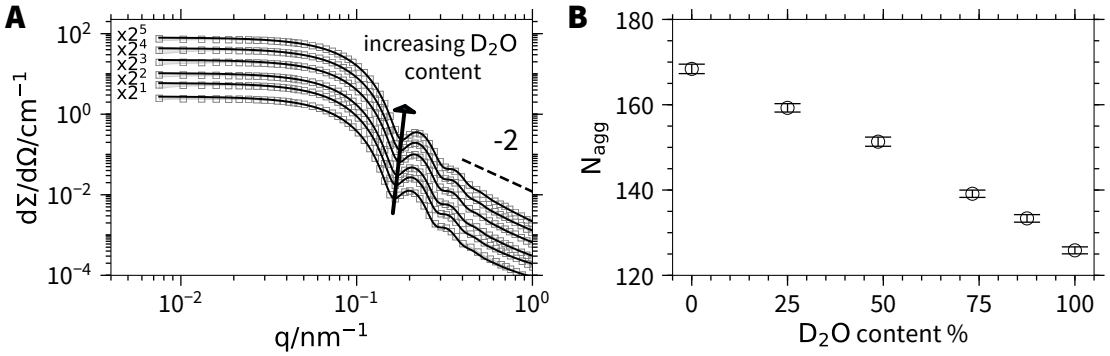


Figure 4.19: SAXS profiles of d_3-$PA_{1190}PSS_{70}$ micelles (c_{poly} = 4 g L^{-1}, $c_{Ca^{2+}}$ = 25 mmol L^{-1}) at various D_2O/H_2O ratios. The solid lines represent fits to the form factor of a polydisperse block copolymer micelle.[29] An overview of the fit results can be found in Table 4.4.

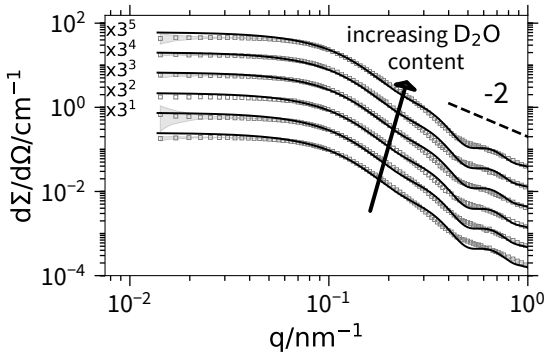


Figure 4.20: SAXS profiles of d_3-$PA_{360}PSS_{400}$ (c_{poly} = 4 g L^{-1}, $c_{Ca^{2+}}$ = 50 mmol L^{-1}) at various D_2O/H_2O ratios. The solid lines represent fits to the form factor of a polydisperse block copolymer micelle.[29] An overview of the fit results can be found in Table 4.4.

a fit to the previously described form factor model. For the sample d_3-$PA_{1190}PSS_{70}$ we obtained a change in aggregation number when changing from H_2O to D_2O. Figure 4.19 shows the aggregation numbers obtained from the form factor analysis as a function of D_2O content.

Model with PSS in the core and d_3-PA in the corona

Figure 4.21 shows the SANS profiles of d_3-$PA_{360}PSS_{400}$ and the model fit with PSS in the core and d_3-PA in the corona. This model can not describe the scattering data sufficiently well.

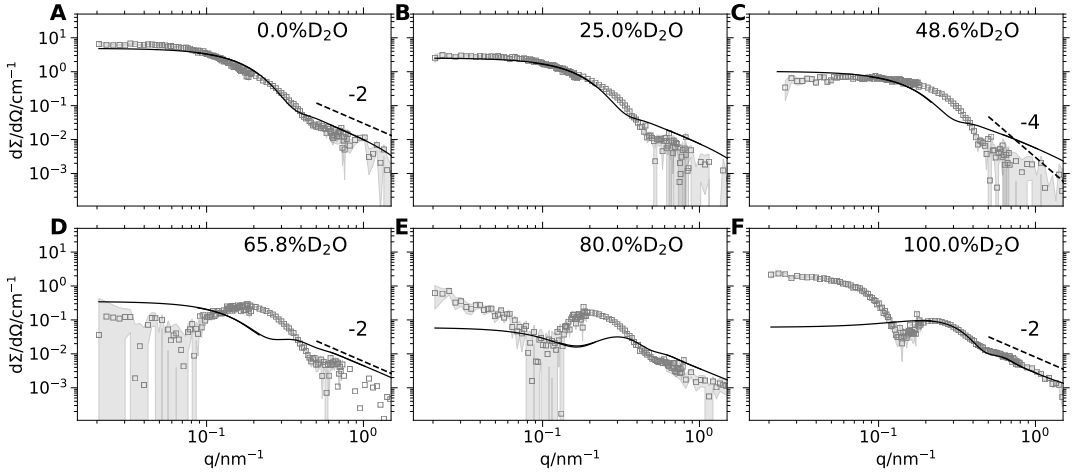


Figure 4.21: SANS profiles of d_3-$PA_{360}PSS_{400}$ micelles at various D_2O/H_2O ratios. The solid lines represents fits to the form factor of a polydisperse block copolymer with PSS in the core and d_3-PA in the corona.

4.4.6 Phase diagrams of the polymers in the presence of Ca^{2+}

The phase diagrams were established by subsequent addition of aliquots of 20 µL of a 50 mmol L^{-1} $CaCl_2$ solution to 1 mL of a solution of block copolymer in 100 mmol L^{-1} NaCl. The transition from single chains to micelles was monitored by turbidity using a UV-Vis spectrometer at 400 nm or the static light scattering signal (using the ALV-CSG3 at a scattering angle of 150°). Figure 4.22A shows the phase diagram with the points indicating single chain, micelle and phase separation regime. The phase boundaries for d_3-$PA_{1190}PSS_{70}$ and h_3-$PA_{1190}PSS_{70}$ were found to be identical within the given accuracy of the $CaCl_2$ injections. For d_3-$PA_{1190}PSS_{70}$/h_3-$PA_{1190}PSS_{70}$ precipitation of the micelles from solution can be found at $CaCl_2$ concentrations above 50 mmol L^{-1}, which we attribute to strong screening of the PSS chains in the corona and consequent destabilization of the micelles. h_3-$PA_{100}PSS_{750}$ does not form micelles in the presence of Ca^{2+}. Figure 4.22B shows a SAXS profile (D2AM, ESRF Grenoble) of h_3-$PA_{100}PSS_{750}$ in 50 mmol L^{-1} $CaCl_2$ solution. The scattering can be well described by the model of

D_2O %		N_{agg}	$\sigma_{N_{agg}}/N_{agg}$	R_{core}/nm	$\sigma_{R_{core}}/R_{core}$	$R_{g,corona}/nm$	s/nm	ν	h	$V_{m,Ca^{2+}}$ / $cm^3\ mol^{-1}$	$\frac{d\Sigma}{d\Omega}_{inc}/cm^{-1}$
d_3-PA_{119} PSS_{70}											
0.0	SANS	168.40 ± 0.11	$0.31 \pm 1.5 \times 10^{-4}$	26.10 ± 0.02	$0.102 \pm 5.0 \times 10^{-5}$	2.12 ± 0.03	$4.05 \pm 8.9 \times 10^{-3}$	$0.00 \pm 7.4 \times 10^{-3}$	11.59 ± 0.01	13.9 ± 0.02	$2.7 \cdot 10^{-3} \pm 1.4 \cdot 10^{-4}$
0.0	SAXS										$\overline{1.3 \cdot 10^{-3} \pm 1.1 \cdot 10^{-4}}$
25.0	SANS	159.27 ± 0.10		25.63 ± 0.02							$2.1 \cdot 10^{-3} \pm 7.5 \cdot 10^{-5}$
25.0	SAXS										$\overline{1.5 \cdot 10^{-3} \pm 4.9 \cdot 10^{-5}}$
48.6	SANS	151.34 ± 0.11		25.20 ± 0.02							$1.7 \cdot 10^{-3} \pm 3.3 \cdot 10^{-5}$
48.6	SAXS										$\overline{2.8 \cdot 10^{-13} \pm 2.3 \cdot 10^{-5}}$
73.3	SANS	139.13 ± 0.09		24.51 ± 0.02							
73.3	SAXS										
87.5	SANS	133.35 ± 0.09		24.17 ± 0.02							
87.5	SAXS										
100.0	SANS	125.86 ± 0.08		23.71 ± 0.02							
100.0	SAXS										
d_3-PA_{360} PSS_{400}											
0.0	SANS	19.6 ± 0.07	$0.21 \pm 9.9 \times 10^{-3}$	8.78 ± 0.03	$0.069 \pm 3.3 \times 10^{-3}$	9.55 ± 0.04	$8.86 \pm 9.5 \times 10^{-3}$	$1.19 \pm 2.3 \times 10^{-2}$	12.21 ± 0.03	19.6 ± 0.05	$2.0 \cdot 10^{-2} \pm 1.8 \cdot 10^{-4}$
0.0	SAXS										$\overline{4.4 \cdot 10^{-3} \pm 1.3 \cdot 10^{-4}}$
25.0	SANS										$4.4 \cdot 10^{-3} \pm 9.2 \cdot 10^{-5}$
25.0	SAXS										$\overline{3.0 \cdot 10^{-3} \pm 6.8 \cdot 10^{-5}}$
48.6	SANS										$1.5 \cdot 10^{-3} \pm 4.5 \cdot 10^{-5}$
48.6	SAXS										$\overline{8.6 \cdot 10^{-4} \pm 5.7 \cdot 10^{-5}}$
65.8	SANS										
65.8	SAXS										
80.0	SANS										
80.0	SAXS										
100.0	SANS										
100.0	SAXS										

Table 4.4: Parameters for the micelles in the presence of $CaCl_2$ obtained for the fits shown in the main manuscript and in Figure 4.19 and 4.20.

a generalized Gaussian chain[60]. We obtain a radius of gyration R_g of $14.0 \pm 0.1\,nm$ and a Flory exponent ν of 0.57 ± 0.05, which indicates that the polymer chains do not aggregate.

Figure 4.22C shows an autocorrelation function of h_3-$PA_{1190}\,PSS_{70}$ micelles and the corresponding fit using eq 4.3. The correlation function shows a mono modal decay, from which we conclude that the majority of polymers are aggregates into micelles and the fraction of free polymer is negligible.

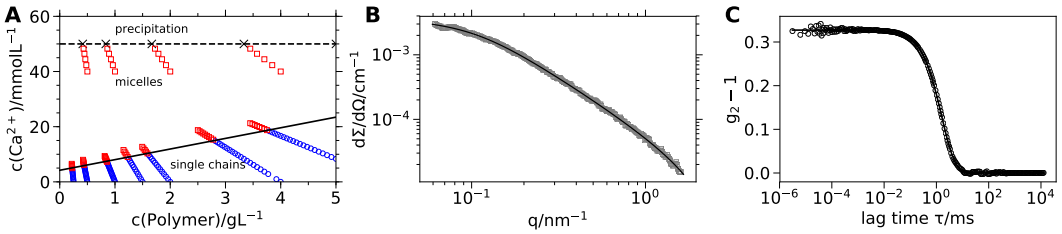


Figure 4.22: **A** Phase diagram of d_3-$PA_{1190}\,PSS_{70}$/h_3-$PA_{1190}\,PSS_{70}$ in the presence of Ca^{2+} in H_2O. The symbols indicate the compositions, which were prepared to identify the phase diagram. Black crosses indicate precipitates, red squares micelles and blue circles single chains. **B** SAXS profile (D2AM, ESRF Grenoble) of h_3-$PA_{100}\,PSS_{750}$ at $1\,g\,L^{-1}$ in $50\,mmol\,L^{-1}$ $CaCl_2$. The solid line represents the fit to the generalized Gaussian chain model[60]. **C** Exemplary autocorrelation function of h_3-$PA_{1190}\,PSS_{70}$ micelles and fit to eq 4.3.

4.5 References

1. Mai, Y.; Eisenberg, A. *Chem. Soc. Rev.* **2012**, *41*, 5969, DOI: 10.1039/c2cs35115c.
2. Zhang, L.; Barlow, R. J.; Eisenberg, A. *Macromolecules* **1995**, *28*, 6055–6066, DOI: 10.1021/ma00122a010.
3. Khougaz, K.; Astafieva, I.; Eisenberg, A. *Macromolecules* **1995**, *28*, 7135–7147, DOI: 10.1021/ma00125a016.
4. Foerster, S.; Khandpur, A. K.; Zhao, J.; Bates, F. S.; Hamley, I. W.; Ryan, A. J.; Bras, W. *Macromolecules* **1994**, *27*, 6922–6935, DOI: 10.1021/ma00101a033.
5. Knoll, A.; Horvat, A.; Lyakhova, K. S.; Krausch, G.; Sevink, G. J.; Zvelindovsky, A. V.; Magerle, R. *Phys. Rev. Lett.* **2002**, *89*, 355011–355014, DOI: 10.1103/PhysRevLett.89.035501.

6. Lodge, T. P.; Pudil, B.; Hanley, K. J. *Macromolecules* **2002**, *35*, 4707–4717, DOI: 10.1021/ma0200975.
7. Hanley, K. J.; Lodge, T. P.; Huang, C. I. *Macromolecules* **2000**, *33*, 5918–5931, DOI: 10.1021/ma000318b.
8. Almgren, M.; Brown, W.; Hvidt, S. *Colloid Polym. Sci.* **1995**, *273*, 2–15, DOI: 10.1007/BF00655668.
9. Förster, S.; Hermsdorf, N.; Böttcher, C.; Lindner, P. *Macromolecules* **2002**, *35*, 4096–4105, DOI: 10.1021/ma011565y.
10. Förster, S.; Abetz, V.; Müller, A. H. E. In *Polyelectrolytes with Defin. Mol. Archit. II*, 2004; Vol. 166, pp 173–210, DOI: 10.1007/b11351.
11. Endo, H.; Schwahn, D.; Cölfen, H. *J. Chem. Phys.* **2004**, *120*, 9410–9423, DOI: 10.1063/1.1691736.
12. Bolze, J.; Pontoni, D.; Ballauff, M.; Narayanan, T.; Cölfen, H. *J. Colloid Interface Sci.* **2004**, *277*, 84–94, DOI: 10.1016/j.jcis.2004.04.029.
13. Yokota, K.; Morvan, M.; Berret, J. F.; Oberdisse, J. *Europhys. Lett.* **2005**, *69*, 284–290, DOI: 10.1209/epl/i2004-10338-7.
14. Volk, N.; Vollmer, D.; Schmidt, M.; Oppermann, W.; Huber, K. In; Chapter 0002, 2004; Vol. 166, pp 29–65, DOI: 10.1007/b11348.
15. Schweins, R.; Goerigk, G.; Huber, K. *Eur. Phys. J. E* **2006**, *21*, 99–110, DOI: 10.1140/epje/i2006-10047-7.
16. Schweins, R.; Lindner, P.; Huber, K. *Macromolecules* **2003**, *36*, 9564–9573, DOI: 10.1021/ma0347722.
17. Schweins, R.; Huber, K. *Eur. Phys. J. E* **2001**, *5*, 117–126, DOI: 10.1007/s101890170093.
18. Huber, K. *J. Phys. Chem.* **1993**, *97*, 9825–9830, DOI: 10.1021/j100140a046.
19. Ikegami, A.; Imai, N. *J. Polym. Sci.* **1962**, *56*, 133–152, DOI: 10.1002/pol.1962.1205616312.
20. Flory, P. J.; Osterheld, J. E. *J. Phys. Chem.* **1954**, *58*, 653–661, DOI: 10.1021/j150518a014.
21. Sabbagh, I.; Delsanti, M. *Eur. Phys. J. E* **2000**, *1*, 75–86, DOI: 10.1007/s101890050009.

22. Sinn, C. G.; Dimova, R.; Antonietti, M. *Macromolecules* **2004**, *37*, 3444–3450, DOI: 10.1021/ma030550s.

23. Lages, S.; Schweins, R.; Huber, K. *J. Phys. Chem. B* **2007**, *111*, 10431–10437, DOI: 10.1021/jp068258k.

24. Hansch, M.; Hämisch, B.; Schweins, R.; Prévost, S.; Huber, K. *J. Chem. Phys.* **2018**, *148*, 014901, DOI: 10.1063/1.5006618.

25. Hansch, M.; Kaub, H. P.; Deck, S.; Carl, N.; Huber, K. *J. Chem. Phys.* **2018**, *148*, 114906, DOI: 10.1063/1.5019877.

26. Yap, H. P.; Hao, X.; Tjipto, E.; Gudipati, C.; Quinn, J. F.; Davis, T. P.; Barner-Kowollik, C.; Stenzel, M. H.; Caruso, F. *Langmuir* **2008**, *24*, 8981–8990, DOI: 10.1021/la8011074.

27. Bruessau, R. J. *Makromol. Chemie. Macromol. Symp.* **1992**, *61*, 190–218, DOI: 10.1002/masy.19920610116.

28. Stuhrmann, H. B. *J. Appl. Crystallogr.* **1974**, *7*, 173–178, DOI: 10.1107/S0021889874009071.

29. Svaneborg, C.; Pedersen, J. S. *Macromolecules* **2002**, *35*, 1028–1037, DOI: 10.1021/ma011046v.

30. Pedersen, J. S.; Gerstenberg, M. C. *Macromolecules* **1996**, *29*, 1363–1365, DOI: 10.1021/ma9512115.

31. Rayleigh, L. *Proc. Roy. Soc. London* **1911**, *A84*, 25–38.

32. Pedersen, J. S. *Adv. Colloid Interface Sci.* **1997**, *70*, 171–210, DOI: 10.1016/S0001-8686(97)00312-6.

33. Braun, M. K.; Wolf, M.; Matsarskaia, O.; Da Vela, S.; Roosen-Runge, F.; Sztucki, M.; Roth, R.; Zhang, F.; Schreiber, F. *J. Phys. Chem. B* **2017**, *121*, 1731–1739, DOI: 10.1021/acs.jpcb.6b12814.

34. Strazielle, C.; Benoit, H. *Macromolecules* **1975**, *8*, 203–205, DOI: 10.1021/ma60044a021.

35. Dai, L.; Douglas, E. P.; Gower, L. B. *J. Non. Cryst. Solids* **2008**, *354*, 1845–1854, DOI: 10.1016/j.jnoncrysol.2007.10.022.

36. Gower, L. B.; Odom, D. J. *J. Cryst. Growth* **2000**, *210*, 719–734, DOI: 10.1016/S0022-0248(99)00749-6.

37. Prabhu, V.; Muthukumar, M.; Wignall, G.; Melnichenko, Y. *Polymer* **2001**, *42*, 8935–8946, DOI: 10.1016/S0032-3861(01)00382-2.

38. Ikeda, Y.; Beer, M.; Schmidt, M.; Huber, K. *Macromolecules* **1998**, *31*, 728–733, DOI: 10.1021/ma970540p.

39. Papadakis, C. M.; Müller-Buschbaum, P.; Laschewsky, A. *Langmuir* **2019**, *35*, 9660–9676, DOI: 10.1021/acs.langmuir.9b01444.

40. Chaduc, I.; Crepet, A.; Boyron, O.; Charleux, B.; D'Agosto, F.; Lansalot, M. *Macromolecules* **2013**, *46*, 6013–6023, DOI: 10.1021/ma401070k.

41. Dao, V. H.; Cameron, N. R.; Saito, K. *Polym. Chem.* **2017**, *8*, 6834–6843, DOI: 10.1039/c7py01410d.

42. Goerigk, G.; Schweins, R.; Huber, K.; Ballauff, M. *Europhys. Lett.* **2004**, *66*, 331–337, DOI: 10.1209/epl/i2003-10215-y.

43. Orthaber, D.; Bergmann, A.; Glatter, O. *J. Appl. Crystallogr.* **2000**, *33*, 218–225, DOI: 10.1107/S0021889899015216.

44. Boesecke, P. *J. Appl. Crystallogr.* **2007**, *40*, 423–427, DOI: 10.1107/S0021889807001100.

45. Zemb, T.; Lindner, P., *Neutrons, X-rays and light: scattering methods applied to soft condensed matter*; North-Holland: 2002.

46. Frisken, B. J. *Appl. Opt.* **2001**, *40*, 4087, DOI: 10.1364/AO.40.004087.

47. Burchard, W.; Schmidt, M.; Stockmayer, W. H. *Macromolecules* **1980**, *13*, 580–587, DOI: 10.1021/ma60075a020.

48. Burchard, W.; Schmidt, M.; Stockmayer, W. H. *Macromolecules* **1980**, *13*, 1265–1272, DOI: 10.1021/ma60077a045.

49. Zimm, B. H. *J. Chem. Phys.* **1948**, *16*, 1093–1099, DOI: 10.1063/1.1746738.

50. Brüssau, R.; Goetz, N.; Mächtle, W.; Stölting, J. *Tenside, Surfactants, Deterg.* **1991**, *28*, 396–406.

51. Tondre, C.; Zana, R. *J. Phys. Chem.* **1972**, *76*, 3451–3459, DOI: 10.1021/j100667a026.

52. Pedersen, J. S.; Svaneborg, C. *Curr. Opin. Colloid Interface Sci.* **2002**, *7*, 158–166, DOI: 10.1016/S1359-0294(02)00044-4.

53. Pedersen, J. S.; Svaneborg, C.; Almdal, K.; Hamley, I. W.; Young, R. N. *Macromolecules* **2003**, *36*, 416–433, DOI: 10.1021/ma0204913.

54. Svaneborg, C.; Pedersen, J. S. *Phys. Rev. E* **2001**, *64*, 010802, DOI: 10.1103/PhysRevE.64.010802.

55. Skov, J.; Schurtenberger, P.; Pedersen, J. S. *Macromolecules* **1996**, *9297*, 7602–7612, DOI: 10.1021/ma9607630.

56. Chen, W. R.; Butler, P. D.; Magid, L. J. *Langmuir* **2006**, *22*, 6539–6548, DOI: 10.1021/la0530440.

57. Sommer, C.; Pedersen, J. S.; Garamus, V. M. *Langmuir* **2005**, *21*, 2137–2149, DOI: 10.1021/la047489k.

58. Pedersen, J. S.; Posselt, D.; Mortensen, K. *J. Appl. Crystallogr.* **1990**, *23*, 321–333, DOI: 10.1107/S0021889890003946.

59. Muthig, M.; Prévost, S.; Orglmeister, R.; Gradzielski, M. *J. Appl. Crystallogr.* **2013**, *46*, 1187–1195, DOI: 10.1107/S0021889813016658.

60. Hammouda, B. *Polym. Charact.* **1993**, *106*, 87–133, DOI: 10.1007/BFb0025862.

Chapter 5

Contrast variation of micelles composed of Ca^{2+} and block copolymers of two negatively charged polyelectrolytes

Abstract

Block copolymers were prepared with two anionic polyelectrolyte blocks: sodium polyacrylate (PA) and sodium polystyrene sulfonate (PSS), in order to investigate their phase behavior in aqueous solution in the presence of Ca^{2+} cations. Depending on the concentration of polymer and Ca^{2+} and on the ratio of the block lengths in the copolymer, spherical micelles were observed. Micelle formation arises from the specific interaction of Ca^{2+} with the PA block only. An extensive small-angle scattering study was performed in order to unravel the structure and dimensions of the block copolymer micelles. Deuteration of the PA block enabled us to perform contrast variation experiments using small-angle neutron scattering at variable ratios of light and heavy water which were combined with information from small-angle X-ray scattering and dynamic light scattering.

This chapter is based on Carl, N.; Prévost, S.; Schweins, R.; Huber, K.; Contrast variation of micelles composed of Ca^{2+} and block copolymers of two negatively charged polyelectrolytes. The article was accepted for publication in *Colloid and Polmyer Science*.

5.1 Introduction

Polyelectrolytes and their interactions with oppositely charged species such as ions,[1] surfactants[2–4] or charged surfaces[5] are essential to understand and control a variety of industrial processes. These include waste water treatment,[6] modification of the rheological behavior of concrete through superplasticizers[7,8] or the properties of consumer goods such as shampoo.[9] The phase behavior of polyelectrolytes with several multivalent cations such as Ca^{2+},[10,11] Sr^{2+},[11–14] Pb^{2+},[15] Al^{3+}[16,17] and La^{3+}[18,19] has been extensively studied during the last decades. These aqueous systems show a rich phase behavior strongly depending on the polyelectrolyte,[20] cation,[16,17,21] temperature[16,22] or concentration of inert salts such as NaCl.[23]

Extensive work on the polyelectrolyte sodium polyacrylate (PA) addressed the specific interaction with Ca^{2+}.[10,11,13,23,24] Upon addition of Ca^{2+} the cation will bind to the negatively charged moieties of the PA chain. When the Ca^{2+} concentration is increased more cations will bind to the polyelectrolyte until a critical concentration $[Ca^{2+}]_c$ is reached. Beyond this concentration the polymer starts to aggregate and precipitate from the solution. A phase boundary according to

$$[Ca^{2+}]_c = r_0 + m[PA] \tag{5.1}$$

is found for this system where [PA] is the concentration of polyacrylate monomer units, r_0 the minimum concentration of Ca^{2+} required to precipitate the polymer at infinite dilution and m defines the stoichiometry of binding. Precipitation at infinite dilution here means an intramolecular coil collapse. Equation 4.1 relates to a complexation equilibrium completely on the side of the Ca^{2+}/PA complex. Specificity of the interaction between Ca^{2+} and PA was further confirmed by isothermal titration calorimetry (ITC), which revealed a large endothermic heat. This large heat of reaction was interpreted by a liberation of around ten water molecules per from hydration shells which coalesce upon complex bond formation between Ca^{2+} and two COO^-.[25] Since one Ca^{2+} binds quantitatively to two polyacrylate monomer units, this system has for example been used for the design of an efficient Ca^{2+} sensor.[26]

In contrast, another common polyelectrolyte polystyrene sulfonate (PSS) does not show specific interactions with Ca^{2+}. No matter how large the concentration of Ca^{2+} is set, no precipitation of the polymer does occur. Furthermore, light scattering demonstrated that the polymer chains do not even aggregate in the presence of Ca^{2+}. Isothermal titration calorimetry revealed just a weak endothermic signal, suggesting that ad-

dition of Ca^{2+} induces only a replacement of two Na^{+} cations condensed into the polyelectrolyte domains by one Ca^{2+} and thus confirming the lack of any binding of Ca^{2+} to the sulfonic residues of PSS.[20]

In a previous work we combined these two different interaction patterns in one polymer by synthesizing a block copolymer (PA-*b*-PSS) of sodium polyacrylate and sodium polystyrene sulfonate.[27] Whereas the anionic residues of the PA block interact specifically with Ca^{2+}, no such interactions are expected for the PSS block. Indeed, it turned out that the block copolyelectrolytes form micelles in aqueous solution. Application of small-angle neutron scattering (SANS) at variable scattering contrasts, revealed the morphology of these micelles: The PA blocks change their solution behavior in water as specific interactions trigger decoration of PA with Ca^{2+} cations thereby establishing the core of the micelles. The PSS block keeps its charges along the polymer backbone due to the lack of any specific interactions and form the stabilizing corona of the micelles. The entropic nature of the specific interactions between Ca^{2+} and PA enabled us to reversibly form and disintegrate the micelles by oscillating the temperature with an increase of temperature inducing formation and a decrease disintegration.

The present work extends the achievements published in Ref. [27] with the following new results: It interprets SANS and SAXS curves with a model[28] giving access to the morphology of the micellar corona; it outlines the benefit of combining SANS at variable contrast with SAXS and it makes full use of Stuhrmann's approach[29,30] in order to unravel the species in the core as well as the core dimensions independently of any model. All these features are established with three different block copolyelectrolytes: one sample with similar block lengths and the PA block fully deuterated and two samples with short PSS blocks and long PA blocks whereby in one case the PA block is fully deuterated and in the other case it is hydrogenated. This for the first time makes accessible a detailed comparative discussion.

The work is grouped in four parts: in the first part we shortly revise the results on PA-*b*-PSS published in our preceding work,[27] in order to help the reader understanding the basis of the present work and to clearly separate it from the previous one. The second part deals with the comparative analysis of a contrast variation SANS experiment of three different block copolymers using a form factor model for micelles based on block copolymers.[28] The result is a comprehensive structural picture of the micelles. In particular, the advantage of joint SANS and SAXS experiments on the same set of samples is demonstrated and used to unravel an isotope effect occurring for two samples. The isotope effect results in a change of aggregation numbers, which was taken

into account in the data analysis. The third part investigates the origin of this isotope effect using isothermal titration calorimetry and relates it to the binding of Ca^{2+} to PA. The fourth part demonstrates a model independent analysis, which yields quantitative structural information. The obtained information is verified against the results from the form factor fits and can be used for systems where mathematical expressions for a form factor model are not available. It is demonstrated that this approach even works on a fully hydrogenated block copolymer, which has important implications for samples where deuteration is impractical or not feasible.

5.2 Experimental details

5.2.1 Materials

Light water (H_2O) was purified using a Milli-Q-system (Millipore) to a final resistivity of 18.2 $M\Omega\,cm$. Heavy water (D_2O, Euriso-top, France, 99.90 atom% deuterium) was filtered with 100 nm PVDF filter (Merck Millex MPSLVV033RS) prior to use. $CaCl_2 \cdot 2\,H_2O$ (Sigma Aldrich, France, >99.9%), NaCl (Sigma Aldrich, France, >99.9%) and NaOH (Sigma Aldrich, France) were used as received.

5.2.2 Polymer synthesis and characterization

The synthesis and characterization of the polymers was described in detail in a previous work.[27] Figure 5.1 shows the chemical structure of the used polymers. All polymers were used as sodium salt. Prior to the small-angle scattering experiments the polymers and their phase behavior with Ca^{2+} were characterized using NMR and static and dynamic light scattering. Detailed information can be found in a previous work.[27] Table 5.1 summarizes the results of the polymer characterization.

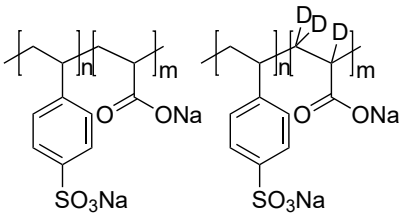


Figure 5.1: Chemical structure of the used polymers. The left structure shows the fully hydrogenated polymer (h_3-PA$-b-$PSS), the right structure shows a PA block which is fully deuterated (d_3-PA$-b-$PSS).

Table 5.1: Overview of polymers, compositions, weight-averaged molecular weights M_w and hydrodynamic radii R_h determined from NMR and static and dynamic light scattering in 100 mmol L^{-1} NaCl as a good solvent and in the absence of $CaCl_2$. The subscript denotes the degree of polymerization, while d_3 and h_3 corresponds to deuteration or hydrogenation of the PA block, respectively.

Sample	PA:PSS /mol %	M_w /kg mol^{-1}	R_h /nm
h_3-$PA_{1190}PSS_{70}$	94:6	160 ± 2	13.8 ± 0.6
d_3-$PA_{1190}PSS_{70}$	94:6	181 ± 3	13.6 ± 0.5
d_3-$PA_{360}PSS_{400}$	47:53	127 ± 1	10.4 ± 0.2

5.2.3 Sample preparation

The sample preparation was performed similarly as in previous works.[22–24,27] The total number of positive charges for all samples was adjusted to 100 mmol L^{-1}. The total concentration of positive charges [+] is

$$[+] = [\mathrm{NaCl}] + 2 \cdot [\mathrm{CaCl_2}] = 100\,\mathrm{mmol\,L^{-1}} \tag{5.2}$$

with [NaCl] being the concentration of sodium chloride and [$CaCl_2$] the concentration of calcium chloride. A sample containing 25 mmol L^{-1} $CaCl_2$ also contained 50 mmol L^{-1} NaCl, whereas a sample with 50 mmol L^{-1} $CaCl_2$ contains no additional NaCl.

5.2.4 SANS

SANS measurements were performed at the D11 small angle scattering instrument of the Institut Laue-Langevin (Grenoble, France). Three sample to detector distances (39.0 m collimation 40.5 m, 8.0 m collimation 8.0 m, 1.4 m collimation 5.5 m) and a neutron wavelength of 0.5 nm (FWHM 9 %) were used to cover a q-range of $2 \times 10^{-2}\,\mathrm{nm^{-1}} - 5\,\mathrm{nm^{-1}}$. We used a circular neutron beam with a diameter of 15 mm. Scattered neutrons were detected with a ^{3}He MWPC detector (CERCA) with 256×256 pixels of 3.75 mm $\times$ 3.75 mm pixel size. Samples were filled in 2 mm Hellma 404 Quartz Suprasil cells. The sample temperature was adjusted to 25 °C using a circulating water bath. The detector images were azimuthally averaged, corrected to transmission of the direct beam and scaled to absolute intensity using the LAMP software. Scaling to absolute intensity was based on a 1 mm H_2O cell as secondary calibration standard ($\frac{d\Sigma}{d\Omega} = 0.929\,\mathrm{cm^{-1}}$ at a neutron wavelength of 5 Å). The scattering from the solvent and the incoherent background were subtracted from the scattering curves. Details for the data reduction can be found in Chapter 2 of Ref. [31].

5.2.5 SAXS

Small-angle X-Ray scattering was performed at the ID02 beamline of the European Synchrotron Radiation Facility (ESRF). Two sample to detector distances (10 m and 1 m) were measured at a X-Ray energy of 12.46 keV (0.0995 nm) using a Rayonix MX-170HS CCD detector to cover a q-range of $8 \times 10^{-3}\,\mathrm{nm}^{-1} - 6\,\mathrm{nm}^{-1}$. Samples were filled in 2 mm quartz glass capillaries (WJM Glas Müller, Berlin, Germany). The detector images were corrected for dark and flat-field, azimuthally averaged, corrected to transmission of the direct beam and scaled to absolute intensity using water as a secondary standard.[32,33] The scattering from the solvent was subtracted from the scattering curves. Details can be found in Ref. [33]. Error bars were estimated as standard deviations from measurements of at least five different positions within the capillary.

5.2.6 Small-angle scattering data analysis

The form factor of spherical self-assembled block copolymers with excluded volume interaction of the polymer chains in the corona[28] was used to fit the SAXS and SANS data. The specific macroscopic scattering cross-section per unit solid angle $\frac{d\Sigma}{d\Omega}(q)$ of a solution of micelles can be written as[28]

$$\begin{aligned}\frac{d\Sigma}{d\Omega}(q) = N\Big[&N_{agg}^2\beta_{core}^2 A_{core}^2(q) + \\ &N_{agg}\beta_{corona}^2 P'_{corona}(q) + \\ &2N_{agg}^2\beta_{core}\beta_{corona}A_{core}(q)\,A_{corona}(q) + \\ &N_{agg}\left(N_{agg} - P'_{corona}(0)\right)\beta_{corona}^2 A_{corona}^2(q)\Big]\end{aligned} \tag{5.3}$$

where N is the number density of micelles, N_{agg} the aggregation number of micelles, β_{core} and β_{corona} are the total excess scattering length of the block forming the spherical core and the corona, respectively. They are defined as

$$\beta_{corona} = V_{m,\,corona}\,DP_{corona}\,\Delta\rho_{corona} \tag{5.4}$$

and

$$\beta_{core} = V_{m,\,core}\,DP_{core}\,\Delta\rho_{core} \tag{5.5}$$

with V_m being the molecular volume of the respective monomer unit, DP_{corona} and DP_{core} the degree of polymerization of the corona and core block and $\Delta\rho$ the corresponding excess scattering length density.

Equation 5.3 consists of four different contributions: scattering from the spherical homogeneous core $A^2_{core}(q)$, scattering from the polymer chains in the corona $P'_{corona}(q)$, the term which takes into account the cross-term between core and corona $A_{core}(q) \cdot A_{corona}(q)$ and a term which takes into account interferences between chains in the corona $A^2_{corona}(q)$. $A_{core}(q)$ is the scattering amplitude of a homogeneous sphere[34] with radius R_{core}

$$A_{core}(q) = 3\frac{\sin(qR_{core}) - qR_{core}\cos(qR_{core})}{(qR_{core})^3} \tag{5.6}$$

$P'_{corona}(q)$ is the form factor of a chain in the corona. It contains the self-correlation of the chain $P_{exv}(q)$ as well as the interaction between the chains, which is expressed by the interaction parameter ν[28,35]

$$P'_{corona}(q) = \frac{P_{exv}(q)}{1 + \nu P_{exv}(q)} \tag{5.7}$$

where $P_{exv}(q)$ is the form factor of a semi flexible self-avoiding chain. This form factor was first derived by Pedersen and Schurtenberger[36] and later corrected.[37] In experiments ν typically adopts values between 0 and 8 and is related to the osmotic compressibility κ by[28,35,38]

$$\kappa = 1 + \nu \tag{5.8}$$

$A_{corona}(q)$ is given by

$$A_{corona}(q) = \frac{\int \rho_{corona}(r) r^2 \frac{\sin(qr)}{qr} dr}{\int \rho_{corona}(r) r^2 dr} \tag{5.9}$$

with $\rho_{corona}(r)$ as the scattering length density profile in the corona. $A_{corona}(q)$ is normalized so that $A_{corona}(0) = 1$. In this work we use a Gaussian profile, which is defined as

$$\rho_{corona}(r) = \begin{cases} 0 & \text{for } r < R_{core} \\ 1 & \text{for } r = R_{core} \\ \exp\left(\frac{-(r-R_{core})^2}{2s^2}\right) & \text{for } r > R_{core} \end{cases} \tag{5.10}$$

with s controlling the thickness of the corona.

In order to take into account the size distribution of micelles we assumed a log-normal distribution of the aggregation number N_{agg}

$$p(N_{agg}) = \frac{1}{H\sqrt{2\pi}N_{agg}} \exp\left(\frac{-\log(N_{agg} - M)^2}{2H^2}\right) \tag{5.11}$$

where H and M define the distribution and are connected to the mean aggregation number $\overline{N_{agg}}$ and standard deviation $\sigma_{\overline{N_{agg}}}$ by

$$\overline{N_{agg}} = \exp\left(M + \frac{H^2}{2}\right) \tag{5.12}$$

$$\sigma_{\overline{N_{agg}}} = \sqrt{\exp\left(H^2 + 2M\right)\left(\exp\left(H^2\right) - 1\right)} \tag{5.13}$$

The macroscopic scattering cross-section is therefore

$$\frac{d\Sigma}{d\Omega}_{\text{polydisperse}}(q) = \int \frac{d\Sigma}{d\Omega}(q) p(N_{agg}) dN_{agg} \tag{5.14}$$

Instrumental resolution for SANS has been taken into account according to Ref. [39]. The macroscopic scattering function is convoluted with a resolution function $R(q, \sigma_q)$, which depends on wavelength spread, finite collimation of the beam and detector resolution

$$\frac{d\Sigma}{d\Omega}_{\text{smeared}}(q) = \int R(q, \sigma_q) \frac{d\Sigma}{d\Omega}_{\text{polydisperse}}(q) dq \tag{5.15}$$

For the form factor fits we used the SASET program,[40] which allows global fitting of several contrasts at the same time. During the data analysis of the SANS curves we took into account the instrumental resolution for each detector configuration and merged the data only for final representation. This approach allowed us to increase the number of available data points since we do not truncate the data in the region of overlapping q. The factor for merging the SANS measurements at 39 m to the other configurations was set as a global fitting parameter for all the curves as using water as an absolute calibration standard is not feasible at this sample to detector distance.

5.2.7 Dynamic light scattering

Dynamic light scattering (DLS) available in the ILL PSCM lab was performed using an ALV CGS-3 (ALV, Langen, Germany) equipped with a HeNe laser operating at $\lambda_0 = 632.8\,\text{nm}$. The samples were filtered in cylindrical quartz glass cells using Millex PVDF filters with a pore size of 0.45 µm. The temperature of the samples was kept at 25 °C. DLS was measured in an angular range from 30° to 150° in steps of 10°.

The intensity-time correlation function $g_2(\tau) - 1$ was analyzed using the method of cumulants[41]

$$g_2(\tau) - 1 = B + \beta \exp\left(-2\Gamma\tau\right)\left(1 + \frac{\mu_2}{2!}\tau^2\right)^2 \tag{5.16}$$

B is a factor correcting the baseline, β a factor, which depends on the experimental setup, Γ the relaxation rate and μ_2 the second cumulant. The apparent diffusion coefficient $D_{app}(c, q)$ for a given q is calculated according to

$$D_{app} = \frac{\Gamma}{q^2} \tag{5.17}$$

The diffusion coefficient is extrapolated towards $q = 0$ according to[42,43]

$$D_{app}(q) = D_0 \left(1 + CR_g^2 q^2\right) \tag{5.18}$$

where C is a constant describing the q dependence of $D_{app}(q)$. The diffusion coefficient D_0 is used to calculate the hydrodynamic radius R_h using the Stokes-Einstein equation

$$R_h = \frac{k_B T}{6\pi\eta D_0} \tag{5.19}$$

where T is the temperature, k_B the Boltzmann constant and η the viscosity of the solvent.

The viscosity of D_2O and H_2O was obtained from Ref. [44], while for mixtures of D_2O and H_2O the viscosity was calculated based on the volume fraction.

5.2.8 Isothermal titration calorimetry (ITC)

Isothermal titration calorimetry (ITC) was performed using a VP-ITC calorimeter from Malvern Instruments at 25.0 °C. The cell contained 1.4 mL of a solution of PA (0.2 g L^{-1} in 100 mmol L^{-1} NaCl). To this solution, between 4 and 24 µL of an aqueous solution containing 12 mmol L^{-1} $CaCl_2$ and 76 mmol L^{-1} NaCl was added. The time span between the injections was 300 s. The experiment was repeated twice, first using H_2O as a solvent and then D_2O. The baseline correction and integration of the peaks was performed using the software NITPIC.[45] The signals were not corrected for the heat of dilution of the polyelectrolyte and the $CaCl_2$ solution as these contributions were considerably smaller than the heat of binding of Ca^{2+} to PA. The data were fitted using the model of a single set of identical binding sites.[46,47]

5.3 Results and discussion

5.3.1 Review of micellization of PA-b-PSS in the presence of Ca^{2+}[27]

Three polymers at three different ratios of block lengths were synthesized and investigated in the context of the previous work: One polymer with a long PA and a short

PSS block (d_3-$PA_{1190}PSS_{70}$), one polymer with a symmetric block ratio between PA and PSS (d_3-$PA_{360}PSS_{400}$) and one polymer with a long PSS and a short PA block (h_3-$PA_{100}PSS_{750}$). In the presence of Ca^{2+}, d_3-$PA_{1190}PSS_{70}$ and d_3-$PA_{360}PSS_{400}$ form spherical block copolymer micelles arising from the specific interaction of Ca^{2+} with the PA block. In contrast, micelle formation was not observed for h_3-$PA_{100}PSS_{750}$ due to the considerably shorter PA block, not rendering the polymer chain hydrophobic enough to form micellar aggregates. Phase diagrams of the two polymers forming micelles were established and are presented in Figure 5.2.

Contrast variation small-angle neutron scattering of the micelles was performed at variable H_2O/D_2O ratios using the two block copolymers with the deuterated PA block, labelled as d_3-PA. The black dots in Figure 5.2 indicate the sample composition where the contrast variation experiments were conducted. A preliminary analysis of the scattering data revealed that d_3-PA blocks complexed by Ca^{2+} form the hydrophobic core of the micelle, while PSS is located in the corona and stabilizes the aggregates.

Furthermore, it was shown that an increase of temperature promotes the binding of Ca^{2+} to PA and was therefore used to induce micelle formation of a sample close to the phase transition. It was demonstrated that micelle formation is reversible and can be induced and reverted by consecutive additions of Ca^{2+} and a complexing agent such as Na_2EDTA and by consecutive cycles of temperature increase and drop respectively.

5.3.2 Scattering analysis with a form factor model

The main motivation for performing a contrast variation experiment on the presented system is to figure out whether PSS or PA forms the hydrophobic core of the anticipated micellar aggregates. This was already elucidated in the previous work[27], however fitting the data with a form factor model also makes accessible information about the exact size of the micelle core, the water content inside the micelle core, the thickness of the corona as well as the interaction of the polymer chains in the corona. In order to assess such information, the model of a block copolymer micelle with self-avoiding chains in the corona (eq. 5.3) was used to fit the experimental data.[28] In addition to the polymers d_3-$PA_{360}PSS_{400}$ and d_3-$PA_{1190}PSS_{70}$ a third fully hydrogenated polymer h_3-$PA_{1190}PSS_{70}$ is investigated in the current work. Deuteration is not always feasible as deuterated monomers do not exist for a wide range of polymers and deuteration of biological molecules such as proteins or sugars is often difficult and very cost intensive. Nevertheless, a contrast variation experiment is still possible if the scattering length

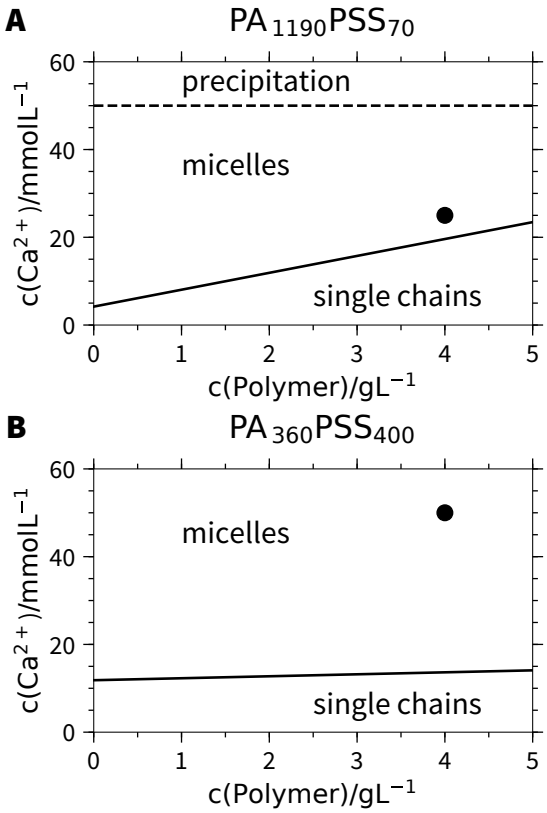


Figure 5.2: Phase diagrams of (A) d_3-$PA_{1190}PSS_{70}$/h_3-$PA_{1190}PSS_{70}$ and (B) d_3-$PA_{360}PSS_{400}$ in the presence of Ca^{2+}. The black points indicate the points where the contrast variation experiments were performed.

densities of two components are sufficiently different. h_3-$PA_{1190}PSS_{70}$ will be used as a showcase to illustrate the feasibility of performing a contrast variation study on a fully hydrogenated block copolymer. Section 5.3.2 will present a comparative and exhaustive interpretation of the SANS and SAXS curves of all three block copolyelectrolyte samples with suitable model form factors.[28]

Figure 5.3 shows the SANS profiles of d_3-$PA_{360}PSS_{400}$ micelles at variable H_2O/D_2O ratios. As has been outlined in Reference [27] the overall shape and the forward scattering of the SANS profiles presented in Figure 5.3 drastically change upon variation of the solvent ratio H_2O/D_2O. SAXS on the same samples was also performed to show that changing from light to heavy water does not influence the aggregation number, size and morphology of the aggregates. Figure 5.4A shows these SAXS profiles. All SAXS curves overlap perfectly (Figure 5.4B), when plotted without the multiplication factor used in

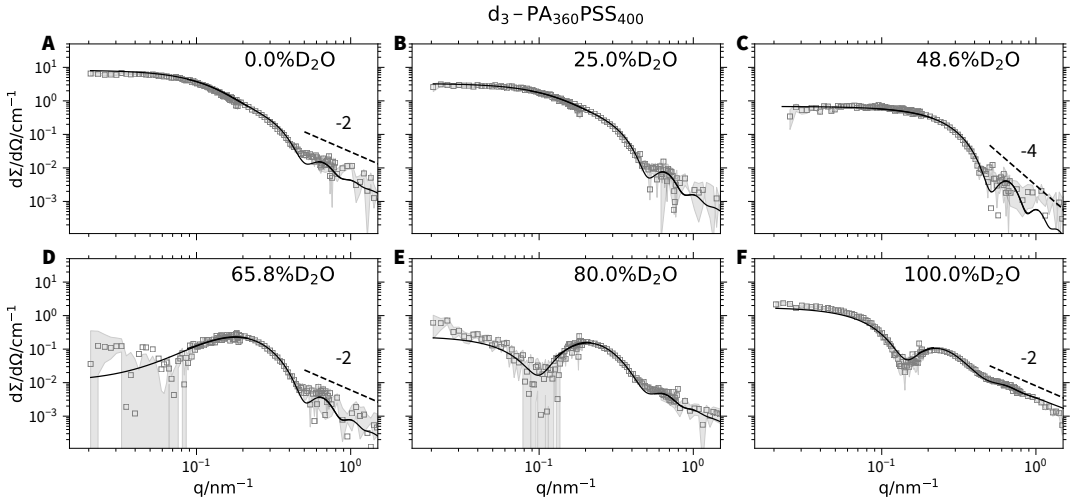


Figure 5.3: SANS profiles of d_3-$PA_{360}PSS_{400}$ (c_{poly} = 4 g L^{-1}, $c_{Ca^{2+}}$ = 50 mmol L^{-1}) in 0.0% D_2O (**A**), 25.0% D_2O (**B**), 48.6% D_2O (**C**), 65.8% D_2O (**D**), 80.0% D_2O (**E**) and 100.0% D_2O (**F**). The solid lines represent fits to the form factor of a polydisperse block copolymer micelle.[28] An overview of the fit results can be found in Table 5.2 and Table 5.7 of the Supporting Information.

Figure 5.4A. The perfect overlay of the SAXS curves clearly demonstrates, that the variation in the D_2O/H_2O ratio does not affect the nature of the aggregates. This finding simplifies interpretation of the scattering data from d_3-$PA_{360}PSS_{400}$ considerably.

Figure 5.5 and Figure 5.7 show the SANS profiles of d_3-$PA_{1190}PSS_{70}$ and h_3-$PA_{1190}PSS_{70}$ micelles in six different H_2O/D_2O mixtures and Figure 5.6A and Figure 5.8A show the SAXS profiles of the corresponding solutions. As observed for d_3-$PA_{360}PSS_{400}$, the forward scattering of the SANS curves changes with varying D_2O content. For d_3-$PA_{1190}PSS_{70}$ the forward scattering continously decreases with increasing content of D_2O, while for h_3-$PA_{1190}PSS_{70}$ the forward scattering decreases until 54.0 % D_2O and subsequently increases again.

oreover, the slope at high q changes. This becomes particularly evident for the partly deuterated polymer when comparing Figure 5.5C and F. In C the PSS block is matched and a slope of -4 is found. Contrast F is the closest possible one to the match of d_3-PA and shows a less step slope, which is closer to -2. The data at high q for the fully hydrogenated polymer show a higher statistical error than the data from the two other polymers. This can be attributed to the higher ^1H content of the fully hydrogenated polymer. Hence, the subtraction of the higher incoherent background introduces more

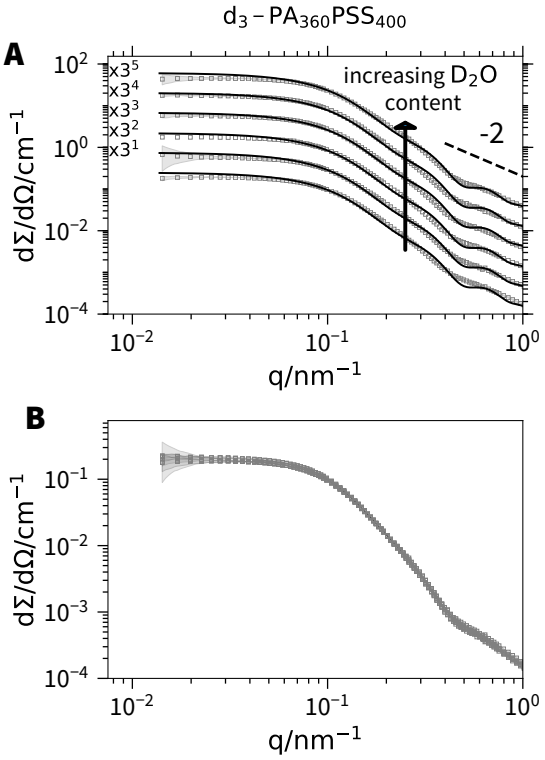


Figure 5.4: SAXS profiles of d_3-$PA_{360}PSS_{400}$ (c_{poly} = 4 g L^{-1}, $c_{Ca^{2+}}$ = 50 mmol L^{-1}) in 0.0% D_2O, 25.0% D_2O, 48.6% D_2O, 65.8% D_2O, 80.0% D_2O and 100.0% D_2O. **A** shows the curves multiplied with an offset, while **B** shows the curves without the multiplication factor. The solid lines represent fits to the form factor of a polydisperse block copolymer micelle.[28] An overview of the fit results can be found in Table 5.2 and Table 5.7 of the Supporting Information.

noise to the data. This makes the determination of slopes at high q for this polymer difficult.

The SAXS profiles of d_3-$PA_{1190}PSS_{70}$ and h_3-$PA_{1190}PSS_{70}$ in Figure 5.6A and Figure 5.8A show well-defined form factor oscillations, however a closer look at the position of the first minimum of $P(q)$ shows, that q_{min} shifts to slightly higher values when the D_2O content is increased. This corresponds to a slightly changing micelle size when changing the D_2O/H_2O ratio. As this feature is very hard to be identified with SANS curves only, it highlights the relevance of a combined SANS and SAXS experiment for all samples of a contrast variation study.

The scattering curves of all three samples were analyzed with two possible configurations: $Ca_{0.5}$-d_3-PA forming the core and PSS the corona as well as $Ca_{0.5}$–PSS forming

the core and PA the corona. SANS profiles at different contrasts as well as the SAXS profiles of the same samples were analyzed simultaneously in a global fit. Furthermore, the fit was heavily constrained due to the knowledge of the polymer composition, polymer concentration, molecular volumes[48] and scattering length densities of the blocks and the solvent.

A structure factor was not considered during the data analysis since the data did not show any evidence for the presence of particle interaction such as an up- or downturn at low q. This is rather unusual for highly charged systems since these systems usually show long range interactions or aggregation.[49]

However, for the present case the absence of a structure factor contribution can be explained by the high ionic strength of the respective polymer solution, which was introduced by adding a certain amount of NaCl as "inert salt" (see Section 5.2.3 for details). This addition of NaCl leads to a strong screening of the charges of the polyelectrolyte. We estimated the ionic strength and Debye length of the solution by assuming that every PA monomer unit binds 0.5 Ca^{2+} cations. For d_3-$PA_{360}PSS_{400}$ we obtain an ionic strength of 141 $mmol\,L^{-1}$ and a Debye length of 0.81 nm and for d_3-$PA_{1190}PSS_{70}$/h_3-$PA_{1190}PSS_{70}$ an ionic strength of 98 $mmol\,L^{-1}$ and a Debye length of 0.97 nm. Previous works[12–16] showed, that this approach can be used to investigate the single chain behavior of homopolyelectrolytes as the added "inert salt" effectively screens interactions between the chains. In the case of the present work this approach was used analogously and explains the lack of any significant impact of inter-micelle repulsions on the present scattering data.

However, for the present case the absence of a structure factor contribution can be explained by the high ionic strength of the respective polymer solution, which leads to a strong screening of the charges of the polyelectrolyte.

This strong screening also results in a conformation of the PSS chains in the corona, which can be well described by a self-avoiding polymer. In previous works the use of "inert salt" such as NaCl allowed to study the single chain behavior of homopolyelectrolytes such as PA and PSS.[16,23]

The best fit obtained from analyzing the data of d_3-$PA_{360}PSS_{400}$ with $Ca_{0.5}$–PSS forming the core and PA the corona is shown in Figure 5.15 of the Supporting Information. It poorly describes the features of the scattering curves. In contrast, the solid lines in Figure 5.3 and Figure 5.4A show the fits for d_3-$PA_{360}PSS_{400}$ with $Ca_{0.5}$–d_3PA forming the core. The main features of the experimental data are considerably better described by the model with a core consisting of d_3-PA.[27,28] This nicely agrees with the conclusions

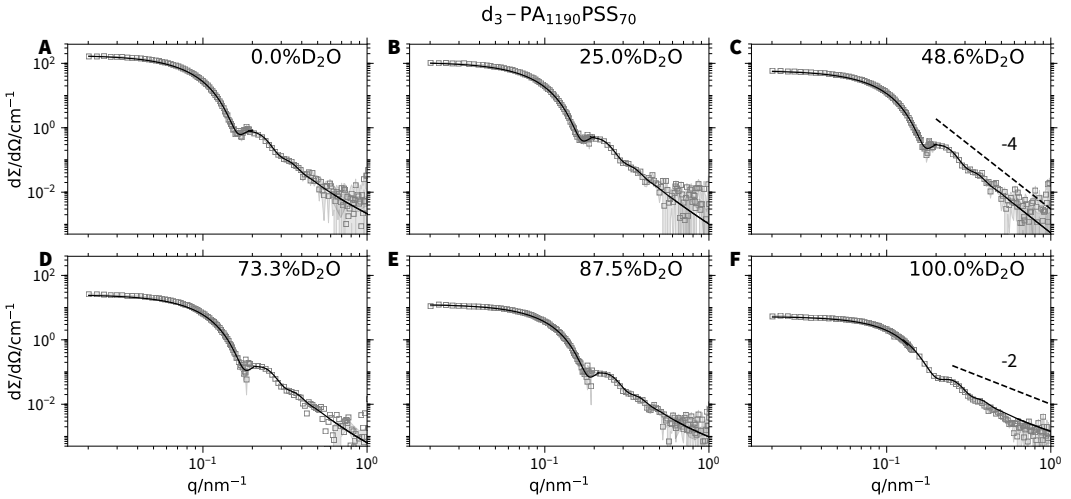


Figure 5.5: SANS profiles of d_3-$PA_{1190}PSS_{70}$ (c_{poly} = 4 g L^{-1}, $c_{Ca^{2+}}$ = 25 mmol L^{-1}) in 0.0% D_2O (**A**), 25.0% D_2O (**B**), 48.6% D_2O (**C**), 73.3% D_2O (**D**), 87.5% D_2O (**E**) and 100.0% D_2O (**F**). The solid lines represent fits to the form factor of a polydisperse block copolymer micelle.[28] An overview of the fit results can be found in Table 5.2 and Table 5.7 of the Supporting Information.

drawn from our previous work[27], confirming once again the fact that d_3-PA/Ca^{2+} forms the core of the micellar aggregates, while PSS is located in the corona. The form factor model with PA/Ca^{2+} in the core was also used for the analysis of d_3-$PA_{1190}PSS_{70}$ and h_3-$PA_{1190}PSS_{70}$. The solid lines in Figure 5.5, Figure 5.7, Figure 5.6A and Figure 5.8A show the form factor fits to the SANS and SAXS profiles. The model describes the data well for all contrasts. Unlike to the form factor analysis of the data from d_3-$PA_{360}PSS_{400}$, where the aggregation number turned out to be independent of the ratio H_2O/D_2O, the slightly changing micelle size with increasing D_2O content observed in the case of the two samples with the long PA block is taken into account by assuming individual aggregation numbers for each contrast. Therefore, each SANS and SAXS profile for a given contrast are attributed to an individual N_{agg}. All the other fit parameters ($\frac{\sigma N_{agg}}{N_{agg}}$, $R_{g,corona}$, s, ν, h, $V_{m,\,Ca^{2+}}$) are fitted simultaneously for the whole data set. Table 5.2 summarizes the resulting fit parameters. The given aggregation numbers and core sizes for d_3-$PA_{1190}PSS_{70}$ and h_3-$PA_{1190}PSS_{70}$ are shown representatively for the sample in 100 % D_2O. Table 5.7 in the Supporting Information summarizes the aggregation numbers N_{agg} for the other contrasts.

d_3-$PA_{360}PSS_{400}$ micelles have an aggregation number of 19 polymers per micelle. Compared to this the aggregation numbers of $168 \geqslant N_{agg} \geqslant 126$ for d_3-$PA_{1190}PSS_{70}$

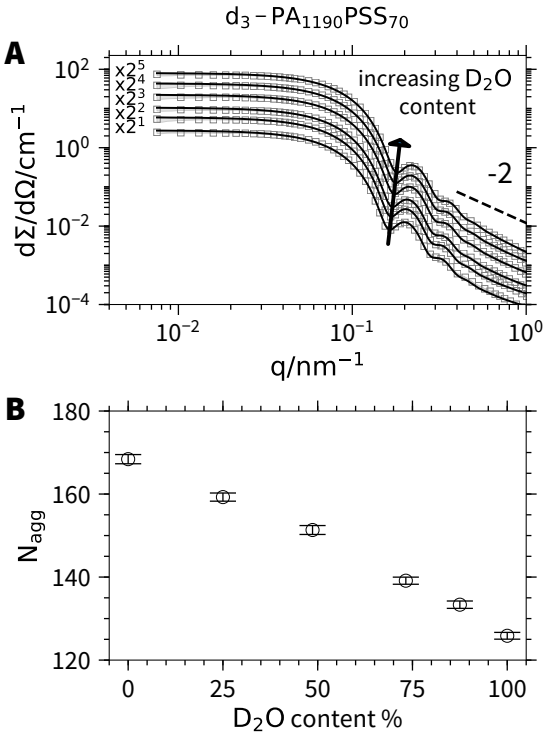


Figure 5.6: **A** SAXS profiles of d_3-$PA_{1190}PSS_{70}$ micelles (c_{poly} = 4 g L^{-1}, $c_{Ca^{2+}}$ = 25 mmol L^{-1}) in 0.0%, 25.0%, 48.6% , 73.3%, 87.5% and 100.0% D_2O. The solid lines represent fits to the form factor of a polydisperse block copolymer micelle.[28] An overview of the fit results can be found in Table 5.7 of the Supporting Information. **B** Aggregation number of the micelles as a function of D_2O content.

and $145 \geqslant N_{agg} \geqslant 117$ for h_3-$PA_{1190}PSS_{70}$ are considerably bigger. This increase in aggregation number can be nicely reconciled with the increase of the PA block length as the block responsible for the formation of the poorly soluble core.

During the data analysis it was turned out that it is necessary to take into account a considerable amount of water in the core. Assuming a dry core consisting of polymer does not fit the data on absolute scale since aggregation number N_{agg} and number density of micelles N are strictly linked to the known polymer concentration. This heavily constrains the fit and shows the importance of calibration to absolute intensity. Therefore, we allowed the core to be swollen by solvent and defined the scattering length density ρ_{core} and the molecular volume of the core as

$$\rho_{core} = \frac{b_{core}}{V_{m,\,core}} = \frac{b_{PA^-} + h b_{solvent} + 0.5 b_{Ca^{2+}}}{V_{m,\,PA^-} + h V_{m,\,solvent} + 0.5 V_{m,\,Ca^{2+}}} \tag{5.20}$$

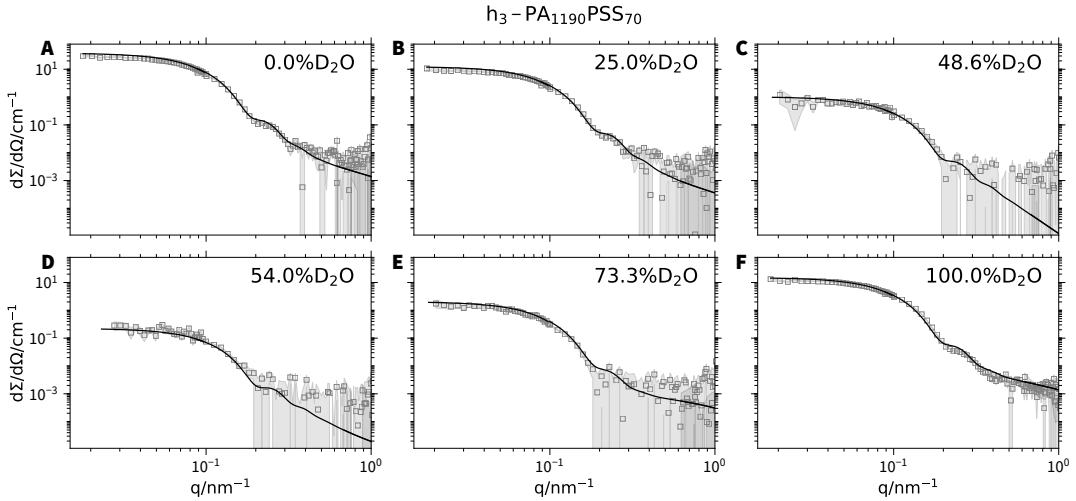


Figure 5.7: SANS profiles of h_3-$PA_{1190}PSS_{70}$ micelles (c_{poly} = 4 g L^{-1}, $c_{Ca^{2+}}$ = 25 mmol L^{-1}) in 0.0% D_2O (**A**), 25.0% D_2O (**B**), 48.6% D_2O (**C**), 54.0% D_2O (**D**), 73.3% D_2O (**E**) and 100.0% D_2O (**F**). The solid lines represent fits to the form factor of a polydisperse block copolymer micelle.[28] An overview of the fit results can be found in Table 5.7 of the Supporting Information.

with b_{core} being the scattering length and $V_{m,\,core}$ the molecular volume of a monomer in the core. h is the number of solvent molecules per monomer unit. We assumed that every Ca^{2+} binds to two PA monomer units. Previous works using isothermal titration calorimetry and calcium selective electrodes[25] suggest that Ca^{2+} binds quantitatively to PA.

The volume fraction of water in the core can be calculated by

$$f_{solvent} = 1 - \frac{\left(V_{m,\,PA^-} + 0.5V_{m,\,Ca^{2+}}\right) DP_{core} N_{agg}}{\frac{4}{3}\pi R_{core}^3} \tag{5.21}$$

where DP_{core} is the degree of polymerization of the core block.

The molar volume of condensed Ca^{2+} $V_{m,\,Ca^{2+}}$ was left free as a fit parameter since the value based on the ionic radius (2.5 cm^3 mol^{-1})[50] and the solvated ion (−28.9 cm^3 mol^{-1})[50] did not give satisfactory results. From the fits of the three block copolymer micelles an averaged value of $V_{m,Ca^{2+}} = 17.0 \pm 2.8$ cm^3 mol^{-1} was obtained. Unlike the negative molar volume of the solvated ion, the value we found is positive, which is attributed to the release of hydrated water molecules upon complexation with PA.

From the fits a quite high volume fraction of 83 %–85 % water in the core of the micelles is obtained. This corresponds to roughly 12 water molecules per monomer unit.

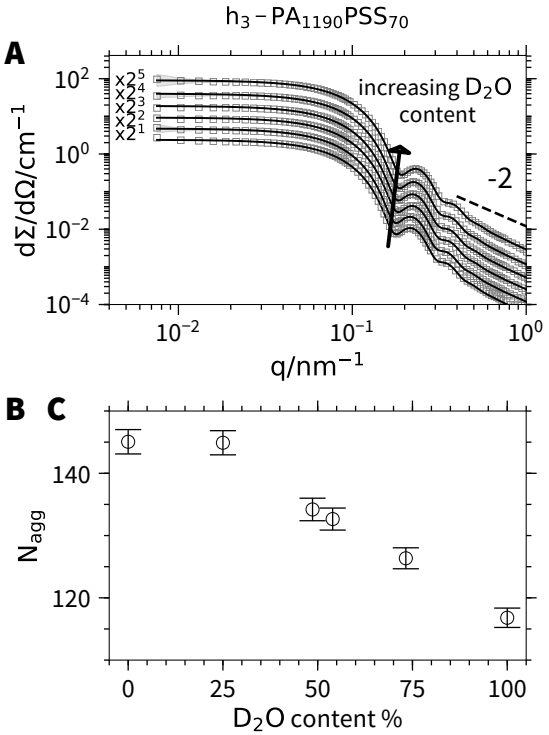


Figure 5.8: **A** SAXS profiles of h_3-$PA_{1190}PSS_{70}$ micelles (c_{poly} = 4 g L^{-1}, $c_{Ca^{2+}}$ = 25 mmol L^{-1}) in 0.0%, 25.0%, 48.6% , 54.0%, 73.3% and 100.0% D_2O. The solid lines represent fits to the form factor of a polydisperse block copolymer micelle.[28] An overview of the fit results can be found in Table 5.7 of the Supporting Information. **B** Aggregation number of the micelles as a function of D_2O content.

In order to achieve the same core volume without solvent in the core an aggregation number of 874 would be necessary for d_3-$PA_{360}PSS_{400}$, which can be safely excluded from fitting the data on absolute scale and given polymer concentration. Similar water contents have been observed for the core of Pluronic P123 micelles.[51]

The core size results from the aggregation number, degree of polymerization of the PA block, molar volumes of PA, Ca^{2+} and the water molecules in the core. For d_3-$PA_{360}PSS_{400}$ a rather small core radius of R_{core} = 8.8 nm together with a well-defined standard deviation of 6.9 % for the log normal distribution was found. In contrast, for d_3-$PA_{1190}PSS_{70}$ and h_3-$PA_{1190}PSS_{70}$ a considerably larger micelle core of 23.7 nm and 22.3 nm was found. This arises from the longer PA block and the higher aggregation numbers of those micelles compared to the polymer with equal ratios of d_3-PA and PSS. The distribution in aggregation numbers and consequently the distribution of the core radius for d_3-$PA_{1190}PSS_{70}$ and h_3-$PA_{1190}PSS_{70}$ is also narrow but slightly broader

Table 5.2: Structural parameters resulting from the analysis of the SANS and SAXS profile with the form factor of a polydisperse block copolymer micelle.[28] An extended version of the table including error bars can be found in the Supporting Information.

	d_3-$PA_{360}PSS_{400}$	d_3-$PA_{1190}PSS_{70}$	h_3-$PA_{1190}PSS_{70}$
N_{agg}	19.1	125.9[a]	116.8[a]
R_{core}/nm	8.8	23.7[a]	22.3[a]
$\frac{\sigma_{R_{core}}}{R_{core}}$	0.069	0.102	0.105
$R_{g,corona}/nm$	8.55	2.12	2.07
s/nm	8.9	4.05	3.53
ν	1.19	0.0	0.0
$f_{solvent}$	0.85	0.85	0.83
$V_{m,Ca^{2+}}/cm^3\ mol^{-1}$	19.6	17.3	14.0
R_h/nm[b]	26.2 ± 0.9	30.9 ± 1.0	34.0 ± 1.0

[a] Quantity shown for the sample in 100 % D_2O. [b] Hydrodynamic radius obtained from dynamic light scattering.

than that of sample d_3-$PA_{360}PSS_{400}$, resulting in a value of $\frac{\sigma_{R_{core}}}{R_{core}} = 10.2\,\%$ and $10.5\,\%$, respectively. This is in particular visible in the SAXS profiles, which show well-defined oscillations.

The radial scattering length density profiles of the micelles are shown in Figure 5.9B–D. The density profile of the PSS corona was assumed to be Gaussian and is determined by the standard deviation s. It was shown previously that the overall dimensions of the corona of block copolymer micelles containing polyelectrolytes cannot safely be determined by small angle scattering,[49] as it is not trivial to define a reasonable cutoff criteria for the scattering length density of the corona. Hence, Förster[49] suggested using the hydrodynamic radius to estimate the dimension of the corona including the part with very low volume fractions on the surface of the micelle. Therefore, the scattering length density profiles shown in Figure 5.9B–D also indicate the hydrodynamic dimensions of the micelles measured by dynamic light scattering. Using this approach, the corona covers nearly $2 \cdot R_{g,corona}$, with $R_{g,corona}$ the radius of gyration of the polymer chain in the corona resulting from the Pedersen-Schurtenberger form factor.[36] We conclude that this method is a reasonable approach to estimate the overall dimensions of the corona.

The scattering length density profiles in Figure 5.9 show the homogeneous micelle core composed of d_3-PA/h_3-PA, which is complexed by Ca^{2+} and considerably bigger for the h_3-$PA_{1190}PSS_{70}$/ d_3-$PA_{1190}PSS_{70}$ micelles. Vice versa, the profiles highlight the substantially bigger corona for d_3-$PA_{360}PSS_{400}$ compared to

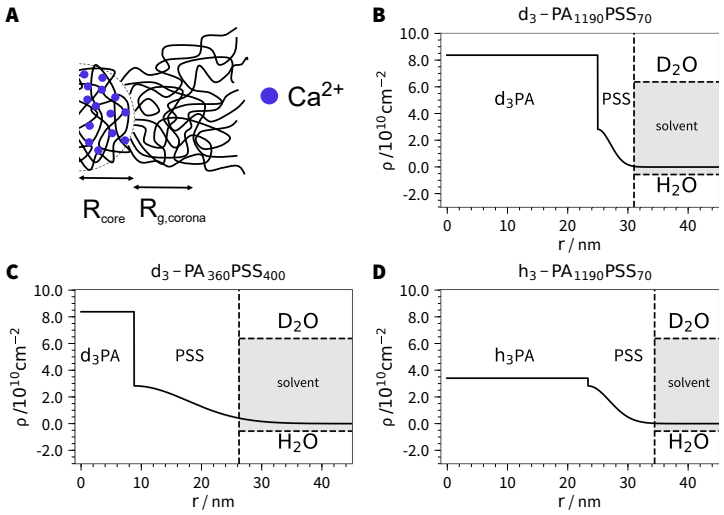


Figure 5.9: **A** Sketch of the d_3-$PA_{360}PSS_{400}$ micelles. **B** Scattering length density profile of d_3-$PA_{1190}PSS_{70}$ micelles. **C** Scattering length density profile of d_3-$PA_{360}PSS_{400}$ micelles. **D** Scattering length density profile of h_3-$PA_{1190}PSS_{70}$ micelles. The vertical dashed lines indicate the hydrodynamic dimensions of the micelles. The horizontal dashed lines indicate the scattering length density of H_2O ($-0.558 \times 10^{-10}\,cm^{-2}$) and D_2O ($6.355 \times 10^{-10}\,cm^{-2}$).

h_3-$PA_{1190}PSS_{70}$/d_3-$PA_{1190}PSS_{70}$. The parameter s controlling the thickness of the corona is similar for d_3-$PA_{1190}PSS_{70}$ (4.05 nm) and h_3-$PA_{1190}PSS_{70}$ (3.53 nm), being in agreement with the radius of gyration $R_{g,corona}$ of 2.12 nm (d_3-$PA_{1190}PSS_{70}$) and 2.07 nm (h_3-$PA_{1190}PSS_{70}$).

The relatively small dimensions of the corona for h_3-$PA_{1190}PSS_{70}$/d_3-$PA_{1190}PSS_{70}$ poses the question if it is necessary to consider the PSS corona in the data analysis. Therefore, SANS curves of two selected contrasts (48.6 % and 100 % D_2O) and a SAXS curve of d_3-$PA_{1190}PSS_{70}$ were analyzed with the model of a polydisperse sphere and are shown in Figure 5.16 of the Supporting Information. The model describes the contrast, where PSS is matched well (48.6 % D_2O). However, for the SANS curve with the contrast in 100 % D_2O and the SAXS curve the model fails to describe the high q part as here the corona scattering contributes to the signal.

Besides the corona dimension, the interaction of the polymer chains in the corona can be derived from ν.[28] It has been demonstrated by Monte Carlo simulations, that the corona of block copolymer micelles can be treated as quasi-two-dimensional dilute or semi-dilute polymer solution with an osmotic compressibility κ related to ν by $\kappa =$

$1 + \nu$.[35] Moreover, ν depends on the reduced surface coverage $\frac{\Sigma}{\Sigma^*}$

$$\frac{\Sigma}{\Sigma^*} = \frac{N_{agg} R_{g,\,corona}^2}{4(R_{core} + R_{g,corona})^2} \tag{5.22}$$

according to a power law.[28] The reduced surface coverage is the two-dimensional analogue of $\frac{c}{c^*}$, where c^* is the overlap concentration.[28] The reduced surface coverage for d_3-$PA_{360}PSS_{400}$ is 1.3, which is above the critical value of unity for the overlap of the chains. This is compatible with the value of $\nu = 1.19$ inferred from the analysis of the scattering profiles. We thus conclude that the PSS chains in the corona of d_3-$PA_{360}PSS_{400}$ micelles are overlapping.

When calculating the reduced surface coverage for h_3-$PA_{1190}PSS_{70}$ and d_3-$PA_{1190}PSS_{70}$ one obtains 0.23 and 0.22, which is significantly smaller than 1.0, indicating that the chains in the corona do not overlap. This is in agreement with the values of ν, which converged to the lower boundary of 0.0 for both samples. The coronas of d_3-$PA_{1190}PSS_{70}$ and h_3-$PA_{1190}PSS_{70}$ micelles contain PSS chains which are not interacting and do not overlap. To confirm this hypothesis we also analyzed the scattering profiles with a block copolymer form factor, assuming Gaussian chains grafted to the surface of a hard sphere.[52] This form factor is less general than the one used before since it is only valid for low surface coverage. The details of the model can be found in the Supporting Information. We were able to describe the scattering data of d_3-$PA_{1190}PSS_{70}$ and h_3-$PA_{1190}PSS_{70}$ micelles with similar fit quality and micelle dimensions. However, when the simpler model[52] was applied to the profiles of d_3-$PA_{360}PSS_{400}$ we were not able to fit the contrast shown in Figure 5.3D–F satisfactorily. The best fit with this model is also shown in Figure 5.14 of the Supporting Information. The simpler model[52] does not allow to take into account interactions between the chains in the corona by a ν parameter and thus fails to reproduce the scattering signal which is dominated by the corona. Accordingly, the polymer chains in the corona for d_3-$PA_{1190}PSS_{70}$/h_3-$PA_{1190}PSS_{70}$ micelles are not overlapping, whereas PSS chains in d_3-$PA_{360}PSS_{400}$ micelles are overlapping.

We conclude the section by stressing again that the H_2O/D_2O ratio influences the aggregation number of d_3-$PA_{1190}PSS_{70}$/h_3-$PA_{1190}PSS_{70}$. This effect deserves further consideration. Figure 5.6B and Figure 5.7B shows that the obtained aggregation numbers of the micelles decrease with increasing content of heavy water. This slight decrease in aggregate size is attributed to an isotope effect occurring upon change of the solvent

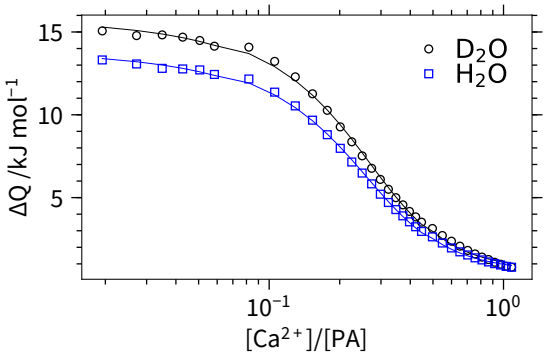


Figure 5.10: Isothermal titration curves of PA homopolymer in the presence of Ca^{2+} in H_2O and D_2O. The curve shows the heat of binding per injection as a function of Ca^{2+}/PA ratio. The solid lines are fits with the model of a single set of identical binding sites. Table 5.3 summarizes the results of the data analysis.

from light to heavy water, irrespective of the use of deuterated or hydrogenated PA and will be addressed in detail in the next section.

5.3.3 Isotope effect

In the previous section it was found that the size of d_3-$PA_{1190}PSS_{70}$ and h_3-$PA_{1190}PSS_{70}$ micelles slightly decreases with increasing D_2O content. For the form factor fits this changing micelle size was taken into account by attributing an individual aggregation number to each contrast and using this N_{agg} for the corresponding SANS and SAXS curves at the respective contrast.

This change in aggregation number is caused by an isotope effect occurring upon change of the solvent from light to heavy water and is observed for a polymer with a deuterated PA block as well as a hydrogenated PA block. Preceding works have shown that the solvent quality and the phase behavior of polymer-solvent systems can change if hydrogenated solvents are replaced by deuterated solvents.[53] Moreover, it has been shown that the phase boundaries of proteins in the presence of multivalent cations may change when going from light to heavy water.[54] These effects arise from the slightly different interaction of the deuterated solvent with the macromolecule. This seems to be also the case for the present system.

The isotope effect only appears for d_3-$PA_{1190}PSS_{70}$ and h_3-$PA_{1190}PSS_{70}$ but not for d_3-$PA_{360}PSS_{400}$. As the effect only appears for the polymers with the long PA block, it is possible that the binding of Ca^{2+} to PA plays an important role in the process.

In order to clarify if the isotope effect is accompanied by a difference in binding of Ca^{2+} to PA in H_2O or D_2O isothermal titration calorimetry was performed in light and heavy water. This technique measures the heat of binding upon addition of Ca^{2+} to a solution of PA. Figure 5.10 shows the titration curves in H_2O and D_2O as well as the fit to the model of a single set of identical binding sites.[46,47] Table 5.3 summarizes the obtained enthalpy of binding $\Delta H^{\ominus}$, entropy of binding $T\Delta S^{\ominus}$, binding constant K and stochiometry of binding n. From the titration curves it is clear that the binding in H_2O and D_2O have identical binding constants K, however the enthalpy of binding $\Delta H^{\ominus}$ and the entropy of binding $T\Delta S^{\ominus}$ is slightly larger for the titration in D_2O. We attribute this slight difference also to an isotope effect and conclude that this isotope effect controls the binding of Ca^{2+} and the aggregation number of the micelles.

5.3.4 Stuhrmann analysis

In section 5.3.2 it was shown that the SANS profiles from the contrast variation experiment can be well described by a suitable form factor model.[28] However, such an analytical expression for a form factor model is not always available, in particular for systems which are not as well-defined as block copolymer micelles. Moreover, deuteration is not always feasible as deuterated monomers do not exist for a wide range of polymers and deuteration of biological molecules such as proteins or sugars is often difficult and very cost intensive. Nevertheless, a contrast variation experiment is still possible if the scattering length densities of two components are sufficiently different.

In order to be able to analyze contrast variation experiments, Stuhrmann[29,30] developed a model-indepedent approach, the so called Stuhrmann analysis. In this section this approach is employed for d_3-$PA_{1190}PSS_{70}$ as well as d_3-$PA_{360}PSS_{400}$ and compared with the results from the form factor fits. Eventually, the potential of the method is demonstrated by applying it to the data of h_3-$PA_{1190}PSS_{70}$, nicely demonstrating that

Table 5.3: Results of the ITC experiments probing the binding of Ca^{2+} to PA in H_2O and D_2O at 25 °C.

	H_2O	D_2O
$K/L\,mol^{-1}$	$6.3 \times 10^3 \pm 0.3 \times 10^3$	$6.4 \times 10^3 \pm 0.5 \times 10^3$
$\Delta H^{\ominus}/kJ\,mol^{-1}$	17.45 ± 0.34	19.76 ± 0.56
$T\Delta S^{\ominus}/kJ\,mol^{-1}$	39.14 ± 0.46	41.49 ± 0.75
$\Delta G^{\ominus}/kJ\,mol^{-1}$	-21.69 ± 0.12	-21.73 ± 0.19
n	0.231 ± 0.002	0.239 ± 0.003

reliable structural information can be obtained even from a fully hydrogenated polymer and more importantly without necessarily using form factor fits.

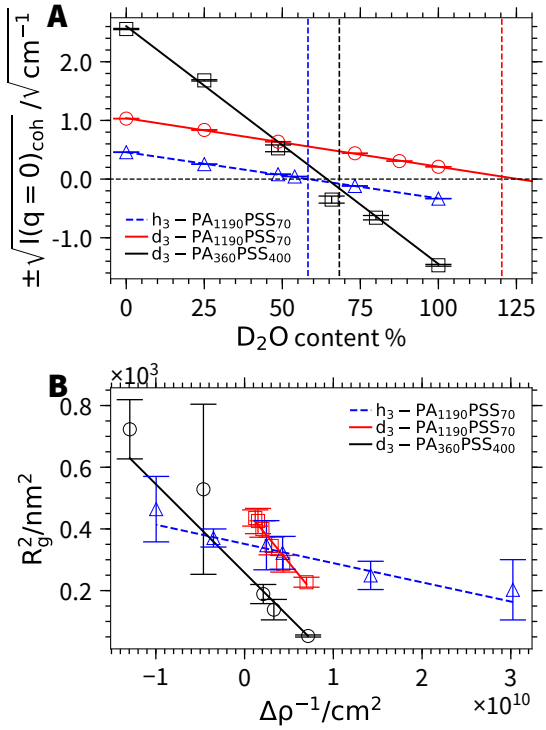


Figure 5.11: A) Coherent forward scattering for d_3-$PA_{360}PSS_{400}$, d_3-$PA_{1190}PSS_{70}$ and h_3-$PA_{1190}PSS_{70}$ from SANS as a function of D_2O content. The solid line represents a linear fit to the data. The data for d_3-$PA_{1190}PSS_{70}$ and h_3-$PA_{1190}PSS_{70}$ are normalized by the aggregation number N_{agg}. The vertical dashed lines indicate the theoretical match points calculated from the chemical composition. (**B**) Squared radius of gyration R_g^2 as a function of inverse scattering contrast for d_3-$PA_{360}PSS_{400}$, d_3-$PA_{1190}PSS_{70}$ and h_3-$PA_{1190}PSS_{70}$. The straight lines are fit to equation 5.23.[29,30]

Figure 5.11A shows the square root of the coherent SANS scattering intensity at $q \to 0$ for the measured contrasts as a function of D_2O content for all three samples. We used N_{agg} (determined from the form factor fits) for the samples d_3-$PA_{1190}PSS_{70}$ and h_3-$PA_{1190}PSS_{70}$ to normalize the coherent forward intensity from SANS in order to account for the effect of a change in aggregation number. The data follow a linear behavior as first shown by Stuhrmann,[29,30] which is expected when the contrast term $\Delta\rho$ is changed. A linear fit of the data shows that the match points of the block copolymer micelles is at 64.3 ± 0.4 % D_2O (d_3-$PA_{360}PSS_{400}$), 125.6 ± 0.7 % D_2O (d_3-$PA_{1190}PSS_{70}$) and 57.4 ± 0.6 % D_2O (h_3-$PA_{1190}PSS_{70}$). Based on the chemical composition of the block

copolymer and the scattering length densities of the two blocks the theoretical match point of the block copolymers and their micelles can be calculated. The theoretical matchpoint for all three polymers is close to the experimentally found, which confirms the successful synthesis and preliminary characterization of the block copolymer.

Further, more quantitative information can be extracted from the scattering curves by plotting the squared apparent radius of gyration R_g^2 from a Guinier analysis at low q as a function of the inverse scattering contrast $\Delta\rho^{-1}$. Figure 5.11B shows the so called Stuhrmann plot.[29,30] Ibel and Stuhrmann[29,30] showed that for a two-component system R_g^2 depends on $\Delta\rho^{-1}$ as

$$R_g^2 = R_m^2 + \alpha\Delta\rho^{-1} + \gamma\Delta\rho^{-2} \tag{5.23}$$

with R_m being the radius of gyration at infinite contrast. The coefficient α is related to the second moment of the scattering length density fluctuations about its mean value. The coefficient γ is the square of the first moment of the density fluctuations about the mean. If α is positive the component of the lower scattering length density is located more towards the inside of the objects. For a negative value of α the component with the higher scattering length density is concentrated in the inside. γ is proportional to the squared separation of the two components, with $\gamma = 0$ indicating that the centers-of-mass are coinciding.

Figure 5.11B shows R_g^2 as a function of $\Delta\rho^{-1}$ for the three samples. For all three polymers the points follow a straight line with γ being close to zero and with a negative slope α.

For all three samples, a negative value for α indicates that the PA blocks are always located in the core of the micelles. It may not have been clear at the outset of the experiment that this also holds for the fully hydrogenated sample h_3-$PA_{1190}PSS_{70}$. However, calculation of the scattering length densities ρ for PSS ($2.82 \times 10^{10}\,cm^{-2}$) and h_3-PA ($4.21 \times 10^{10}\,cm^{-2}$) reveals that they are sufficiently different also for the fully hydrogenated sample, with h_3-PA having a larger ρ. This nicely demonstrates the benefit of additionally analyzing a fully hydrogenated sample.

The fact that γ is close to zero shows that the center-of-mass of PSS and d_3-PA/h_3-PA coincide. Such a situation is only compatible with a highly symmetrical core-shell structure of the micelles. Furthermore, the scattering curves do not show any indication for the presence of cylindrical or vesicular micelles, which would also be compatible with a value of γ close to zero. Accordingly, we can already conclude from the model free analysis and without using information from the form factor fits that the micelles are

spherical with a core composed of d_3-PA/h_3-PA and a corona of PSS, being in full agreement with the form factor fits.

Using the parallel axis theorem one can relate α and R_m^2 to the radius of gyration of the core $R_{g,core}$ and the radius of gyration of the shell $R_{g,shell}$[55]

$$R_m^2 = f_{core} R_{g,core}^2 + f_{shell} R_{g,shell}^2 \tag{5.24}$$

$$\alpha = (\rho_{core} - \rho_{shell}) f_{core} f_{shell} (R_{g,core}^2 - R_{g,shell}^2) \tag{5.25}$$

with f_{core} and f_{corona} being the volume fraction of core and corona block and ρ_{core} and ρ_{corona} the scattering length densities of the core and corona block, respectively. All the information is available from the chemical composition and molar volumes of the monomer units. Equation 5.24 and 5.25 can be solved for $R_{g,core}$ and $R_{g,shell}$, making the dimensions of the micelles directly accessible from a model-independent analysis of the scattering data. Table 5.4 summarizes the values of R_m, α, $R_{g,core}$ and $R_{g,shell}$ for all three samples.

For d_3-$PA_{360}PSS_{400}$ a value of $R_{g,core} = 7.1\,nm$ and $R_{g,shell} = 18.0\,nm$ is found. This indicates that the micelles contain a d_3-PA core which is surrounded by a rather thick shell of PSS, in perfect agreement with the scattering length density profiles obtained from the form factor fits. The core radius R_{core} from the form factor fits can be used to calculate a value for $R_{g,core}$ by[31]

$$R_{g,core} = \sqrt{\frac{3}{5}} R_{core} \tag{5.26}$$

$R_{g,core}$ calculated accordingly is $6.8\,nm$, in perfect agreement with the value obtained from the model independent analysis ($7.1 \pm 2.5\,nm$).

Table 5.4: Micelle dimensions obtained from the Stuhrmann plot (R_g^2 versus $\Delta\rho^{-1}$).

Polymer	R_m/nm	α	$R_{g,core}/nm$	$R_{g,shell}/nm$
d_3-$PA_{360}PSS_{400}$	16.1 ± 1.4	$(-2.9 \pm 0.3)10^6$	7.1 ± 2.5	18.0 ± 1.7
d_3-$PA_{1190}PSS_{70}$	21.6 ± 1.0	$(-3.5 \pm 0.4)10^6$	19.9 ± 1.1	29.7 ± 4.9
h_3-$PA_{1190}PSS_{70}$	18.7 ± 1.2	$(-6.2 \pm 2.5)10^5$	16.8 ± 2.3	30.1 ± 5.1

Using equations 5.24-5.25 for d_3-$PA_{1190}PSS_{70}$ yields $R_{g,core} = 19.9\,nm$ and $R_{g,shell} = 29.7\,nm$, nicely illustrating the considerably bigger d_3-PA core for this sample and the rather thin PSS corona. Comparing the core radius from the form factor analysis with $R_{g,core}$ using eq. 5.26 yields a value of $18.4\,nm$ from the form factor fit. This shows a good agreement between both methods, in particular when taking into account that the

isotope effect and therefore the slightly changing micelle dimensions is not considered in Figure 5.11B of the Stuhrmann analysis.

Finally, the micelle dimensions for the fully hydrogenated polymer h_3-$PA_{1190}PSS_{70}$ are calculated. The values of $R_{g,core} = 16.8\,nm$ and $R_{g,shell} = 30.1\,nm$ are very similar to the results found for d_3-$PA_{1190}PSS_{70}$ micelles, showing that the h_3-$PA_{1190}PSS_{70}$ micelles also consists of a large PA core and a thin PSS corona. The radius of gyration of the core according to eq. 5.26 and the form factor fit is 17.3 nm, which is in perfect agreement with the result from the Stuhrmann plot ($16.8 \pm 2.3\,nm$).

The quantitative discussion presented above is a nice verification of the power of the Stuhrmann analysis, for which we could provide a highly suitable model system. The model independent analysis does not only offer values for important size parameters of the micelles, but provides evidence for a core shell structure of these micelles, with the PA blocks located at the core of the micelles. These features and conclusions could be consistently and independently derived from investigating three different block copolyelectrolyte samples of the type PA-*b*-PSS. This nicely shows the potential of the model free analysis given in the present section and at the same time confirms the form factor fits.

5.4 Conclusion

We investigated self-assemblies of block copolymers of the two polyelectrolytes polyacrylate (PA) and polystyrene sulfonate (PSS) by a combination of contrast variation small-angle neutron scattering, small-angle X-ray scattering and dynamic light scattering. In a previous work[27] we showed that such block copolymers form well-defined micelles in the presence of Ca^{2+}. In order to investigate the morphology of these micelles, the PA block was selectively deuterated.

First and foremost, SANS and SAXS reveal a spherical micellar shape for the aggregates with a well-defined size and a low polydispersity for three different block copolyelectrolytes of the type PA-*b*-PSS, using the model of a block copolymer micelle with a homogeneous scattering length density in the core and self-avoiding chains in the corona.[28] Model interpretation confirmed the micellar shape of the aggregates and unambiguously proved that Ca^{2+} cations are binding to PA and that this complex forms the hydrophobic core of the micelles. This core contains up to 85 vol% of water. PSS forms the corona of the micelles and adopts the conformation of self-avoiding polymer chains. Furthermore we found, that the PSS chains in the corona do not overlap for a

block copolymer with a high fraction of PA, while they start to show excluded volume effects once they overlap due to an increase of the PSS fraction. As the interactions of the Ca^{2+} cations with the PSS chains are only non-specifiic being dominated by electrostatically based screening of electrostatic forces, the resulting PSS corona stabilizes the micelles and keeps the phase separation otherwise observed with pure PA and Ca^{2+} confined to the core of the micelles.

For a set of block copolymers with a long PA and a short PSS block a small change in dimensions was observed in the SAXS profiles when going from H_2O to D_2O. This was attributed to an isotope effect arising from a slightly different binding enthalpy of Ca^{2+} to PA in H_2O and D_2O. Having SAXS and contrast variation SANS data available it was possible to take into account this as a change in aggregation number in the data analysis. Such effects are at risk to be neglected in contrast variation experiments and the present example stresses the importance of combining SAXS and SANS in order to elucidate such effects and take them into account during the data analysis.

Finally, we demonstrated that contrast variation can also be performed on a fully hydrogenated block copolymer as long as the scattering length densities of the blocks are sufficiently different. In combination with the SAXS data it was possible to reliably determine the size, structure and morphology of the micelles. This is particularly interesting for samples where deuteration is not possible and nicely illustrates the future potential of novel, more powerful neutron sources.

Acknowledgments

The authors thank the Institut Laue-Langevin (https://doi.ill.fr/10.5291/ILL-DATA.9-11-1888) and the European Synchrotron Radiation Facility for the provision of beam time, the Partnership for Soft Condensed Matter (PSCM) for supply of the light scattering and Narayanan Theyencheri and the ID02 team for the supply of in-house time at ID02. N.C. acknowledges funding for a PhD scholarship from Institut Laue-Langevin.

Conflict of interest

The authors declare that they have no conflict of interest.

5.5 Supporting Information

5.5.1 Scattering length densities

Table 5.5 shows the molar volumes V_m, scattering length b and scattering length densities ρ for neutrons and X-rays (at 12.46 keV) used for the analysis of the data. The scattering length density of a given compound is given by

$$\rho = \frac{b}{V_m} N_a \tag{5.27}$$

with N_A being the Avogadro constant.

Table 5.5: Molar volumes, neutron and X-ray scattering length and scattering length density of the used compounds. $\rho_{X\text{-rays}}$ was calculated for a X-ray energy of 12.46 keV.

Compound	V_m $/cm^3\ mol^{-1}$	$b_{neutrons}$ $/fm$	$b_{X\text{-Rays}}$ $/fm$	$\rho_{neutrons}$ $/1 \times 10^{10}\ cm^{-2}/$	$\rho_{X\text{-rays}}$ $/1 \times 10^{14}\ cm^{-2}$
$h_3\,PA^-$	29.1[a]	20.327	107.269	4.208	22.21
$d_3\,PA^-$	29.1[a]	51.557	107.269	10.674	22.21
NaPSS	108.7	50.881	299.823	2.818	16.61
D_2O	18.141	19.145	28.242	6.355	9.375
H_2O	18.069	−1.675	28.242	−0.558	9.398
Ca^{2+}	17.0 ± 2.8[b]	4.7	51.652	1.665	1.830×10^{-3}
d_3-$PA_{1190}PSS_{70}$[c]				7.789	
h_3-$PA_{1190}PSS_{70}$[c]				3.506	
d_3-$PA_{360}PSS_{400}$[c]				4.200	

[a] Taken from reference [48]. [b] The molar volume of Ca^{2+} was fitted. The shown value is the average value we obtained from analysis of the three different polymers. [c] We assumed that every PA monomer is complexed by 0.5 equivalents of Ca^{2+}.

5.5.2 Scattering from block copolymer micelles with Gaussian chains in the corona

The form factor for block copolymer micelles with Gaussian chains in the corona was first derived by Pedersen[52]. It assumes a homogeneous core, with Gaussian chains in the corona. The Gaussian chains are displaced from the surface of the core to avoid

penetration into the core. The form factor is given by

$$\begin{aligned}\frac{d\Sigma}{d\Omega}(q) = N\Big[&N_{agg}^2\beta_{core}^2 A_{core}^2(q)\\ &+ N_{agg}\beta_{corona}^2 P_{corona}(q)\\ &+ 2N_{agg}^2\beta_{core}\beta_{corona}A_{core}(q)\,A_{corona}(q)\\ &+ N_{agg}\left(N_{agg}-1\right)\beta_{corona}^2 A_{corona}^2(q)\Big]\end{aligned} \tag{5.28}$$

The form factor is similar to the one given in eq 5.3 of the main manuscript. It contains four different terms: The scattering from the homogeneous core A_{core}^2, the form factor of the chains in the corona $P_{corona}(q)$, the cross-term between core and chains in the corona $A_{core}(q)\,A_{corona}(q)$ and the cross-term between chains in the corona $A_{corona}^2(q)$. Furthermore, the pre-factors of the individual terms are the aggregation number of the micelle N_{agg} and the excess scattering length densities of the block forming the spherical core β_{core} and the corona β_{corona}.

A_{core} is given by the scattering amplitude of a homogeneous sphere with radius R_{core}

$$A_{core}(q) = 3\frac{\sin(qR_{core}) - qR_{core}\cos(qR_{core})}{(qR_{core})^3} \tag{5.29}$$

$P_{corona}(q)$ is given by the Debye function, describing the form factor of a Gaussian chain with radius of gyration R_g

$$P_{corona}(q) = \frac{2\left(\exp\left(-q^2R_g^2\right) - 1 + q^2R_g^2\right)}{\left(q^2R_g^2\right)^2} \tag{5.30}$$

$A_{corona}(q)$ is given by

$$A_{corona}(q) = \frac{1-\exp\left(-q^2R_g^2\right)}{q^2R_g^2}\frac{\sin\left(q\left(R_{core}+dR_g\right)\right)}{q\left(R_{core}+dR_g\right)} \tag{5.31}$$

The parameter d describes the displacement of the Gaussian chains from the surface of the core and is usually around 1.

In order to take into account the size distribution of micelles we assumed a log-normal distribution of the aggregation number N_{agg}

$$p\left(N_{agg}\right) = \frac{1}{H\sqrt{2\pi}N_{agg}}\exp\left(\frac{-\log\left(N_{agg}-M\right)^2}{2H^2}\right) \tag{5.32}$$

where H and M define the distribution and are connected to the mean aggregation number $\overline{N_{agg}}$ and standard deviation $\sigma_{\overline{N_{agg}}}$ by

$$\overline{N_{agg}} = \exp\left(M + \frac{H^2}{2}\right) \tag{5.33}$$

$$\sigma_{\overline{N_{agg}}} = \sqrt{\exp\left(H^2 + 2M\right)\left(\exp\left(H^2\right) - 1\right)} \tag{5.34}$$

The macroscopic scattering cross-section is therefore

$$\frac{d\Sigma}{d\Omega}_{\text{polydisperse}}(q) = \int \frac{d\Sigma}{d\Omega}(q) p(N_{agg}) dN_{agg} \tag{5.35}$$

Instrumental resolution for SANS has been taken into account according to Ref. [39]. The macroscopic scattering function is convoluted with a resolution function $R(q, \sigma_q)$, which depends on wavelength spread, finite collimation of the beam and detector resolution

$$\frac{d\Sigma}{d\Omega}_{\text{smeared}}(q) = \int R(q, \sigma_q) \frac{d\Sigma}{d\Omega}_{\text{polydisperse}}(q) dq \tag{5.36}$$

Figure 5.13 and 5.12 show the SANS and SAXS profiles of d_3-$PA_{1190}PSS_{70}$ micelles fitted with the model described in equation 5.28. The model is able to describe the data sufficiently well. Table 5.7 shows the fit parameters as well as χ^2 of this fit together with the fits presented in the main manuscript.

Figure 5.14 shows the SANS profiles of d_3-$PA_{360}PSS_{400}$ micelles fitted with the model described in equation 5.28. The data for the contrasts shown in sub-figure D–F are not well described by the model. Since the model in equation 5.28 does not take into account interaction between the chains in the corona, contrast where the scattering signal is dominated by the corona are poorly described.

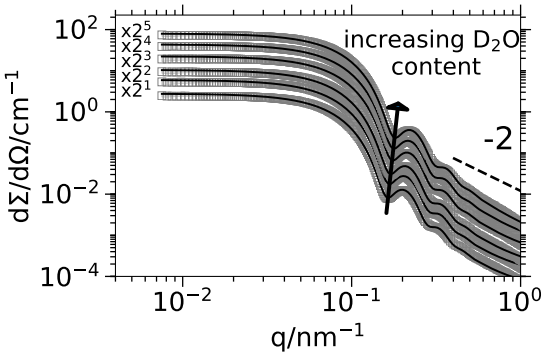


Figure 5.12: SAXS profiles of d_3-$PA_{1190}PSS_{70}$ micelles in 0.0 %, 25.0 %, 48.6 % , 73.3 %, 87.5 % and 100.0 % D_2O. The solid lines represent fits to equation 5.28.

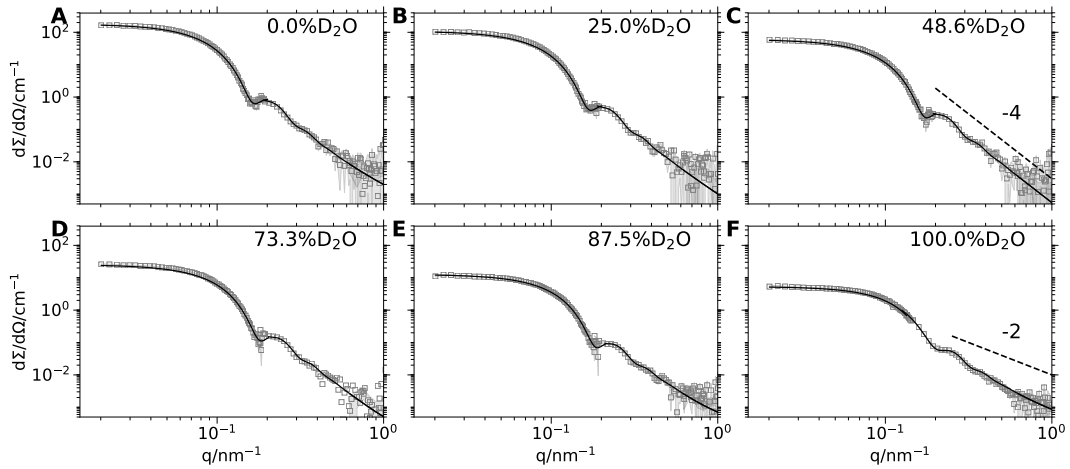


Figure 5.13: SANS profiles of d_3-$PA_{1190}PSS_{70}$ micelles in 0.0 % D_2O (**A**), 25.0 % D_2O (**B**), 48.6 % D_2O (**C**), 73.3 % D_2O (**D**), 87.5 % D_2O (**E**) and 100.0 % D_2O (**F**). The solid lines represent fits to equation 5.28.

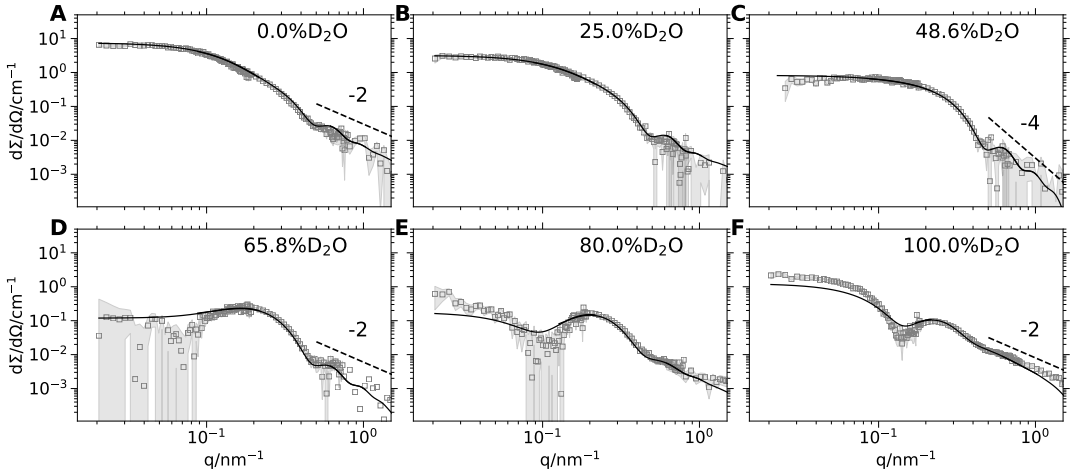


Figure 5.14: SANS profiles of d_3-$PA_{360}PSS_{400}$ micelles (c_{poly} = 4 g L^{-1}, $c_{Ca^{2+}}$ = 50 mmol L^{-1}) in 0.0 % D_2O (**A**), 25.0 % D_2O (**B**), 48.6 % D_2O (**C**), 65.8 % D_2O (**D**), 80.0 % D_2O (**E**) and 100.0 % D_2O (**F**). The solid lines represent fits fit to equation 5.28.

5.5.3 Model with PSS core and d_3-PA corona

Figure 5.15 shows the SANS profiles of d_3-$PA_{360}PSS_{400}$ and the model fit (self-avoiding chains in the corona, c.f. equation 5.3 in the main manuscript) with PSS in the core and d_3-PA corona. This model can not describe the scattering data sufficiently well.

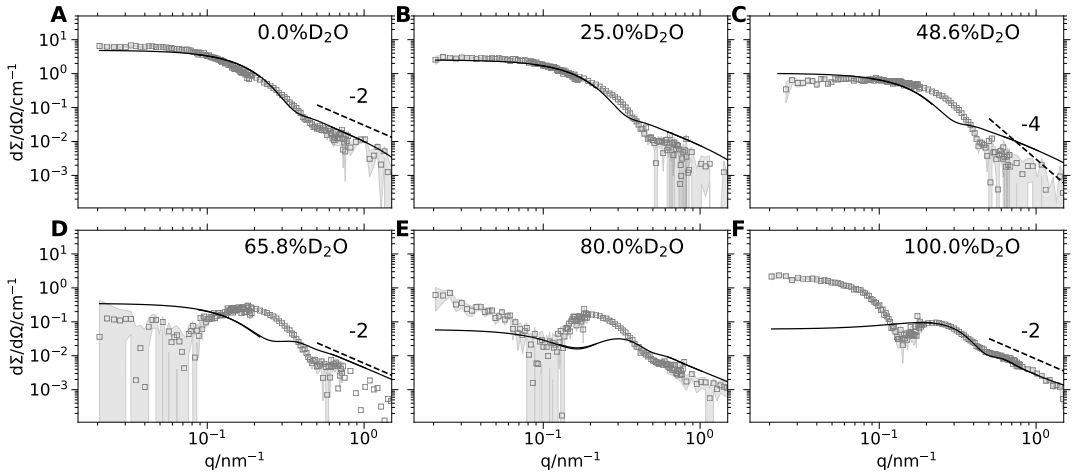


Figure 5.15: SANS profiles of d_3-$PA_{360}PSS_{400}$ (c_{poly} = 4 g L^{-1}, $c_{Ca^{2+}}$ = 50 mmol L^{-1}) in 0.0 % D_2O (**A**), 25.0 % D_2O (**B**), 48.6 % D_2O (**C**), 65.8 % D_2O (**D**), 80.0 % D_2O (**E**) and 100.0 % D_2O (**F**). The solid lines represent fits to the form factor of a polydisperse block copolymer micelle with PSS in the core and d_3-PA in the corona.

5.5.4 Fitting procedure

For the form factor fits we used the SASET program,[40] which allows global fitting of several contrasts at the same time. During the data analysis of the SANS curves we took into account the instrumental resolution for each detector configuration and merged the data only for final representation. This approach allows us to increase the number of available data points since we do not truncate the data in the region of overlapping q. We performed a global fit to the SANS and SAXS data with a single set of shared fitting parameters. For the samples, where the aggregation number changes with D_2O content we attributed a common aggregation number to the corresponding SANS and SAXS curves but left the rest of the fitting parameters as global fitting parameters.

In order to constrain the fit we used the molar volumes of the individual blocks, known from the degree of polymerization and the molar volumes listed in Table 5.5. Moreover, we restricted the fit by giving the used polymer concentration. Together with the aggregation number N_{agg} (which is a fitting parameter) the number density N of micelles in L^{-1} is directly obtained by

$$N = \frac{c}{M_{polymer} N_{agg}} N_A \tag{5.37}$$

with c the polymer concentration in g L^{-1}, the molecular weight of the polymer $M_{polymer}$ and the aggregation number N_{agg}.

5.5.5 Overview of the fit parameters from SANS and SAXS

Table 5.6 shows an overview of the obtained values of χ^2. Table 5.7 shows an overview of the obtained fitparameters for the SANS and SAXS profiles as well as the estimated errors. Note, that the error obtained from the least-squared fitting routine tends to underestimate the errors of the fit parameters. They also do not take into account systematic errors (e.g. from the difficult background subtraction for SAXS data at high q) and the correlation terms between the standard deviations of different fit parameters.[56]

Table 5.6: χ^2_{red} for the fits shown in the main manuscript (Figure 5.3, 5.4, 5.5, 5.6, 5.7, 5.8) and Figure 5.13 and 5.12 in the supporting information.

Sample	Model	χ^2_{red}
h_3-PA_{1190} PSS_{70}	Self-avoiding chain	16.8
d_3-PA_{1190} PSS_{70}	Self-avoiding chain	55.0
d_3-PA_{1190} PSS_{70}	Gaussian chain	57.6
d_3-PA_{360} PSS_{400}	Self-avoiding chain	5.6

Table 5.7: Parameters for the micelles in the presence of $CaCl_2$ obtained for the fits shown in the main manuscript (Figure 5.3, 5.4, 5.5, 5.6, 5.7, 5.8).

D_2O %		N_{agg}	$\sigma_{N_{agg}}/N_{agg}$	R_{core}/nm	$\sigma_{R_{core}}/R_{core}$	$R_{g,corona}$/nm	s/nm	ν	h	$V_{m,Ca^{2+}}$/cm^3 mol^{-1}	$\frac{d\Sigma}{d\Omega}_{inc}$/cm^{-1}
h_3-PA_{1190} PSS_{70}											
0.0	SANS	145.06 ± 0.20	$0.32 \pm 1.5 \times 10^{-4}$	23.98 ± 0.03	$0.105 \pm 4.8 \times 10^{-5}$	2.07 ± 0.02	$3.53 \pm 6.3 \times 10^{-3}$	$0.00 \pm 3.8 \times 10^{-3}$	10.22 ± 0.02	17.2 ± 0.03	$1.4 \times 10^{-2} \pm 2.4 \times 10^{-4}$
0.0	SAXS										$1.1 \times 10^{-3} \pm 1.8 \times 10^{-4}$
25.0	SANS	144.90 ± 0.19		23.98 ± 0.03							$9.8 \times 10^{-4} \pm 1.3 \times 10^{-4}$
25.0	SAXS										$1.7 \times 10^{-3} \pm 5.8 \times 10^{-5}$
48.6	SANS	134.19 ± 0.18		23.38 ± 0.03							$9.9 \times 10^{-4} \pm 4.9 \times 10^{-5}$
48.6	SAXS										$3.1 \times 10^{-13} \pm 3.5 \times 10^{-5}$
54.0	SANS	132.65 ± 0.18		23.29 ± 0.03							
54.0	SAXS										
73.3	SANS	126.35 ± 0.17		22.92 ± 0.03							
73.3	SAXS										
100.0	SANS	116.80 ± 0.16		22.33 ± 0.03							
100.0	SAXS										
d_3-PA_{1190} PSS_{70}											
0.0	SANS	168.40 ± 0.11	$0.31 \pm 1.5 \times 10^{-4}$	26.10 ± 0.02	$0.102 \pm 5.0 \times 10^{-5}$	2.12 ± 0.03	$4.05 \pm 8.9 \times 10^{-3}$	$0.00 \pm 7.4 \times 10^{-3}$	25.0% 11.59 ± 0.01	13.9 ± 0.02	$2.7 \times 10^{-3} \pm 1.4 \times 10^{-4}$
0.0	SAXS										$1.3 \times 10^{-3} \pm 1.1 \times 10^{-4}$
25.0	SANS	159.27 ± 0.10		25.63 ± 0.02							$2.1 \times 10^{-3} \pm 7.5 \times 10^{-5}$
25.0	SAXS										$1.5 \times 10^{-3} \pm 4.9 \times 10^{-5}$
48.6	SANS	151.34 ± 0.11		25.20 ± 0.02							$1.7 \times 10^{-3} \pm 3.3 \times 10^{-5}$
48.6	SAXS										$2.8 \times 10^{-13} \pm 2.3 \times 10^{-5}$
73.3	SANS	139.13 ± 0.09		24.51 ± 0.02							
73.3	SAXS										
87.5	SANS	133.35 ± 0.09		24.17 ± 0.02							
87.5	SAXS										
100.0	SANS	125.86 ± 0.08		23.71 ± 0.02							
100.0	SAXS										
d_3-PA_{360} PSS_{400}											
0.0	SANS	19.6 ± 0.07	$0.21 \pm 9.9 \times 10^{-3}$	8.78 ± 0.03	$0.069 \pm 3.3 \times 10^{-3}$	9.55 ± 0.04	$8.86 \pm 9.5 \times 10^{-3}$	$1.19 \pm 2.3 \times 10^{-2}$	12.21 ± 0.03	19.6 ± 0.05	$2.0 \times 10^{-2} \pm 1.8 \times 10^{-4}$
0.0	SAXS										$4.4 \times 10^{-3} \pm 1.3 \times 10^{-4}$
25.0	SANS										$4.4 \times 10^{-3} \pm 9.2 \times 10^{-5}$
25.0	SAXS										$3.0 \times 10^{-3} \pm 6.8 \times 10^{-5}$
48.6	SANS										$1.5 \times 10^{-3} \pm 4.5 \times 10^{-5}$
48.6	SAXS										$8.6 \times 10^{-4} \pm 5.7 \times 10^{-5}$
65.8	SANS										
65.8	SAXS										
80.0	SANS										
80.0	SAXS										
100.0	SANS										
100.0	SAXS										

D_2O %		N_{agg}	$\sigma_{N_{agg}}/N_{agg}$	R_{core}/nm	$\sigma_{R_{core}}/R_{core}$	$R_{g,corona}$/nm	d		h	$V_{m,Ca^{2+}}$/cm^3 mol^{-1}	$\frac{d\Sigma}{d\Omega}_{inc}$/cm^{-1}
d_3-PA_{1190} PSS_{70} with Gaussian chains in the corona											
0.0	SANS	163.81 ± 0.11	$0.31 \pm 1.5 \times 10^{-4}$	26.13 ± 0.02	$0.102 \pm 5.0 \times 10^{-5}$	3.11 ± 0.01	1		12.02 ± 0.01	13.8 ± 0.02	$2.7 \times 10^{-3} \pm 1.4 \times 10^{-4}$
0.0	SAXS										$1.3 \times 10^{-3} \pm 1.1 \times 10^{-4}$
25.0	SANS	155.0 ± 0.09		25.65 ± 0.02							$2.1 \times 10^{-3} \pm 7.5 \times 10^{-5}$
25.0	SAXS										$1.5 \times 10^{-3} \pm 4.9 \times 10^{-5}$
48.6	SANS	147.1 ± 0.10		25.22 ± 0.02							$1.7 \times 10^{-3} \pm 3.3 \times 10^{-5}$
48.6	SAXS										$2.8 \times 10^{-13} \pm 2.3 \times 10^{-5}$
73.3	SANS	135.4 ± 0.08		24.54 ± 0.02							
73.3	SAXS										
87.5	SANS	129.7 ± 0.09		24.19 ± 0.02							
Figure87.5	SAXS										
100.0	SANS	122.5 ± 0.08		23.73 ± 0.02							
100.0	SAXS										

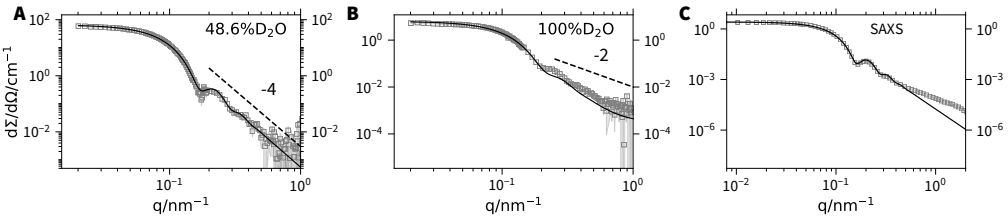


Figure 5.16: Fit of SANS and SAXS data of d_3-$PA_{1190}PSS_{70}$ micelles with the model of a polydisperse sphere.

5.5.6 Fit with the form factor of a polydisperse sphere

A selection of three scattering curves, SANS curves recorded at 48.6 % D_2O and 100 % D_2O and one SAXS curve of d_3-$PA_{1190}PSS_{70}$ are fitted in addition by the simpler model of a polydisperse sphere[34] neglecting the corona. The results from these fits are illustrated in Figure 5.16. For the SANS curve recorded at the contrast at 48.6 % D_2O the data are well described as the corona is matched. However, the SANS curve at 100 % D_2O and the SAXS curve are poorly described at mid and high q. Hence, the SANS and SAXS data of d_3-$PA_{1190}PSS_{70}$ can not be adequately described by the model of a polydisperse sphere and an additional corona has to be taken into account.

5.6 References

1. Volk, N.; Vollmer, D.; Schmidt, M.; Oppermann, W.; Huber, K. In; Chapter 0002, 2004; Vol. 166, pp 29–65, DOI: 10.1007/b11348.
2. Chiappisi, L.; Hoffmann, I.; Gradzielski, M. *Soft Matter* **2013**, *9*, 3896, DOI: 10.1039/c3sm27698h.
3. Bain, C. D.; Claesson, P. M.; Langevin, D.; Meszaros, R.; Nylander, T.; Stubenrauch, C.; Titmuss, S.; von Klitzing, R. *Adv. Colloid Interface Sci.* **2010**, *155*, 32–49, DOI: 10.1016/j.cis.2010.01.007.
4. Tummino, A.; Toscano, J.; Sebastiani, F.; Noskov, B. A.; Varga, I.; Campbell, R. A. *Langmuir* **2018**, acs.langmuir.7b03960, DOI: 10.1021/acs.langmuir.7b03960.
5. Szilagyi, I.; Trefalt, G.; Tiraferri, A.; Maroni, P.; Borkovec, M. *Soft Matter* **2014**, *10*, 2479–2502, DOI: 10.1039/c3sm52132j.
6. Bolto, B.; Gregory, J. *Water Res.* **2007**, *41*, 2301–2324, DOI: 10.1016/j.watres.2007.03.012.

7. Pochard, I.; Labbez, C.; Nonat, A.; Vija, H.; Jönsson, B. *Cem. Concr. Res.* **2010**, *40*, 1488–1494, DOI: 10.1016/j.cemconres.2010.06.002.
8. Marchon, D.; Sulser, U.; Eberhardt, A.; Flatt, R. J. *Soft Matter* **2013**, *9*, 10719–10728, DOI: 10.1039/c3sm51030a.
9. Llamas, S.; Guzmán, E.; Ortega, F.; Baghdadli, N.; Cazeneuve, C.; Rubio, R. G.; Luengo, G. S. *Adv. Colloid Interface Sci.* **2015**, *222*, 461–487, DOI: 10.1016/j.cis.2014.05.007.
10. Huber, K. *J. Phys. Chem.* **1993**, *97*, 9825–9830, DOI: 10.1021/j100140a046.
11. Michaeli, I. *J. Polym. Sci. Vol. Xlviii* **1960**, *XLVIII*, 291–299.
12. Goerigk, G.; Schweins, R.; Huber, K.; Ballauff, M. *Europhys. Lett.* **2004**, *66*, 331–337, DOI: 10.1209/epl/i2003-10215-y.
13. Schweins, R.; Goerigk, G.; Huber, K. *Eur. Phys. J. E* **2006**, *21*, 99–110, DOI: 10.1140/epje/i2006-10047-7.
14. Goerigk, G.; Huber, K.; Schweins, R. *J. Chem. Phys.* **2007**, *127*, 154908, DOI: 10.1063/1.2787008.
15. Lages, S.; Goerigk, G.; Huber, K. *Macromolecules* **2013**, *46*, 3570–3580, DOI: 10.1021/ma400427d.
16. Hansch, M.; Hämisch, B.; Schweins, R.; Prévost, S.; Huber, K. *J. Chem. Phys.* **2018**, *148*, 014901, DOI: 10.1063/1.5006618.
17. Narh, K. A.; Keller, A. *J. Polym. Sci. Part B Polym. Phys.* **1993**, *31*, 231–234, DOI: 10.1002/polb.1993.090310213.
18. Drifford, M.; Delsanti, M. In *Phys. Chem. polyelectrolytes*; CRC Press: 2001, pp 157–184.
19. De la Cruz, M. O.; Belloni, L.; Delsanti, M.; Dalbiez, J. P.; Spalla, O.; Drifford, M. *J. Chem. Phys.* **1995**, *103*, 5781–5791, DOI: 10.1063/1.470459.
20. Hansch, M.; Kaub, H. P.; Deck, S.; Carl, N.; Huber, K. *J. Chem. Phys.* **2018**, *148*, 114906, DOI: 10.1063/1.5019877.
21. Ikeda, Y.; Beer, M.; Schmidt, M.; Huber, K. *Macromolecules* **1998**, *31*, 728–733, DOI: 10.1021/ma970540p.
22. Lages, S.; Schweins, R.; Huber, K. *J. Phys. Chem. B* **2007**, *111*, 10431–10437, DOI: 10.1021/jp068258k.

23. Schweins, R.; Huber, K. *Eur. Phys. J. E* **2001**, *5*, 117–126, DOI: 10.1007/s101890170093.

24. Schweins, R.; Lindner, P.; Huber, K. *Macromolecules* **2003**, *36*, 9564–9573, DOI: 10.1021/ma0347722.

25. Sinn, C. G.; Dimova, R.; Antonietti, M. *Macromolecules* **2004**, *37*, 3444–3450, DOI: 10.1021/ma030550s.

26. Ishiwari, F.; Hasebe, H.; Matsumura, S.; Hajjaj, F.; Horii-Hayashi, N.; Nishi, M.; Someya, T.; Fukushima, T. *Sci. Rep.* **2016**, *6*, 24275, DOI: 10.1038/srep24275.

27. Carl, N.; Prévost, S.; Schweins, R.; Huber, K. *Soft Matter* **2019**, *15*, 8266–8271, DOI: 10.1039/C9SM01138B.

28. Svaneborg, C.; Pedersen, J. S. *Macromolecules* **2002**, *35*, 1028–1037, DOI: 10.1021/ma011046v.

29. Stuhrmann, H. B. *J. Appl. Crystallogr.* **1974**, *7*, 173–178, DOI: 10.1107/S0021889874009071.

30. Ibel, K.; Stuhrmann, H. *J. Mol. Biol.* **1975**, *93*, 255–265, DOI: 10.1016/0022-2836(75)90131-X.

31. Zemb, T.; Lindner, P., *Neutrons, X-rays and light: scattering methods applied to soft condensed matter*; North-Holland: 2002.

32. Orthaber, D.; Bergmann, A.; Glatter, O. *J. Appl. Crystallogr.* **2000**, *33*, 218–225, DOI: 10.1107/S0021889899015216.

33. Boesecke, P. *J. Appl. Crystallogr.* **2007**, *40*, 423–427, DOI: 10.1107/S0021889807001100.

34. Rayleigh, L. *Proc. Roy. Soc. London* **1911**, *A84*, 25–38.

35. Svaneborg, C.; Pedersen, J. S. *Phys. Rev. E* **2001**, *64*, 010802, DOI: 10.1103/PhysRevE.64.010802.

36. Skov, J.; Schurtenberger, P.; Pedersen, J. S. *Macromolecules* **1996**, *9297*, 7602–7612, DOI: 10.1021/ma9607630.

37. Chen, W. R.; Butler, P. D.; Magid, L. J. *Langmuir* **2006**, *22*, 6539–6548, DOI: 10.1021/la0530440.

38. Sommer, C.; Pedersen, J. S.; Garamus, V. M. *Langmuir* **2005**, *21*, 2137–2149, DOI: 10.1021/la047489k.

39. Pedersen, J. S.; Posselt, D.; Mortensen, K. *J. Appl. Crystallogr.* **1990**, *23*, 321–333, DOI: 10.1107/S0021889890003946.

40. Muthig, M.; Prévost, S.; Orglmeister, R.; Gradzielski, M. *J. Appl. Crystallogr.* **2013**, *46*, 1187–1195, DOI: 10.1107/S0021889813016658.

41. Frisken, B. J. *Appl. Opt.* **2001**, *40*, 4087, DOI: 10.1364/AO.40.004087.

42. Burchard, W.; Schmidt, M.; Stockmayer, W. H. *Macromolecules* **1980**, *13*, 580–587, DOI: 10.1021/ma60075a020.

43. Burchard, W.; Schmidt, M.; Stockmayer, W. H. *Macromolecules* **1980**, *13*, 1265–1272, DOI: 10.1021/ma60077a045.

44. Cho, C. H.; Urquidi, J.; Singh, S.; Robinson, G. W. *J. Phys. Chem. B* **1999**, *103*, 1991–1994, DOI: 10.1021/jp9842953.

45. Scheuermann, T. H.; Brautigam, C. A. *Methods* **2015**, *76*, 87–98, DOI: 10.1016/j.ymeth.2014.11.024.

46. Wiesman, T.; Williston, S.; Brandts, J. F. *Anal. Biochem.* **1989**, *179*, 131–137, DOI: 10.1016/0003-2697(89)90213-3.

47. Merabet, E.; Ackers, G. K. *Biochemistry* **1995**, *34*, 8554–8563, DOI: 10.1021/bi00027a005.

48. Tondre, C.; Zana, R. *J. Phys. Chem.* **1972**, *76*, 3451–3459, DOI: 10.1021/j100667a026.

49. Förster, S.; Hermsdorf, N.; Böttcher, C.; Lindner, P. *Macromolecules* **2002**, *35*, 4096–4105, DOI: 10.1021/ma011565y.

50. Marcus, Y., *Ion Properties*; Marcel Dekker: New York, New York (USA), 1997.

51. Manet, S.; Lecchi, A.; Impéror-Clerc, M.; Zholobenko, V.; Durand, D.; Oliveira, C. L. P.; Pedersen, J. S.; Grillo, I.; Meneau, F.; Rochas, C. *J. Phys. Chem. B* **2011**, *115*, 11318–11329, DOI: 10.1021/jp200212g.

52. Pedersen, J. S.; Gerstenberg, M. C. *Macromolecules* **1996**, *29*, 1363–1365, DOI: 10.1021/ma9512115.

53. Strazielle, C.; Benoit, H. *Macromolecules* **1975**, *8*, 203–205, DOI: 10.1021/ma60044a021.

54. Braun, M. K.; Wolf, M.; Matsarskaia, O.; Da Vela, S.; Roosen-Runge, F.; Sztucki, M.; Roth, R.; Zhang, F.; Schreiber, F. *J. Phys. Chem. B* **2017**, *121*, 1731–1739, DOI: 10.1021/acs.jpcb.6b12814.

55. Moore, P. B. In *Methods Exp. Phys.* Elsevier: 1982; Vol. 20, pp 337–390.

56. Press, W. H.; Teukolsky, S. A.; Vetterling, W. T.; Flannery, B. P., *Numerical recipes 3rd edition: The art of scientific computing*, 3rd ed.; Cambridge University Press: 2007.

Chapter 6

Invertible micelles based on ion specific interactions of Sr^{2+} and Ba^{2+} with double anionic block copolyelectrolytes

Abstract

Polyelectrolytes show diverse ion-specific effects with a wide variety of ions. In the present work, we study the solution behavior of diblock copolymers with poly acrylate (PA) and poly styrenesulfonate (PSS) blocks in the presence of the earth alkaline cations Ca^{2+}, Sr^{2+} and Ba^{2+}. Micellization can be triggered by a variation in temperature. For Ca^{2+}, this micelle formation occurs at high temperatures, while for Sr^{2+} and Ba^{2+}, it occurs at high and low temperatures with an intermediate temperature regime of single chains. Small-angle neutron scattering on a partly deuterated block copolymer unambiguously revealed that at low temperatures, PSS/M^{2+} forms the core of the micelles, whereas at high temperatures, PA/M^{2+} forms the core, effectively allowing to reverse the micelle structure by changing the temperature. This inversion of the micellar morphology, induced by a dual-responsive behavior, can be understood by using isothermal titration calorimetry and elucidating the thermodynamics of cation binding.

Reprinted with permission from Carl, N.; Prévost, S.; Schweins, R.; Houston, J. E.; Morfin, I.; Huber, K.; Invertible micelles based on ion specific interactions of Sr^{2+} and Ba^{2+} with double anionic block copolyelectrolytes; *Macromolecules*, **2019**, 52, 22, 8759-8770, DOI: 10.1021/acs.macromol.9b01924. Copyright 2019 American Chemical Society.

6.1 Introduction

Amphiphilic block copolymers self-assemble into structures ranging from spherical[1] to worm-like micelles[2] or vesicles.[3] Extensive research has been conducted to develop block copolymers where one of the blocks responds to external stimuli such as temperature,[4] pH,[5] pressure,[6] or light[7] in order to affect the hydrophobicity of the respective block and hence to switch between the monomeric and self-assembled state. So far, such stimuli or combinations thereof have been used to generate switchable emulsifiers,[8] to control rheology[9] or to release active agents.[10] In order to create even more versatile systems, research efforts were aiming at block copolymers where each of the two blocks responds to a different stimulus. Such systems were expected to accomplish an inversion of the micellar structure by reversibly addressing the stimulus of the two blocks one by one. Accordingly, the term schizophrenic micelles has been coined for these systems.[11–19]

The underlying concept of many of such systems makes use of one block with an upper critical solution temperature (UCST) and a second block with a lower critical solution temperature (LCST). Furthermore, it is ensured that a significant temperature gap exists between the UCST and LCST.[11] Only such a gap makes accessible the state of single block copolymer chains in between the state of micelles and of inverted micelles.[11] However, a problem observed during those efforts was that in the regime, where both blocks should be soluble the chains tend to aggregate.[11,17,18] In the light of potential applications such as the controlled uptake, transport, or release of low-molecular weight compounds, these effects are undesirable as they might provide cavities which keep back the cargo and prevent the complete release of it.

In the present work, we pursue a slightly different strategy to realize such an invertible system. Block copolymers of two negatively charged polyelectrolytes, sodium polyacrylate (PA) and sodium polystyrene sulphonate (PSS), are synthesized.[20,21] Polyelectrolytes are commonly used as building blocks for block copolymers, because of their water solubility, pH responsivity, and the ability to form charge-stabilized self-assembled structures.[1,22,23] The selection of PA and PSS is based on previous works,[24–26] which demonstrated unambiguously that the two polyanions interact specifically and in a different manner with alkaline earth cations. This interaction is temperature-dependent, whereby the temperature dependence also differs when going from PA to PSS.[24,26]

In more detail, earth alkaline metal cations M^{2+} complex the anionic moieties of PA and neutralize the negative charges. This results in phase separation of the polymer at a critical concentration of $[M^{2+}]_c$, which depends on the PA concentration [PA][25,27]

$$[M^{2+}]_c = r_0 + m[PA] \tag{6.1}$$

with [PA] being the concentration of PA monomer units, r_0 being the minimum concentration of M^{2+} required for precipitation and m being the stoichiometry of binding. Strikingly, the binding of M^{2+} to PA is endothermic with all three cations,[26,28,29] and phase separation is thus promoted by an increase of temperature,[26] discernible in a decrease in r_0 with an increase of temperature.

In contrast, PSS shows a completely different phase behavior with earth alkaline cations. No macroscopic phase separation is observed in the presence of Ca^{2+} and Sr^{2+}.[24,29] For Ba^{2+}, a horizontal phase boundary according to

$$[Ba^{2+}]_c = r_0 \tag{6.2}$$

is observed.[24,30,31] Above all, the binding of Ba^{2+} to the anionic moieties of PSS is dominated by an exothermic complexation[29] and r_0 decreases in this case with decreasing temperature.[24]

We deliberately used the term phase separation instead of precipitation for all these cases as we are most likely dealing with a liquid-liquid phase separation (LLPS) of the dissolved polyelectrolytes neutralized via specific interactions with alkaline earth cations.[32] In fact Kanai and Muthukumar[33] could demonstrate that the LLPS observed with Ba^{2+} and PSS obeys an UCST behavior. As the impact of temperature on the binding of Ba^{2+} to PA is inverse to the binding of Ba^{2+} to PSS, we have a good reason to assume that the interaction with Ba^{2+} exhibits a LCST. Given that the interaction of PA with M^{2+} obeys a LCST behavior whereas the interaction of PSS with Ba^{2+} is of an UCST type, a combination of these two features in a block copolyelectrolyte may pave the road to invertible micelles with Ba^{2+} and PA-*b*-PSS diblock copolymers, in analogy to the concept pursued by Papadakis *et al.*[11,17,18] It is this idea, which is at the center of the present work. A first step along this line has already been accomplished in a preceding work, in which we showed that these differing modes of interaction with Ca^{2+} can be used to self-assemble PA-*b*-PSS block copolymers into well-defined micelles.[20]

Herein, we report on the effect of temperature on the self-assembly of PA-*b*-PSS in the presence of Ca^{2+}, Sr^{2+}, and Ba^{2+}. Small-angle neutron scattering (SANS) in combination with isothermal titration calorimetry (ITC) is employed to unambiguously prove

that it is possible to create an invertible system with this type of block copolymer and that the inversion of the micelle structure passes a regime of single chains. At the same time, the present results introduce multivalent cations in combination with block copolyelectrolytes as a new toolbox for temperature-responsive polymers and dual-responsive systems.

6.2 Experiments and Data Analysis

Materials. Light water was purified using a Milli-Q-system; heavy water (D_2O, Eurisotop, France, 99.90 at.% deuterium) was filtered with a 100 nm PVDF filter (Merck Millex MPSLVV033RS) prior to use. $CaCl_2 \cdot 2\,H_2O$ (Sigma-Aldrich, France, $>$ 99.9 %), $SrCl_2 \cdot 6\,H_2O$ (Fluka, Germany, $>$ 99 %), $BaCl_2 \cdot 2\,H_2O$ (Sigma Aldrich, Germany, $>$ 99.999 %), NaCl (Sigma-Aldrich, France, $>$ 99.9 %), and NaOH (Sigma-Aldrich, France) were used as received.

Polymer Synthesis. The synthesis of the (block) copolymers was done using reversible addition-fragmentation chain-transfer polymerization and is described in detail in the Supporting Information. The investigated PA-*b*-PSS block copolymers have a block ratio of PA to PSS of 94 : 6.

Sample Preparation. In general, the samples were prepared according to a previously suggested approach. The concentration of positive charges is kept constant at 100 mmol L^{-1}. In order to achieve this, the solvent contains 100 mmol L^{-1} NaCl and M^{2+} cations are added by replacing a certain amount of 100 mmol L^{-1} NaCl by the corresponding amount of solution of MCl_2.

For the scattering experiments, first, an aqueous stock solution of the freeze-dried polymer in 100 mmol L^{-1} NaCl was prepared at a polymer concentration of 8 g L^{-1} and adjusted to pH of 9 using a 100 mmol L^{-1} NaOH solution. The solution is filled up with 100 mmol L^{-1} NaCl solution and the desired amount of 50 mmol L^{-1} $CaCl_2$ ($SrCl_2$/$BaCl_2$) by drop wise addition under vigorous stirring. The final polymer concentration was 1 or 4 g L^{-1}.

The samples for small-angle X-ray scattering (SAXS) and ITC were prepared in H_2O; otherwise, the samples were prepared in D_2O or a mixture of H_2O and D_2O.

Density Measurements. The density of the sodium salt of PA and PSS was measured using a DSA 5000 M densitometer (Anton-Paar) in a temperature range from 5 °C to 65 °C. Details can be found in the Supporting Information.

Small-Angle Neutron Scattering. Small-angle neutron scattering (SANS) measurements were performed at the D11 SANS instrument of the Institut Laue-Langevin (Grenoble, France). Three sample-to-detector distances (39.0 m collimation 40.5 m, 8.0 m collimation 8.0 m, and 1.4 m collimation 5.5 m) and a neutron wavelength of 0.5 nm (full width at half maximum 9 %) were used to cover a q-range of 2×10^{-2} to $5\,nm^{-1}$. We used a circular neutron beam with a diameter of 15 mm. Scattered neutrons were detected with a ^{3}He MWPC detector (CERCA) with 256×256 pixels of 3.75 mm × 3.75 mm pixel size. The detector images were azimuthally averaged, corrected to transmission of the direct beam and scaled to absolute intensity using the LAMP software. A 1 mm H_2O cell was used as secondary calibration standard ($\frac{d\Sigma}{d\Omega} = 0.929\,cm^{-1}$). The incoherent background and the scattering from the solvent and the incoherent background were subtracted from the scattering curves. Details for the data reduction can be found in Chapter 2 of ref [34]. The sample temperature was adjusted to values between 6 °C to 65 °C using a circulating water bath.

Additional SANS measurements were performed at the KWS2 small-angle scattering instrument of the Heinz Maier-Leibnitz Zentrum (Garching, Germany).[35] Three sample-to-detector distances (19.6 m collimation 20.0 m $\lambda = 10$ Å, 7.7 m collimation 8.0 m $\lambda = 5$ Å, 1.7 m collimation 2.0 m $\lambda = 5$ Å) were used to cover a q-range of 3×10^{-2} to $1.0\,nm^{-1}$. Scattered neutrons were detected with a ^{3}He multitube detector (GE Reuter Stokes Inc).[36] The detector images were azimuthally averaged, corrected to transmission of the direct beam, and scaled to absolute intensity of plexiglass as the secondary calibration standard using the QtiKWS software. The scattering from the solvent and the incoherent background were subtracted from the scattering curves.

Small Angle X-ray Scattering. SAXS experiments were performed at the ID02 beamline of the European Synchrotron Radiation Facility (ESRF). Two sample-to-detector distances (10 m and 1 m) were measured at an X-ray energy of 12.46 keV (0.0995 nm) using a Rayonix MX-170HS CCD detector to cover a q-range of $8 \times 10^{-3}\,nm^{-1}$ to $6\,nm^{-1}$.

Additional SAXS data were obtained from the D2AM beamline of the ESRF. Two sample-to-detector distances (2.2 m and 0.6 m) were measured at an X-ray energy of

16.00 keV (0.0775 nm) using a XPAD-D5 hybrid pixel detector to cover a q-range of $5 \times 10^{-2}\,\mathrm{nm}^{-1}$ to $7\,\mathrm{nm}^{-1}$.

Samples were filled in a 2 mm flow-through quartz glass capillary (WJM Glas Müller, Berlin, Germany) to facilitate accurate background subtraction. The detector images were corrected for dark and flat-field, azimuthally averaged and corrected to transmission of the direct beam. The data were scaled to absolute intensity using water as a secondary standard.[37,38] Error bars were estimated assuming Poisson statistics.

Static and Dynamic Light Scattering. Static and dynamic light scattering (SLS, DLS) available in the ILL PSCM lab were performed using an ALV CGS-3 (ALV, Langen, Germany) equipped with a HeNe laser operating at $\lambda_0 = 632.8\,\mathrm{nm}$. The samples were filtered in cylindrical quartz glass cells using Millex PDVF filters with a pore size of 0.45 µm. SLS and DLS were measured simultaneously in an angular range from 30° to 150° in steps of 10 °C at temperatures ranging from 6 °C to 65 °C.

The intensity-time correlation function $g_2(\tau) - 1$ measured with DLS was analyzed using the method of cumulants[39]

$$g_2(\tau) - 1 = \beta \exp\left(-2\Gamma\tau\right)\left(1 + \frac{\mu_2}{2!}\tau^2\right)^2 \tag{6.3}$$

β is a factor, which depends on the experimental setup, Γ is the relaxation rate and μ_2 is the second cumulant. The apparent diffusion coefficient $D_{app}(c, q)$ for a given q is calculated according to

$$D_{app} = \frac{\Gamma}{q^2} \tag{6.4}$$

The diffusion coefficient is extrapolated toward $q = 0$ and where applicable, to $c = 0$ according to[**Burchard1980a**, 40]

$$D_{app}(c, q) = D_0\left(1 + CR_g^2 q^2 + k_D c\right) \tag{6.5}$$

where C and k_D are constants describing q and the concentration dependence of D_{app}, respectively. The diffusion coefficient D_0 is used to calculate the hydrodynamic radius R_h using the Stokes-Einstein equation

$$R_h = \frac{k_B T}{6\pi\eta D_0} \tag{6.6}$$

where T is the temperature, k_B is the Boltzmann constant, and η the viscosity of the solvent. The temperature-dependent viscosity of D_2O, which differs from that of H_2O, was obtained from ref [41].

Static light scattering was evaluated with the Zimm equation[42]

$$\frac{Kc}{\Delta R_\theta} = \frac{1}{M_w} + 2A_2c + \frac{R_g^2}{3M_w}q^2 \tag{6.7}$$

where c is the mass concentration of the polymer, M_w is the weight averaged molar mass of the polymer, A_2 is the second osmotic virial coefficient, and R_g is the radius of gyration. ΔR_θ is the Rayleigh ratio and corresponds to the macroscopic scattering cross-section; $\frac{d\Sigma}{d\Omega}$ is used to express the scattering intensity in SANS and SAXS. K is the contrast factor given by

$$K = \frac{4\pi^2}{N_A\lambda_0^4}\left(n_{\text{standard}}\frac{dn}{dc}\right)^2 \tag{6.8}$$

It contains the Avogadro constant N_A, the wavelength of the laser in vacuo λ_0, the refractive index of the standard (in this case toluene) n_{standard}, and the refractive index increment of the polymer in the solvent $\frac{dn}{dc}$.

SLS data were corrected for the scattering from the solvent and normalized to absolute intensities by comparison to a toluene standard.

Small-Angle Scattering Analysis. The form factor fits of the small-angle scattering data were done using the SASET program.[43] Instrumental resolution for SANS has been taken into account according to ref [44]. The form factor is convoluted with a resolution function $R(q, \sigma_q)$, which depends on wavelength spread, finite collimation of the beam, and detector resolution

$$P(q)_{\text{smeared}}(q) = \int R(q, \sigma_q)P(q)dq \tag{6.9}$$

We took into account the instrumental resolution for all points from each detector configuration and merged the data only for final representation. This approach does not involve truncation of the data in the region of overlapping q, which leads to a larger number of available data points in the analysis.

Scattering for Gaussian and Generalized Gaussian Chains. The scattering of a Gaussian chain with a radius of gyration R_g and a Flory exponent ν of 0.5 can be described by the Debye equation[45]

$$P(q) = \frac{2\left(\exp\left(-q^2R_g^2\right) - 1 + q^2R_g^2\right)}{\left(q^2R_g^2\right)^2} \tag{6.10}$$

In order to be able to describe the scattering from polymer chains where the Flory exponent is deviating from $\nu = 0.5$, the equation can be generalized to[46]

$$P(q) = \frac{1}{\nu U^{\frac{1}{2\nu}}}\gamma(\frac{1}{2\nu}, U) - \frac{1}{\nu U^{\frac{1}{\nu}}}\gamma(\frac{1}{\nu}, U) \tag{6.11}$$

with U being defined as

$$U = (2\nu + 1)(2\nu + 2)\frac{q^2 R_g^2}{6} \tag{6.12}$$

and $\gamma(a, x)$ being the incomplete Gamma function

$$\gamma(a, x) = \int_0^x t^{a-1} \exp(-t) dt \tag{6.13}$$

Scattering from Block Copolymer Micelles with Self-Avoiding Chains in the Corona. The form factor of self-assembled block copolymers with excluded volume interaction of the polymer chains was first treated by Pedersen.[47–50] The macroscopic scattering cross-section $\frac{d\Sigma}{d\Omega}(q)$ of a solution of block copolymer micelles can be written as[49]

$$\begin{aligned}\frac{d\Sigma}{d\Omega}(q) = N\Big[&N_{agg}^2 \beta_{core}^2 A_{core}^2(q) \\ &+ N_{agg}\beta_{corona}^2 P'_{corona}(q) \\ &+ 2N_{agg}^2 \beta_{core}\beta_{corona} A_{core}(q) A_{corona}(q) \\ &+ N_{agg}\left(N_{agg} - P'_{corona}(0)\right)\beta_{corona}^2 A_{corona}^2(q)\Big]\end{aligned} \tag{6.14}$$

where N is the number density of micelles, N_{agg} is the aggregation number of micelles, β_{core} and β_{corona} are the total excess scattering length of the block forming the spherical core and the corona, respectively. They are defined as

$$\beta_{corona} = V_{m,\,corona} DP_{corona} \Delta\rho_{corona} \tag{6.15}$$

and

$$\beta_{core} = V_{m,\,core} DP_{core} \Delta\rho_{core} \tag{6.16}$$

with V_m being the molecular volume of the respective monomer unit, DP_{corona} and DP_{core} are the degree of polymerization of the corona and core block, respectively, and $\Delta\rho$ is the corresponding excess scattering length density.

Equation 6.14 consists of four different contributions: scattering from the spherical and homogeneous core $A_{core}^2(q)$, scattering from the polymer chains in the corona

$P'_{corona}(q)$, the cross-term between core and corona $A_{core}(q) \cdot A_{corona}(q)$, and the cross-term between different chains $A^2_{corona}(q)$. $A_{core}(q)$ is the scattering amplitude of a homogeneous sphere[51] with radius R_{core}

$$A_{core}(q) = 3\frac{\sin(qR_{core}) - qR_{core}\cos(qR_{core})}{(qR_{core})^3} \tag{6.17}$$

$P'_{corona}(q)$ is the form factor of a chain in the corona. It contains the self-correlation of the chain $P_{exv}(q)$ as well as the interaction between the chains, which is expressed by the interaction parameter ν[49,52]

$$P'_{corona}(q) = \frac{P_{exv}(q)}{1 + \nu P_{exv}(q)} \tag{6.18}$$

where $P_{exv}(q)$ is the form factor of a semi flexible self-avoiding chain, which is characterized by a radius of gyration of the polymer chains in the corona $R_{g,corona}$. This form factor was first derived by Pedersen and Schurtenberger[53] and later corrected[54]. In experiments, ν typically adopts values between 0 and 8 and is related to the osmotic compressibility κ by[49,52,55]

$$\kappa = 1 + \nu \tag{6.19}$$

$A_{corona}(q)$ is given by

$$A_{corona}(q) = \frac{\int \rho_{corona}(r) r^2 \frac{\sin(qr)}{qr} dr}{\int \rho_{corona}(r) r^2 dr} \tag{6.20}$$

with $\rho_{corona}(r)$ as the scattering length density profile in the corona. In this work, we use a Gaussian profile, which is defined as

$$\rho_{corona}(r) = \begin{cases} 0 & \text{for } r < R_{core} \\ 1 & \text{for } r = R_{core} \\ \exp\left(\frac{-(r-R_{core})^2}{2s^2}\right) & \text{for } r > R_{core} \end{cases} \tag{6.21}$$

with s controlling the thickness of the corona.

In order to take into account the size distribution of micelles, we assumed a log-normal distribution of the aggregation number N_{agg}

$$p(N_{agg}) = \frac{1}{H\sqrt{2\pi}N_{agg}} \exp\left(\frac{-\log(N_{agg} - M)^2}{2H^2}\right) \tag{6.22}$$

where H and M define the distribution and are connected to the mean aggregation number $\overline{N_{agg}}$ and standard deviation $\sigma_{\overline{N_{agg}}}$ by

$$\overline{N_{agg}} = \exp\left(M + \frac{H^2}{2}\right) \tag{6.23}$$

$$\sigma_{\overline{N_{agg}}} = \sqrt{\exp\left(H^2 + 2M\right)\left(\exp\left(H^2\right) - 1\right)} \tag{6.24}$$

The macroscopic scattering cross-section is therefore

$$\frac{d\Sigma}{d\Omega}_{\text{polydisperse}}(q) = \int \frac{d\Sigma}{d\Omega}(q)p(N_{agg})dN_{agg} \tag{6.25}$$

Isothermal Titration Calorimetry. Isothermal titration calorimetry (ITC) measurements were performed using a VP-ITC from Malvern Instruments. Typically, the cell contained 1.4 mL of polymer solution, and the injection volumes were increased continuously during the titration ranging from 3 µL to 16 µL with a time span of 300 s in between the injections. In order to avoid the "first injection anomaly", a short down motion of the plunger was performed prior to insertion of the syringe into the active chamber.[56] The range of values of the M^{2+}/polymer ratios was extended by performing several titrations with changing concentration of earth alkaline metal cations.[57] The baseline correction and integration were performed using NITPITC.[58] We did not correct the signals for the heat of dilution of the polyelectrolyte and the metal cations because those contributions were considerably smaller than the heat of binding. The data were, if possible, fitted using the model of a single set of identical sites or two sets of independent sites. The details of the models are described in the Supporting Information.

6.3 Results and Discussion

Solution Behavior. We showed previously that aqueous solutions of PA-*b*-PSS block copolymers form spherical block copolymer micelles in the presence of Ca^{2+}. Because Ca^{2+} shows a specific interaction with PA but not with PSS, Ca^{2+} complexes the PA block and forms the core of the micelles, while PSS forms the corona. Furthermore, we demonstrated that micelle formation can be triggered for a sample in the single chain state by an increase of temperature because of the entropic nature of Ca^{2+} binding to PA.[20]

The main focus of this work is to clarify if similar micelles can be found for the two other earth alkaline cations Sr^{2+} and Ba^{2+} and in particular how temperature changes affect the binding of the multivalent cations to the block copolyelectrolyte. For the present work we choose a polymer with a long PA block and a relatively short PSS block. In order to exploit the full potential of SANS we use a block copolymer which contains a deuterated PA block. Deuteration allows us to match different parts of the polymer in

Table 6.1: Overview of Polymer Composition, Weight-Averaged Molecular Weight M_w, and Hydrodynamic Radius R_h Determined from NMR and SLS and DLS in 100 mmol L^{-1} NaCl and in the Absence of M^{2+}

Sample	PA:PSS /mol %[a]	M_w /kg mol^{-1}[b]	R_h /nm[c]
h_3-$PA_{1190}PSS_{70}$	94:6	160 ± 2	13.8 ± 0.6
d_3-$PA_{1190}PSS_{70}$	94:6	181 ± 3	13.6 ± 0.5

[a] Obtained by NMR. [b] Obtained by SLS. [c] Obtained by DLS.

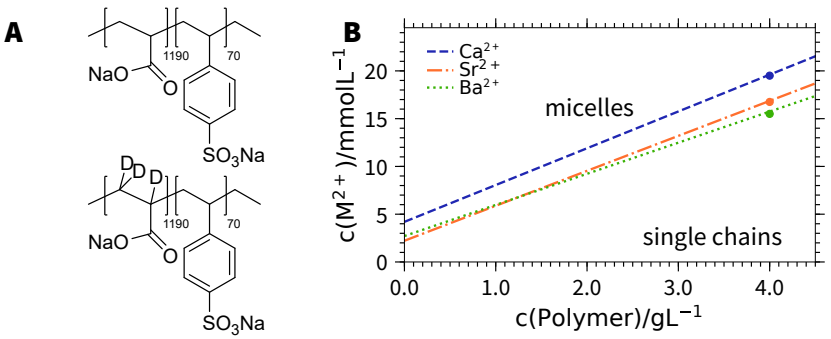


Figure 6.1: **(A)** Chemical structure of the block copolymers. **(B)** Simplified diagram of micelle formation with d_3-PA_{1190} PSS_{70}/h_3-PA_{1190} PSS_{70} in the presence of Ca^{2+}, Sr^{2+}, and Ba^{2+}. The points indicate the compositions, where temperature-dependent SANS and light scattering experiments were performed. An extended version of the phase diagram can be found in the Supporting Information.

neutron scattering by using mixtures of light and heavy water as a solvent.[59] The corresponding polymer is denoted as d_3-$PA_{1190}PSS_{70}$. In addition, we use an identical block copolymer with fully hydrogenated blocks, denoted as h_3-$PA_{1190}PSS_{70}$. Figure 6.1A shows the chemical structure of the block copolymers, and Table 6.1 summarizes the molecular weights and hydrodynamic radii from DLS/SLS as well as the ratio between PA and PSS of the block copolymers determined by NMR. Details of the characterization can be found in ref [20] and in the Supporting Information.

Figure 6.1B illustrates the solution behavior of h_3-PA_{1190} PSS_{70}/d_3-PA_{1190} PSS_{70} in the presence of Ca^{2+}, Sr^{2+}, and Ba^{2+} at room temperature. The boundaries for micelle formation with h_3-PA_{1190} PSS_{70} and d_3-PA_{1190} PSS_{70} are identical within the experimental accuracy. The block copolymer shows a solution behavior, which is similar to the one observed for PA homopolymers described by eq 6.1. This means that with increasing polymer concentration, the amount of M^{2+} required to induce a phase transition increases. However, instead of precipitation as found for PA homopolymers,[25,27,60] the formation of stable micelles takes place in the case of block copolyelectrolytes.

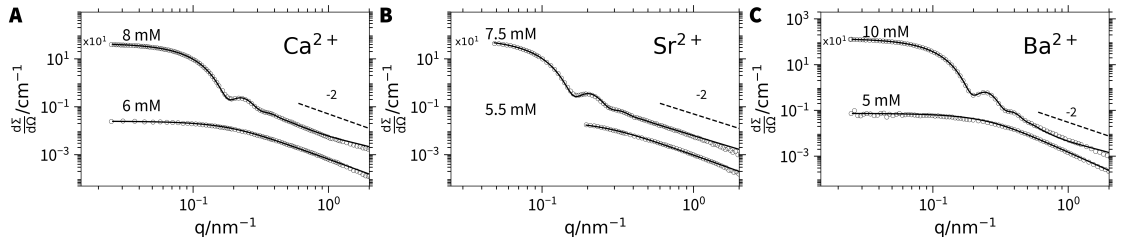


Figure 6.2: SAXS profiles of h_3-$PA_{1190}PSS_{70}$ ($c = 1\,g\,L^{-1}$) in the presence of different concentrations of Ca^{2+} (**A**), Sr^{2+} (**B**), and Ba^{2+} (**C**). The solid lines represent fits to the model of the generalized Gaussian chain[46] or a spherical polydisperse block copolymer micelle.[47,49] Table 6.11 summarizes the results of the fits.

In order to facilitate meaningful scattering experiments and suppress potential interparticular interferences by electrostatic screening, all experiments were performed in the presence of additional NaCl as an inert salt. Addition of NaCl was limited to accomplish an overall level of cationic charges of $0.1\,M = 2[M^{2+}] + [Na^{+}]$. Variation of this level would have generated one further parameter to control the interactions[24,60] but was not applied in the present work to keep the complexity as low as possible.

In order to investigate the structure of the micelles in the presence of Ca^{2+}, Sr^{2+}, and Ba^{2+} we performed SAXS experiments of h_3-$PA_{1190}PSS_{70}$ in the micelle regime in the presence of the three cations. Figure 6.2 shows the corresponding SAXS profiles of a sample in the single chain region and in the micelle region for all three cations, respectively.

The curve with the lowest concentration of M^{2+} shows a slope close to -2 at high q. Upon increase of the M^{2+} concentration, a dramatic increase of the forward scattering is observed together with the formation of well-defined minima in the scattering curves. This shows that block copolymer micelles are formed in the presence of all three cations.

The curves in the single-chain region can be well described by the model of a generalized Gaussian chain[46] with Table 6.2 summarizing the fit parameters. The resulting radii of gyration $R_{g,free}$ range between $6.3\,nm$ and $8.2\,nm$. Moreover, we find Flory exponents ν between 0.4 and 0.5, which is close to the value of polymers in a θ solvent. We do not observe a structure factor, which implies that the charges of the polyelectrolytes are highly screened because of the large amount of salt present in solution.

We used the previously suggested model of spherical block copolymer micelles,[20,47,49] consisting of a PA core complexed by the multivalent cation M^{2+} and PSS chains in the corona to describe the data of the samples in the micelle region. This

Table 6.2: Structural Parameters from the Form Factor Fits of the SAXS Data Shown in Figure 6.2[a]

	Ca^{2+}		Sr^{2+}		Ba^{2+}	
$c(M^{2+})$/ mM	6	8	5.5	7.5	5	10
$\phi_{micelles}$	0.0	0.79	0.0	0.73	0.0	1.0
$R_{g,free}$/nm	8.2	5.2	6.3	6.2	6.7	—
ν	0.49	0.36	0.44	0.53	0.38	—
R_{core}/nm	—	22.8	—	25.6	—	21.6
$\frac{\sigma_{R_{core}}}{R_{core}}$	—	0.109	—	0.104	—	0.113
$R_{g,corona}$/nm	—	0.7	—	2.3	—	1.0
$f_{solvent}$	—	0.83	—	0.60	—	0.90

[a] An extended version including errors of the fitting parameters can be found in the Supporting Information. Fits at the lower $c(M^{2+})$ were carried out with the model of generalized Gaussian chains[46] and fits at the higher $c(M^{2+})$ with the model of a spherical block copolymer micelle[20,47,49] or a mixture of block copolymers and free generalized Gaussian chains.

model has been shown to describe the situation for Ca^{2+} and is expected to be similar for all three cations as the binding to PA is similar and the PA block is considerably longer than the PSS block. The fit parameters are summarized in Table 6.2. The scattering curves for the micelles formed in the presence of all three cations can be well described by the suggested model. The micelles have similar dimensions, consisting of a relatively large core formed of PA/M^{2+} with a radius R_{core} between 21.6 and 25.6 nm. The corona is formed by PSS and is rather thin with a radius of gyration of the polymers in the corona $R_{g,\,corona}$ between 0.7 and 2.3 nm. The overall micelles are rather monodisperse with polydispersities $\frac{\sigma_{R_{core}}}{R_{core}}$ close to 10%. By fitting the scattering data in absolute intensities, knowing the polymer concentration, scattering length densities, and block lengths, it turned out that the micelle cores contain a large volume fraction $f_{solvent}$ of water. $f_{solvent}$ is defined as

$$f_{solvent} = 1 - \frac{\left(V_{m,\,monomer\,unit} + 0.5V_{m,\,M^{2+}}\right) DP_{core} N_{agg}}{\frac{4}{3}\pi R_{core}^3} \tag{6.26}$$

where $V_{m,\,monomer\,unit}$ is the molecular volume of one monomer unit of the core forming block, in this case PA, and $V_{m,\,M^{2+}}$ is the molecular volume of the corresponding divalent cation, DP_{core} is the degree of polymerization of the core block, and N_{agg} is the aggregation number. The high volume fractions of water found for the core of the micelles are in agreement with our previous contrast-variation study of PA-*b*-PSS in the presence of Ca^{2+}.[20]

For the micelles in the presence of Ca^{2+} and Sr^{2+}, we had to take into account a small fraction of non-micellized polymer chains ($\phi_{micelles} < 1.0$).

Because Ba^{2+} also interacts with the PSS block, we also tried a model with Ba^{2+}/PSS in the core of the micelles and PA in the corona. The polymer concentration, knowledge of block length, and the corresponding molar volumes of the blocks allowed us to heavily constrain the fit. This model was not able to describe the data sufficiently well and furthermore gave unreasonable values for the parameter s controlling the corona thickness and the radius of gyration of the polymers in the corona $R_{g,corona}$. The best fit is shown in Figure 6.17 of the supporting information.

In short, we find spherical micelles with similar dimensions for Ca^{2+}, Sr^{2+} and Ba^{2+}. The core of the micelles is formed by PA/M^{2+} together with a high volume fraction of water. The corona of the micelles is formed by PSS. PA is complexed by the bivalent earth alkaline cation, and therefore, a microphase separation of the M^{2+}/PA blocks is taking place. The complex forms the core of the micelle and is highly swollen with water, typical for liquid-liquid phase transitions.[20,32] PSS forms the corona of the micelles and stabilizes the aggregates by charge repulsion.

Temperature Effect on the Solution Behavior. In order to study the effect of temperature on the self-assembly of the block copolymer in the presence of earth alkaline cations, we choose points in the phase diagram which are close to the single chain to micelle transition indicated as dots in Figure 6.1B. Because we also performed SANS measurements on those samples, we used the block copolymer d_3-$PA_{1190}PSS_{70}$. At room temperature, all of these samples are considered to be in the single-chain state. We performed temperature-dependent DLS and SLS on these samples. Figure 6.3 shows the hydrodynamic radii R_h and the apparent molecular weight $M_{w,app}$ obtained from the temperature-dependent light scattering measurements.

Figure 6.3A shows the results for the block copolyelectrolyte in the presence of Ca^{2+}. The hydrodynamic radius at low temperatures (6 °C to 25 °C) is close to 8 nm, which we attribute to the presence of single chains of block copolymers in solution. Above 25 °C R_h increases to around 30 nm. Similarly, the apparent molecular weight $M_{w,app}$ increases from 4×10^5 g mol^{-1} to 6×10^7 g mol^{-1}. We attribute this strong increase to the formation of block copolymer micelles. It has been shown previously for PA homopolymers that an increase in temperature can be used to promote binding of Ca^{2+} to the polyelectrolyte chain.[26] This results in a chain collapse and eventually in aggregation and precipitation of the polymer. As demonstrated in our previous work,[20]

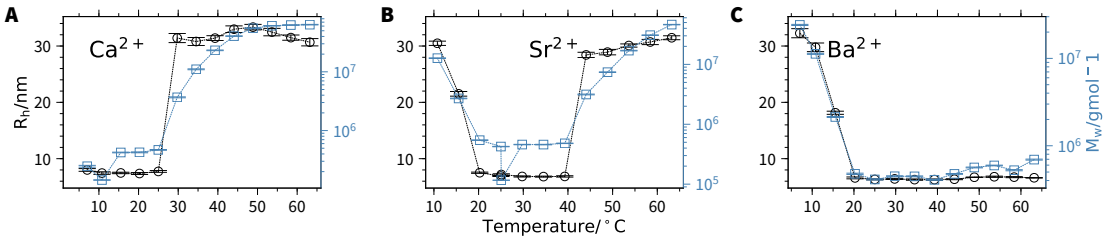


Figure 6.3: Hydrodynamic radius R_h and apparent molecular weight $M_{w,app}$ of d_3-$PA_{1190}PSS_{70}$ in the presence of Ca^{2+} (**A**), Sr^{2+} (**B**) and Ba^{2+} (**C**) as a function of temperature. The lines are guide to the eyes. The polymer concentration is $4\,g\,L^{-1}$. The concentration of M^{2+} is $19.5\,mmol\,L^{-1}$ (Ca^{2+}), $16.75\,mmol\,L^{-1}$ (Sr^{2+}), $15.5\,mmol\,L^{-1}$ (Ba^{2+}). The solvent is composed of 25.2 % D_2O.

stronger binding of Ca^{2+} to the PA block leads to microphase separation because of the same temperature-promoted binding of Ca^{2+} to PA. A detailed analysis of the structure using small-angle neutron scattering confirming this feature is presented later. We performed temperature cycles with the same sample several times and found that the temperature-induced single-chain to micelle transition was reversible and highly reproducible.[20]

Figure 6.3B shows R_h and $M_{w,app}$ as a function of temperature for the PA-*b*-PSS block copolymer in the presence of Sr^{2+}. Again, a hydrodynamic radius of around 8 nm and an apparent molecular weight of $4 \times 10^5\,g\,mol^{-1}$ indicate the presence of single chains in solution at room temperature. Upon increase of the temperature above 40 °C a strong increase of R_h as well as $M_{w,app}$ occurs similar to the increase observed with Ca^{2+} cations. However, at temperatures below 20 °C, R_h and $M_{w,app}$ also increase. From this, we conclude that block copolymer micelles are formed at high as well as low temperatures with an intermediate region, where the polymers are present as single chains. A previous work already showed that an increase of temperature promotes the binding of Ca^{2+} and Sr^{2+} to PA because of the entropic nature of the complexation.[26] However, lowering the temperatures did not show a chain collapse or aggregation of PA homopolymers. Even though PSS does not show a precipitation threshold with Sr^{2+} at room temperature, we hypothesize that the PSS block plays an important role in the formation of the micelles at low temperatures. In order to shed light onto the binding situation we will use SANS and ITC experiments.

Figure 6.3C shows the results for the block copolymer in the presence of Ba^{2+}. In contrast to the samples with Ca^{2+}, there is an increase in R_h and $M_{w,app}$ at low temper-

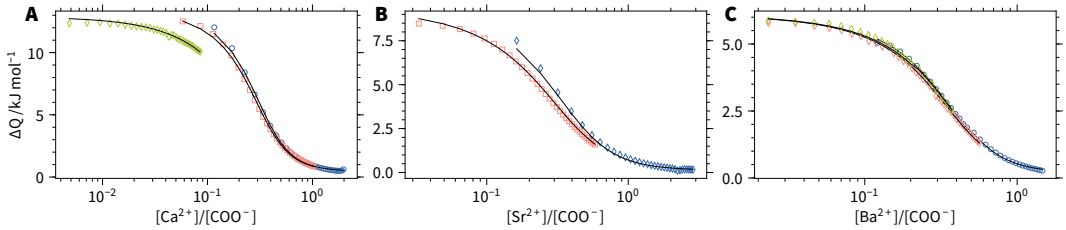


Figure 6.4: Isothermal titration curve of PA in the presence of Ca^{2+} (**A**), Sr^{2+} (**B**), and Ba^{2+} (**C**). The curves show the heat of binding per injection as a function of the M^{2+}/PA ratio. We performed several titrations with varying concentrations of M^{2+} to cover a large range of M^{2+}/PA. The solid lines are global fits with the model of a single set of identical binding sites. Details can be found in the Supporting Information. Table 6.3 summarizes the results.

atures comparable to the sample with Sr^{2+}. Both quantities show a value close to the typical value of single chains at 25 °C. From this, we conclude that micelles are formed at low temperatures, while at temperatures in the regime of 20 °C $<$ T $<$ 40 °C, the sample contains single chains.

Figure 6.21 in the Supporting Information shows the hydrodynamic radius R_h of d_3-$PA_{1190}PSS_{70}$ in the presence of Sr^{2+} during several heating and cooling cycles between 10 °C, 25 °C and 65 °C. Micelles are formed at low temperatures, return to single chains at room temperature, and reform at high temperatures. This demonstrates that the samples are in thermodynamic equilibrium and the temperature effect on the solution behavior is fully reversible.

Thermodynamics of Cation Binding and Micelle Formation. In order to gain further insights into the origin of the described temperature behavior, we used ITC to link the information we obtained from temperature-dependent light scattering with thermodynamic quantities. ITC allows us to measure the consumed or released heat upon addition of M^{2+} to a solution of the polyelectrolyte for a given temperature. The measured heat can be attributed to the binding of the metal cation to the anionic moiety.

There are several driving forces for the binding of multivalent cations and micelle formation which have to be taken into account. The binding of multivalent cations to the anionic moiety results in a gain in entropy because two Na^+ are replaced by one M^{2+}. A release of water molecules from hydration shells also results in a gain of entropy. Equally important, the enthalpy of binding has to be taken into account.

In order to compare the contributions from the PA and PSS blocks, we performed ITC experiments on PA and PSS homopolymers in the presence of the three earth alkaline metal cations. Figure 6.4 shows the titration curves of PA with the three investigated earth alkaline metal cations at 25.0 °C. The heat of binding ΔQ is positive for all cations and follows a sigmoidal curve. This indicates that the binding of M^{2+} to PA is an endothermic process. We performed several titrations with varying concentrations of M^{2+} in the syringe to access a larger range of M^{2+}/PA. The data can be described by the model of a single set of identical binding sites, which is described in detail in the Supporting Information. All titrations for a given combination of M^{2+} were analyzed globally using the same fitting parameters. Table 6.3 summarizes the results of the data analysis.

From the fits, we obtain the enthalpy of binding ΔH, entropy of binding ΔS, binding constant K, and the binding stoichiometry n. We find a positive binding enthalpy for all three cations demonstrating that the binding of M^{2+} to PA is driven by entropy for all three metal cations. In a previous work[28] on PA and Ca^{2+}, this gain of entropy has been attributed to the release of two sodium cations as well as several water molecules upon binding. Compared to the previous work, we find slightly smaller binding enthalpies which we attribute to the presence of NaCl in our experiments compared to pure water. In fact, an increase in ionic strength in the solution leads to a decrease in ΔH for the binding of multivalent cations to DNA.[61] The binding enthalpy ΔH and along with it, the entropy of binding ΔS decreases according to $Ca^{2+} > Sr^{2+} > Ba^{2+}$. We attribute the decrease of ΔS when going from Ca^{2+}, Sr^{2+}, and Ba^{2+} to a decreased amount of water released from hydration shells upon binding.

Next, we performed titration experiments for a PSS homopolymer in the presence of the three metal cations. Figure 6.5 shows the corresponding titration curves. For Ca^{2+}, the curves can be well described by the model of a single set of identical binding sites with a positive binding enthalpy. Compared to Ca^{2+}/PA the binding enthalpy ΔH, entropy ΔS and the binding constant K are considerably smaller for Ca^{2+}/PSS. Table 6.3 summarizes the results from the data analysis. The smaller binding constant K is in agreement with the macroscopic observation that there is no phase separation for PSS in the presence of Ca^{2+}.

Figure 6.5B shows the titration curve of Sr^{2+}/PSS. The curve differs considerably from the one found for Ca^{2+}/PSS. Clearly, there are two processes occurring upon addition of Sr^{2+} to PSS: first, a binding process with a positive ΔH is taking place at low Sr^{2+}/PSS ratios. This is followed by a second process which has a negative ΔH contri-

Table 6.3: Thermodynamic Data for the M^{2+} Binding to PA and PSS from ITC at 25 °C

Polymer	M^{2+}	K /L mol^{-1}	ΔH /kJ mol^{-1}	TΔS /kJ mol^{-1}	ΔG /kJ mol^{-1}	n
PA	Ca^{2+}	$(5.60 \pm 0.16) \cdot 10^3$	16.3 ± 0.2	37.7 ± 0.3	-21.4 ± 0.1	0.264 ± 0.002
PA	Sr^{2+}	$(3.68 \pm 0.21) \cdot 10^3$	13.4 ± 0.4	33.8 ± 0.5	-20.4 ± 0.1	0.266 ± 0.005
PA	Ba^{2+}	$(4.99 \pm 0.16) \cdot 10^3$	7.6 ± 0.1	26.2 ± 0.2	-21.1 ± 0.1	0.321 ± 0.002
PSS	Ca^{2+}	$(2.82 \pm 0.19) \cdot 10^2$	4.3 ± 0.4	18.3 ± 0.6	-14.0 ± 0.2	0.228 ± 0.016
PSS	Sr^{2+}-(I)	$(5.13 \pm 2.91) \cdot 10^3$	2.2 ± 0.2	19.0 ± 1.8	-21.2 ± 1.4	0.187 ± 0.008
	Sr^{2+}-(II)	$(4.27 \pm 2.82) \cdot 10^2$	-0.23 ± 0.61	14.8 ± 1.7	-15.0 ± 1.6	2.156 ± 0.160

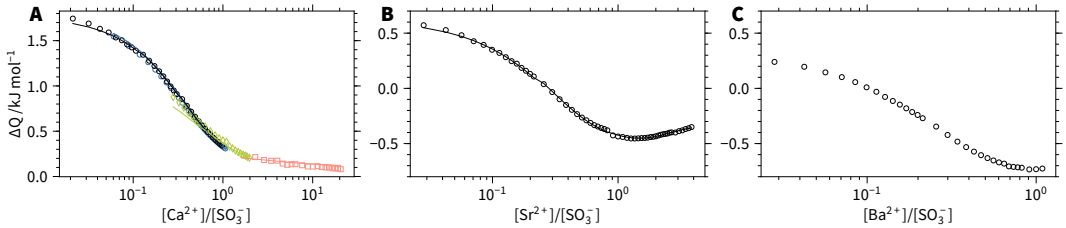


Figure 6.5: Isothermal titration curve of PSS in the presence of Ca^{2+} (**A**), Sr^{2+} (**B**) and Ba^{2+} (**C**). The curves show the heat of binding per injection as a function of the M^{2+}/PA ratio. We performed several titrations for Ca^{2+} with varying concentrations of the polymer to cover a large range of Ca^{2+}/PSS. The solid lines are global fits with the model of a single set of identical binding sites (**A**) and two sets of independent sites (**B**). Details can be found in the Supporting Information. Table 6.3 summarizes the results of the data analysis

bution. Similarly, we find a two-step binding process for the titration of Ba^{2+} to PSS, where again the first binding process has a positive ΔH contribution and the second process has a negative one.

A previous work[29] already revealed this two-step process for the Ba^{2+}/PSS system. In a first step, two Na^{+} cations are replaced per Ba^{2+} entering the polyelectrolyte domains, which results in a gain of entropy ΔS and a positive ΔH contribution. At higher M^{2+}/PSS ratios, the actual binding of the metal cation to the polyelectrolyte chain takes place as a second step with a negative ΔH term. From a qualitative comparison of the two curves in Figure 6.5B , C it is obvious that this second contribution is weaker for Sr^{2+} than for Ba^{2+}. This is in agreement with the macroscopic phase behavior. Whereas the system Sr^{2+}/PSS shows no precipitation threshold at 25 °C, Ba^{2+}/PSS does show one. We tried to fit the data with the model of two independent binding sites, which was successful for Sr^{2+}. However, for Ba^{2+}, using this model was not successful, which we mostly attribute to the smaller accessible M^{2+}/PSS range compared to Sr^{2+} due to the precipitation of Ba^{2+}/PSS from solution at the end of the titration. This makes the data at high Ba^{2+}/PSS ratios unusable. The result of the fit for Sr^{2+}/PSS is summarized in Table 6.3. The obtained values confirm that two successive binding processes (I and II), one with positive ΔH (I) and one with negative ΔH (II), occur. The same two successive binding processes occur with alkaline earth cations and PA. They are however more difficult to be discerned as both processes are endothermic.

After elucidating the effect of earth alkaline metal cations on the PA and PSS homopolymers, we performed ITC measurements on the h_3-$PA_{1190}PSS_{70}$ block copolymer

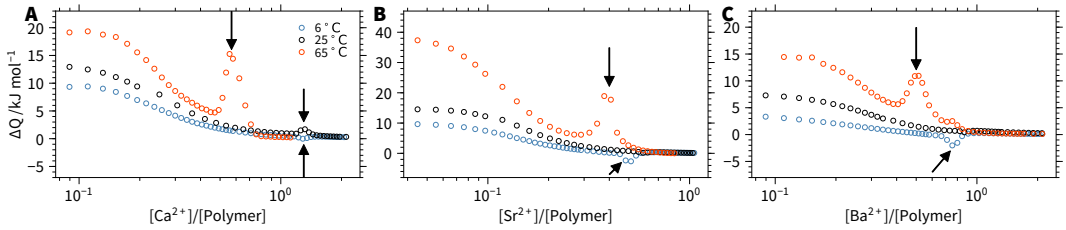


Figure 6.6: Isothermal titration curve of h_3-$PA_{1190}PSS_{70}$ in the presence of Ca^{2+} (**A**), Sr^{2+} (**B**) and Ba^{2+} (**C**) at 6 °C, 25 °C, and 65 °C. The curves show the heat of binding per injection as a function of the M^{2+}/monomer unit ratio. Vertical arrows denote micelle formation with PA cores and inclined arrows indicate M^{2+} binding to PSS.

system. As the length of the PA block is much longer than the length of the PSS block, we expect the ITC experiments to be dominated by the binding of M^{2+} to the PA block. Figure 6.6A shows the titration curves with Ca^{2+} at 6 °C, 25 °C, and 65 °C. The titration curves are composed of two parts: the first part, which shows that heat is consumed upon addition of M^{2+}, resembles the binding curves observed for M^{2+} to PA. The second part consists of a peak at higher M^{2+}/polymer ratios. The peak at 25 °C corresponds to the sample composition, where micellization was observed (Figure 6.1B), which is also an endothermic process and hence driven by entropy. We marked the micellization peaks for all curves with a vertical arrow.

When decreasing the temperature the heat consumed upon addition of Ca^{2+} decreases, in agreement with the entropy-driven binding of Ca^{2+} to PA. A decrease in temperature reduces the term $T\Delta S$ and consequently, ΔH becomes smaller in order to get similar values for the free energy ΔG. Furthermore, when the temperature is lowered, the height of the micellization peak decreases. At 6 °C, the peak nearly disappears.

Figure 6.6B shows titration curves with Sr^{2+} at 6 °C, 25 °C, and 65 °C. Similar to Ca^{2+}, the first part of the titration curve shows positive values for ΔQ and resembles the binding of Sr^{2+} to PA. At higher Sr^{2+}/polymer ratios we again observe a micellization peak. The same positive peak appears at 65 °C and disappears at 25 °C as observed in the case of Ca^{2+}. However, the titrations at 6 °C with Sr^{2+} revealed a noticeable difference from the respective results observed in the presence of Ca^{2+} as a small negative peak occurs at high Sr^{2+}/polymer ratios. The ITC experiments carried out with the PSS homopolymer and Sr^{2+} suggest that the negative peak at 6 °C might arise from the second binding process of Sr^{2+} to PSS which has a negative sign. Because the PSS block is considerably shorter than the PA block, the signal arising from binding of Sr^{2+}

is expected to be weak resulting in a very small contribution, which becomes more pronounced at low temperatures.

Figure 6.6C shows titration curves with Ba^{2+} at 6 °C, 25 °C, and 65 °C. Again, we find a decrease of the initial values of ΔQ with decreasing temperature. Similar to Sr^{2+}, we find a positive peak at high temperatures and a negative peak at low temperatures. Applying the same argument used already for Sr^{2+}, we could expect the negative contribution arising from the second binding step of Ba^{2+} to PSS.

A quantitative comparison of the titration curves of the block copolyelectrolytes with those of the respective homopolymers shown in Figure 6.5B, 6.5C also explains why the negative peak of the second process in the case of Ba^{2+}/PSS binding has a more negative ΔH term than the negative peak of the Sr^{2+}/PSS binding. Moreover, the binding enthalpy of Ba^{2+}/PA during the initial period of titration is smaller than the one for Sr^{2+}/PA.

We believe that a subtle balance of all these individual contributions results in the observed temperature behavior. We conclude that binding of Sr^{2+} and Ba^{2+} to the PSS block promotes the formation of micelles at low temperatures with PSS in the core because it makes the PSS block more hydrophobic, while the PA block becomes more hydrophilic.

Invertible Micelles as Seen by SANS In order to get a more detailed insight into the structures of the micelles, we performed temperature-dependent SANS for the three samples discussed in Figure 6.3. The use of a deuterated PA block allowed us to match out the scattering from the PSS block. Accordingly, use of a mixture of 74.8 % light and 25.2 % heavy water as solvent results in a scattering contrast, where the scattering from d_3-PA is dominating, while the scattering from PSS is very weak. This facilitates the investigation of the micellar structure because the scattering patterns make it easy to distinguish between a model of PA forming the core or the corona. Figure 6.7 shows the SANS profiles for d_3-$PA_{1190}PSS_{70}$ in the presence of Ca^{2+} (A), Sr^{2+} (B), and Ba^{2+} (C) at distinct temperatures. For all samples, we choose 8 °C and 65 °C as temperatures. For the sample with Sr^{2+}, we additionally performed a SANS measurement at 25 °C.

The blue curve in Figure 6.7A shows the SANS profile of d_3-$PA_{1190}PSS_{70}$ in the presence of Ca^{2+} at 8 °C. The curve shows a slope close to -2 at high q and has no distinct oscillations. The curve can be well described by the form factor of a generalized Gaussian chain[46] with a radius of gyration $R_{g,free}$ of 6.9 nm and a Flory exponent ν of 0.4. Table 6.4 summarizes the hydrodynamic radius from DLS and the $R_{g,free}$ and ν

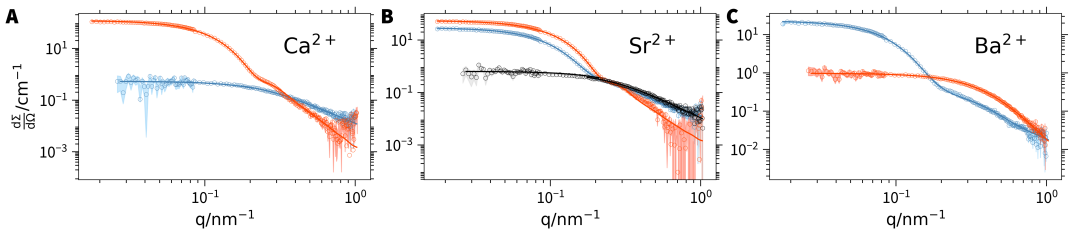


Figure 6.7: SANS profiles of d_3-$PA_{1190}PSS_{70}$ in the presence of Ca^{2+}, Sr^{2+}, and Ba^{2+} at 8 °C (blue), 25 °C (black) and 65 °C (red). The solvent is composed of 25.2 % D_2O. The samples are identical to the ones in Figure 6.3. The solid lines represent fits to the model of a generalized Gaussian chain[46] or block copolymer micelles.[47,49] Table 6.4 summarizes the resulting fit parameters.

obtained from the form factor analysis of the SANS data. Hence, the block copolymers exist as single chains in solution at low temperatures in the presence of Ca^{2+}.

The red curve in Figure 6.7A shows the SANS profile at 65 °C. Compared to the curve at low temperatures, the forward scattering is higher and there is a characteristic oscillation at around $q = 0.22\,nm^{-1}$. At high q, we find a slope considerably steeper, indicating a compact morphology of the PA chains at high temperatures. From the Guinier analysis at low momentum transfer q, we obtain a radius of gyration of 16.7 nm. Based on this and the previous results,[20] we used the model of a polydisperse block copolymer micelle to describe the data.[47,49] This model assumes that PA complexed by Ca^{2+} forms the core of the micelle, while the corona is formed by PSS. In order to get reliable results for the aggregation number and the structure, we heavily constrained the fit using the known block ratio, molar volumes, polymer concentration, and scattering length densities.[20] Details can be found in the Supporting Information. The red solid line in Figure 6.7A shows the best fit with this model. Table 6.4 summarizes the fit parameters. We obtain an aggregation number of 145 together with a core radius of 17.6 nm. Moreover, we find a radius of gyration for the PSS blocks in the corona of 1.0 ± 1.0 nm, which is close to the value we found in a previous study using the same polymer.[20] Recovery of this finite size for the value of $R_{g,corona}$ can be attributed to the fact that there is a slight mismatch of the scattering length density of the solvent. One also should keep in mind the large error bar of this parameter, which indeed shows that the scattering from the corona is very weak. In a previous work,[20] we investigated the micelle structure deep in the micelle regime in the presence of Ca^{2+} at 25 °C. Compared to this previous work, the micelles formed with Ca^{2+} at 65 °C (Figure 6.7A) contain a slightly lower amount of water. We attribute this lower water content to a larger

amount of released water molecules from PA/Ca^{2+}. This is in agreement with the ITC measurements, which showed that the binding is driven by entropy which mainly arises from the release of water molecules, getting more pronounced at high temperatures.

Table 6.4: Structural Parameters from the Form Factor Fits of the SANS Data Shown in Figure 6.7 for d_3-$PAA_{1190}PSS_{70}$ in a Solvent Containing 25.2 % D_2O[a]

	Ca^{2+}		Sr^{2+}			Ba^{2+}	
Temperature	8 °C	65 °C	8 °C	25 °C	65 °C	8 °C	65 °C
R_h[b]	8.0	30.7	30.5	7.2	31.5	29.8	6.6
R_g[c]	6.3	16.7	21.6	6.5	19.8	20.7	4.7
$R_{g,free}$	6.9	—	—	6.7	—	—	5.0
ν	0.40	—	—	0.37	—	—	0.26
Micelle core	—	PA/Ca^{2+}	PSS/Sr^{2+}	—	PA/Sr^{2+}	PSS/Ba^{2+}	—
N_{agg}	—	145	38	—	81	36	—
R_{core}	—	17.6	7.0	—	18.3	5.6	—
$\frac{\sigma_{R_{core}}}{R_{core}}$	—	0.19	0.10	—	0.17	0.02	—
$R_{g,corona}$	—	1.0	9.8	—	1.2	8.0	—
$f_{solvent}$	—	0.650	0.669	—	0.705	0.707	—

[a] An extended version including error estimates can be found in the Supporting Information. [b] Obtained from DLS. [c] Obtained from Guinier analysis of the SANS data.

Figure 6.7B shows SANS profiles of d_3-$PAA_{1190}PSS_{70}$ in the presence of Sr^{2+} at a temperature of 8 °C, 25 °C, and 65 °C. The black curve shows the sample at 25 °C. The profile looks similar to the blue curve in Figure 6.7A recorded at 8 °C. From the Guinier analysis, we obtain a R_g of 6.5 nm. The scattering curve can be well described by the model of a generalized Gaussian chain with a radius of gyration of 6.7 nm and a ν of 0.40. This nicely agrees with the results from temperature-dependent light scattering, where the sample at 25 °C was found to be in the single-chain region. Upon increase of the temperature to 65 °C, the scattering curve shows an increase of forward scattering. Moreover, a characteristic form factor oscillation becomes visible. We find a similar value of R_g as for the Ca^{2+} sample at 65 °C. From this, we conclude that micelles are formed. We employ the same model as used for the Ca^{2+} sample to describe the scattering curve. The resulting aggregation number of 81 is close to the value estimated from static light scattering. In addition, a core radius of 18.3 nm and a value of $R_{g,corona}$ of 1.2 nm is obtained from the analysis. Similarly as for Ca^{2+}, the core is highly swollen by water. A micelle containing a PA/Sr^{2+} core is in agreement with the results from ITC because high temperatures promote the entropy-driven binding of Sr^{2+} to COO^- of the acrylate groups.

The blue curve in Figure 6.7B shows the sample at a temperature of 8 °C. Again, the forward scattering increases quite dramatically with respect to the single-chain state at 25 °C. However, the high q part of the scattering curves is nearly identical with the one of the single chains. This indicates that the conformation of the PA chains barely changes. Based on this observation and the results obtained from ITC, we tried to fit the data with two hypothetical models: one, which assumes that PA complexed by Sr^{2+} forms the core of the micelle and PSS the corona and a second one with PSS/Sr^{2+} in the core and PA in the corona. The fit was heavily constrained by knowing the molar volumes of the corresponding blocks, scattering length densities and the used polymer concentration. The model assuming a core of PSS/Sr^{2+} yielded considerably lower values of χ^2 than the one assuming PA/Sr^{2+} to be in the core. The solid blue line in Figure 6.7B therefore shows the model based on PSS/Sr^{2+} cores, whereas Figure 6.20 in the Supporting Information shows the best fit obtained with PA/Sr^{2+} in the core. Table 6.4 summarizes the fitting parameters. The micelles are formed by a rather small core of 7.0 nm formed by PSS/Sr^{2+} and a considerable amount of water. The PA corona is rather large with $R_{g,corona}$ of 9.8 nm, which agrees with the fact that the PA block is rather long. The resulting overall dimension of the micelles is in good agreement with the hydrodynamic radius measured by DLS.

Figure 6.7C shows SANS profiles of the polymer sample in the presence of Ba^{2+} at 8 °C and 65 °C. The sample at the high temperature can be well described by a generalized Gaussian[46] chain with a radius of gyration of 5.0 nm and ν of 0.26. This is in agreement with the result from DLS and SLS, from which we already expected the polymer to be present as a single chain. In contrast, the curve at 8 °C has a considerably larger forward scattering and shows a well-defined oscillation at $q = 0.19\,nm^{-1}$. Similarly as for the micelles formed at low temperatures in the presence of Sr^{2+}, there are two hypothetical models: PSS/Ba^{2+} or PA/Ba^{2+} forming the core of the micelle. Again, the model with a core formed by PSS/Ba^{2+} describes the data considerably better and is shown as a solid blue line in Figure 6.7C. The alternative model of a PA/Ba^{2+} core poorly describes the data and is shown in Figure 6.20 in the Supporting Information. The obtained micelle dimensions are similar to those of the sample in the presence of Sr^{2+} at low temperatures. The PSS/Ba^{2+} core is rather small with a radius of 5.6 nm, whereas the PA corona is rather thick with $R_{g,corona}$ of 8.0 nm.

We were surprised to not observe micelle formation in the presence of Ba^{2+} at high temperatures as the binding of Ba^{2+} to PA is also entropically driven. Therefore, another sample was prepared, this time even closer to the phase boundary. Figure 6.22

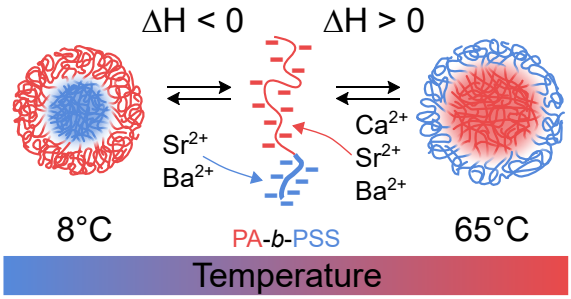


Figure 6.8: Illustration of the temperature induced micellization of PA-*b*-PSS in the presence of Ca^{2+}, Sr^{2+}, and Ba^{2+}.

shows the temperature-dependent light scattering results of this sample. Similarly as before, micelle formation can be observed at low temperatures but this time also at high temperatures with an intermediate regime of single chains. However, the aggregation numbers and hydrodynamic radius for the micelles at high temperatures are considerably smaller as for Sr^{2+} and Ca^{2+}. We attribute this to the considerably smaller entropy of binding ΔS for the combination PA/Ba^{2+}, making it harder to trigger the micellization by an increase of the temperature.

We performed similar SANS experiments with the completely hydrogenated polymer h_3-$PA_{1190}PSS_{70}$ in D_2O, which yielded identical temperature behaviors. However, the SANS data on this fully hydrogenated polymer, in particular of the samples with Sr^{2+} and Ba^{2+} at low temperatures, yield similar χ^2 for the model with the PSS/M^{2+} and the PA/M^{2+} core. Thus, deuteration of one block is required to be able to differentiate between PA/M^{2+} and PSS/M^{2+} in the core of the micelles.

To sum up, we found two different-temperature dependent trends of $PA_{1190}PSS_{70}$ in the presence of earth alkaline cations. For all three cations, micelle formation can be triggered by increasing the temperature, arising from the strong endothermic binding to the PA block. Consequently, the micelles contain a core formed by PA/M^{2+} and a corona formed by PSS. In contrast, micelle formation at low temperatures can only be observed for Sr^{2+} and Ba^{2+}. This micelle formation at low temperatures arises from the exothermic binding of M^{2+} to PSS and consequently leads to a micelle core formed by PSS/M^{2+} and a corona formed by PA. As a result it is possible to generate an invertible micellar system with Sr^{2+} and Ba^{2+}, which allows to change the core-forming block by a change in temperature.

6.4 Conclusions

Polyelectrolytes exhibit ion-specific interactions with a large variety of metal cations. This ion specificity depends on the nature of the polyelectrolytes. Ca^{2+}, Sr^{2+}, and Ba^{2+} as a representative set of bivalent alkaline earth cations interact specifically with the negative residues of PAs.[25–27] The interaction is endothermic in nature due to the liberation of water molecules from solvation shells of the ionic residues.[28,29] Accordingly, addition of those cations to solutions of PA triggers separation of a polymer phase once a threshold of cation concentration is surpassed. An increase of temperature further promotes this phase separation. Unlike to PA, PSS only interacts specifically with Sr^{2+} and Ba^{2+} and the interaction is exothermic in nature.[29–31] Now, the addition of Sr^{2+} and Ba^{2+}, triggers phase separation with PSS which is further promoted by a decrease in temperature.

The present work makes use of these characteristic and differing interaction patterns in order to present a new route to micelle formation and its inversion by changing the temperature. The new route has been accomplished by combining the different patterns in a PA-*b*-PSS block copolyelectrolyte. As it turned out, the phase separation characteristic to the homo-polyelectrolyte is confined to the respective micellar cores. The starting point is always a solution of the block copolyelectrolytes in their single coil state at a distinct concentration of alkaline earth cations low enough to not yet reach the threshold concentration but large enough to enable induction of micelle formation by a suitable change in temperature.

In the presence of Ca^{2+}, micelles are only formed via a temperature increase as this induces neutralization of the PA blocks by the specific bonding of Ca^{2+} to the COO^- residues.[20] The PA blocks form the core of the micelles, surrounded by stabilizing PSS blocks. With Sr^{2+} and Ba^{2+}, the same types of micelles are generated by an increase of temperature. These micelles are also re-dissolved by decreasing the temperature, whereby the state of single coils is reached again. However, a further decrease in temperature generates a new type of micelle, now with PSS blocks in the core being neutralized by either Sr^{2+} or Ba^{2+} cations respectively and solubilized by dangling PA blocks. This establishes a complete inversion of micelles by a variation of temperature (Figure 6.8). The process of micellar inversion could be unambiguously resolved by a combination of SANS with ITC. The morphological changes could be made visible by SANS on a polymer sample with one block of the copolyelectrolyte being fully deuterated. ITC reflected the heat changes accompanying the process of micellar inversion with micelle

formation with PA/M^{2+} cores at high temperatures unambiguously related to an endothermic metal cation binding process and micelle formation with PSS/M^{2+} cores at low temperatures to an exothermic metal binding process.

Acknowledgments

This work used the platforms of the Grenoble Instruct center (ISBG; UMS 3518 CNRS-CEA-UJF-EMBL) with support from FRISBI (ANR-10-INSB-05-02) and GRAL (ANR-10-LABX-49-01) within the Grenoble Partnership for Structural Biology (PSB). The authors thank the Institut Laue-Langevin (https://doi.ill.fr/10.5291/ILL-DATA.9-11-1910) and the European Synchrotron Radiation Facility for the provision of beam time. The authors gratefully acknowledge the financial support provided by JCNS to perform the neutron scattering measurements at the KWS2 instrument of the Heinz Maier-Leibnitz Zentrum (MLZ), Garching, Germany. The authors thank Aurel Radulescu for fruitful discussions and Caroline Mas for support with the ITC experiments and the Partnership for Soft Condensed Matter (PSCM) for supply of the light scattering. N.C. acknowledges funding for a PhD scholarship from Institut Laue-Langevin.

Supporting Information Available

Additional data including an extensive overview of the fitting parameters with error bars, scattering length densities, measurements of the molar volume of PA and PSS, details regarding the ITC data analysis, description of the synthesis and characterization of all used polymers, reversibility of micelle formation, and Ba^{2+}-based inversion of micelles can be found in the Supporting Information.

6.5 Supporting Information

6.5.1 Isothermal titration calorimetry

Figure 6.9 shows the result of a typical ITC experiment. Typically, the heat flow between the reference and the sample cell are recorded as a function of time by the instrument. The raw data are shown in Figure 6.9A The peaks arise from injections of titrant into the analyte solution. The first step of the data analysis is the baseline correction. The resulting data are shown in Figure 6.9B. The area under the peak can be integrated to yield the heat of injection $Q(i)$ of the respective given peak i. Each heat of injection is consequently normalized by the injected volume of titrant, which yields the heat of injection per mole of titrant shown in Figure 6.9C.

The cumulative heat Q for the model of a single set of identical binding sites is given by[62,63]

$$Q = \frac{nM_t\Delta HV_0}{2}\left(1+\frac{X_t}{nM_t}+\frac{1}{nKM_t}-\sqrt{\left(1+\frac{X_t}{nM_t}+\frac{1}{nKM_t}\right)^2-\frac{4X_t}{nM_t}}\right) \tag{6.27}$$

with n being the stochiometry of binding or number of sites, V_0 the active cell volume, M_t the total macromolecule concentration, X_t the total titrant concentration, K the binding constant and ΔH the enthalpy of binding.

Data evaluation of a titration experiments does not use the cumulative heat Q but rather the difference between an injection $i-1$ and i. Therefore the measured signal is translated to ΔQ

$$\Delta Q(i) = Q(i) - Q(i-1) \tag{6.28}$$

Since in our experiment we use an overflow type of cell this expression has to be corrected by a factor, which yields

$$\Delta Q(i) = Q(i) - Q(i-1) + \frac{\Delta V_i}{V_0}\left(\frac{Q(i)+Q(i-1)}{2}\right) \tag{6.29}$$

with ΔV_i being the injection volume of the i-th injection. The factor arises from the assumption that 50 % of the displaced volume contributes to the heat effect.

The fitting procedure involves an initial guess of the parameters n, K and ΔH. Consequently, ΔQ is calculated for the set of given M_t and X_t and compared to the measured data. The parameters n, K and ΔH are optimized using a Levenberg-Marquardt algorithm.

The cumulative heat for the model of two sets of independent sites is given by[64]

$$Q = M_t V_0 (n_1 \Delta H \frac{K_1[X]}{1 + K_1[X]} + n_2 \Delta H \frac{K_2[X]}{1 + K_2[X]}) \tag{6.30}$$

with the two binding stoichiometries n_1 and n_2, binding constants K_1 and K_2 and binding enthalpies ΔH_1 and ΔH_2. The concentration of free ligand $[X]$ can be numerically calculated by solving

$$[X]^3 + p[X]^2 + q[X] + r = 0 \tag{6.31}$$

with

$$p = \frac{1}{K_1} + \frac{1}{K_2} + (n_1 + n_2)M_t - X_t \tag{6.32}$$

$$q = (\frac{n_1}{K_2} + \frac{n_2}{K_1})M_t - (\frac{1}{K_1} + \frac{1}{K_2})X_t + \frac{1}{K_1 K_2} \tag{6.33}$$

$$r = \frac{-X_t}{K_1 K_2} \tag{6.34}$$

Table 6.5 shows the used concentrations for the ITC experiments. $c_{polymer}$ denotes the polymer concentration in the sample cell and $c_{M^{2+}}$ the concentration of earth alkaline cation in the syringe.

Table 6.5: Polymer and M^{2+} concentrations used for the ITC experiments. $c_{polymer}$ denotes the polymer concentration in the titration cell, $c_{M^{2+}}$ denotes the concentration of M^{2+} in the syringe.

Polymer	M^{2+}	$c_{polymer}/g\,L^{-1}$	$c_{M^{2+}}\,mmol\,L^{-1}$
PA	Ca^{2+}	0.243	25.5
PA	Ca^{2+}	0.243	12.75
PA	Ca^{2+}	0.200	0.875
PA	Sr^{2+}	0.200	29.5
PA	Sr^{2+}	0.200	6.0
PA	Ba^{2+}	0.200	25.0
PA	Ba^{2+}	0.2	12.0
PA	Ba^{2+}	0.2	6.0
PSS	Ca^{2+}	2.0	50.0
PSS	Ca^{2+}	1.0	50.0
PSS	Ca^{2+}	0.1	50.0
PSS	Sr^{2+}	2.0	200.0
PSS	Ba^{2+}	2.0	200.0

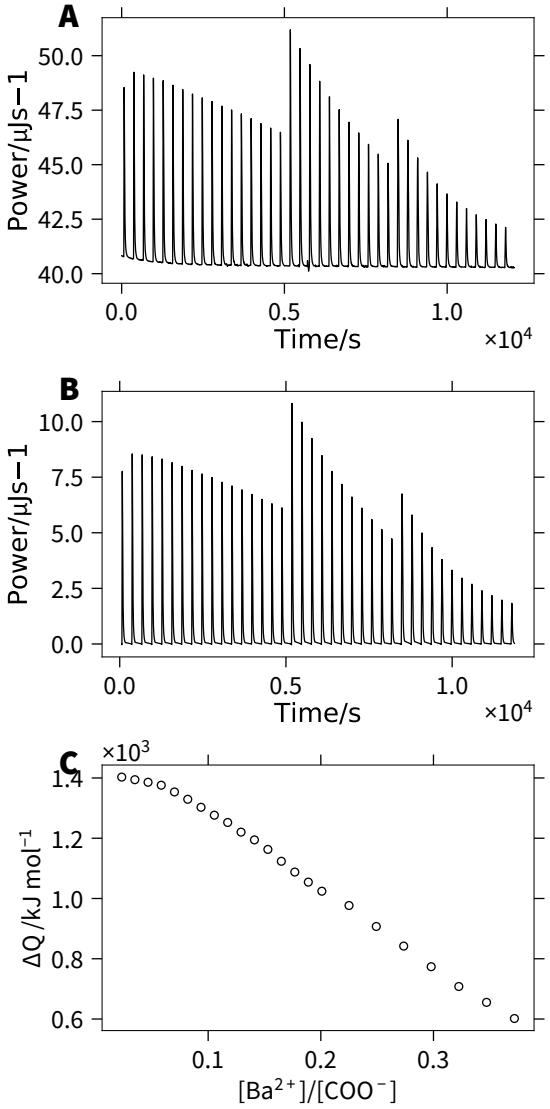


Figure 6.9: Isothermal titration calorimetry. **A** Uncorrected heat flow as a function of time of a typical ITC experiment. **B** Baseline corrected heat flow as a function of time. **C** Heat of injection as a function of the ratio Ba^{2+} to PA concentration.

6.5.2 Synthesis of PA, PSS and PSS-b-PA

In total four polymer samples were investigated in this work: a PA homopolymer, a PSS homopolymer and two block copolymers. One block copolymer carried a completely deuterated PA block ($d_{3P}A_{1190}PSS_{70}$), whereas the other one was the corresponding completely hydrogenated equivalent ($h_{3P}A_{1190}PSS_{70}$). All polymers were synthesized using the RAFT technique and the RAFT agent 2-(2-carboxyethylsulfanylthiocarbonylsulfanyl)propionic acid.

Water was purified using a Milli-Q-system. Acrylic acid (Sigma Aldrich, France, >99 %), sodium styrene sulfonate (Sigma Aldrich, France), 4,4-azobis(4-cyanovaleric acid) (Sigma Aldrich, France, >98 %), 2-(2-carboxyethylsulfanylthiocarbonylsulfanyl)propionic acid (Sigma Aldrich, France) and NaOH were used as received.

For the PA homopolymer 20 g of acrylic acid, 14.1 mg of 2-(2-carboxyethylsulfanylthiocarbonylsulfanyl)propionic acid and 3.9 mg of 4,4-azobis(4-cyanovaleric acid) were dissolved in 100 mL of deionized water at room temperature. Next, the mixture was degassed by flushing with argon for 30 min. The polymerization was performed for 24 h at 70 °C under argon atmosphere.

The PSS homopolymer was synthesized by dissolving 20 g of sodium styrene sulfonate, 1.8 mg of 4,4-azobis(4-cyanovaleric acid) and 16.5 mg of 2-(2-carboxyethylsulfanylthiocarbonylsulfanyl)propionic acid in 200 mL deionized water. The mixture was degassed with argon for 30 min and polymerized for 10 h at 70 °C under argon atmosphere.

The synthesis of the two block copolymers $h_{3P}A_{1190}PSS_{70}$ and $d_{3P}A_{1190}PSS_{70}$ was previously described in Reference [20].

After the reaction the product was allowed to cool to room temperature. For the PA homopolymer and the PA-*b*-PSS block copolymer the pH of the solution was adjusted to 9. Next, the product was dialyzed (regenerated cellulose, Spectra/Por 6 MWCO = 1 kDa) against a large excess of water for 3 days with an exchange of water every 12 h. Finally, the polymers were freeze dried.

Figure 6.10, 6.11, 6.12 and 6.13 show the results from static and dynamic light scattering of the polymers in 100 mmol L^{-1} NaCl at various concentrations. Table 6.6 summarizes the results from the SLS and DLS data analysis.

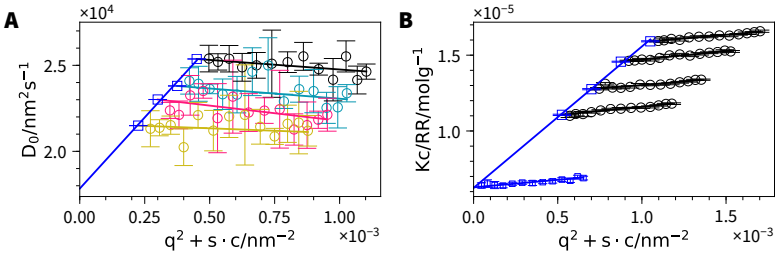


Figure 6.10: **A** Dynamic Zimm plot of h_3-$PA_{1190}PSS_{70}$ in 100 mmol L^{-1} NaCl. **B** Zimm plot of h_3-$PA_{1190}PSS_{70}$ in 100 mmol L^{-1} NaCl.

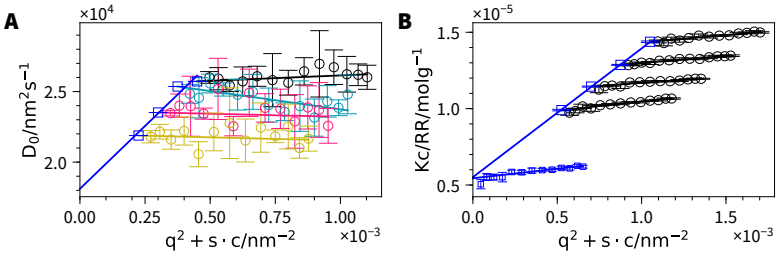


Figure 6.11: **A** Dynamic Zimm plot of d_3-$PA_{1190}PSS_{70}$ in 100 mmol L^{-1} NaCl. **B** Zimm plot of d_3-$PA_{1190}PSS_{70}$ in 100 mmol L^{-1} NaCl.

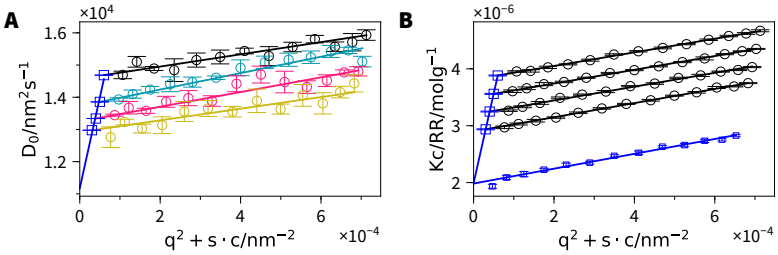


Figure 6.12: **A** Dynamic Zimm plot of PSS in 100 mmol L^{-1} NaCl. **B** Zimm plot of PSS in 100 mmol L^{-1} NaCl.

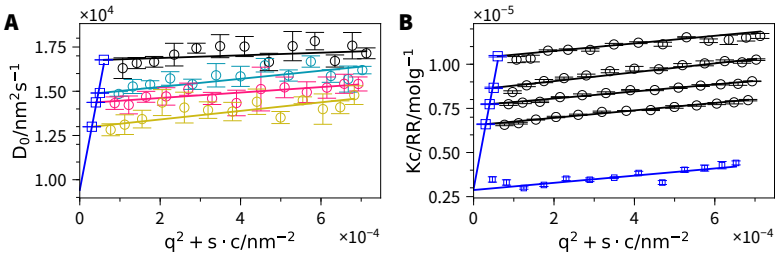


Figure 6.13: **A** Dynamic Zimm plot of PA in 100 mmol L^{-1} NaCl. **B** Zimm plot of PA in 100 mmol L^{-1} NaCl.

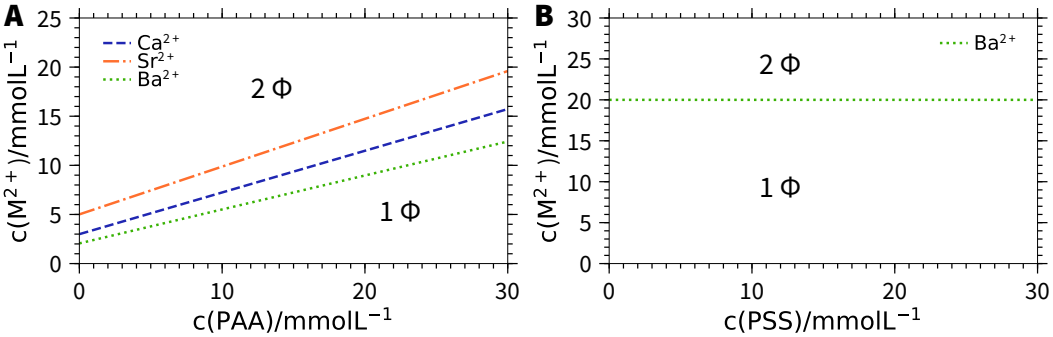


Figure 6.14: Phase diagram of PA (**A**) and PSS (**B**) in the presence of Ca^{2+}, Sr^{2+} and Ba^{2+} in 100 mmol L^{-1} NaCl at 25 °C.

6.5.3 Phase behavior of PA and PSS in the presence of earth alkaline metal cations

The phase behavior of PA and PSS homopolymers in the presence of earth alkaline metal cations was previously investigated.[24,25,29] Figure 6.14 shows the phase diagrams of PA and PSS in the presence of earth alkaline metal cations in 100 mmol L^{-1} of NaCl at 25 °C. 1Φ denotes the one phase regime, whereas 2Φ indicates the region where phase separation takes place.

For PA the critical M^{2+} concentration $[M^{2+}]_c$ where phase separation takes place follows

$$[M^{2+}]_c = r_0 + m[PE] \tag{6.35}$$

where [PE] is the concentration of polyelectrolyte monomer unit, m the stochiometry of binding and r_0 the minimum amount of M^{2+} necessary to precipitate the polymer at infinite dilution. Table 6.7 shows the values for r_0 and m.

The phase behavior of PSS with earth alkaline cations shows no precipitation with Ca^{2+} and Sr^{2+}. For Ba^{2+} we find a horizontal phase boundary corresponding to a value of $m = 0$ in equation 6.35.

6.5.4 Phase behavior of PA-b-PSS in the presence of earth alkaline cations

Figure 6.15 shows the phase diagrams of PA-*b*-PSS in 100 mmol L^{-1} NaCl at 25 °C in the presence of Ca^{2+}, Sr^{2+} and Ba^{2+}. In general, the phase diagram can be divided in three parts: At low concentrations of M^{2+} the block copolymer is present as individual chain in solution. Upon increase of the M^{2+} concentration block copolymer micelles

Table 6.6: Results from the light scattering analysis of the used polymers in aqueous 100 mmol L^{-1} NaCl solution.

Polymer	R_h/nm	R_g/nm	M_w/kg mol^{-1}	$A_2/10^4 cm^3$ mol g^{-1}	$k_D/cm^3\,g^{-1}$	$\frac{R_g}{R_h}$	$\frac{dn}{dc}/cm^3\,g^{-1}$
d_3-$PA_{1190}PSS_{70}$	13.6 ± 0.5	24.0 ± 2.4	181.4 ± 3.2	29.5 ± 0.4	284 ± 41	1.8 ± 0.2	0.157
h_3-$PA_{1190}PSS_{70}$	13.9 ± 0.6	23.5 ± 1.9	160.0 ± 2.1	32.6 ± 0.3	275 ± 48	1.7 ± 0.2	0.172
PA	26.2 ± 1.4	43.0 ± 1.8	340.5 ± 6.7	30.2 ± 0.4	601 ± 84	1.6 ± 0.2	0.171
PSS	22.5 ± 0.3	44.0 ± 1.0	502.5 ± 4.3	7.9 ± 0.1	267 ± 16	2.0 ± 0.2	0.170

Table 6.7: Details on the phase boundaries of PA and PSS in the presence of Ca^{2+}, Sr^{2+} and Ba^{2+} in 100 mmol L^{-1} NaCl. The phase diagrams are shown in Figure 6.14.

Polymer	M^{2+}	m	r_0
PA	Ca^{2+}	0.424	2.995
PA	Sr^{2+}	0.486	5.009
PA	Ba^{2+}	0.346	2.056
PSS	Ca^{2+}	—	—
PSS	Sr^{2+}	—	—
PSS	Ba^{2+}	0	20.0

are formed. Upon further increase of the M^{2+} concentration these micelles eventually precipitate from solution. The precipitation shows a clear difference between Ca^{2+}/Sr^{2+} and Ba^{2+}. For Ca^{2+}/Sr^{2+} this precipitation takes place at around 50 mmol L^{-1} of M^{2+}, whereas for Ba^{2+} it already occurs at around 20 mmol L^{-1}. We attribute this to the specific interaction of Ba^{2+} with the PSS corona. For Ca^{2+} and Sr^{2+} the multivalent cations simply screen the PSS chains in the corona and eventually lead to a destabilization of the block copolymer micelle. However, for Ba^{2+} there is a specific interaction with the corona and we observe a precipitation threshold which is identical to the one of the PSS homopolymer with Ba^{2+}.

6.5.5 Molar volumes of PA and PSS as a function of temperature

In order to be able to calculate the correct scattering length density of the polyelectrolyte blocks we performed temperature dependent density measurement. For this we prepared PSS as well as PA solutions at various concentrations in H_2O. The polymer concentrations were ranging from 1 g L^{-1} to 20 g L^{-1} . The densities at different concentrations were measured in a range from 5 °C to 65 °C. The apparent molar volume at a given concentration $V_m(c)$ can consequently be calculated as

$$V_m(c) = \frac{M}{d_0} - 10^3 \frac{d - d_0}{d_0 c} \tag{6.36}$$

with M being the molar mass of the monomer repeating unit, d_0 the density of the solvent, and d the density measured at a certain concentration c. $V_m(c)$ is finally extrapolated to $c = 0$ to obtain V_m.

Figure 6.16 shows V_m as a function of temperature for the sodium salts of PA and PSS in H_2O. The molar volume shows a continous increase with increasing temperature for both polyelectrolytes. This has previously been shown for PA in a much narrower

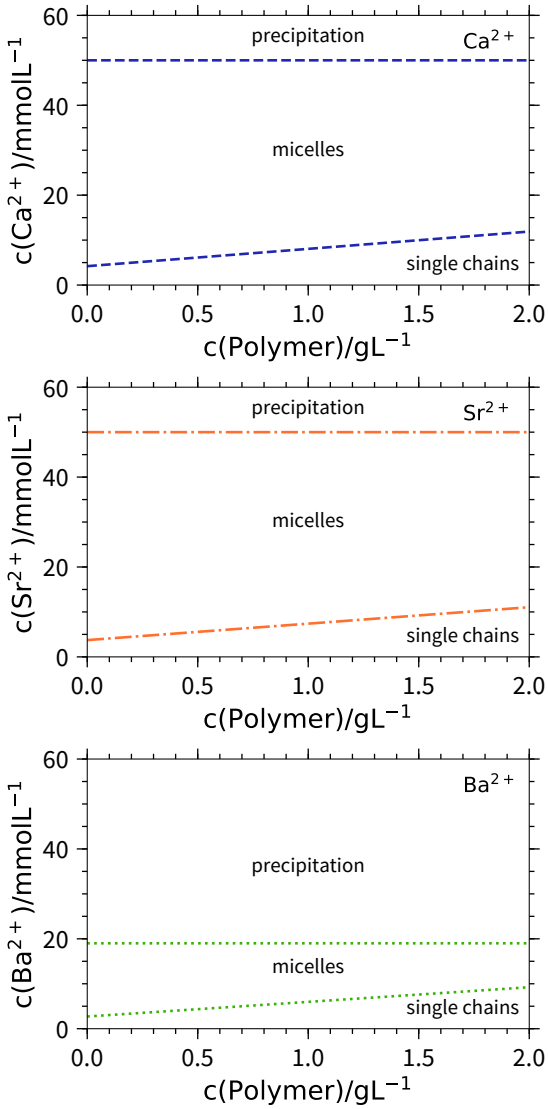


Figure 6.15: Phase diagram of PA-*b*-PSS in the presence of Ca^{2+} (**A**), Sr^{2+} (**B**) and Ba^{2+} (**C**) in 100 mmol L^{-1} NaCl at 25 °C.

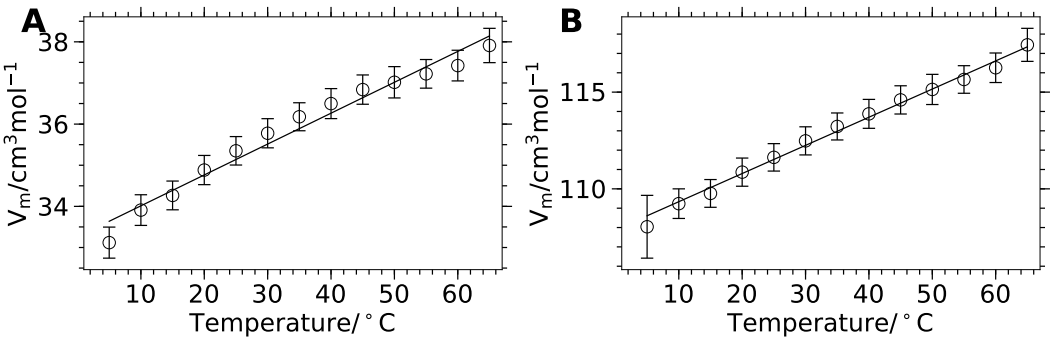


Figure 6.16: Molar volumes of PA (**A**) and PSS (**B**) in H_2O as a function of temperature. The solid line represents a linear fit of the data.

temperature range. It can be attributed to the fact, that hydration becomes more unstable with increasing temperature. This leads to an increase of the measured molar volume since the electrostriction of water is less strong and therefore the hydration layer gets less dense.[65] Table 6.8 lists the measured molar volumes as a function of temperature.

Table 6.8: Molar volumes for NaPA and NaPSS as a function of temperature.

	V_m /cm^3 mol^{-1}	
Temperature /°C	NaPA	NaPSS
5.0	33.12 ± 0.38	108.04 ± 1.62
10.0	33.91 ± 0.37	109.23 ± 0.77
15.0	34.27 ± 0.35	109.76 ± 0.72
20.0	34.88 ± 0.36	110.86 ± 0.73
25.0	35.35 ± 0.35	111.63 ± 0.71
30.0	35.78 ± 0.35	112.48 ± 0.73
35.0	36.18 ± 0.34	113.22 ± 0.70
40.0	36.50 ± 0.36	113.88 ± 0.75
45.0	36.84 ± 0.36	114.60 ± 0.73
50.0	37.02 ± 0.38	115.14 ± 0.78
55.0	37.22 ± 0.35	115.65 ± 0.71
60.0	37.42 ± 0.37	116.26 ± 0.76
65.0	37.91 ± 0.42	117.44 ± 0.85

6.5.6 Scattering length

Table 6.9 shows scattering length b for neutrons and X-rays (at 12.46 keV and if relevant at 16.00 keV) used for the analysis of the data. The scattering length densities ρ are

calculated by

$$\rho = \frac{b}{V_m} N_A \tag{6.37}$$

with the corresponding molar volume V_m and the Avogadro constant N_A. The molar volumes of the polyelectrolytes for various temperatures are listed in Table 6.8. The molar volume of H_2O and D_2O at different temperatures were taken from the densities reported in Reference [66].

The molar volume of PA^- was assumed to be identical to the one measured for NaPA. It has been shown, that for polyelectrolytes the molar volume is given by

$$V_m = V_{m,PA^-} + V_{m,Na^+} + V_{m,electrostriction} \tag{6.38}$$

At 25 °C the two terms V_{m,Na^+} ($-6.7\,cm^3\,mol^{-1}$)[67] and $V_{m,electrostriction}$ ($6.3\,cm^3\,mol^{-1}$)[68] cancel out each other. Based on this, we approximate, that the molar volume of PA^- and NaPA are identical and we use the measured value V_m of NaPA for the calculation of the scattering length density of PA^-.

Table 6.9: Neutron and X-ray scattering length of the used compounds.

Compound	$b_{neutrons}$ / fm	$b_{X\text{-rays, }12.46\,keV}$ / fm	$b_{X\text{-rays, }16.00\,keV}$ / fm
PA^-	20.327	107.259	107.190
NaPSS	50.881	299.825	299.430
D_2O	19.145	28.242	28.217
H_2O	−1.675	28.242	28.217
Ca^{2+}	4.7	51.652	
Sr^{2+}	7.02		89.018
Ba^{2+}	5.07	152.250	

6.5.7 Overview of the fit parameters from SAXS

Table 6.11 shows the fit parameters from the SAXS data including error bar estimation. Table 6.10 shows the obtained values of $\chi^2_{red} = \frac{\chi^2}{N-M}$, where N is the number of data points and M the number of free parameters for the fits. Note that the χ^2_{red} values for the SAXS fits are considerably larger than 1.0. This arises from the difficult estimations of errors. The available errors only take into account the statistical error, which is relatively low due to the high counting statistics at modern synchrotron. However, systematic errors are not taken into account, which leads to an underestimation of the errors and to χ^2_{red} values considerably larger than unity.

Table 6.10: χ^2_{red} for the SANS and SAXS fits shown in the main manuscript (Figure 6.2 and 6.7) and in the Supporting Information (Figure 6.19).

Sample	SANS/SAXS	Figure	χ^2_{red}
h_3-$PA_{1190}PSS_{70}/Ca^{2+}/25\,°C$	SAXS	Figure 6.2A	47.3[a]
h_3-$PA_{1190}PSS_{70}/Sr^{2+}/25\,°C$	SAXS	Figure 6.2B	503.9[a]
h_3-$PA_{1190}PSS_{70}/Ba^{2+}/25\,°C$	SAXS	Figure 6.2C	63.3[a]
h_3-$PA_{1190}PSS_{70}/Ca^{2+}/6\,°C$	SANS	Figure 6.19A	0.4
h_3-$PA_{1190}PSS_{70}/Ca^{2+}/65\,°C$	SANS	Figure 6.19A	1.4
h_3-$PA_{1190}PSS_{70}/Sr^{2+}/6\,°C$	SANS	Figure 6.19B	5.7
h_3-$PA_{1190}PSS_{70}/Sr^{2+}/30\,°C$	SANS	Figure 6.19B	0.4
h_3-$PA_{1190}PSS_{70}/Sr^{2+}/65\,°C$	SANS	Figure 6.19B	0.8
h_3-$PA_{1190}PSS_{70}/Ba^{2+}/6\,°C$	SANS	Figure 6.19C	1.6
h_3-$PA_{1190}PSS_{70}/Ba^{2+}/65\,°C$	SANS	Figure 6.19C	1.2
d_3-$PA_{1190}PSS_{70}/Ca^{2+}/8\,°C$	SANS	Figure 6.7A	1.1
d_3-$PA_{1190}PSS_{70}/Ca^{2+}/65\,°C$	SANS	Figure 6.7A	38.0
d_3-$PA_{1190}PSS_{70}/Sr^{2+}/8\,°C$	SANS	Figure 6.7B	4.8
d_3-$PA_{1190}PSS_{70}/Sr^{2+}/65\,°C$	SANS	Figure 6.7B	21.2
d_3-$PA_{1190}PSS_{70}/Sr^{2+}/25\,°C$	SANS	Figure6.77B	1.3
d_3-$PA_{1190}PSS_{70}/Ba^{2+}/8\,°C$	SANS	Figure 6.7C	5.6
d_3-$PA_{1190}PSS_{70}/Ba^{2+}/65\,°C$	SANS	Figure 6.7C	1.1

[a] Obtained from a global fit of all samples shown in the corresponding Figure.

6.5.8 Fit of the Ba^{2+}-SAXS data with an inverse model

Figure 6.17 shows the SAXS data of the micelles in the presence of Ba^{2+} at 25 °C together with the model of a polydisperse block copolymer with Ba^{2+}/PSS in the core and PA in the corona. Table 6.12 shows the obtained fit parameters. The model does not correctly describe the mid q part of the data. Furthermore, the obtained values of the corona

Table 6.11: Structural parameters from the form factor fits of the SAXS data shown in Figure 6.2 in the main manuscript.

	Ca^{2+}		Sr^{2+}		Ba^{2+}	
$c(M^{2+})$/ mM	6	8	5.5	7.5	5	10
$\phi_{micelles}$	0.0	0.79 ± 0.02	0.0	0.73 ± 0.1	0.0	1.0
$R_{g,free}$/nm	8.2 ± 0.1	5.2 ± 0.1	6.3 ± 0.1	6.2 ± 0.1	6.7 ± 0.1	—
ν_{free}	0.49 ± 0.01	0.36 ± 0.01	0.44 ± 0.01	0.53 ± 0.01	0.38 ± 0.01	—
R_{core}/nm	—	22.8 ± 1.3	—	25.6 ± 0.05	—	21.6 ± 0.1
$\frac{\sigma_{R_{core}}}{R_{core}}$	—	0.109 ± 0.002^a	—	0.104 ± 0.001^a	—	0.113 ± 0.001
$R_{g,corona}$/nm	—	0.7 ± 0.1	—	2.3 ± 1.3	—	1.0 ± 0.1
s /nm	—	4.5 ± 0.1	—	4.7 ± 0.1	—	5.9 ± 0.1
ν_{corona}	—	0.0 ± 0.1^a	—	0.0 ± 0.1^a	—	0.0 ± 0.1
$f_{solvent}$	—	0.83 ± 0.02^a	—	0.60 ± 0.01^a	—	0.90 ± 0.01

[a] Global fitting parameter for the corresponding M^{2+} dataset.

Table 6.12: Structural parameters from the form factor fits of the SAXS data shown in Figure 6.17 measured at 25 °C.

	Ba^{2+}
$c(M^{2+})/mM$	10
R_{core}	9.8 ± 0.3
$\frac{\sigma_{R_{core}}}{R_{core}}/nm$	0.15 ± 0.03
$R_{g,corona}/nm$	28.5 ± 0.9
s/nm	7.3 ± 0.1
ν_{corona}	0.27 ± 0.98
$f_{solvent}$	0.95 ± 0.01

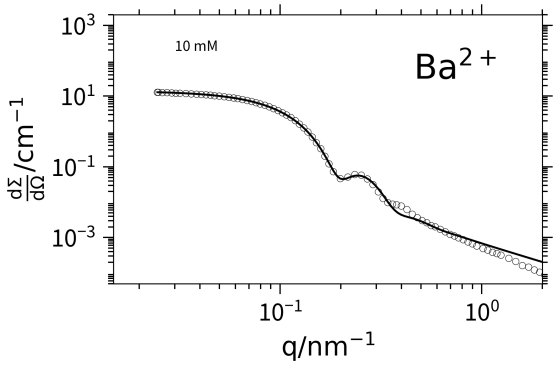


Figure 6.17: SAXS profile of h_3-$PA_{1190}PSS_{70}$ ($c = 1\,g\,L^{-1}$) in the presence of $10\,mmol\,L^{-1}$ Ba^{2+} measured at 25 °C. The solid line represents a fit to the model of a polydisperse block copolymer micelle with Ba^{2+}/PSS in the core and PA in the corona. Table 6.12 summarizes the results of the fit.

thickness s and the radius of gyration of the polymer chains in the corona $R_{g,corona}$ adopt unreasonable values.

6.5.9 Overview of the fit parameters from SANS

Table 6.13 shows the fit parameters with error bars from the fits of the SANS data of d_3-$PA_{1190}PSS_{70}$, which are presentend in Figure 6.7 in the main manuscript. Table 6.10 summarizes the obtained χ^2_{red} values.

In addition to the experiments performed with the polymer containing a deuterated PA block we also performed SANS experiments with the fully hydrogenated polymer h_3-$PA_{1190}PSS_{70}$. Figure 6.18 and 6.19 show the results from temperature dependent light scattering as well as SANS. Table 6.14 summarizes the obtained fit parameters. Table 6.10 lists the obtained values of χ^2_{red}.

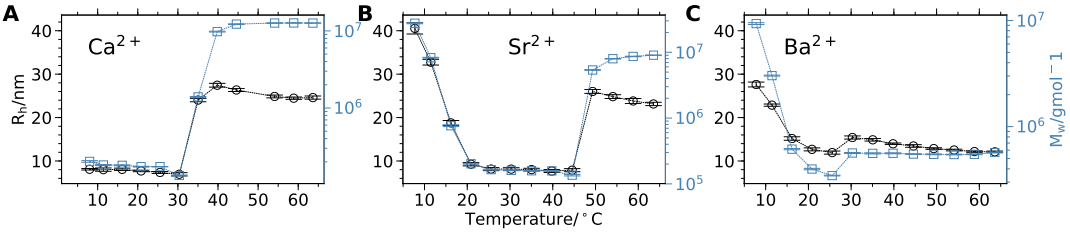


Figure 6.18: Hydrodynamic radius R_h and apparent molecular weight $M_{w,app}$ of h_3-$PA_{1190}PSS_{70}$ in the presence of Ca^{2+} (A), Sr^{2+} (B) and Ba^{2+} (C) as a function of temperature. The solvent is composed of 100.0 % D_2O. The lines are guide to the eyes. The polymer concentration is 1 g L^{-1}. The concentration of M^{2+} is: Ca^{2+} 6.1 mmol L^{-1}, Sr^{2+} 5.4 mmol L^{-1}, Ba^{2+} 4.65 mmol L^{-1}. The solvent is composed of 100.0 % D_2O.

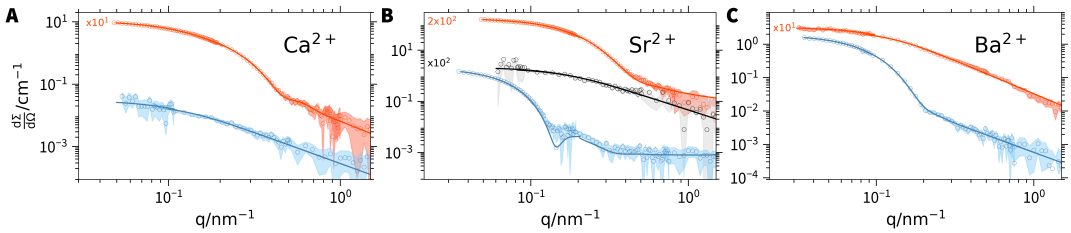


Figure 6.19: SANS profiles of h_3-$PA_{1190}PSS_{70}$ in the presence of Ca^{2+}, Sr^{2+} and Ba^{2+} at 6 °C (blue), 25 °C (black) and 65 °C (red). The solvent is composed of 100.0 % D_2O. The samples are identical to the ones in Figure 6.18. The solid lines represent fits to the model of a Gaussian chain or block copolymer micelles. Table 6.14 summarizes the resulting fit parameters.

The SANS curves of d_3-$PA_{1190}PSS_{70}$ in the presence of Sr^{2+} and Ba^{2+} at 8 °C can not be described by using a model consisting of a PA/M^{2+} core and a PSS. Figure 6.20 shows the best fits obtained with such a model. It is obvious from the fit, that a homogeneous core composed of PA/M^{2+} results in a slope close to −4 at high q, whereas the SANS profiles show a considerably flatter slope.

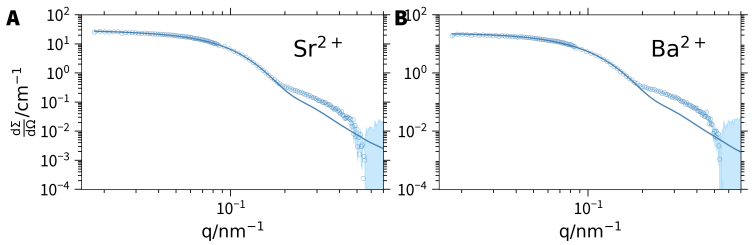


Figure 6.20: SANS profiles of d_3-$PA_{1190}PSS_{70}$ in the presence of Sr^{2+} and Ba^{2+} at 8 °C. The solvent is composed of 25.2 % D_2O. The solid lines represent fits to the model of a block copolymer micelles with a PA/M^{2+} core and a PSS corona.

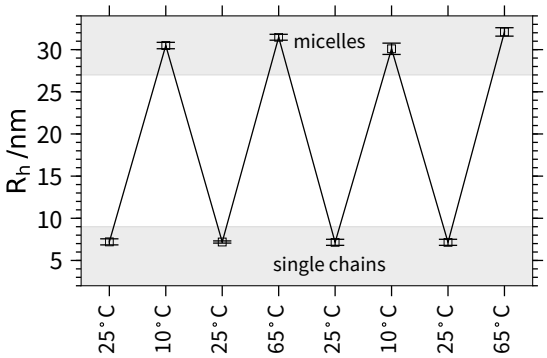


Figure 6.21: Hydrodynamic radius R_h of d_3-$PA_{1190}PSS_{70}$ in the presence of Sr^{2+} during several heating and cooling cycles.

6.5.10 Reversibility of micelle formation induced by temperature variation

In order to demonstrate that the temperature induced micelle formation is a reversible process and the samples are in thermodynamic equilibrium Figure 6.21 shows the hydrodynamic radius R_h of d_3-$PA_{1190}PSS_{70}$ in the presence of Sr^{2+} during several heating and cooling cycles. At 25 °C the polymer is present as single chains. Temperature decrease to 10 °C results in the formation of micelles with a core composed of PSS/Sr^{2+}. A temperature increase to 65 °C also results in micellization, however this time micelles contain a PA/Sr^{2+} core. Upon return to 25 °C after each cycle the polymer returns to the state of single chains.

Table 6.13: Structural parameters from the form factor fits of the SANS data shown in Figure 6.7 for d_3-$PAA_{1190}PSS_{70}$ in a solvent containing 25.2 % D_2O.

	Ca^{2+}		Sr^{2+}			Ba^{2+}	
Temperature	8 °C	65 °C	8 °C	25 °C	65 °C	8 °C	65 °C
R_h [a]	8.0 ± 0.1	30.7 ± 0.1	30.5 ± 0.1	7.2 ± 0.1	31.5 ± 0.1	29.8 ± 0.1	6.6 ± 0.1
R_g [b]	6.3 ± 0.6	16.7 ± 1.1	21.6 ± 3.3	6.5 ± 0.4	19.8 ± 4.3	20.7 ± 5.6	4.7 ± 0.5
$R_{g,free}$	6.9 ± 0.1	—	—	6.7 ± 0.1	—	—	5.0 ± 0.1
ν	0.40 ± 0.01			0.37 ± 0.01			0.26 ± 0.01
Micelle core	—	PA/Ca^{2+}	PSS/Sr^{2+}	—	PA/Sr^{2+}	PSS/Ba^{2+}	—
N_{agg}	—	145 ± 21	38 ± 12	—	81 ± 10	36 ± 12	—
R_{core}	—	17.6 ± 1.5	7.0 ± 1.0	—	18.3 ± 1.2	11.6 ± 0.6	—
$\frac{\sigma_{R_{core}}}{R_{core}}$	—	0.189 ± 0.001	0.097 ± 0.032	—	0.173 ± 0.001	0.02 ± 0.05	—
$R_{g,corona}$	—	1.0 ± 1.0	9.8 ± 0.4	—	1.2 ± 1.0	7.4 ± 0.4	—
s	—	11.7 ± 0.7	11.0 ± 0.5	—	17.5 ± 1.2	10.3 ± 0.2	—
ν_{corona}	—	0.0 ± 1.1	0.9 ± 0.8	—	0.0 ± 1.8	0.0 ± 0.2	—
$f_{solvent}$	—	0.650 ± 0.123	0.669 ± 0.093	—	0.705 ± 0.059	0.862 ± 0.063	—

[a] Obtained from DLS. [b] Obtained from Guinier analysis of the SANS data.

Table 6.14: Structural parameters from the form factor fits of the SANS data shown in Figure 6.19 for h_3-$PAA_{1190}PSS_{70}$ in a solvent containing 100.0 %.

	Ca^{2+}		Sr^{2+}			Ba^{2+}	
Temperature	6 °C	65 °C	6 °C	30 °C	65 °C	6 °C	65 °C
R_h [a]	8.1 ± 0.04	24.6 ± 0.07	40.5 ± 2.6	8.1 ± 0.07	23.1 ± 0.08	27.6 ± 0.1	12.1 ± 0.04
R_g [b]	13.5 ± 2.0	15.8 ± 0.6	32.6 ± 1.0	10.6 ± 1.8	14.3 ± 1.5	22.6 ± 1.5	13.8 ± 0.8
ρ	1.67 ± 0.25	0.64 ± 0.03	0.80 ± 0.03	1.30 ± 0.24	0.62 ± 0.07	0.80 ± 0.06	1.14 ± 0.07
$R_{g,free}$	14.4 ± 1.1	—	—	9.7 ± 0.7	—	2.7 ± 0.5	13.7 ± 0.1
N_{agg}	—	61 ± 1	133 ± 53	—	49 ± 5	101 ± 12	—
R_{core}	—	10.0 ± 0.5	11.8 ± 3.6	—	8.0 ± 0.5	23.2 ± 2.7	—
$\frac{\sigma_{R_{core}}}{R_{core}}$	—	0.15 ± 0.01	0.01 ± 0.03	—	0.17 ± 0.03	0.01 ± 0.03	—
$R_{g,corona}$	—	1.9 ± 0.9	10.0 ± 1.2	—	2.0 ± 1.1	2.7 ± 1.2	—
s	—	8.5 ± 0.1	12.9 ± 0.7	—	4.0 ± 0.7	5.8 ± 0.9	—
ν_{corona}	—	0.0 ± 0.02	0.0 ± 0.4	—	0.0 ± 0.02	0.0 ± 0.01	—
$f_{solvent}$	—	0.015 ± 0.072	0.859 ± 0.057	—	0.022 ± 0.029	0.871 ± 0.004	—

[a] Obtained from DLS. [b] Obtained from Guinier analysis of the SANS data.

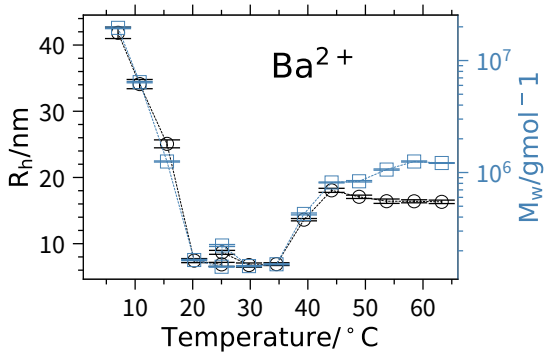


Figure 6.22: Hydrodynamic radius R_h and apparent molecular weight $M_{w,app}$ of d_3-$PA_{1190}PSS_{70}$ in the presence of Ba^{2+}. The lines are guides to the eye. The polymer concentration is 1 g L^{-1} and the concentration of Ba^{2+} is 4.9 mmol L^{-1}.

6.5.11 Micelle inversion in the presence of Ba^{2+}

Figure 6.22 shows the hydrodynamic radius R_h and the apparent molecular weight $M_{w,app}$ for a sample of d_3-$PA_{1190}PSS_{70}$ in the presence of Ba^{2+} as a function of temperature. Similarly to the sample in the presence of Sr^{2+}, micelle formation is observed at low and high temperatures with an intermediate region of single chains. However the molecular weight and R_h at high temperatures are considerably smaller than for Sr^{2+}. This can be attributed to the smaller entropy of binding ΔS of Ba^{2+} to PA compared to the system PA/Sr^{2+}. Consequently, the micelle formation at high temperatures is less pronounced.

6.6 References

1. Zhang, L.; Eisenberg, A. *Science (80-.).* **1995**, *268*, 1728–1731, DOI: 10.1126/science.268.5218.1728.

2. Massey, J.; Nicole Power, K.; Manners, I.; Winnik, M. A. *J. Am. Chem. Soc.* **1998**, *120*, 9533–9540, DOI: 10.1021/ja981803d.

3. Du, J. *Adv. Hierarchical Nanostructured Mater.* **2014**, *9783527333*, 177–192, DOI: 10.1002/9783527664948.ch5.

4. Schilli, C. M.; Zhang, M.; Rizzardo, E.; Thang, S. H.; Chong,) Y. K.; Edwards, K.; Karlsson, G.; Müller, A. H. E. *Macromolecules* **2004**, *37*, 7861–7866, DOI: 10.1021/ma035838w.

5. Lee, A. S.; Gast, A. P.; Bütün, V.; Armes, S. P. *Macromolecules* **1999**, *32*, 4302–4310, DOI: 10.1021/ma9818650.
6. Zhou, S.; Chu, B. *Macromolecules* **1998**, *31*, 5300–5308, DOI: 10.1021/ma980262+.
7. Zhao, Y. *Macromolecules* **2012**, *45*, 3647–3657, DOI: 10.1021/ma300094t.
8. Ranka, M.; Katepalli, H.; Blankschtein, D.; Hatton, T. A. *Langmuir* **2017**, *33*, 13326–13331, DOI: 10.1021/acs.langmuir.7b03008.
9. Dompé, M.; Cedano-Serrano, F. J.; Heckert, O.; van den Heuvel, N.; van der Gucht, J.; Tran, Y.; Hourdet, D.; Creton, C.; Kamperman, M. *Adv. Mater.* **2019**, *31*, DOI: 10.1002/adma.201808179.
10. Kotsuchibashi, Y.; Ebara, M.; Aoyagi, T.; Narain, R. *Polymers (Basel).* **2016**, *8*, DOI: 10.3390/polym8110380.
11. Papadakis, C. M.; Müller-Buschbaum, P.; Laschewsky, A. *Langmuir* **2019**, *35*, 9660–9676, DOI: 10.1021/acs.langmuir.9b01444.
12. Bütün, V.; Liu, S.; Weaver, J. V. M.; Bories-Azeau, X.; Cai, Y.; Armes, S. P. *React. Funct. Polym.* **2006**, *66*, 157–165, DOI: 10.1016/j.reactfunctpolym.2005.07.021.
13. Feng, A.; Zhan, C.; Yan, Q.; Liu, B.; Yuan, J. *Chem. Commun. (Cambridge, U. K.)* **2014**, *50*, 8958–8961, DOI: 10.1039/C4CC03156C.
14. Wang, D.; Wu, T.; Wan, X.; Wang, X.; Liu, S. *Langmuir* **2007**, *23*, 11866–11874, DOI: 10.1021/la702029a.
15. Vasantha, V. A.; Jana, S.; Lee, S. S.-C.; Lim, C.-S.; Teo, S. L.-M.; Parthiban, A.; Vancso, J. G. *Polym. Chem.* **2015**, *6*, 599–606, DOI: 10.1039/C4PY01113A.
16. Guragain, S.; Bastakoti, B. P.; Nakashima, K. *J. Colloid Interface Sci.* **2010**, *350*, 63–68, DOI: 10.1016/j.jcis.2010.06.007.
17. Vishnevetskaya, N. S.; Hildebrand, V.; Niebuur, B.-J.; Grillo, I.; Filippov, S. K.; Laschewsky, A.; Müller-Buschbaum, P.; Papadakis, C. M. *Macromolecules* **2017**, *50*, 3985–3999, DOI: 10.1021/acs.macromol.7b00356.
18. Vishnevetskaya, N. S.; Hildebrand, V.; Dyakonova, M. A.; Niebuur, B. J.; Kyriakos, K.; Raftopoulos, K. N.; Di, Z.; Müller-Buschbaum, P.; Laschewsky, A.; Papadakis, C. M. *Macromolecules* **2018**, *51*, 2604–2614, DOI: 10.1021/acs.macromol.8b00096.
19. Liu, S.; Billingham, N. C.; Armes, S. P. *Angew. Chemie - Int. Ed.* **2001**, *40*, 2328–2331, DOI: 10.1002/1521-3773(20010618)40:12⟨2328::AID-ANIE2328⟩3.0.CO;2-M.

20. Carl, N.; Prévost, S.; Schweins, R.; Huber, K. *Soft Matter* **2019**, *15*, 8266–8271, DOI: 10.1039/C9SM01138B.

21. Yap, H. P.; Hao, X.; Tjipto, E.; Gudipati, C.; Quinn, J. F.; Davis, T. P.; Barner-Kowollik, C.; Stenzel, M. H.; Caruso, F. *Langmuir* **2008**, *24*, 8981–8990, DOI: 10.1021/la8011074.

22. Förster, S.; Hermsdorf, N.; Böttcher, C.; Lindner, P. *Macromolecules* **2002**, *35*, 4096–4105, DOI: 10.1021/ma011565y.

23. Van der Maarel, J. R. C.; Groenewegen, W.; Egelhaaf, S. U.; Lapp, A. *Langmuir* **2000**, *16*, 7510–7519, DOI: 10.1021/la000299z.

24. Hansch, M.; Hämisch, B.; Schweins, R.; Prévost, S.; Huber, K. *J. Chem. Phys.* **2018**, *148*, 014901, DOI: 10.1063/1.5006618.

25. Schweins, R.; Goerigk, G.; Huber, K. *Eur. Phys. J. E* **2006**, *21*, 99–110, DOI: 10.1140/epje/i2006-10047-7.

26. Lages, S.; Schweins, R.; Huber, K. *J. Phys. Chem. B* **2007**, *111*, 10431–10437, DOI: 10.1021/jp068258k.

27. Huber, K. *J. Phys. Chem.* **1993**, *97*, 9825–9830, DOI: 10.1021/j100140a046.

28. Sinn, C. G.; Dimova, R.; Antonietti, M. *Macromolecules* **2004**, *37*, 3444–3450, DOI: 10.1021/ma030550s.

29. Hansch, M.; Kaub, H. P.; Deck, S.; Carl, N.; Huber, K. *J. Chem. Phys.* **2018**, *148*, 114906, DOI: 10.1063/1.5019877.

30. Prabhu, V.; Muthukumar, M.; Wignall, G.; Melnichenko, Y. *Polymer* **2001**, *42*, 8935–8946, DOI: 10.1016/S0032-3861(01)00382-2.

31. Prabhu, V. M.; Muthukumar, M.; Wignall, G. D.; Melnichenko, Y. B. *J. Chem. Phys.* **2003**, *119*, 4085–4098, DOI: 10.1063/1.1592496.

32. Lee, C. L.; Muthukumar, M. *J. Chem. Phys.* **2009**, *130*, 1–9, DOI: 10.1063/1.3054140.

33. Kanai, S.; Muthukumar, M. *J. Chem. Phys.* **2007**, *127*, 244908, DOI: 10.1063/1.2806299.

34. Zemb, T.; Lindner, P., *Neutrons, X-rays and light: scattering methods applied to soft condensed matter*; North-Holland: 2002.

35. Zentrum, H. M.-L. *J. large-scale Res. Facil.* **2015**, *A29*, 2–6, DOI: http://dx.doi.org/10.17815/jlsrf-1-27.

36. Houston, J. E.; Brandl, G.; Drochner, M.; Kemmerling, G.; Engels, R.; Papagiannopoulos, A.; Sarter, M.; Stadler, A.; Radulescu, A. *J. Appl. Crystallogr.* **2018**, *51*, 323–336, DOI: 10.1107/S1600576718004132.

37. Orthaber, D.; Bergmann, A.; Glatter, O. *J. Appl. Crystallogr.* **2000**, *33*, 218–225, DOI: 10.1107/S0021889899015216.

38. Boesecke, P. *J. Appl. Crystallogr.* **2007**, *40*, 423–427, DOI: 10 . 1107 / S0021889807001100.

39. Frisken, B. J. *Appl. Opt.* **2001**, *40*, 4087, DOI: 10.1364/AO.40.004087.

40. Burchard, W.; Schmidt, M.; Stockmayer, W. H. *Macromolecules* **1980**, *13*, 580–587, DOI: 10.1021/ma60075a020.

41. Cho, C. H.; Urquidi, J.; Singh, S.; Robinson, G. W. *J. Phys. Chem. B* **1999**, *103*, 1991–1994, DOI: 10.1021/jp9842953.

42. Zimm, B. H. *J. Chem. Phys.* **1948**, *16*, 1093–1099, DOI: 10.1063/1.1746738.

43. Muthig, M.; Prévost, S.; Orglmeister, R.; Gradzielski, M. *J. Appl. Crystallogr.* **2013**, *46*, 1187–1195, DOI: 10.1107/S0021889813016658.

44. Pedersen, J. S.; Posselt, D.; Mortensen, K. *J. Appl. Crystallogr.* **1990**, *23*, 321–333, DOI: 10.1107/S0021889890003946.

45. Debye, P. *J. Phys. Colloid Chem.* **1947**, *51*, 18–32, DOI: 10.1021/j150451a002.

46. Hammouda, B. *Polym. Charact.* **1993**, *106*, 87–133, DOI: 10.1007/BFb0025862.

47. Pedersen, J. S.; Gerstenberg, M. C. *Macromolecules* **1996**, *29*, 1363–1365, DOI: 10.1021/ma9512115.

48. Pedersen, J. S.; Svaneborg, C. *Curr. Opin. Colloid Interface Sci.* **2002**, *7*, 158–166, DOI: 10.1016/S1359-0294(02)00044-4.

49. Svaneborg, C.; Pedersen, J. S. *Macromolecules* **2002**, *35*, 1028–1037, DOI: 10.1021/ma011046v.

50. Pedersen, J. S.; Svaneborg, C.; Almdal, K.; Hamley, I. W.; Young, R. N. *Macromolecules* **2003**, *36*, 416–433, DOI: 10.1021/ma0204913.

51. Rayleigh, L. *Proc. Roy. Soc. London* **1911**, *A84*, 25–38.

52. Svaneborg, C.; Pedersen, J. S. *Phys. Rev. E* **2001**, *64*, 010802, DOI: 10 . 1103 / PhysRevE.64.010802.

53. Skov, J.; Schurtenberger, P.; Pedersen, J. S. *Macromolecules* **1996**, *9297*, 7602–7612, DOI: 10.1021/ma9607630.

54. Chen, W. R.; Butler, P. D.; Magid, L. J. *Langmuir* **2006**, *22*, 6539–6548, DOI: 10.1021/la0530440.

55. Sommer, C.; Pedersen, J. S.; Garamus, V. M. *Langmuir* **2005**, *21*, 2137–2149, DOI: 10.1021/la047489k.

56. Mizoue, L. S.; Tellinghuisen, J. *Anal. Biochem.* **2004**, *326*, 125–127, DOI: 10.1016/j.ab.2003.10.048.

57. Turnbull, W. B.; Daranas, A. H. *J. Am. Chem. Soc.* **2003**, *125*, 14859–14866, DOI: 10.1021/ja036166s.

58. Scheuermann, T. H.; Brautigam, C. A. *Methods* **2015**, *76*, 87–98, DOI: 10.1016/j.ymeth.2014.11.024.

59. Stuhrmann, H. B. *J. Appl. Crystallogr.* **1974**, *7*, 173–178, DOI: 10.1107/S0021889874009071.

60. Schweins, R.; Huber, K. *Eur. Phys. J. E* **2001**, *5*, 117–126, DOI: 10.1007/s101890170093.

61. Matulis, D.; Rouzina, I.; Bloomfield, V. A. *J. Mol. Biol.* **2000**, *296*, 1053–1063, DOI: 10.1006/jmbi.1999.3470.

62. Wiesman, T.; Williston, S.; Brandts, J. F. *Anal. Biochem.* **1989**, *179*, 131–137, DOI: 10.1016/0003-2697(89)90213-3.

63. Merabet, E.; Ackers, G. K. *Biochemistry* **1995**, *34*, 8554–8563, DOI: 10.1021/bi00027a005.

64. Lin, L. N.; Mason, A. B.; Woodworth, R. C.; Brandts, J. F. *Biochemistry* **1991**, *30*, 11660–11669, DOI: 10.1021/bi00114a008.

65. Ise, N.; Okubo, T. *J. Am. Chem. Soc.* **1968**, *90*, 4527–4533, DOI: 10.1021/ja01019a003.

66. Haynes, W., *CRC Handbook of Chemistry and Physics*; CRC Press: 2014.

67. Marcus, Y., *Ion Properties*; Marcel Dekker: New York, New York (USA), 1997.

68. Tondre, C.; Zana, R. *J. Phys. Chem.* **1972**, *76*, 3451–3459, DOI: 10.1021/j100667a026.

Chapter 7

Controlling self-assembly with light and temperature

Abstract

Complexes between the anionic polylelectrolyte sodium polyacrylate (PA) and an oppositely charged divalent azobenzene dye are prepared in aqueous solution. Depending on the ratio between dye and polyelectrolyte stable aggregates with a well-defined spherical shape are observed. Upon exposure of these complexes to UV light, the *trans* $\longrightarrow$ *cis* transition of the azobenzene is excited resulting in a better solubility of the dye and a dissolution of the complexes. The PA chains reassemble into well-defined aggregates when the dye is allowed to relax back into the *trans* isomer. Varying the temperature during this reformation step has a direct influence on the final size of the aggregates rendering temperature in an efficient way to easily change the size of the self-assemblies. Application of time-resolved small-angle neutron scattering (SANS) to study the structure formation reveals that the *cis* $\longrightarrow$ *trans* isomerization is the rate-limiting step followed by a nucleation and growth process.

Reprinted with permission from Carl N.; Müller W.; Schweins R.; Huber K.; Controlling self-assembly with light and temperature; *Langmuir*, **2019**, DOI: 10.1021/acs.langmuir.9b03040 Copyright 2019 American Chemical Society.

7.1 Introduction

Electrostatic interactions are widely used to assemble colloids with interesting optical,[1] magnetic[2] or mechanical[3] properties. This includes the complexation of oppositely charged nanoparticles[4] or polyelectrolytes,[5] the salt-induced aggregation of colloids into fractals,[6,7] or the self-assembly of polyelectrolytes in the presence of multivalent cations[8] or surfactants.[9,10] One common but rarely reported problem for all of these approaches is that the timescale on which self-assembly takes place is usually considerably faster than the timescale required for proper mixing via diffusion. This prevents homogeneous mixing before the self-assembly takes place and often results in undesired nonequilibrium effects[11,12] like the appearance of micrometer-sized, kinetically frozen aggregates. Most importantly, it makes reproducible sample preparation extremely challenging and may result in different conclusions drawn when the same experiment is performed by different researchers.

The most promising approach to tackle this problem is to use an external stimulus to control or trigger the self-assembly process. Temperature is a widely used noninvasive stimulus, often applied in combination with thermoresponsive polymers.[13–15] Visible light is another noninvasive stimulus, which can be applied nearly instantaneously and is easily accessible with high intensity and high monochromaticity. Light as an external stimulus has been successfully used to create molecular machines[16] and switches[17], to control chemical reactions[18] or to create novel catalysts[19] and organic light-emitting transistors.[20] The application of a stimulus by light, which however is most relevant to the present work was established by Gröhn *et al.*[21,22]

Based on the concept of electrostatic self-assembly between positively charged polyelectrolytes and oppositely charged azo dyes,[23,24] Gröhn *et al.* developed procedures to trigger or tune the self-assembly process, with both components acting as building units. In a proof of principle, poly(amidoamine) dendrimers were used in combination with the anionic dye acid yellow 38 (ay38) to generate a two-component mixture, which responds to UV light exposure and pH variations.[22] Irradiation with UV light transforms the *trans* state of the dye to its *cis* state and a drop in pH to 3.5 turns the dendrimer into a fully charged polycation. These responses gave access to a cycle, which may start with a mixture of the dye in its *cis* state and the neutral nonaggregated dendrimer. A drop in pH to 3.5 induces aggregation with a final aggregate size of 65 nm. Successive exposure to UV light induces a transformation of the dye to its trans state, which is accompanied by an increase in the size of the aggregates by more than

a factor of 5. This further growth was made possible by a partial liberation of dyestuff anions accompanied by a decrease in the electric charge of the aggregates. In the step to follow, an increase in pH to 10.5 disintegrates the aggregates. At the same time, the *cis* state as the thermodynamically more stable state of the dye is gradually reformed. Finally, a drop in pH back to 3.5 recovers the small aggregates. Noteworthy, such a switch in size was only observed at a limited regime of charge ratios $\frac{[RSO_3^-]}{[NR_4^+]}$ larger than the stoichiometric point. Based on this success, Gröhn *et al.* extended their concept to linear polyelectrolytes. With poly(diallyldimethyl-ammonium chloride) (PDADMAC) or poly(*N* methyl-4-vinylpyridinium nitrate) (QPVP) as polycation and three azo dyes (acid red 27, acid red 28 and ay38) as oppositely charged dyes, respectively.[21,25] Only in the presence of ay38, both polyelectrolytes exhibited light-induced changes. Whereas PDADMAC aggregates shrank below the stoichiometric charge ratio and increased in size above the stoichiometric point, aggregates with QPVP shrank on both sides of the stoichiometric point.[25] PDADMAC showed even a change in morphology after exposure to UV light.[21]. In all cases, the *trans* $\longrightarrow$ *cis* isomerization of ay38 was at the origin of the morphological changes but only over-stoichiometric mixtures of ay38 and PDADMAC exhibited a similar trend as observed with the dendrimers. This already indicates that the nature of the aggregates depends on the concentration ratio of the two components and on the nature of the dyestuff as well as on the polycation.

In the present work, we extend this concept to a combination of sodium polyacrylate (NaPA) as an anionic, linear polyacrylate with a divalent cationic dye 2,2'-((diazene-1,2-diylbis(4,1-phenylene))bis(oxy))bis-(*N*,*N*,*N*,*N*-trimethylethan-1-aminium) dichloride (diAzoEt), with diAzoEt being able to undergo a light-induced *trans* $\longrightarrow$ *cis* isomerization. As is shown in the present case, a combination of NaPA with diAzoEt in its trans state reveals aggregates at substoichiometric compositions. Contrary to the systems investigated by Gröhn *et al.*[21,22,25] where the aggregate size changes massively upon light irradiation, our system does fully disassemble in a reversible manner. Thermal energy recovers the *trans* state of diAzoEt, which permits the components to reassemble. Controlling and understanding the mechanism of the reassembly process allows us to tailor the size of the self-assembled structures and therefore opens a new route to well-defined complexes between oppositely charged molecules. Morphological changes in the present work were analyzed by the small angle neutron scattering method and a mechanism is suggested for the reassembly process of the coaggregates.

7.2 Experimental Details

7.2.1 Sample preparation

A solution of 2.5 g L^{-1} sodium polyacrylate in D_2O (Euriso-top, France, 99.90 atom % deuterium) was prepared by dissolving the freeze-dried polymer and adjusting the pD to 9 using NaOD. Similarly, a stock solution of 2,2'-((diazene-1,2-diylbis(4,1-phenylene))bis(oxy))bis(*N*,*N*,*N*-trimethylethan-1-aminium) dichloride (diAzoEt, structure shown in Figure 7.1A) at a concentration of 50 mmol L^{-1} was prepared in D_2O and the pD was adjusted to 9. For the preparation of PA-diAzoEt complexes the PA stock solution was diluted with the required amount of D_2O and diAzoEt stock solution added under heavy stirring. Typically, a final polymer concentration of 0.5 g L^{-1} was used.

A detailed description of the synthesis and characterization of PA and diAzoEt can be found in the Supporting Information.

7.2.2 Small-Angle Neutron Scattering (SANS)

SANS measurements were performed at the D11 small-angle neutron scattering instrument of the Institut Laue-Langevin (Grenoble, France). Three sample to detector distances (39.0 m collimation 40.5 m, 8.0 m collimation 8.0 m, and 1.4 m collimation 5.5 m) and a neutron wavelength of 0.5 nm (full width at half maximum (FWHM) 9 %) were used to cover a q range of $2 \times 10^{-2} - 5\,nm^{-1}$. We used a circular neutron beam with a diameter of 15 mm. Scattered neutrons were detected with a ^{3}He MWPC detector (CERCA) with 256 × 256 pixels of 3.75 mm × 3.75 mm pixel size. The detector images were azimuthally averaged, corrected to the transmission of the direct beam and scaled to absolute intensity using the LAMP software. Scaling to absolute intensity was based on a 1 mm H_2O cell as a secondary standard ($\frac{d\Sigma}{d\Omega} = 0.929\,cm^{-1}$). The scattering from the solvent and the incoherent background were subtracted from the scattering curves. Details for the data reduction can be found in Chapter 2 of Ref. [26]. The sample temperature was adjusted to temperatures between 25 °C and 66 °C using a circulating water bath. For the time-resolved SANS measurements, acquisition times of 30 s (66 °C) and 1 min (45 °C and 58 °C) were used. The kinetics were recorded at two sample to detector distances (40 m and 8 m) with irradiation of the sample with UV light at 365 nm in between the acquisitions.

The scattering model used to describe the SANS curves is described in detail in the Supporting Information.

7.2.3 UV-VIS Absorbance Spectroscopy

UV-Vis absorbance spectroscopy was performed using a V-630 spectrometer from Jasco. The samples were filled into 1 mm quartz glass cuvettes and typically measured in a wavelength range from 200 nm to 1100 nm. Prior to the measurement of the sample the corresponding solvent (typically D_2O) was measured as a background. The temperature was controlled using a circulating water bath connected to the sample holder. The temperature at the sample position was controlled by placing a cuvette filled with water and a digital thermometer in the sample position.

7.3 Results

Polyelectrolyte-Azobenzene Complexes Sodium polyacrylate (PA) was chosen as an anionic polyelectrolyte, as its solution behavior is well studied and previous works showed that PA exhibits a specific interaction with monovalent and multivalent cations.[27–33] The used polymer was characterized by dynamic and static light scattering and has a weight-averaged molecular weight of 341 kg mol^{-1}. To be able to control the self-assembly with light, a divalent diazophenol cation (diAzoEt), which undergoes a *trans* $\longrightarrow$ *cis* isomerization when exposed to light, was employed.[34] Figure 7.1A shows the chemical structure of the *trans* and *cis* isomer of the diAzoEt cation and Figure 7.1B shows the corresponding UV-Vis absorbance spectrum in aqueous solutions. The *trans* state which is the thermodynamically stable isomer of the molecule, shows a strong absorption band at around 365 nm. By exciting this absorption band, the *trans* state is converted into the *cis* state. This isomer lacks an absorption band at 365 nm but shows one at a longer wavelength of 436 nm.

The *cis* isomer is metastable and therefore isomerization back to *trans* state takes place with time due to thermal energy. The thermal activation energy was obtained by monitoring the absorbance at 365 nm as a function of time at several temperatures yielding an activation energy of around 88.2 ± 2.9 kJ mol^{-1}. This value is close to literature values for similar azobenzene compounds in aqueous solution.[35] Details can be found in the Supporting Information.

Based on this knowledge, complexes of this cation with the negatively charged polyelectrolyte PA were prepared. To identify a ratio of polymer concentration to diAzoEt concentration [diAzoEt], where stable complexes between polymer and dye are found,

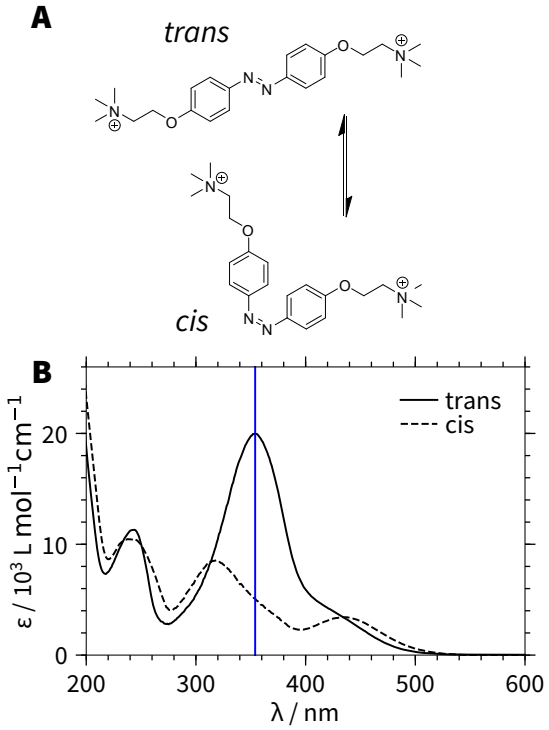


Figure 7.1: **A** Chemical structure of the azobenzene cation diAzoEt in the *trans* as well as in the *cis* state. **B** UV-VIS absorbance spectra of *trans* and *cis* dye. The blue line indicates the wavelength of the UV lamp used for *trans* to *cis* isomerization.

we introduced the charge ratio Z as

$$Z = \frac{2 \cdot [\text{diAzoEt}]}{[\text{PA}]} \tag{7.1}$$

with [PA] being the PA monomer unit concentration. The factor of 2 in eq. 7.1 arises from the divalent character of diAzoEt. Previous works showed that such a charge ratio is an important quantity in the case of electrostatic self-assembly with the self-assembly typically commencing close to charge neutrality ($Z \approx 1.0$).[24,36]

Several samples with a polymer concentration of $0.5\,\mathrm{g\,L^{-1}}$ and increasing dye concentration were prepared. Below a charge ratio of 0.7 solutions stayed clear. In the range of $0.7 \leqslant Z \leqslant 1.0$ highly turbid solutions, which are stable for an extended period of time, are found. The turbidity of the samples in the range of Z between 0.7 and 1.0 indicates the formation of self-assembled structures giving rise to strong scattering of light. Figure 7.2 shows a photograph of the corresponding samples. Above a charge ratio of 1.0 fast precipitation (within several minutes) was found and unlike

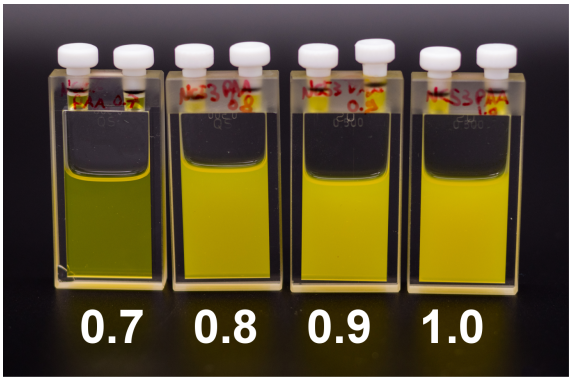


Figure 7.2: Photographs of polyelectrolyte-diAzoEt complexes with increasing charge ratio Z.

to the findings by Gröhn *et al.*[22], even at charge ratios as high as 10 no stable solutions were observed.

The formation of highly turbid solutions can be attributed to the binding of *trans*-diAzoEt to the PA moieties. This binding neutralizes the charge of the polyelectrolyte chain and consequently makes it more hydrophobic. Below $Z = 0.7$ the number of complexed carboxylate groups COO^- is too low to affect the solution behavior of the polymer chains. Once the critical ratio of $Z = 0.7$ is reached, the polymer becomes too hydrophobic to stay molecularly dissolved in solution and forms self-assembled structures with other polyelectrolyte-diAzoEt complexes. These aggregates are stabilized by negatively charged COO^- groups, which are not complexed by diAzoEt. On increasing Z more and more COO^- groups are neutralized and above a charge ratio of 1.0 corresponding to charge neutrality aggregates get too hydrophobic to stay in solution and therefore precipitate.

Structure of the Self-Assemblies To obtain a more detailed knowledge about the structure of the polyelectrolyte-diAzoEt complexes small-angle neutron scattering (SANS) was performed on the complexes. This technique provides ensemble-averaged information about structures from a few nanometers to several micrometer.[26] More importantly, neutrons are weakly interacting with matter. This allows the study of optically turbid samples and metastable states such as the *cis* isomer of diAzoEt, which is not possible using X-ray or light scattering. Accordingly, neutrons do not interfere with the light-induced *trans* $\longrightarrow$ *cis* isomerization of diAzoEt. Unfortunately, this isomer-

ization excludes any meaningful light scattering experiments as exposure to the laser wavelength of 632 nm accelerates the recovery of *trans*-isomers.

For all of the following experiments, a sample at $Z = 0.8$ was chosen. The black data in Figure 7.3A show the SANS profile of the corresponding sample mixed at room temperature. The scattering profile of the complexes with the *trans*-diAzoEt shows well-defined form factor oscillations with two characteristic slopes: a slope close to -4 at medium momentum transfers and a flatter slope of -2 at high q. The slope of -4 is attributed to the scattering arising from a homogeneous object with a sharp interface to the surrounding such as a homogeneous sphere.[37] The form factor oscillations indicate that the PA-diAzoEt complexes have a well-defined size and shape. The second slope of -2 is typical for swollen polymers in a θ solvent.[37] This scattering contribution can arise either from free polymers, which are not incorporated into the complexes or from polymer chains within the complexes. It was previously shown that block copolymers where the core forming block is highly swollen show such a scattering contribution from concentration fluctuations characterized by a correlation length ξ.[38]

Consequently, two different models were tested. The first assumes a mixture of spherical aggregates[39] and free polymer chains,[40] whereas the second model assumes spherical aggregates where the polymer chains in the aggregate form meshes with a characteristic correlation length ξ.[38] The models are described in detail in the Supporting Information. Knowledge of the polymer and dye concentrations, molar volumes, and scattering lengths allows to heavily constrain the fitting procedure. Comparing both models allowed identifying homogeneous spheres composed of partially swollen polymers with a correlation length ξ as the more suitable model because a mixture of spheres and free chains yielded nonphysical fitting parameters.Table 7.1 summarizes the fitting parameters and Figure 7.3B illustrates the structure of the aggregates.

The spherical aggregates have an aggregation number N_{agg} of 576 resulting in a radius R of 76.4 nm with a low polydispersity $\frac{\sigma_R}{R}$ of 5.4 %. The core consists of PA complexed by *trans*-diAzoEt and a considerable amount of water, namely 67.8 vol% ($f_{solvent}$). Such high volume fractions of solvent are not unusual and have been previously reported for micelles including a PA/Ca^{2+} core.[8] Such high water contents may be considered as typical for liquid-liquid phase separations.[8] The high volume fraction of water also explains the scattering contribution from the polymers at high q due to the high amount of water the polymer chains are swollen and form meshes with a correlation length of ξ resulting in a structure similar to the ones found in microgels.[41] The

structure of the aggregates is illustrated in Figure 7.3B. Table 7.1 shows the parameters obtained from the fitting.

Table 7.1: Structural parameters from the form factor fits[40,42] of the SANS data shown in Figure 7.3A.

	Before irradiation	After irradiation	Model
$R_{g,sc}/nm$	—	11.0 ± 0.3	Generalized Gaussian chain[40]
ν	—	0.60 ± 0.01	
R/nm	76.4 ± 3.4	—	Homogeneous spheres composed of swollen polymers[38]
$\frac{\sigma_R}{R}$	0.054 ± 0.001	—	
N_{agg}	576 ± 3	—	
ξ/nm	1.9 ± 0.1	—	
$f_{solvent}$	0.678 ± 0.002	—	

To investigate how a *trans* $\longrightarrow$ *cis* isomerisation of diAzoEt affects the aggregates, the sample was exposed to UV light at 365 nm for 30 min to trigger the *trans* $\longrightarrow$ *cis* isomerization. Surprisingly, the turbidity of the sample completely disappeared accompanied by a slight change of color from yellow to orange. Figure 7.3A also shows the SANS profiles of this sample after UV irradiation. The scattering profile completely changes upon exposure to UV light. The forward scattering decreases by nearly 3 orders of magnitude and the characteristic form factor oscillations completely vanish. Instead, the scattering curve only shows a characteristic slope close to -2 at high q. The data can be well-described by the model of a generalized Gaussian chain[40] with a radius of gyration of the single chains $R_{g,sc}$ of 11.0 nm and a Flory exponent ν of 0.60. Compared to *trans*-diAzoEt, the *cis*-diAzoEt has a higher dipole moment and therefore a better water solubility.[43] As a result, the PA-diAzoEt complexes dissolve to individual PA chains since the diAzoEt dye becomes more hydrophilic and the binding between it and the PA groups is weakened. Dissolution to individual polyelectrolyte chains, whose charges are screened by the *cis*-diAzoEt cations is in fact compatible with a form factor, which is typical for polymers in a good solvent. It has been shown previously that a sufficient concentration of electrolytes screens the charges of polyelectrolytes, resulting in a coiled structure close to the one observed for uncharged polymers.[44] Figure 7.3B illustrates this process and shows photographs of the respective samples.

The complete dissolution of the aggregates triggered by *trans* $\longrightarrow$ *cis* isomerization of diAzoEt at a substoichiometric charge ratio of $Z = 0.8$ makes such NaPA/diAzoEt mixtures a particularly interesting candidate for switchable systems. The present system differs significantly from the respective behavior observed by Gröhn *et al.*[21,25] with

PDADMAC or QPVP and the anionic dye ay38. For both polyelectrolytes, Gröhn *et al.*[21,25] only found a decrease of the aggregate size at substoichiometric ratios and not a complete disintegration. For the dendrimer-like polyelectrolyte, the difference to the present system is even more pronounced as no variation was observed at $Z < 1$ and an increase of the aggregate size was induced by the *trans* $\longrightarrow$ *cis* isomerization of ay38 once the dye was added in excess to the polyelectrolyte.

After showing that the PA-diAzoEt complexes can be effectively disassembled by UV irradiation, the dye was allowed to return to the thermodynamically stable *trans* state. For this, the sample was left for several hours at a constant temperature of 25 °C, which resulted in a color change back from orange to yellow as well as an increase in turbidity. The SANS curve of the final state is shown in Figure 7.3C. The forward scattering increased together with the formation of well-defined form factor oscillations indicating that the PA-diAzoEt are reformed once diAzoEt is converted back from *cis* to *trans*. The scattering curve looks similar to the one shown in Figure 7.3A, however without reaching the Guinier plateau. It is obvious that the initial state is not fully identical to the state after irradiation and relaxation. This can be attributed to the kinetic effects occurring upon the preparation of the initial samples. The outcome of mixing oppositely charged components can strongly depend on the way of mixing. This was previously shown for polyelectrolytes and oppositely charged surfactants.[11,12]

It is hypothesized that upon irradiation and consequent relaxation, it is possible to shift from a kinetically trapped state to the state of thermodynamic equilibrium. As the equilibration at 25 °C results in relatively large structures, which are not fully accessible by the available q range in SANS, the relaxation was performed at several temperatures ranging from 25 °C to 66 °C. The final structures were characterized by SANS and the corresponding scattering profiles are shown in Figure 7.4. Again well-defined form factor oscillations occur and the scattering curves look similar to the one shown in Figure 7.3A.

The UV illumination and reassembly step at 45 °C was repeated several times and the obtained SANS profiles were always identical. Figure 7.11 in the Supporting Information shows the SANS curves after two subsequent irradiation and relaxation cycles. This implies that the structure formation is fully reversible. Further on, we hypothesize that this structure formation can be directed by controlling the temperature during the *cis* $\longrightarrow$ *trans* isomerization. In fact, a continuous shift of the form factor minimum to higher q can be observed upon the increase of the temperature. This shows that the formed structures are becoming smaller as the temperature during the *cis* $\longrightarrow$ *trans* iso-

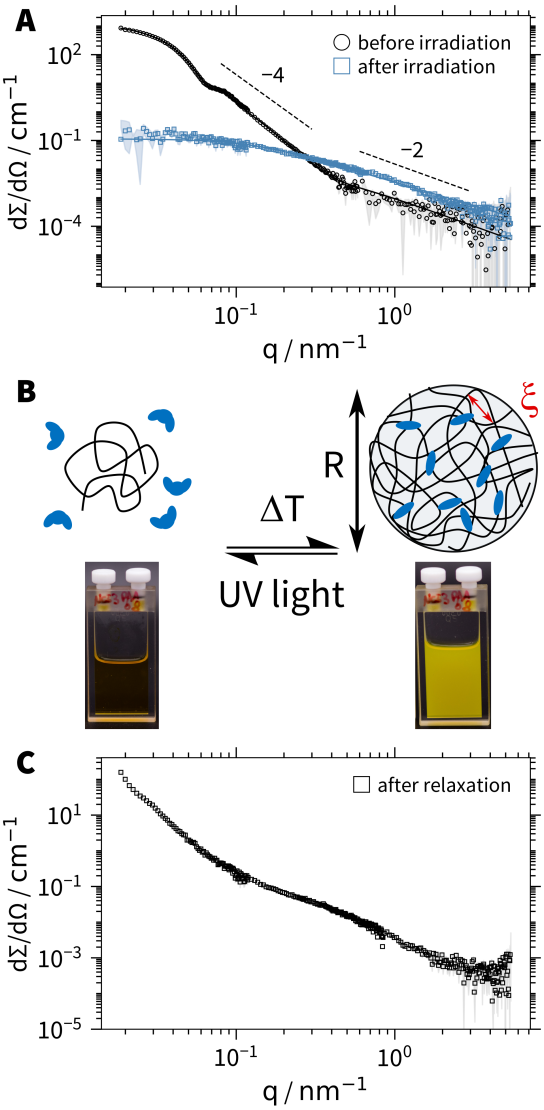


Figure 7.3: **A** SANS profiles of PA-diAzoEt complexes at a charge ratio Z = 0.8 after mixing (black) and after irradiation of the same sample (blue). The solid lines represent fits to the model of a homogeneous sphere composed of swollen polymer coils[38] (black) and the model of a generalized Gaussian chain[40] (blue) at 25 °C. **B** Sketch of the structure before and after irradiation and photographs of the corresponding samples. **C** SANS profile of PA-diAzoEt complexes of the sample shown in **A** after irradiation and relaxation back to the *trans* state at 25 °C.

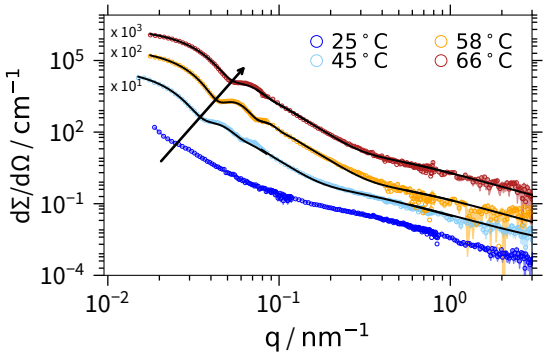


Figure 7.4: SANS profiles of PA-diAzoET complexes at a charge ratio $Z = 0.8$ after irradiation and reassembly at different temperatures ranging from 25 °C to 66 °C. The solid lines represent fits to the model of a homogeneous sphere composed of swollen polymer coils.[38] Data recorded at 25 °C are identical to those in Figure 7.3C.

merization increases, which allows an effective control over the size of the aggregates. To better compare the size of the structures, the data in Figure 7.4 were fitted with the same form factor models used already in Figure 7.3.[38] Table 7.2 summarizes the fitting parameters. For the sample at 25 °C the Guinier plateau was not reached by the covered q range and one form factor oscillation is visible at low q. It was not possible to reliably fit this scattering curve with the form factor model. The minimum size based on the position of the form factor minimum was therefore estimated by $R = \frac{4.49}{q_{min}} \approx 180\,nm$.[26] The radius of the aggregates decreases from 180 nm to 96 nm when going from 25 °C to 66 °C. The degree of aggregation N_{agg} decreases with increasing temperature from 2890 to 980 and in all cases is much larger than that in the initial state at 25 °C. The other parameters such as the mesh size ξ, water content, and polydispersity are similar, indicating that the morphology of the particles does not change significantly.

Table 7.2: Structural parameters from the form factor fits of the SANS data shown in Figure 7.4.

	25 °C	45 °C	58 °C	66 °C
R_g/nm		111.3 ± 7.5	86.5 ± 3.2	71.8 ± 2.1
R/nm	> 180	143.1 ± 1.6	110.0 ± 0.6	96.0 ± 0.8
$\frac{\sigma_R}{R}$	—	0.047 ± 0.001	0.035 ± 0.001	0.052 ± 0.001
N_{agg}	—	2888 ± 44	1539 ± 10	982 ± 5
ξ/nm	—	3.5 ± 0.1	1.7 ± 0.1	2.1 ± 0.1
$f_{solvent}$		0.756 ± 0.003	0.696 ± 0.001	0.709 ± 0.001

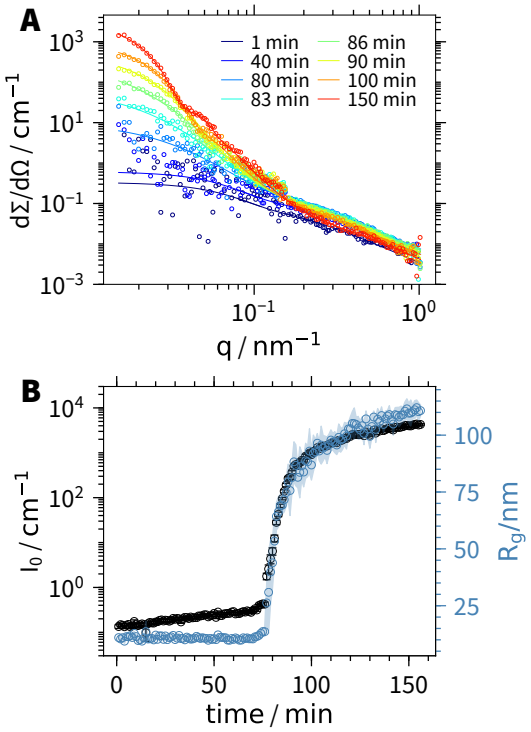


Figure 7.5: **A** Selected SANS profiles of reforming PA-diAzoEt complexes after irradiation and reassembly at 45 °C. The solid lines represent fits to the model of a mixture of free polymer chains and complexes. **B** Forward scattering I_0 and radius of gyration R_g as a function of time for the reforming PA-diAzoEt complexes at 45 °C. The acquisition time for each point was 1 min.

Mechanism of the Self-Assembly Process To understand the findings described above, the reassembly process was monitored using time-resolved SANS experiments. Observing the structure formation as a function of time allows us to obtain important information required to understand the mechanism of the self-assembly process and the effect of temperature on the final aggregate size. Figure 7.5A shows selected SANS profiles from the sample, which was irradiated and allowed to reassemble at 45 °C. The initial scattering curves are similar to one of the irradiated samples presented in Figure 7.3A. With progressing time, the forward scattering slightly increases, however, the curves barely change their shape for the first 80 min. After this, a strong and fast increase in forward scattering takes place, accompanied by the formation of well-defined form factor oscillations. From there on until the end of the process, the form factor oscillations continuously shift to lower q, indicating a further increase in the aggregate size.

First, a Guinier analysis was performed in the low q region of the scattering curves, which allows to obtain model-independent information from the scattering curves. Figure 7.5B shows the forward scattering I_0 as well as the radius of gyration R_g obtained from this analysis as a function of time. Up to 80 min the radius of gyration stays constant at around 11 nm, while the forward scattering increases slightly. From there on I_0 as well as R_g rapidly increase until they approach a constant value. This model-free analysis already gives a first idea of the self-assembly mechanism. In the first step of the reaction, denoted as step I, the polymer dimensions stay constant whereas the forward scattering slightly increases. The increase of I_0 can be attributed to the continuous conversion of *cis* to *trans* dye, as the *trans* state will bind to two monomer units of PA and therefore change the scattering length of the polymer chain, resulting in an increase of the forward scattering. Once a critical fraction of dye is converted and bound to the polyelectrolyte the polymer chains rapidly aggregate and form bigger structures followed by a slower growth to the final size.

To get more quantitative information about the course of the self-assembly, the SANS data were analyzed with a form factor model assuming a mixture of free polymer chains and PA-diAzoEt complexes with varying aggregation number.[38] Together with the information about scattering length densities, molecular volumes, and polymer concentration the fit can be heavily constrained. Furthermore, several parameters such as the water content of the PA-diAzoEt complexes $f_{solvent}$, correlation length ξ, the radius of gyration of the free chains $R_{g,sc}$ and their Flory exponent ν were assumed to be the same for all scattering curves. The solid lines in Figure 7.5A show the obtained fits with the form factor model and Table 7.3 summarizes the global fitting parameters. Setting ξ and $f_{solvent}$ as global fitting parameters is a simplification regarding the following discussion of the self-assembly mechanism. It assumes that the aggregate structures remain unchanged during the process. However, it allows to reliably fit the entire set of scattering curves including the beginning of the aggregation, where the statistical uncertainty is high.

The form factor analysis yields the fraction of polymer chains, which are not associated with aggregates. Figure 7.6A shows this fraction of free polymer as a function of time. As already concluded from the Guinier analysis, in the first part of the process the fraction of free polymer stays constant until around 80 min. From there on the fraction of free polymers rapidly deceases, arising from the formation of first aggregates. From the semi-logarithmic plot of the free polymer fraction, it is obvious that this decrease in the amount of free polymer chains is a process composed of two further steps with

Table 7.3: Structural parameters from the form factor fits of the SANS data recorded during the aggregation kinetics at the three different temperatures.

	45 °C	58 °C	66 °C
ξ/nm	2.1 ± 0.1	2.9 ± 0.1	2.5 ± 0.1
$f_{solvent}$	0.820 ± 0.051	0.836 ± 0.062	0.761 ± 0.059
$R_{g,sc}$/nm	8.0 ± 0.1	11.1 ± 0.2	9.3 ± 0.2
ν	0.56 ± 0.01	0.65 ± 0.01	0.61 ± 0.01

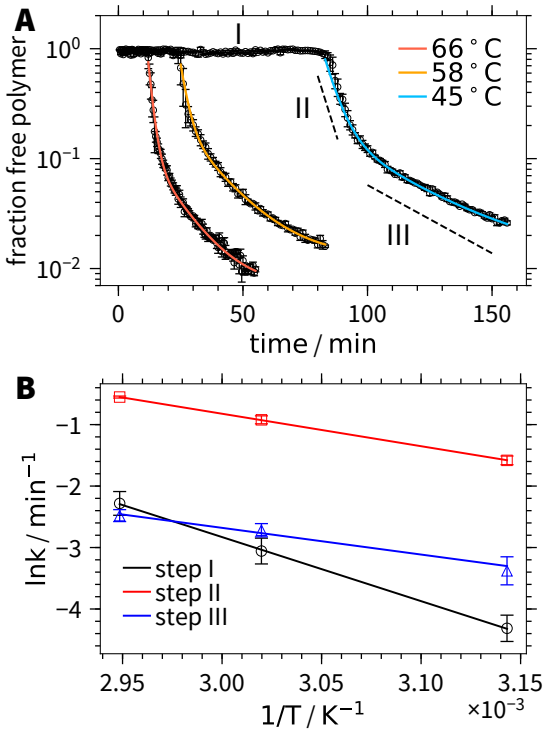


Figure 7.6: **A** Fraction of free polymer as a function of time for the aggregation kinetics recorded at 45 °C, 58 °C and 66 °C. The solid line is a double exponential fit. **B** Arrhenius plot of the rate constant for steps I, II, and III. The solid line is a linear fit, yielding the activation energy E_a.

different characteristic times: a very fast process (step II) and a second slower process (step III). A first indication for such a two-step process is already visible in the semi-logarithmic plot of the forward scattering as a function of time in Figure 7.5B. A double exponential function was used to describe the decay in Figure 7.6A yielding a relaxation rate of $0.21 \pm 0.01\,\mathrm{min}^{-1}$ (step II) and $0.034 \pm 0.002\,\mathrm{min}^{-1}$ (step III).

To estimate the activation energy of the steps I, II, and III the same experiment was performed at two further temperatures: 58 °C and 66 °C. The scattering curves look similar and follow a similar trend as the ones of the experiment at 45 °C. They are shown in the Supporting Information, together with the results from the Guinier analysis. The scattering curves can be described by the same form factor model,[38] yielding the fraction of free polymer as a function of time included in Figure 7.6A. The self-assembly process becomes considerably faster when going from 45 °C to 58 °C and 66 °C. The decay of the free polymer fraction can be well-described by a double exponential function, yielding characteristic rate constants for step II and III of the process. A characteristic time for step I can be obtained by determining the time after which the aggregation starts.

Table 7.4: Activation energies from the form factor fits of the SANS data shown in Figure 7.6.

Step	$E_a/\mathrm{kJ\,mol}^{-1}$
I	86.7 ± 12.3
II	43.9 ± 15.0
III	36.1 ± 10.4

Figure 7.6B shows an Arrhenius plot of the relaxation rates obtained at the three temperatures. They follow a linear behavior, which allows to estimate an activation energy E_a for the three processes summarized in Table 7.4.

The activation energy E_a of $86.7\,\mathrm{kJ\,mol}^{-1}$ for step I is similar to the activation energy found for the *cis* $\longrightarrow$ *trans* isomerization of diAzoEt in the absence of PA ($88.2\,\mathrm{kJ\,mol}^{-1}$). Consequently, step I can be attributed to the conversion of *cis* to *trans* dye, which results in complexation of the PA chains. This is the rate-limiting step of the whole self-assembly process as it has the highest activation energy. As soon as the PA chains are complexed by a sufficient number of *trans* dye, step II starts, which has a lower activation energy of $43.9\,\mathrm{kJ\,mol}^{-1}$. Step II is the very rapid formation of first aggregates, which can be linked to the formation of first nuclei. From there on step III with an activation energy of $36.1\,\mathrm{kJ\,mol}^{-1}$ results in the growth of the structures to

the final size. It is worth mentioning that step II and III have very similar activation energies.

Further information about the mechanism of the self-assembly can be obtained from the model-independent analysis by correlating the radius of gyration R_g with the molecular weight M_w obtained from the forward scattering I_0.[45,46]

$$R_g \propto M_w^{\alpha} \tag{7.2}$$

The exponent α is characteristic of the fractal dimension d_f of the aggregating particles as well as the aggregation mechanism.[45,46] For a coagulation mechanism, where particles of all sizes can aggregate with each other obeying what is called a step-growth process in polymer chemistry, a slope of $\frac{1}{d_f}$ can be found. In contrast, a slope of $\frac{1}{2 \cdot d_f}$ is found when the growth takes place through a monomer-addition mechanism or chain reaction process.. In our example, this would mean that individual PA chains aggregate onto already existing clusters and therefore lead to a growth of those clusters. The factor $\frac{1}{2}$ only occurs in the case of monomer addition, as this process leads to a bimodal reaction mixture. In combination with a different result for the two different averaging formulas (z-averaged R_g^2 and weight-averaged M_w) the bimodal distribution gives different results compared to the monomodal distribution of a step-growth process.[45,46]

Figure 7.7A shows the radius of gyration R_g as a function of the forward scattering I_0, with I_0 being directly proportional to M_w. From the double logarithmic representation, it is obvious that two characteristic slopes are present: a slope in the beginning of the growth with a value close to $\frac{1}{3}$ followed by a second flatter slope of $\frac{1}{6}$. As growing structures during step III are self-similar and spherical (see Section 9 of the Supporting Information) the fractal dimension of the final structures is 3 and the slope of $\frac{1}{6}$ can be clearly attributed to a monomer-addition mechanism taking place during step III ($\frac{1}{2 d_f} = \frac{1}{2 \cdot 3}$). In contrast, the slope of $\frac{1}{3}$ is compatible with two different scenarios. Spherical structures aggregating according to a coagulation mechanism would give rise to a slope of $\frac{1}{3}$, while a monomer-addition mechanism of polymer chains ($d_f = \frac{5}{3}$ for good solvent) would also yield a slope close to $\frac{1}{3} \approx \frac{1}{2 d_f} = \frac{3}{2 \cdot 5}$. To verify whether the structures formed in this regime can be considered as sufficiently dense and spherical, the scattering curves in this regime are plotted in a dimensionless Kratky plot in Figure 7.18. In this representation, a pronounced peak is characteristic of dense structures. At beginning of the aggregation (77 min - 80 min) there is no clear peak visible, which is expected when the self-assembly process starts from individual polymer chains. From this, we conclude that growth in step II produces intermediates, which change their

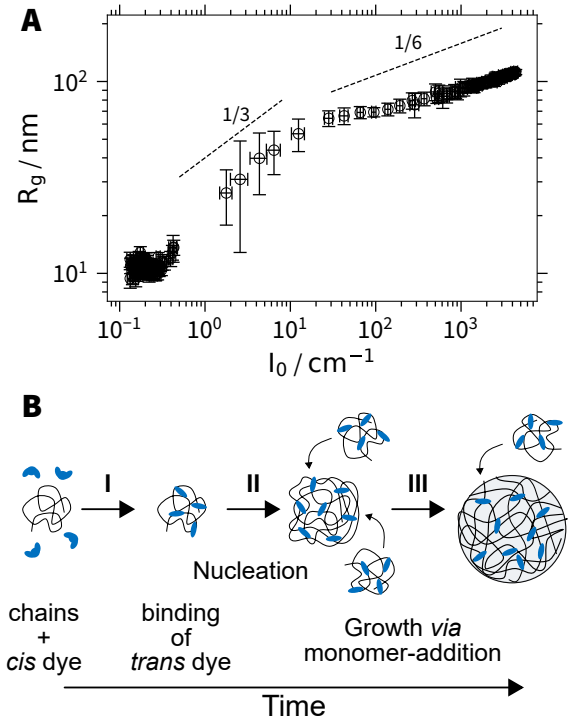


Figure 7.7: **A** Double logarithmic plot of the radius of gyration R_g and the forward scattering I_0 obtained from Guinier analysis of the aggregation kinetics at 45 °C. **B** Illustration of the mechanism of the self-assembly of PA-diAzoEt complexes.

morphology and hence are not self-similar, making an interpretation with power laws questionable. Likely, growth during step II takes place via a monomer-addition mechanism of individual polymer chains to growing particles. The growing particles at the onset of step II have fractal dimensions closer to (crosslinked) polymer coils and gradually change to homogeneous spherical structures, once a sufficient number of polymer chains are aggregated. Those spheres then simply continue to grow according to a monomer-addition mechanism during step III, in accord with the exponent of $\frac{1}{6}$.

Figure 7.7B illustrates the mechanism of the structure formation. First, *cis* diAzoEt gets converted into the *trans* isomer, which binds to the PA chains. Once a certain amount of diAzoEt is bound to the PA coils, rapid nucleation takes place via a monomer-addition mechanism of individual polymer chains to growing species, which gradually change their morphology from coil-like fractals (beginning of step II) to spherical objects (step III). An increase in the temperature during the self-assembly results in a faster nucleation phase and therefore a smaller size and a higher concentration of

nuclei. Since the final growth step follows a monomer-addition mechanism, the final number of particles is directed by the number of nuclei, in turn, determining the size of the final structures.

7.4 Conclusions

Mixtures of the anionic polyelectrolyte polyacrylate (PA) and the *trans* isomer of a divalent diazophenol cation (diAzoEt) form well-defined spherical complexes in aqueous solution. The self-assembly and stability of the aggregates strongly depend on the ratio between PA and diAzoEt. The structures can be reversibly disassembled by triggering the *trans* $\longrightarrow$ *cis* isomerization with UV light, resulting in individual polyelectrolyte chains, which adopt the conformation of polymers in a good solvent. Upon return of the *cis* isomer into the thermodynamically stable *trans* isomer the PA-diAzoEt complexes are reformed, resulting in monodisperse spherical aggregates. Variation of the temperature during this reassembly processes allows to control the size of the final structures with smaller structures forming at high temperatures. The mechanism of this reassembly process was studied with time-resolved small-angle neutron scattering and revealed that it is a process consisting of three steps: The first, rate-limiting step is the *cis* $\longrightarrow$ *trans* isomerization (step I). This involves the binding of the transformed *trans* isomer to the polyelectrolyte chain. Once a sufficient number of dye molecules are bound to PA, the chain is too hydrophobic to stay in solution, resulting in a very rapid nucleation. Nucleation triggers step II taking place via a monomer-addition mechanism. During aggregation in step II the aggregates undergo a morphological change from a loosely packed rugged aggregate to a homogeneous and dense spherical aggregate, which grows during step III via a monomer-addition mechanism to the final size. Control of the nucleation phase allows to influence the number of nuclei and therefore the final aggregate size.

The presented system opens new possibilities in the field of self-assembly by controlling the affinity of binding through an external stimulus such as light. This allows not only reproducible sample preparation but also reversible assembly and disassembly of the oppositely charged building blocks. The presented approach is suitable to convert an initial state, which is kinetically trapped due to mixing into the thermodynamically stable structure.

Acknowledgments

The authors thank the Institut Laue-Langevin (https://doi.ill.fr/10.5291/ILL-DATA.9-11-1910) for the provision of beam time. The authors gratefully acknowledge the Partnership for Soft Condensed Matter (PSCM). N.C. acknowledges funding for a Ph.D. scholarship from Institut Laue-Langevin.

Supporting Information Available

Additional data on the synthesis of the polymer and diAzoEt, determination of the activation energy of the *cis* $\longrightarrow$ *trans* isomerization, scattering length density and molecular volumes of diAzoEt and PA, form factor models and the aggregation kinetics at 58 °C and 66 °C.

7.5 Supporting Information

7.5.1 Materials and synthesis

Materials

4,4'-Dihydroxyazobenzene (TCI Chemicals, France, > 98.0 %), 1,2-dibromoethane (Sigma Aldrich, France, 98.0 %), K_2CO_3 (Sigma Aldrich, France, ⩾ 99.0 %), ethanol (Sigma Aldrich, France, p.a. ⩾ 99.8 %), propan-2-ol (Sigma Aldrich, France, p.a. ⩾ 99.8 %), $CDCl_3$ (Euriso-top, France, 99.50 atom$ deuterium), 4.2 $mol\,L^{-1}$ trimethylamine in ethanol (Sigma Aldrich, France), acetonitrile (Sigma Aldrich, France, ⩾ 99.5 %), D_2O (Euriso-top, France, 99.90 atom% deuterium), Amberlite IRA-402 Cl^- (Merck, France), acrylic acid (Sigma Aldrich, France, >99 %), 4,4-azobis(4-cyanovaleric acid) (Sigma Aldrich, France, >98 %) and 2-(2-carboxyethylsulfanylthiocarbonylsulfanyl)propionic acid (Sigma Aldrich, France) were used as received. Water was purified using a Milli-Q-system.

Synthesis of sodium polyacrylate (PA)

20 g of acrylic acid, 14.1 mg of 2-(2-carboxyethylsulfanylthiocarbonylsulfanyl)propionic acid and 3.9 mg of 4,4-azobis(4-cyanovaleric acid) were dissolved in 100 mL of deionized water at room temperature. Next, the mixture was degassed by flushing with argon for 30 min. The polymerization was performed for 24 h at 70 °C under argon atmosphere. After the reaction the product was allowed to cool to room temperature. Next, the pH of the solution was adjusted to 9 and the product dialyzed (regenerated cellulose, Spectra/Por 6 MWCO = 1 kDa) against a large excess of water for 3 days with an exchange of water every 12 h. Finally, the polymer was freeze dried.

The polymer was characterized in 100 $mmol\,L^{-1}$ NaCl by angular dependent dynamic and static light scattering. The corresponding dynamic and static Zimm plots are shown in Figure 7.8. Table 7.5 summarizes the hydrodynamic radius R_h, radius of gyration R_g and the molecular weight obtained from this analysis.

Table 7.5: Results from the light scattering analysis of PA in aqueous 100 $mmol\,L^{-1}$ NaCl solution.

Polymer	R_h/nm	R_g/nm	M_w/kg mol^{-1}
PA	26.2 ± 1.4	43.0 ± 1.8	340.5 ± 6.7

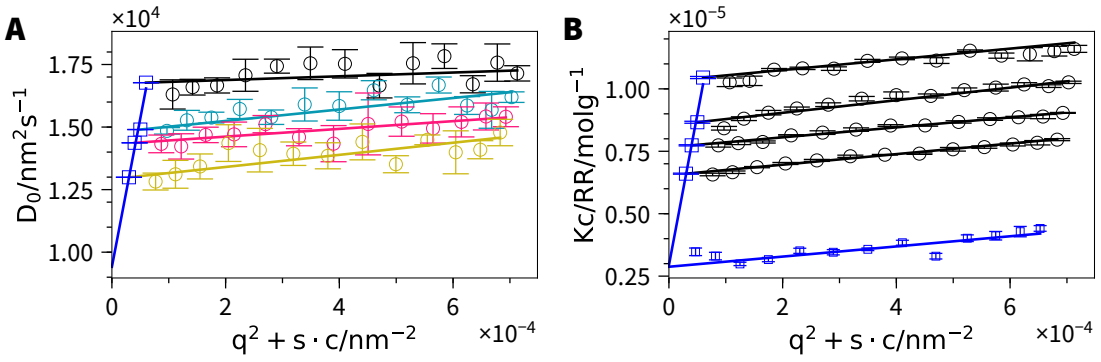


Figure 7.8: Dynamic (**A**) and static (**B**) Zimm plot of PA in 100 mmol L^{-1} NaCl.

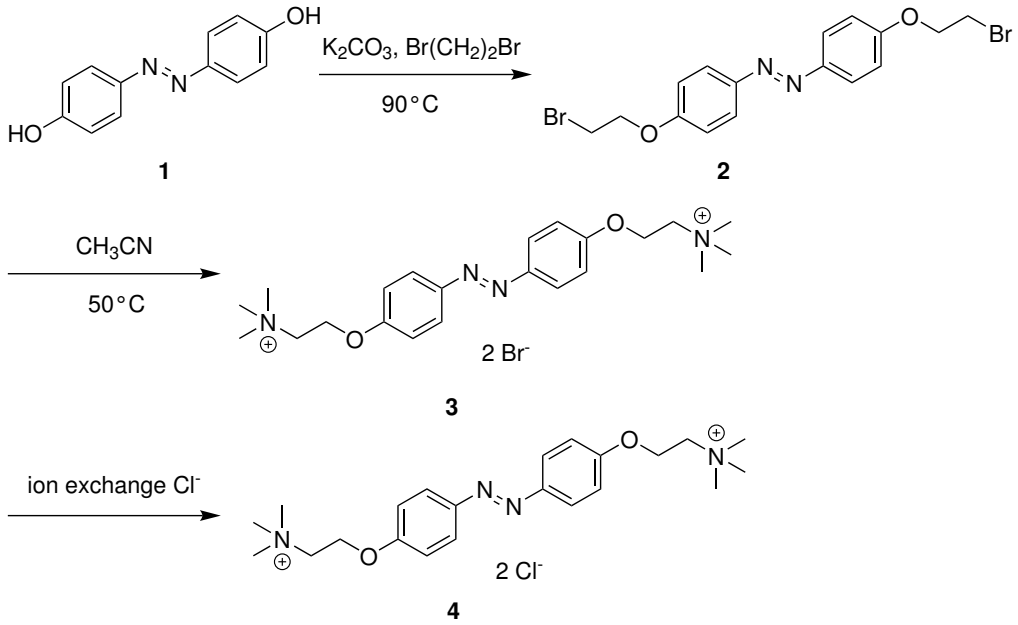


Figure 7.9: Synthesis of diAzoEt.

Synthesis of diAzoEt

Synthesis of 1,2-bis(4-(2-bromoethoxy)phenyl)diazene 2 3 g of 4,4′-dihydroxyazobenzene (14.0 mmol), 26.3 g of 1,2-dibromoethane (140 mmol) and 8.0 g of K_2CO_3 (58.0 mmol) were dissolved in 200 mL acetonitril. The mixture was heated under reflux for 48 h. The mixture was extracted with hot ethanol (2 × 100 mL) and the solution concentrated on a rotary evaporator. The crude product was recrystallized three times from a mixture of ethanol/propan-2-ol (1:1, *v*/*v*), yielding **2** as yellow needles. Yield: 40.4 % (2.41 g, 5.66 mmol).

^{1}H-NMR (500 MHz, $CDCl_3$) $\delta(ppm) = 7.88$ (d, J = 9.0 Hz, 4 H) , 7.02 (d, J = 9.0 Hz, 4 H), 4.37 (t, J = 6.3 Hz, 4 H), 3.68 (t, J = 6.3 Hz, 4 H).

Synthesis of 2,2′-((diazene-1,2-diylbis(4,1-phenylene))bis(oxy))bis(*N*,*N*,*N*-trimethylethan-1-aminium) dichloride 4 A mixture of 1.30 g of **2** (3.04 mmol), 100 mL of a 4.2 mmol L^{-1} solution of trimethylamine in ethanol and 130 mL of acetonitrile was heated to 60 °C and stirred for 48 h in a glass pressure bottle. After cooling down, the mixture was stirred for another 48 h at room temperature. The solvent and excess trimethylamine were removed with a rotary evaporator, the crude product dissolved in H_2O and precipitates removed by centrifugal seperation.

For the ion exchange the aqueous solution of the product was brought onto a column of Amberlite IRA-402 Cl. H_2O was used as an eluent, the eluate was collected and freeze dried. The product was obtained as a yellow powder after recrystallization (3×) in dry ethanol. Yield: 71.2 % (0.84 g, 2.16 mmol)

^{1}H-NMR (500 MHz, D_2O) $\delta(ppm) = 7.91$ (d, J = 9.0 Hz, 4 H), 7.24 (d, J = 9.0 Hz, 4 H), 4.66 (t, J = 4.4 Hz, 4 H), 3.91 (t, J = 4.4 Hz, 4 H), 3.31 (s, 18 H).

7.5.2 Activation energy of cis ⟶ trans isomerization

The activation energy for the *cis* ⟶ *trans* isomerization of diAzoEt was measured by irradiating a sample of diAzoEt (0.5 mmol L^{-1} in D_2O) in the *trans* state with a UV lamp at 365 nm (Spectroline SB-100PA/FB) for at least 30 min and consequently observing the absorbance at 365 nm as a function of time. The recorded increase in absorbance is related to the *cis* ⟶ *trans* isomerization and is a process of first-order. It was consequently fitted with an exponential function according to

$$\mathrm{Abs}_{365\,nm}(t) = \mathrm{Abs}_{365\,nm}(0) \cdot \exp(-t \cdot k) + C \tag{7.3}$$

This experiment was performed at several temperatures ranging from 15 °C to 45 °C. The natural logarithm of the obtained rate constant k is plotted as a function of $\frac{1}{T}$ as shown in Figure 7.10. The slope of the Arrhenius plot yields an activation energy of 88.2 ± 2.9 kJ mol^{-1}.

7.5.3 Molecular volume of diAzoEt and PA

Table 7.6 summarizes the molecular volume of D_2O, diAzoEt and PA for a selection of temperatures. The molecular volume of diAzoEt and PA was determined by measur-

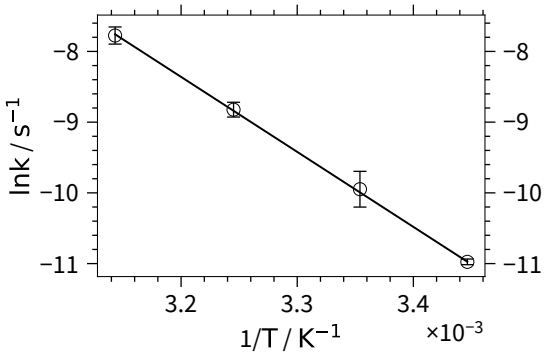


Figure 7.10: Arrhenius plot for the *cis* ⟶ *trans* isomerization of diAzoEt in D_2O.

ing the densities of PA (or diAzoEt) solutions in H_2O at various concentrations. The apparent molecular volume for a given concentration is calculated by

$$V_m(c) = \frac{M}{d_0} - 10^3 \frac{d - d_0}{d_0 c} \tag{7.4}$$

with M being the molar mass of the monomer repeating unit, d_0 the density of the solvent and d the density measured at a given concentration c. Extrapolation of $V_m(c)$ to c_0 yields V_m.

Table 7.6: Molecular volumes for several compounds as a function of temperature.

Compound	Temperature /°C	Molecular volume V_m/nm^3
D_2O	25	0.030113[47]
	45	0.030291[47]
	55	0.030424[47]
	65	0.030581[47]
diAzoEt ($C_{22}H_{34}N_4O_2^{2+}$)[a]	25	0.621
	45	0.638
	55	0.646
	65	0.654
PA^-/NaPA[b]	25	0.0587
	45	0.0600
	55	0.0612
	65	0.0630

[a] Measured molecular volume of the dichloride. [b] The molecular volume of the anion and the sodium salt is approximated to be identical.

7.5.4 Neutron scattering length

The neutron scattering length of the compounds used in the present work are calculated with the respective values of the molecular volumes given in Section 4 and are listed in Table 7.7.

Table 7.7: Neutron scattering length for compounds used in the present work.

Compound	b/fm
D_2O	19.145
diAzoEt ($C_{22}H_{34}N_4O_2{}^{2+}$)	68.132
PA^- ($C_3H_3O_2{}^-$)	20.327
NaPA ($C_3H_3O_2Na$)	23.957

7.5.5 Form factor models

The scattering curves of the PA-diAzoEt complexes were described by the model of a homogeneous sphere composed of blobs of swollen polymer chains. This model was previously used to describe the scattering from block copolymers where the block of the micelles was partially swollen by the solvent.[38]

The macroscopic scattering cross-section is given by

$$\frac{d\Sigma}{d\Omega}(q) = N\left(\frac{4}{3}\pi R^3\right)^2 (\Delta\rho)^2 \left[n_{blob}\left(n_{blob}-1\right)\psi^2\left(q, R_{g,blob}\right)\cdot F^2_{sphere}\left(q, R\right) + \frac{n_{blob} F_{chain}\left(q, R_{g,blob}\right)}{n_{blob}{}^2}\right] \tag{7.5}$$

with N being the number of aggregates, R the radius of the spherical aggregate and $\Delta\rho$ the scattering length density of the aggregate, n_{blob} the number of polymer blobs, $\psi\left(q, R_{g,blob}\right)$ is the form factor amplitude of the polymer chain, $F_{sphere}(q, R)$ the form factor amplitude of a homogeneous sphere and $F_{chain}(q, R_{g,blob})$ the self-correlation term of Gaussian chains.

The number of polymer blobs n_{blobs} is given by

$$n_{blob} = \frac{a_1 V_{sphere}}{V_{blob}} \tag{7.6}$$

with a_1 being a scaling factor (fitting parameter), V_{sphere} the volume of the spherical aggregate ($\frac{4}{3}\pi R^3$) and V_{blob} the volume of the blob given by

$$V_{blob} = \frac{4}{3}\pi R^3_{g,blob} \tag{7.7}$$

with $R_{g,blob}$ the radius of gyration of a blob. $R_{g,blob}$ is connected to the correlation length ξ by

$$R_{g,blob} = \xi\sqrt{3} \tag{7.8}$$

The volume and consequently the radius of the sphere is given by

$$V_{sphere} = N_{agg} \cdot V_m \tag{7.9}$$

with N_{agg} being the aggregation number and V_m the molecular volume of one polymer chain. It is defined by the degree of polymerization DP and the molecular volume of one monomer unit $V_{m,monomer\ unit}$

$$V_m = DP \cdot V_{m,monomer\ unit} \tag{7.10}$$

The molecular volume of one monomer unit is composed of several contributions

$$V_{m,monomer\ unit} = ZV_{m,PA^-} + 0.5ZV_{m,diAzoEt} + (1-Z)V_{m,NaPA} + hV_{m,D_2O} \tag{7.11}$$

Z is the charge ratio ($\frac{2[diAzoEt]}{[PA]}$), V_{m,PA^-} the molecular volume of PA^- monomer unit, $V_{m,diAzoEt}$ the molecular volume of the diAzoEt dye, $V_{m,NaPA}$ the molecular volume of sodium polyacrylate, h the number of water molecules per monomer unit and V_{m,D_2O} the molecular volume of heavy water.

Similarly the scattering length $b_{monomer\ unit}$ of a monomer unit can be defined as

$$b_{monomer\ unit} = Zn_{PA^-} + 0.5Zb_{diAzoEt} + (1-Z)b_{NaPA} + hb_{D_2O} \tag{7.12}$$

The scattering length density ρ is defined as

$$\rho = \frac{b_{monomer\ unit}}{V_{m,monomer\ unit}} \tag{7.13}$$

The form factor amplitude of the polymer chain $\psi(q, R_{g,blob})$ is given by

$$\psi(q, R_{g,blob}) = \frac{1 - \exp\left(-q^2R_{g,blob}^2\right)}{q^2R_{g,blob}^2} \tag{7.14}$$

The form factor amplitude of a homogeneous sphere with a radius R is defined as

$$F_{sphere}(q, R) = 3\frac{\sin(qR) - qR\cos(qR)}{(qR)^3} \tag{7.15}$$

The self-correlation term of Gaussian chains (Debye function) is given by

$$F_{chain}\left(q, R_{g,blob}\right) = 2\frac{\exp\left(-q^2R_{g,blob}^2\right) - 1 + q^2R_{g,blob}^2}{\left(q^2R_{g,blob}^2\right)^2} \tag{7.16}$$

In order to take into account the size distribution of micelles we assumed a log-normal distribution of the aggregation number N_{agg}

$$p\left(N_{agg}\right) = \frac{1}{H\sqrt{2\pi}N_{agg}} \exp\left(\frac{-\log\left(N_{agg} - M\right)^2}{2H^2}\right) \tag{7.17}$$

where H and M define the distribution and are connected to the mean aggregation number $\overline{N_{agg}}$ and standard deviation $\sigma_{\overline{N_{agg}}}$ by

$$\overline{N_{agg}} = \exp\left(M + \frac{H^2}{2}\right) \tag{7.18}$$

$$\sigma_{\overline{N_{agg}}} = \sqrt{\exp\left(H^2 + 2M\right)\left(\exp\left(H^2\right) - 1\right)} \tag{7.19}$$

The macroscopic scattering cross-section is therefore

$$\frac{d\Sigma}{d\Omega}_{\text{polydisperse}}(q) = \int \frac{d\Sigma}{d\Omega}(q)p(N_{agg})dN_{agg} \tag{7.20}$$

In order to be able to describe the scattering from polymer chains where the Flory exponent is deviating from $\nu = 0.5$ the generalized Gaussian chain form factor can be used. It is given by[40]

$$P(q) = \frac{1}{\nu U^{\frac{1}{2\nu}}}\gamma(\frac{1}{2\nu}, U) - \frac{1}{\nu U^{\frac{1}{\nu}}}\gamma(\frac{1}{\nu}, U) \tag{7.21}$$

with U being defined as

$$U = (2\nu + 1)(2\nu + 2)\frac{q^2 R_g^2}{6} \tag{7.22}$$

and $\gamma(a, x)$ the incomplete Gamma function

$$\gamma(a, x) = \int_0^x t^{a-1} \exp\left(-t\right)dt \tag{7.23}$$

The form factor fits of the small-angle scattering data were done using the SASET program.[48] Instrumental resolution for SANS has been taken into account according to Reference [49]. The macroscopic scattering function is convoluted with a resolution function $R\left(q, \sigma_q\right)$, which depends on wavelength spread, finite collimation of the beam and detector resolution

$$\frac{d\Sigma}{d\Omega}_{\text{smeared}}(q) = \int R(q, \sigma_q)\frac{d\Sigma}{d\Omega}(q)dq \tag{7.24}$$

We took into account the instrumental resolution for all points from each detector configuration and merged the data only for final representation. This approach does not involve truncation of the data in the region of overlapping q, which leads to a larger number of available data points in the analysis.

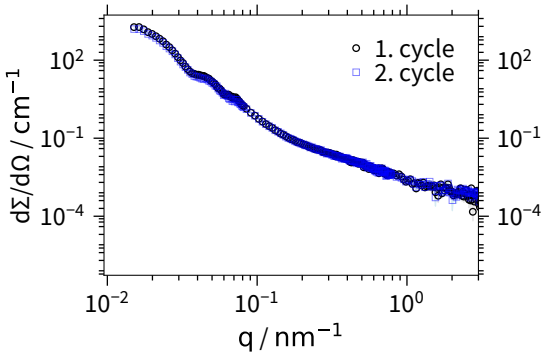


Figure 7.11: SANS profiles of PA-diAzoEt complexes after two illumination and reassembly cycles at 45 °C.

7.6 Reversibility of structure formation

Figure 7.11 shows the SANS curves of PA-diAzoEt after two illumination and reassembly cycles at 45 °C. The data overlap perfectly, indicating reversibility of the process.

7.6.1 Aggregation kinetics

Figure 7.12, 7.13 and 7.14 show 3D plots of the aggregation kinetics at 45 °C, 58 °C and 66 °C.

A selection of scattering curves including the fit with the form factor model of a mixture of free polymer chains and PA-diAzoEt complexes at 58 °C and 66 °C are shown in Figure 7.15A and 7.16A. The radius of gyration R_g and forward scattering I_0 obtained from a Guinier analysis at low q is shown in Figure 7.15B and 7.16B.

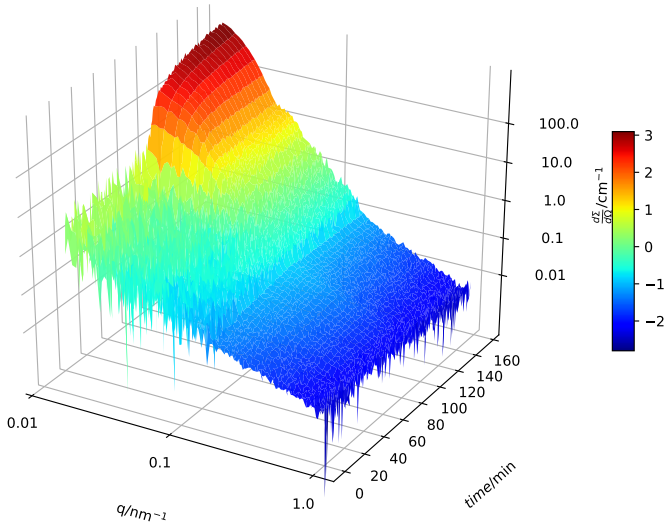


Figure 7.12: 3D plot of the SANS data of the aggregation kinetics at 45 °C.

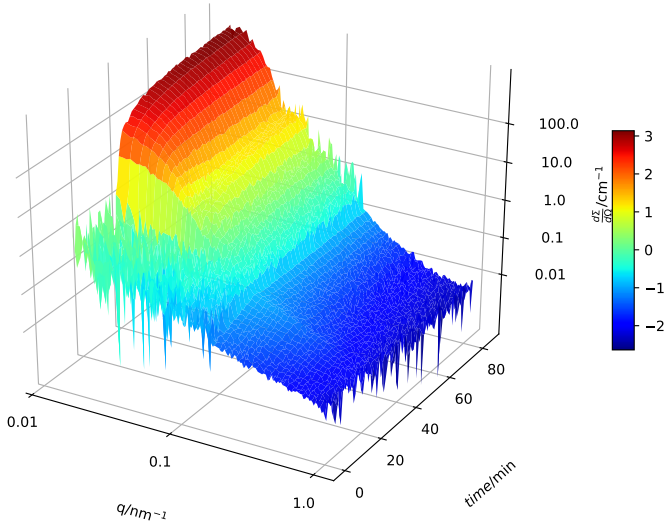


Figure 7.13: 3D plot of the SANS data of the aggregation kinetics at 55 °C.

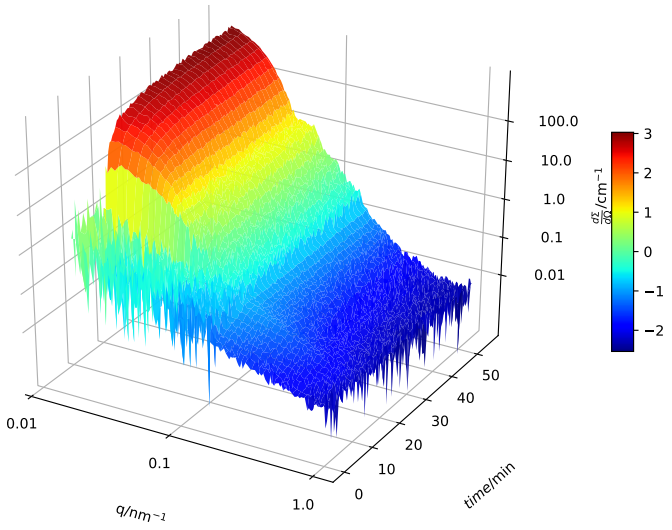


Figure 7.14: 3D plot of the SANS data of the aggregation kinetics at 65 °C.

7.6.2 Correlation of R_g and I_0

The correlation between R_g and I_0 obtained from a Guinier analysis at 58 °C and 66 °C is shown in Figure 7.17. Similarly as for the data at 45 °C presented in the main manuscript two characteristic slopes can be identified: A slope close to $\frac{1}{3}$ and one close to $\frac{1}{6}$.

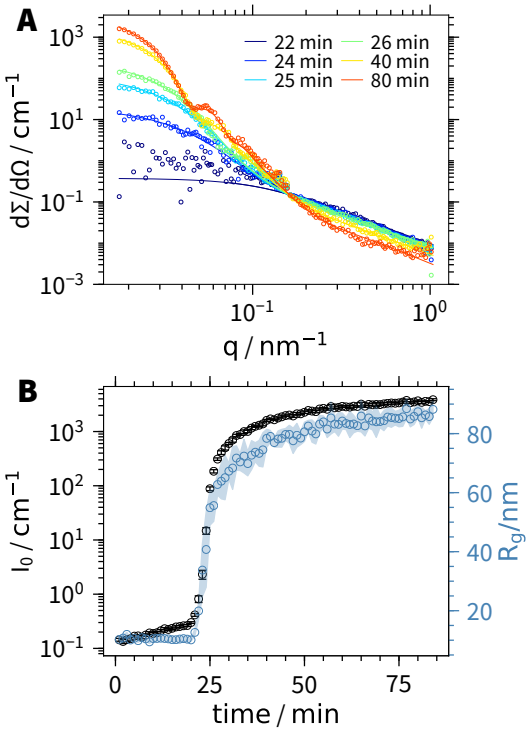


Figure 7.15: **A** Selected SANS profiles of PA-diAzoEt complexes reforming after irradiation at 58 °C. The solid lines represent fit to the model of a mixture of free polymer chains and complexes. **B** Forward scattering I_0 and radius of gyration R_g as a function of time for the reforming PA-diAzoEt complexes at 58 °C.

7.6.3 Kratky plots

In order to elucidate whether the structures in the beginning of the aggregation can already be considered as dense homogeneous spheres we plotted a selection of scattering curves in the Kratky representation $P(q)(q \cdot R_g)^2$ as a function of $q \cdot R_g$ in Figure 7.18A. The data cover the scattering curves from the aggregation kinetics at 45 °C from 71 min to 85 min (step II). The maximum in the Kratky representation is typical for dense objects with characteristic form factor oscillations. Moreover, a selection of three scattering curves covering step III of the aggregation are plotted in Figure 7.18B.

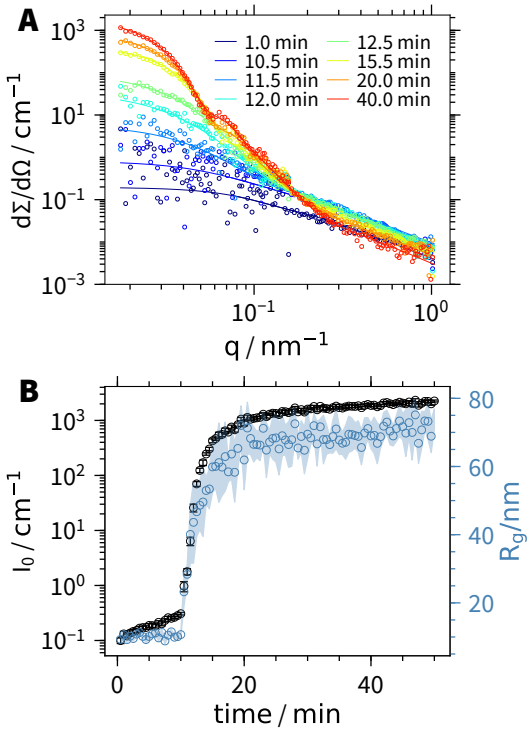


Figure 7.16: **A** Selected SANS profiles of PA-diAzoEt complexes reforming after irradiation at 66 °C. The solid lines represent fit to the model of a mixture of free polymer chains and complexes. **B** Forward scattering I_0 and radius of gyration R_g as a function of time for the reforming PA-diAzoEt complexes at 66 °C.

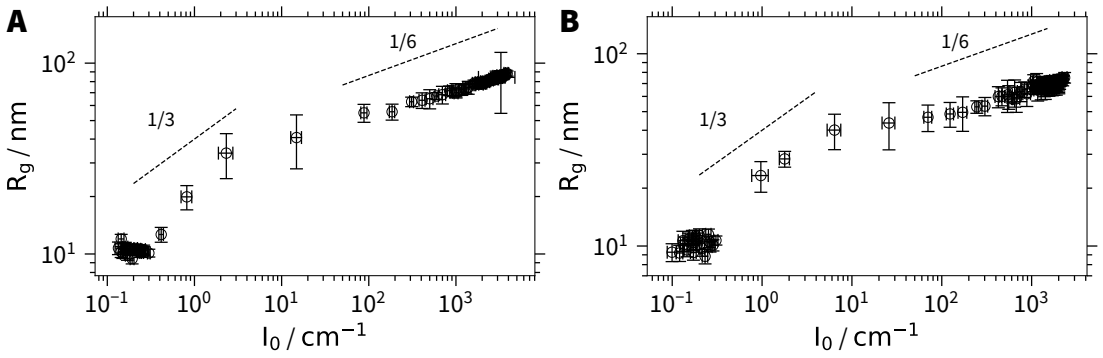


Figure 7.17: **A** and **B** Double logarithmic plot of the radius of gyration R_g and the forward scattering I_0 obtained from Guinier analysis of the aggregation kinetics 58 °C (**A**) and 66 °C (**B**).

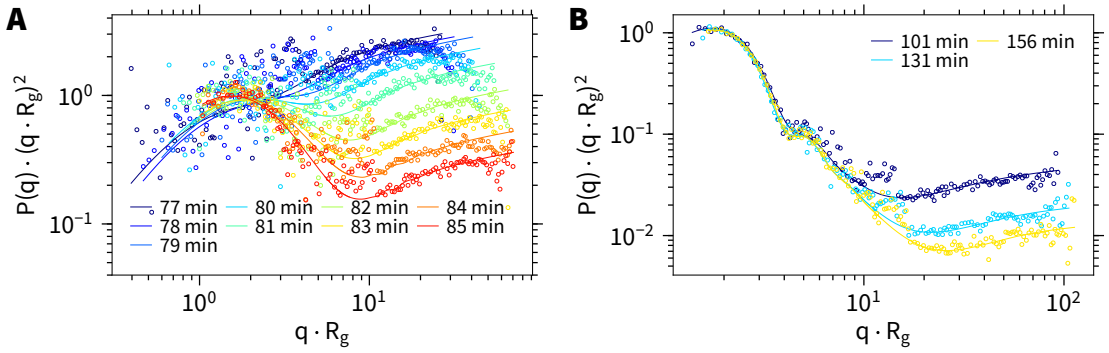


Figure 7.18: Kratky plot of the scattering curves during step II (**A**) and step III (**B**) of the aggregation process at 45 °C. The solid lines are fits using the form factor model of a mixture between free chains and spherical aggregates.

7.7 References

1. Zheng, Y.; Thai, T.; Reineck, P.; Qiu, L.; Guo, Y.; Bach, U. *Adv. Funct. Mater.* **2013**, *23*, 1519–1526, DOI: 10.1002/adfm.201202073.
2. Kostiainen, M. A.; Hiekkataipale, P.; Laiho, A.; Lemieux, V.; Seitsonen, J.; Ruokolainen, J.; Ceci, P. *Nat. Nanotechnol.* **2013**, *8*, 52–56, DOI: 10.1038/nnano.2012.220.
3. Appel, E. A.; Tibbitt, M. W.; Greer, J. M.; Fenton, O. S.; Kreuels, K.; Anderson, D. G.; Langer, R. *ACS Macro Lett.* **2015**, *4*, 848–852, DOI: 10.1021/acsmacrolett.5b00416.
4. Kalsin, A. M.; Fialkowski, M.; Paszewski, M.; Smoukov, S. K.; Bishop, K. J. M.; Grzybowski, B. A. *Science (80-.).* **2006**, *312*, 420–424, DOI: 10.1126/science.1125124.
5. Spruijt, E.; Leermakers, F. A.; Fokkink, R.; Schweins, R.; Van Well, A. A.; Cohen Stuart, M. A.; Van Der Gucht, J. *Macromolecules* **2013**, *46*, 4596–4605, DOI: 10.1021/ma400132s.
6. Lin, M. Y.; Lindsay, H. M.; Weitz, D. A.; Ball, R. C.; Klein, R.; Meakin, P. *Nature* **1989**, *339*, 360–362, DOI: 10.1038/339360a0.
7. Carl, N.; Prévost, S.; Fitzgerald, J. P. S.; Karg, M. *Phys. Chem. Chem. Phys.* **2017**, *19*, 16348–16357, DOI: 10.1039/C7CP01807J.
8. Carl, N.; Prévost, S.; Schweins, R.; Huber, K. *Soft Matter* **2019**, *15*, 8266–8271, DOI: 10.1039/C9SM01138B.

9. Chiappisi, L.; Prévost, S.; Grillo, I.; Gradzielski, M. *Langmuir* **2014**, *30*, 1778–1787, DOI: 10.1021/la404718e.
10. Chiappisi, L.; Hoffmann, I.; Gradzielski, M. *Soft Matter* **2013**, *9*, 3896–3909, DOI: 10.1039/c3sm27698h.
11. Mezei, A.; Mészáros, R.; Varga, I.; Gilányi, T. *Langmuir* **2007**, *23*, 4237–4247, DOI: 10.1021/la0635294.
12. Mészáros, R.; Thompson, L.; Bos, M.; Varga, I.; Gilányi, T. *Langmuir* **2003**, *19*, 609–615, DOI: 10.1021/la026616e.
13. Papadakis, C. M.; Müller-Buschbaum, P.; Laschewsky, A. *Langmuir* **2019**, *35*, 9660–9676, DOI: 10.1021/acs.langmuir.9b01444.
14. Vishnevetskaya, N. S.; Hildebrand, V.; Dyakonova, M. A.; Niebuur, B. J.; Kyriakos, K.; Raftopoulos, K. N.; Di, Z.; Müller-Buschbaum, P.; Laschewsky, A.; Papadakis, C. M. *Macromolecules* **2018**, *51*, 2604–2614, DOI: 10.1021/acs.macromol.8b00096.
15. Liu, S.; Billingham, N. C.; Armes, S. P. *Angew. Chemie - Int. Ed.* **2001**, *40*, 2328–2331, DOI: 10.1002/1521-3773(20010618)40:12⟨2328::AID-ANIE2328⟩3.0.CO;2-M.
16. Kathan, M.; Hecht, S. *Chem. Soc. Rev.* **2017**, *46*, 5536–5550, DOI: 10.1039/C7CS00112F.
17. Bléger, D.; Hecht, S. *Angew. Chemie Int. Ed.* **2015**, *54*, 11338–11349, DOI: 10.1002/anie.201500628.
18. Göstl, R.; Senf, A.; Hecht, S. *Chem. Soc. Rev.* **2014**, *43*, 1982, DOI: 10.1039/c3cs60383k.
19. Ihrig, S. P.; Eisenreich, F.; Hecht, S. *Chem. Commun.* **2019**, *55*, 4290–4298, DOI: 10.1039/C9CC01431D.
20. Hou, L.; Zhang, X.; Cotella, G. F.; Carnicella, G.; Herder, M.; Schmidt, B. M.; Pätzel, M.; Hecht, S.; Cacialli, F.; Samorì, P. *Nat. Nanotechnol.* **2019**, *14*, 347–353, DOI: 10.1038/s41565-019-0370-9.
21. Mariani, G.; Krieger, A.; Moldenhauer, D.; Schweins, R.; Gröhn, F. *Macromol. Rapid Commun.* **2018**, *1700860*, 1700860, DOI: 10.1002/marc.201700860.
22. Willerich, I.; Gröhn, F. *Angew. Chemie - Int. Ed.* **2010**, *49*, 8104–8108, DOI: 10.1002/anie.201003271.
23. Gröhn, F. *Soft Matter* **2010**, *6*, 4296, DOI: 10.1039/cosm00411a.

24. Willerich, I.; Ritter, H.; Gröhn, F. *J. Phys. Chem. B* **2009**, *113*, 3339–3354, DOI: 10.1021/jp8096605.

25. Moldenhauer, D.; Gröhn, F. *J. Polym. Sci. Part B Polym. Phys.* **2013**, *51*, 802–816, DOI: 10.1002/polb.23276.

26. Zemb, T.; Lindner, P., *Neutrons, X-rays and light: scattering methods applied to soft condensed matter*; North-Holland: 2002.

27. Lages, S.; Lindner, P.; Sinha, P.; Kiriy, A.; Stamm, M.; Huber, K. *Macromolecules* **2009**, *42*, 4288–4299, DOI: 10.1021/ma8027547.

28. Goerigk, G.; Schweins, R.; Huber, K.; Ballauff, M. *Europhys. Lett.* **2004**, *66*, 331–337, DOI: 10.1209/epl/i2003-10215-y.

29. Schweins, R.; Goerigk, G.; Huber, K. *Eur. Phys. J. E* **2006**, *21*, 99–110, DOI: 10.1140/epje/i2006-10047-7.

30. Schweins, R.; Huber, K. *Eur. Phys. J. E* **2001**, *5*, 117–126, DOI: 10.1007/s101890170093.

31. Huber, K. *J. Phys. Chem.* **1993**, *97*, 9825–9830, DOI: 10.1021/j100140a046.

32. Huber, K.; Witte, T.; Hollmann, J.; Keuker-Baumann, S. *J. Am. Chem. Soc.* **2007**, *129*, 1089–1094, DOI: 10.1021/ja063368q.

33. Lages, S.; Goerigk, G.; Huber, K. *Macromolecules* **2013**, *46*, 3570–3580, DOI: 10.1021/ma400427d.

34. Zinchenko, A. A.; Tanahashi, M.; Murata, S. *ChemBioChem* **2012**, *13*, 105–111, DOI: 10.1002/cbic.201100492.

35. Momotake, A.; Arai, T. *Tetrahedron Lett.* **2004**, *45*, 4131–4134, DOI: 10.1016/j.tetlet.2004.03.152.

36. Mariani, G.; Schweins, R.; Gröhn, F. *Macromol. Chem. Phys.* **2017**, *218*, 1–9, DOI: 10.1002/macp.201700191.

37. Pedersen, J. S. *Adv. Colloid Interface Sci.* **1997**, *70*, 171–210, DOI: 10.1016/S0001-8686(97)00312-6.

38. Pedersen, J. S.; Hamley, I. W.; Ryu, C. Y.; Lodge, T. P. *Macromolecules* **2000**, *33*, 542–550, DOI: 10.1021/ma990740w.

39. Rayleigh, L. *Proc. Roy. Soc. London* **1911**, *A84*, 25–38.

40. Hammouda, B. *Polym. Charact.* **1993**, *106*, 87–133, DOI: 10.1007/BFb0025862.

41. Dulle, M.; Jaber, S.; Rosenfeldt, S.; Radulescu, A.; Förster, S.; Mulvaney, P.; Karg, M. *Phys. Chem. Chem. Phys.* **2015**, *17*, 1354–1367, DOI: 10.1039/C4CP04816D.

42. Pedersen, J. S. *J. Appl. Crystallogr.* **2000**, *33*, 637–640, DOI: 10 . 1107 / S0021889899012248.

43. Hartley, G. S.; Le Fèvre, R. J. W. *J. Chem. Soc.* **1939**, 531–535, DOI: 10 . 1039 / JR9390000531.

44. Schweins, R.; Hollmann, J.; Huber, K. *Polymer* **2003**, *44*, 7131–7141, DOI: 10.1016/j.polymer.2003.07.005.

45. Liu, J.; Pancera, S.; Boyko, V.; Shukla, A.; Narayanan, T.; Huber, K. *Langmuir* **2010**, *26*, 17405–17412, DOI: 10.1021/la101888c.

46. Liu, J.; Rieger, J.; Huber, K. *Langmuir* **2008**, *24*, 8262–8271, DOI: 10.1021/la8006519.

47. Haynes, W., *CRC Handbook of Chemistry and Physics*; CRC Press: 2014.

48. Muthig, M.; Prévost, S.; Orglmeister, R.; Gradzielski, M. *J. Appl. Crystallogr.* **2013**, *46*, 1187–1195, DOI: 10.1107/S0021889813016658.

49. Pedersen, J. S.; Posselt, D.; Mortensen, K. *J. Appl. Crystallogr.* **1990**, *23*, 321–333, DOI: 10.1107/S0021889890003946.

Chapter 8

List of publications

This thesis is based upon the following publications

- Carl, N.; Prévost, S.; Schweins, R.; Huber, K. *Soft Matter* **2019**, *15*, 8266–8271, DOI: 10.1039/C9SM01138B
- Carl, N.; Prévost, S.; Schweins, R.; Houston, J. E.; Morfin, I.; Huber, K. *Macromolecules* **2019**, *52*, 8759–8770, DOI: 10.1021/acs.macromol.9b01924
- Carl, N.; Prévost, S.; Schweins, R.; Huber, K. *Colloid Polym. Sci* **2019**, accepted.
- Carl, N.; Müller, W.; Schweins, R.; Huber, K. *Langmuir* **2019**, DOI: 10.1021/acs.langmuir.9b03040

Other publications by the author

- Carl, N.; Prévost, S.; Fitzgerald, J. P. S.; Karg, M. *Phys. Chem. Chem. Phys.* **2017**, *19*, 16348–16357, DOI: 10.1039/C7CP01807J
- Rauh, A.; Carl, N.; Schweins, R.; Karg, M. *Langmuir* **2018**, *34*, 854–867, DOI: 10.1021/acs.langmuir.7b01595
- Hansch, M.; Kaub, H. P.; Deck, S.; Carl, N.; Huber, K. *J. Chem. Phys.* **2018**, *148*, 114906, DOI: 10.1063/1.5019877
- Penttilä, P. A.; Vierros, S.; Utriainen, K.; Carl, N.; Rautkari, L.; Sammalkorpi, M.; Österberg, M. *Langmuir* **2019**, *35*, 8373–8382, DOI: 10.1021/acs.langmuir.9b01135
- Penttilä, P. A.; Altgen, M.; Carl, N.; van der Linden, P.; Morfin, I.; Österberg, M.; Schweins, R.; Rautkari, L. *Cellulose* **2019**, *7*, DOI: 10.1007/s10570-019-02781-7
- Carl, N.; Sindram, J.; Gallei, M.; Egelhaaf, S. U.; Karg, M. *Phys. Rev. E* **2019**, *100*, 052605, DOI: 10.1103/PhysRevE.100.052605

Chapter 9

List of conference contributions

Oral presentations

- Nico Carl, Sylvain Prévost, Ralf Schweins, Klaus Huber : *Self-assembly of block copolymers of negatively charged polyelectrolytes and multivalent cations*

  XVII International Small Angle Scattering conference, Traverse City, United States of America, 2018.

- Nico Carl, Ralf Schweins, Klaus Huber : *Controlling Self-assembly with Light*

  European Conference on Neutron Scattering, Saint Petersburg, Russia, 2019.

- Nico Carl, Ralf Schweins, Klaus Huber : *Controlling Self-assembly with Light*

  Conference of the European Colloid and Interface Society, Leuven, Belgium, 2019.

Poster presentations

- Nico Carl, Sylvain Prévost, Ralf Schweins, Klaus Huber : *Metal cations/anionic block copolyelectrolytes - Using specific interactions for self-assembly*

  Bayreuther Polymer Symposium, Bayreuth, Germany, 2016.

- Nico Carl, Sylvain Prévost, Ralf Schweins, Klaus Huber : *Self-assembly of block copolymers of negatively charged polyelectrolytes and multivalent cations*

  International Symposium on Polyelectrolytes, Wageningen, The Netherlands, 2018.